

**THE SYNERGISTIC EFFECT OF NIOBIUM
AND BORON ON RECRYSTALLIZATION IN HOT
WORKED AUSTENITE**

by

• © L.T. Mavropoulos

**A Thesis Submitted to the Faculty of Graduate Studies
and Research in Partial Fulfilment of the Requirements
for the Degree of Doctor of Philosophy**

**Department of Mining and Metallurgical Engineering
McGill University
Montreal, Canada**

October 1986

Permission has been granted to the National Library of Canada to microfilm this thesis and to lend or sell copies of the film.

The author (copyright owner) has reserved other publication rights, and neither the thesis nor extensive extracts from it may be printed or otherwise reproduced without his/her written permission.

L'autorisation a été accordée à la Bibliothèque nationale du Canada de microfilmer cette thèse et de prêter ou de vendre des exemplaires du film.

L'auteur (titulaire du droit d'auteur) se réserve les autres droits de publication; ni la thèse ni de longs extraits de celle-ci ne doivent être imprimés ou autrement reproduits sans son autorisation écrite.

ISBN 0-315-38302-X

ABSTRACT

Four ultra low carbon bainitic steels were tested under interrupted and continuous loading conditions. These materials were made from a base steel containing 0.026% C, to which were added one or both of 0.055% Nb and/or 30 ppm of B. In this way, the influence on the rapidity of recrystallization of additions of: (i) Nb; (ii) B; and (iii) Nb + B was assessed independently.

The static recrystallization kinetics of the hot worked austenite were determined for prestrains of 0.12, 0.25 and 0.50 in the temperature range 900 to 1100°C. The static results are presented in the form of percentage softening vs. log time plots. These results, together with static RTT diagrams, indicate that the addition of B is most effective in retarding recrystallization in the presence of Nb. Furthermore, the degree of retardation is influenced by both the prestrain and temperature. The kinetics of recovery and recrystallization are characterized in terms of the Avrami equation; the influence of prestrain, temperature and alloy composition on the coefficients and exponents is described.

The kinetics of dynamic recrystallization were evaluated in the temperature interval from 1000 to 1100°C and at strain rates from 10^{-3} to 0.5 s^{-1} . The peak strain ϵ_p was taken as a measure of the onset of dynamic recrystallization, and the recrystallization strain ϵ_x of the duration of dynamic recrystallization. These two quantities, divided by the testing strain rate $\dot{\epsilon}$, provided the nucleation and recrystallization times, respectively. The dynamic RTT (DRTT) curves produced in this way are consistent with the static ones.

Carbon extraction replicas and autoradiographic photographs were prepared. These indicate that boron acts as a solute and segregates to the moving grain boundaries. A physical model based on the strain induced segregation of boron is proposed. It relies on the ratio of grain boundary to matrix diffusivity of the Nb present to explain the synergistic action between Nb and B. Finally, the solute drag theory is employed to show that the order of effectiveness of microalloying elements is that of their interaction energies E_0 . The elements with the highest interaction energies also have the highest

diffusivities in steels. As a result, elements with high diffusivities can be expected to exert the highest drag forces.

RESUME

Quatre aciers à très bas taux de carbone et de structure bainitique ont été soumis à deux types de tests: interrompus et continus. La composition de base de ces aciers consistait en 0.026% C, auquel ont été ajoutés l'un ou l'autre ou les deux éléments Nb (0.055%) et B (30 ppm). De cette façon, l'influence des différents éléments d'addition: (i) Nb; (ii) B; (iii) Nb + B sur la vitesse de recristallisation a pu être estimée à tour de rôle.

Les cinétiques de recristallisation statique correspondant à l'austénite écrouie à chaud ont été déterminées pour des prédéformations de 0.12, 0.25 et 0.50 et pour des températures variant de 900 à 1100°C. Ces résultats sont présentés sous la forme du pourcentage d'adoucissement en fonction du logarithme du temps. Ils indiquent, lorsqu' utilisés avec les courbes RTT, que l'addition de B est plus efficace en présence de Nb pour retarder la recristallisation. De plus, les deux paramètres prédéformation et température influent sur cet effet retardateur. L'équation d'Avrami est utilisée pour caractériser les cinétiques de restauration et de recristallisation; l'influence de la prédéformation, de la température et de la composition de l'alliage sur les coefficients et exposants de cette équation est également étudiée.

Les cinétiques de recristallisation dynamique ont été évaluées pour des températures variant de 1000 à 1100°C et pour des vitesses de déformation allant de 10^{-3} à 0.5 s^{-1} . La déformation ϵ_p correspondant au pic ainsi que la déformation ϵ_x correspondant à la recristallisation ont été utilisées respectivement comme mesures du début et de la durée de la recristallisation dynamique. Lorsqu'elles sont normalisées par la vitesse de déformation $\dot{\epsilon}$ du test, ces deux quantités conduisent respectivement aux temps de nucléation et de recristallisation. Les courbes dynamiques RTT (DTT) estimées de cette manière sont en accord avec les courbes statiques correspondantes.

Les répliques de carbone ainsi que les photos autoradiographiques indiquent que le bore agit comme un soluté et que sa ségrégation se produit aux joints de grains qui migrent. Un modèle physique fondé sur la ségrégation du bore induite par la déformation est proposé. Il fait appel au rapport de

diffusivité joint de grain/matrice du niobium présent pour expliquer l'action synergétique entre Nb et B. Finalement la théorie du "trainage de soluté" est utilisée pour montrer que l'ordre d'efficacité d'éléments de microaddition est le même que celui de leurs énergie d'interaction E_0 . Les éléments possédant les plus fortes énergies d'interaction ont aussi les plus fortes diffusivités dans les aciers. Il est donc conclu que les éléments à diffusivité élevée produisent les forces de trainage les plus importantes.

ACKNOWLEDGEMENTS

The author would like to express his sincere appreciation to his thesis supervisor, Professor John J. Jonas, for his guidance and encouragement throughout the course of this research. His paradigmatic enthusiasm in gaining scientific insight into particular aspects of metallurgy together with his fatherly kindness and generosity made this work possible.

The author is thankful to Drs. N. Christodoulou, L.M. Howe, and G.M. Hood, as well as to Messrs. A.D. Lane, L.N. Herbert and J.F. Mecke, all of Atomic Energy of Canada, Ltd. for their scientific and technical assistance, respectively. Special thanks are also due to Dr. J.M. Gray (Microalloying International) for his understanding and help in the chemical analysis of the materials used.

Much gratitude is due to Professors He Xin Lai (Beijing University of Iron and Steel Technology) and G.R. Purdy (McMaster University) for their useful suggestions, which led to improvements in this work and contributed to its quality.

The pleasant and friendly environment created by his fellow graduate students, along with their suggestions regarding various aspects of this study, are deeply appreciated. The author would also like to express his gratitude to Martin Knoepfel and Bruno Grondin for their assistance in the preparation of test specimens and to Lorraine Mello for typing this thesis.

Finally, the author is indebted to the Physical Metallurgy Research Laboratories of CANMET for providing the experimental materials and for financial support, and particularly to Dr. G.E. Ruddle for his personal interest in the progress of the research and for his involvement in the preparation of the testing materials.

TABLE OF CONTENTS

		<u>Page</u>
	ABSTRACT	i
	RESUME	ii
	ACKNOWLEDGEMENTS	v
	TABLE OF CONTENTS	vi
	LIST OF FIGURES	xi
	LIST OF TABLES	xx
CHAPTER		
1	INTRODUCTION	1
2	LITERATURE REVIEW	3
	2.1 METALLURGICAL ASPECTS OF BORON STEELS	3
	2.1.1 BORON STEELMAKING PRACTICE AND PROTECTION	4
	2.1.2 MECHANISMS OF BORON HARDENABILITY	8
	2.1.2.1 Reduction in Grain Boundary Energy of the Austenite	8
	2.1.2.2 Reduction in Fe Self-Diffusivity	10
	2.1.2.3 Reduction in the Number of Nucleation Sites	10
	2.1.2.4 Nucleation on Borocarbides	10
	2.1.3 COMPOSITIONAL EFFECTS	11
	2.1.3.1 Carbon Content	11
	2.1.3.2 Alloying Elements	15
	2.1.4 BORON SEGREGATION	15
	2.1.5 MECHANICAL PROPERTIES AND USES OF BORON STEELS	17
	2.1.5.1 Tempering Response, Formability	17
	2.1.5.2 Considerations Regarding Temper Embrittlement	18
	2.1.5.3 Hot Workability	18

CHAPTER

	2.1.5.4	Creep Resistance	19
	2.1.5.5	Boron in HSLA Steels	19
2.2		CONTROLLED ROLLING OF HSLA STEELS	20
	2.2.1	REHEATING AND SOAKING	20
	2.2.2	CHANGES IN AUSTENITE STRUCTURE DURING HOT ROLLING.	22
	2.2.3	COOLING CONDITIONS	24
2.3		HIGH TEMPERATURE SOFTENING MECHANISMS.	25
	2.3.1	RECOVERY.	25
	2.3.1.1	Static Recovery	26
	2.3.2	RECRYSTALLIZATION	26
	2.3.2.1	Static Recrystallization	26
2.4		SOLUTE DRAG	27
	2.4.1	THE COMPOSITION PROFILE.	30
	2.4.2	IMPURITY DRAG	32
	2.4.2.1	High Velocity Limit	32
	2.4.2.2	Low Velocity Limit.	33
	2.4.2.3	Approximate Equation for Impurity Drag	33
3		EXPERIMENTAL MATERIALS AND PROCEDURE	37
	3.1	EXPERIMENTAL MATERIALS	37
	3.2	EXPERIMENTAL EQUIPMENT	40
	3.3	EXPERIMENTAL METHOD AND CONDITIONS	40
	3.3.1	STATIC RECRYSTALLIZATION	40
	3.3.2	DYNAMIC RECRYSTALLIZATION	47
	3.4	METALLOGRAPHY	49
	3.4.1	OPTICAL MICROSCOPY	49
	3.4.2	ELECTRON MICROSCOPY	49
	3.4.3	BORON AUTORADIOGRAPHY	50

CHAPTER

4	EXPERIMENTAL RESULTS	53
4.1	STATIC SOFTENING RESULTS	54
4.1.1	FLOW CURVES OBTAINED IN INTERRUPTED COMPRESSION TESTS	54
4.1.2	FRACTIONAL SOFTENING DETERMINED BY THE OFFSET METHOD	59
4.2	DYNAMIC SOFTENING RESULTS	68
4.2.1	FLOW CURVES OBTAINED IN COMPRESSION	68
4.2.2	DEPENDENCE OF ϵ_p and ϵ_x ON DEFORMATION CONDITIONS	71
4.3	METALLOGRAPHIC RESULTS	76
4.3.1	OCCURRENCE OF PRECIPITATION DURING STATIC RECRYSTALLIZATION	76
4.3.2	BORON AUTORADIOGRAPHY RESULTS	84
4.3.3	DETERMINATION OF INITIAL GRAIN SIZE	90
5	DISCUSSION	92
5.1	STATIC STRUCTURAL CHANGES	92
5.1.1	CALCULATION OF THE PARAMETERS k AND n	93
5.1.1.1	Static Recovery	96
5.1.1.2	Static Recrystallization	102
5.1.2	STRAIN DEPENDENCE OF STATIC RECRYSTALLIZATION	116
5.1.3	TEMPERATURE DEPENDENCE OF STATIC RECRYSTALLIZATION	119
5.1.4	STATIC RECRYSTALLIZATION-TIME- TEMPERATURE (RTT) CURVES	122
5.1.5	INFLUENCE OF BORON ON CARBIDE PRECIPITATION	122
5.1.6	THE ROLE OF BORON IN THE SOFTENING PROCESS	125

CHAPTER

5.1.6.1	State of Solute Atoms During Retardation of the Softening Process	126
5.1.6.2	The Solute Drag Theory and Substitutional Solutes.	128
5.1.6.2.1	A Qualitative Look at Solute Drag	129
5.1.6.2.2	Effect of the Type of E(x) and D(x) Profiles on the Magnitude of Solute Drag	137
5.1.6.2.3	The Hillert and Sundman Model of Solute Drag	142
5.1.6.3	The Strain Induced Segregation of Boron	147
5.1.6.3.1	The Mechanism of Boron Segregation	151
5.1.6.3.2	Implications of the Proposed Strain Induced Segregation Model.	154
5.1.6.4	Boron in Solid Solution: Interstitial or Substitutional?	158
5.2	THE EFFECT OF BORON ON DYNAMIC STRUCTURAL CHANGE	159
5.2.1	EFFECT OF TEST TEMPERATURE ON ϵ_p AND ϵ_x	160
5.2.2	EFFECT OF AUSTENITIZATION TEMPERATURE ON ϵ_p AND ϵ_x	163
5.2.3	EFFECT OF STRAIN RATE ON ϵ_p AND ϵ_x	164
6	CONCLUSIONS	165
7	STATEMENT OF ORIGINALITY AND CONTRIBUTION TO KNOWLEDGE	169

Page

REFERENCES	172
APPENDIX I INTERRUPTED COMPRESSION TEST FLOW CURVES.	183
APPENDIX II CONTINUOUSLY COMPRESSED TEST FLOW CURVES.	197
APPENDIX III COMPUTER PROGRAMS FOR CONTINUOUS AND INTERRUPTED COMPRESSION TESTS.	207

LIST OF FIGURES

<u>Figure</u>		<u>Page</u>
2.1	Comparison of the boron effect on martensite hardenability for low austenitizing temperatures (boron effect is normalized to maximum effect (10).	5
2.2	Statistically predicted effect of boron on hardenability for various levels of titanium and nitrogen (12).	7
2.3	Temperature dependence of the grain boundary energy in iron (1) and Fe-B alloy (2), (19).	9
2.4	Schematic diagram for the nucleation and growth of primary ferrite nucleated adjacent to the Fe ₂₃ (B, C) ₆ /austenite interface (27).	12
2.5	Schematic diagram showing the effect of boron on the TTT characteristics of a steel (28).	13
2.6	Schematic illustration of the controlled rolling process and the resulting microstructures.	21
2.7	Changes in austenite grains during controlled rolling (73).	23
2.8	Moving grain boundary between deformed and undeformed crystals (schematic). The boundary moves under the influence of the higher density of dislocation lines in the deformed crystal in the direction of the arrow, leaving somewhat behind the atmosphere of foreign atoms (80).	29

<u>Figure</u>		<u>Page</u>
2.9	The interaction energy profile $E(x)$ used. (a) $E < 0$; (b) $E > 0$.	35
2.10	Impurity drag for various velocities (83).	36
3.1	Compression test sample geometry and groove design (84).	39
3.2	External view of the high temperature compression testing equipment.	41
3.3	External view of the computer and control consoles for vacuum and temperature regulation.	42
3.4	Interior view of the CENTORR high temperature furnace and compression tools.	43
3.5	Typical experimental flow curves for interruption times of 1.5 and 10 seconds.	45
3.6	Determination of the percentage softening by the offset method.	46
3.7	Typical stress/strain curve and the values of ϵ_p and ϵ_x .	48
3.8	Neutron radiography unit at NRX south thermal column (91).	52
4.1	Interrupted flow curve for the plain C steel tested at 1000°C, after a holding time of 2 seconds.	55
4.2	Interrupted flow curve for the plain C plus boron steel tested at 1000°C, after a holding time of 2 seconds.	56

<u>Figure</u>		<u>Page</u>
4.3	Interrupted flow curves for the Nb steel tested at 1000°C after two different holding times.	57
4.4	Interrupted flow curves for the Nb + B steel tested at 1000°C after two different holding times.	58
4.5(a)	Static recovery and recrystallization of the Nb and Nb + B steels after a predeformation of 0.25.	61
4.5(b)	Static recovery in the Nb and Nb + B steels after a predeformation of 0.25.	62
4.6	Comparison of the softening behaviour of the plain C; plain C plus B and Nb, Nb + B steels deformed 0.25 at 1000 and 900°C.	63
4.7(a)	Static recovery and recrystallization of the Nb and Nb + B steels after a predeformation of 0.5.	65
4.7(b)	Static recovery in the Nb and Nb + B steels after a predeformation of 0.5.	66
4.8	Static recovery and recrystallization of the Nb and Nb + B steels after a predeformation of 0.12.	67
4.9	Effect of microalloying additions on the shapes of the dynamic recrystallization flow curves.	69
4.10	Effect of strain rate on the shapes of the dynamic recrystallization flow curves.	70
4.11	Effect of austenitizing temperature on the shapes of the dynamic recrystallization flow curves.	72

<u>Figure</u>		<u>Page</u>
4.12	Effect of test temperature on ϵ_p and ϵ_x .	73
4.13	Effect of austenitization temperature on ϵ_p and ϵ_x .	74
4.14	Effect of testing strain rate on ϵ_p and ϵ_x .	75
4.15	Undissolved TiN precipitates in a Nb + B steel solution treated and then deformed 25% at 1000°C and immediately quenched.	77
4.16	Undissolved TiN precipitates in a solution treated Nb + B steel deformed 25% at 1000°C and quenched 100 seconds after deformation.	78
4.17	X-ray spectrum analysis of the precipitates shown in Figs. 4.15 and 4.16.	79
4.18	Undissolved MnS precipitates in a solution treated Nb steel deformed 25% at 900°C and quenched after 100 seconds.	80
4.19	X-ray spectrum analysis of the MnS precipitates shown in Fig. 4.18.	81
4.20	Comparison of the precipitates in solution treated Nb and Nb + B steels deformed 25% at 900°C and quenched after 1000 seconds.	82
4.21	X-ray spectrum analysis of the precipitates in solution treated Nb (a) and Nb + B (b) steels deformed 25% at 900°C and quenched after 1000 seconds.	83

<u>Figure</u>		<u>Page</u>
4.22	Fe ₂₃ (B,C) ₆ precipitates at a γ -grain boundary in a solution treated Nb + B steel deformed 25% at 900°C and quenched after 1000 seconds.	85
4.23	Photomicrograph (a) and boron autoradiograph (b) of a Nb + B steel quenched from 1000°C after austenitization at 1100°C. No segregation of boron can be seen (thermal neutron dose: 5×10^{14} n/cm ²).	86
4.24	Photomicrograph (a) and boron autoradiograph (b) of a Nb + B steel quenched immediately after deformation of 25% at 1000°C showing no segregation of boron (thermal neutron dose: 5×10^{14} n/cm ²).	87
4.25	Photomicrograph (a) and boron autoradiograph (b) of a Nb + B steel deformed 25% at 1000°C and quenched after 60 seconds. Some boron segregation can be seen at the recrystallizing grain boundaries (thermal neutron dose: 5×10^{14} n/cm ²).	88
4.26	Photomicrograph (a) and boron autoradiograph (b) of a Nb + B steel deformed 25% at 1000°C and quenched after 600 seconds showing considerable segregation of boron (thermal neutron dose: 5×10^{14} n/cm ²).	89
4.27	Austenite grain size as a function of austenitization temperature.	91
5.1	Dependence of $\log \ln(1/1 - x)$ on $\log t$ at three different temperatures in the Nb and Nb + B steels.	94
5.2	Dependence of $\log \ln (X_{\infty}^r/X_{\infty}^r - X^r)$ on $\log(t)$ for $\epsilon = 0.12$.	97

<u>Figure</u>	<u>Page</u>
5.3 Dependence of $\log \ln(X_{\infty}^r/X_{\infty}^r - X^r)$ on $\log(t)$ for $\varepsilon = 0.25$.	98
5.4 Dependence of $\log \ln(X_{\infty}^r/X_{\infty}^r - X^r)$ on $\log(t)$ for $\varepsilon = 0.5$.	99
5.5 Dependence of time exponent n^r on the prestrain ε_p .	101
5.6 Dependence of the rate constant k^r on the inverse absolute temperature.	103
5.7 Dependence of A^r on the prestrain ε_p .	104
5.8 Dependence of $\log \ln(X_{\infty}^R/X_{\infty}^R - X^R)$ on $\log(t - t_0)$ for $\varepsilon = 0.12$.	105
5.9 Dependence of $\log \ln(X_{\infty}^R/X_{\infty}^R - X^R)$ on $\log(t - t_0)$ for $\varepsilon = 0.25$.	106
5.10 Dependence of $\log \ln(X_{\infty}^R/X_{\infty}^R - X^R)$ on $\log(t - t_0)$ for $\varepsilon = 0.5$.	107
5.11 Dependence of k^R on temperature at constant prestrain ε_p .	110
5.12 Dependence of A^R on prestrain ε_p .	111
5.13(a) Dependence of incubation time (t_0) on the temperature for the Nb and Nb + B steels at constant prestrain ε_p .	112
5.13(b) Comparison of the two-component softening curves and the experimental data points.	113

<u>Figure</u>		<u>Page</u>
5.13(c)	Comparison of the softening curves derived from the experimental data with the data points themselves (Nb steel).	114
5.13(d)	Comparison of the softening curves derived from the experimental data with the data points themselves (Nb, + B steel).	115
5.14	Fractional softening vs. holding time at 1000°C for strains of 0.12, 0.25 and 0.5.	117
5.15	Dependence of time for 50% recrystallization (62.5% softening) on the prestrain ϵ_p .	118
5.16	Dependence of time for 50% recrystallization (62.5% softening) on the inverse absolute temperature.	120
5.17	Recrystallization start times (R_s) as a function of temperature.	123
5.18	Recrystallization finish times (R_f) as a function of temperature.	124
5.19(a)	Impurity drag vs. normalized velocity profiles for various elements in γ -iron.	133
5.19(b)	Impurity drag vs. velocity profiles for various elements in γ -iron.	135
5.20	Impurity drag vs. normalized velocity profiles for Nb at 1000 and 1100°C.	136

<u>Figure</u>		<u>Page</u>
5.21	The interaction energy profiles $E(x)$ and diffusivity profiles $D(x)$ used in calculating the impurity drag parameters α and α/β^2 in Table 5.9.	139
5.22	Top diagram: A grain boundary model with four different zones. Middle diagram: Concentration profiles calculated for three migration rates. Bottom diagram: The integrand in the calculation of solute drag from the concentration profiles (125).	144
5.23	The solute drag as a function of the migration rate, calculated for a variable diffusivity. D_{GB} holds in the center of the boundary and \bar{D}^M holds in the undisturbed crystals.	145
5.24	The solute drag contributions from different zones in the grain boundary, evaluated for two different ratios of D_{GB}/\bar{D}^M (125).	146
5.25	Ratio of times for 50% recrystallization of the Nb + B and Nb steel vs. temperature.	148
5.26	Ratio of times for 50% recrystallization of the Nb + B and Nb steels vs. grain boundary velocity of the Nb steel.	150
5.27(a)	Schematic time/temperature diagram for isothermal heat treatment.	152

<u>Figure</u>		<u>Page</u>
5.27(b)	The ratio (L/L_0) as a function of isothermal holding time at 1000°C. L: the total length of grain boundary with boron segregation revealed by PTA on unit area. L ₀ : the total length of austenite grain boundary per corresponding unit area (127).	152
5.28	Effect of selected alloying elements on recrystallization stop temperature of austenite (129).	157
5.29	Dynamic recrystallization start times (R_s) as a function of temperature for the four steels investigated.	161
5.30	Dynamic recrystallization finish times (R_f) as a function of temperature for the four steels investigated.	162

LIST OF TABLES

<u>Table</u>	<u>Page</u>
3.1 Chemical Compositions of the Steels Investigated (wt.%).	38
5.1 Empirical Constants k^r and n^r Obtained from the Softening Data.	100
5.2 Empirical Constants k^R and n^R Obtained from the Softening Data.	108
5.3 Measured Activation Energies for Static Recrystallization (KJ/mole).	121
5.4 Impurity Diffusion parameters in γ -iron.	130
5.5 Impurity Diffusivities in γ -iron.	130
5.6 Atomic Radii of Common Alloying Elements (Å) (121).	132
5.7 Calculated Values of α , β and E_0 at 1000°C.	134
5.8 Relationship Between Ratio of Matrix D^M and Boundary DGB Diffusion Coefficients and Grain Size at Which Equal Amounts of Diffusion Take Place by the Two Processes (12).	137
5.9 Theoretical Equation for α and α/β^2 .	140
5.10 Calculated Values of α , β and P_i max for Nb at 1000°C.	141
5.11 Calculated Values of α , β and P_i max for Mo at 1000°C.	141

<u>Table</u>		<u>Page</u>
5.12	Vacancy [V], Complex [C] and Boron [I] Concentrations as a Function of Solution Treatment Temperature (45).	153
5.13	Boron Monovacancy Complex Diffusivities and Diffusion Distances for 65 Seconds at 950, 1000 and 1050°C.	155

CHAPTER 1

INTRODUCTION

The appearance of low-carbon bainitic steels on a commercial scale was almost simultaneous with that of the ferrite-pearlite HSLA grades. The former steels offered a strength advantage but were inferior in toughness to those with ferrite-pearlite microstructures. The rather recent realization that reducing the carbon level to very low concentrations improves the impact properties of these steels renewed the early interest and led the way to the development of the ultra-low-carbon-bainitic grades (ULCB). A very important microalloying element in these steels, especially from the hardenability point of view, is boron. Its effect is particularly strong in the presence of niobium.

For further improvement in the inherently low toughness of these steels, it is important to refine the austenite grain size prior to the bainite transformation. This is because the effective grain size for the cleavage fracture of bainitic steels has a strong dependence on the austenite grain size, in a manner similar to that of the ferrite-pearlite steels. The above goal can be achieved through the introduction of controlled rolling. However, the design of proper rolling schedules is not an easy task. It requires knowledge of a number of important metallurgical characteristics of the material with respect to temperature, deformation and time. These have, to a great extent, been predetermined through the choice of the chemical composition. Consequently, clarification of the roles played by the different microalloying elements is of prime importance in understanding the physical metallurgy of these alloys.

The aim of the present investigation was therefore to assess the recrystallization behaviour of a series of hot worked austenites containing boron. In particular, the main objectives were the following:

- (i) To determine whether the presence of boron, alone or in conjunction with Nb, influences the rapidity of the softening processes.

- (ii) To follow its possible influence, under both static and dynamic testing conditions, for a variety of prestrains and holding temperatures over ranges of industrial interest.
- (iii) To establish the "state" of the boron (i.e. whether it is in the form of solute, cluster or precipitate) when it is effective.
- (iv) In the case of the synergistic interaction with Nb, to provide possible physical explanations for such behaviour.
- (v) To understand, on a physical basis, the reasons for the variations in the effectiveness of the different microalloying elements in retarding the recrystallization process.

Before presenting the results of this investigation, some of the literature associated with the metallurgical uses of boron will first be introduced, together with the different stages of the controlled rolling process. Then the theoretical framework dealing with the influence of solute atoms in retarding the motion of moving grain boundaries will be considered. The detailed description of the materials and the experimental techniques used follows. After a presentation of the experimental results, the discussion section is presented, which is divided into two parts: the first deals with a mathematical description of the experimental data and is applicable to the computer modelling of steel rolling; the second deals almost entirely with the problem of understanding the behaviour of boron during recrystallization, especially when Nb is present. Finally, a combined model based on the strain-induced segregation of boron on the one hand, and on the solute drag theory on the other is employed to explain the synergism between Nb and B that was observed.

CHAPTER 2

LITERATURE REVIEW

2.1 METALLURGICAL ASPECTS OF BORON STEELS

Boron was first considered as a potential alloying element in steel in 1907 (1). From then on, through the early 1920's, various investigators studied steels containing what would now be regarded as extremely high concentrations of the element. Not until 1921 was it recognized that large amounts of boron, up to 2% in some cases, were responsible for making steels extremely hard and brittle and that even an amount as minute as 10 parts per million of boron was sufficient to produce significant effects on steel properties (2, 3). These early studies were characterized by a lack of understanding of hardenability, while the commercial production of boron steels suffered from the inability to control the steelmaking process to the extent needed to maintain small amounts of effective boron in solution.

The 1930's and early 1940's brought an appreciation of the concept of hardenability and the way it is affected by alloying elements, including boron (4, 5). It was then realized that boron is by far the most potent hardenability intensifier, a use which remains its predominant function in carbon and alloy steels to this day (6, 7). The development of the Jominy hardenability test during this same period brought with it a convenient way of measuring the effectiveness of the boron contained in the steel (8). This was extremely significant because it replaced the need for chemical analysis in the parts per million range with a simple procedure providing meaningful quantitative information.

The initiation of World War II caused a severe shortage of many critical alloying elements, including nickel and chromium, and since it was already known that boron could replace many of these alloying elements, the commercial development of boron steels was on its way, even though many of the old problems associated with the use of boron remained to be satisfactorily solved. It was known that boron had to be protected from reaction with oxygen

and nitrogen in order to insure its hardenability capability, but steelmaking technology was not always up to the task of doing that. As a result, boron steels gained an unfavorable reputation for erratic behaviour, a stigma which was to persist for several decades. Unable to guarantee a consistent product, steelmakers therefore returned to the more costly but easier to produce alloy steels as soon as the war ended. There was a renewal of interest in boron steels during the Korean war and during periods when, for example, nickel or molybdenum was in short supply for various reasons, but it appeared as though they only gained favor when times were hard, only to lose their popularity once other elements were cheap and readily available.

Today the situation has changed in many aspects. From the technological point of view, there is now a far better understanding of the way boron produces its beneficial effects. The advent of sophisticated analytical instruments and microprocessor based controls has greatly increased the steelmaker's ability to produce consistent, high quality products on a routine basis. From the point of view of availability, we now face an era when assured, long term supplies of low cost raw materials can no longer be taken for granted. Also, competition from plastics and non-ferrous metals has created a need for steels that provide maximum strength to weight ratios at the lowest possible cost. Finally, there is now permanent concern for energy conservation and both steelmakers and their customers must constantly strive to reduce the energy consumed in melting, heat treating and deformation. As will be discussed in later sections, boron steels are well known for their ability to conserve energy, both in the furnace and in the work required for hot and cold deformation.

Now that definitely reproducible properties can be obtained regularly with boron steels, it seems that these materials have finally come into their own.

2.1.1 BORON STEELMAKING PRACTICE AND PROTECTION

It has long been recognized that the hardenability of boron steels does not increase continuously with boron level, but that there exists an optimum boron content range. Most authors (9-12) tend to locate this optimum range between 10 and 30 ppm of 'soluble' boron, as illustrated in Fig. 2.1. This range

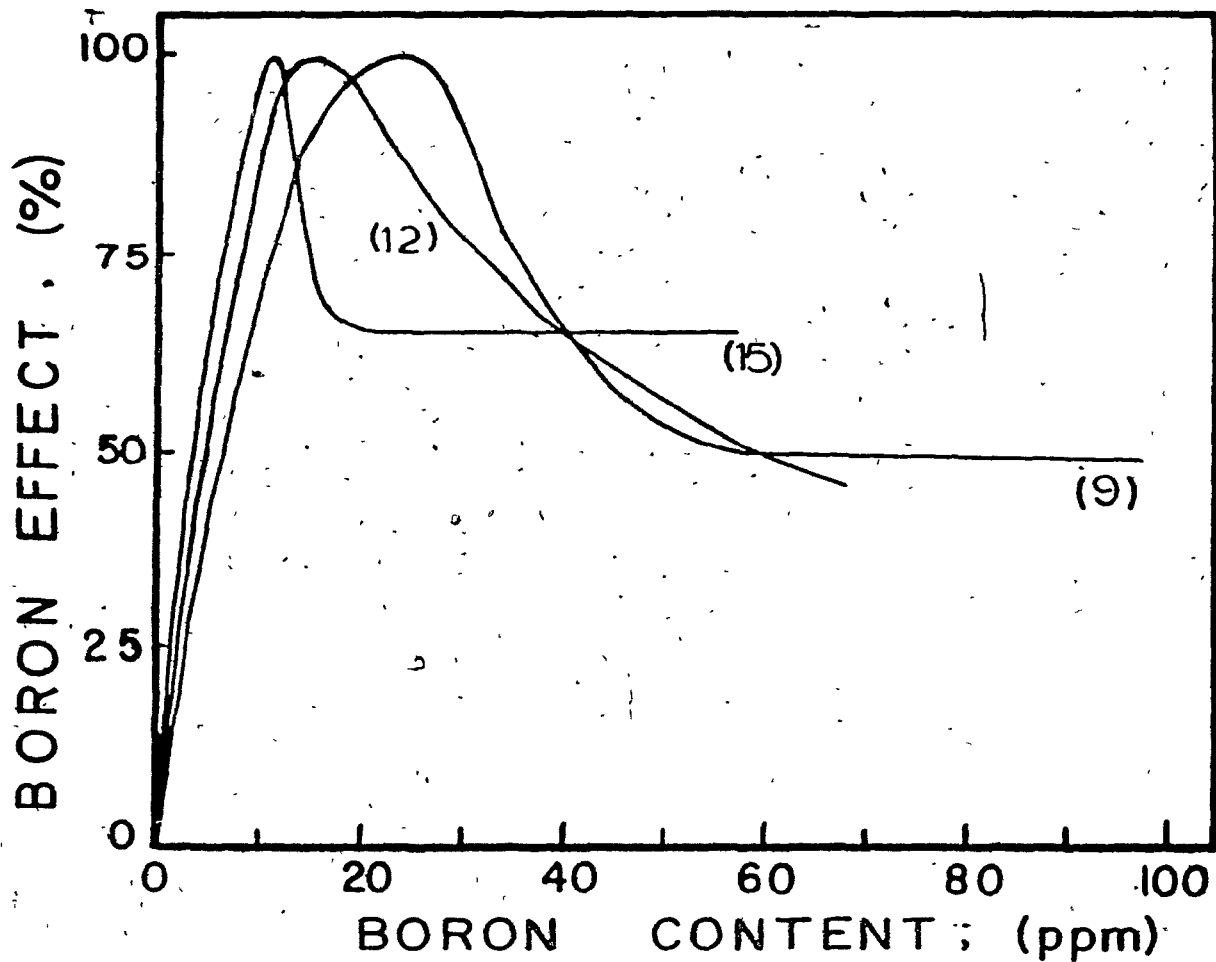


Figure 2.1 Comparison of the boron effect on martensite hardenability for low austenitizing temperatures (boron effect is normalized to maximum effect (10)).

is, however, sometimes located at very low concentrations (13-15), and the most important explanation for such a discrepancy pertains to differences in chemical analysis practices and the resulting errors at low boron concentrations. Soluble or effective boron is the amount of boron available for (i) segregation at grain boundaries and (ii) precipitation as $\text{Fe}_{23}(\text{B,C})_6$. As boron is a very reactive element, it reacts with oxygen forming B_2O_3 and nitrogen to form BN; this fraction of the concentration is called the insoluble or ineffective boron. The primary problem in producing steels with optimum hardenability has therefore been the control required to assure the optimum effective (soluble) boron content of the final product. Loss of effective boron by the formation of B_2O_3 is prevented by making the boron addition after all the deoxidizers have been introduced, i.e., after manganese, silicon and aluminum have been added, and by using good ladle and/or mold practices to avoid reoxidation while pouring the steel. (Boron addition begins after the ladle is 1/3 full and is generally completed before it is 2/3 full (1)). Loss of effective boron by the formation of BN is prevented by combining the available nitrogen with strong nitride formers such as Ti or Zr, as can be seen in Fig. 2.2 (12). A study by Kapadia et al. (12) showed that the effective boron content could be calculated from the total boron added, the N concentration, and the amounts of the nitride forming elements. The effective boron is given in this way by Eq. 2.1 as:

$$B_{(\text{effective boron})} = \left[B_{\text{Tot}} - \left\{ (N - 0.002) - \frac{\text{Ti}}{5} - \frac{\text{Zr}}{15} \right\} \geq 0 \right] \geq 0 \quad (2.1)$$

The value of 0.002 is taken to be the part of the nitrogen content that is always bound to the aluminum and silicon.

Provided that sufficient titanium is added to bind the amount of nitrogen remaining, $B_{\text{eff}} = B_{\text{Tot}}$. To calculate the amount of titanium required, equation (2.1) may be written as:

$$\text{Ti} = 5(N - 0.002) \quad (2.2)$$

(Here it is assumed that the amount of zirconium is equal to zero).

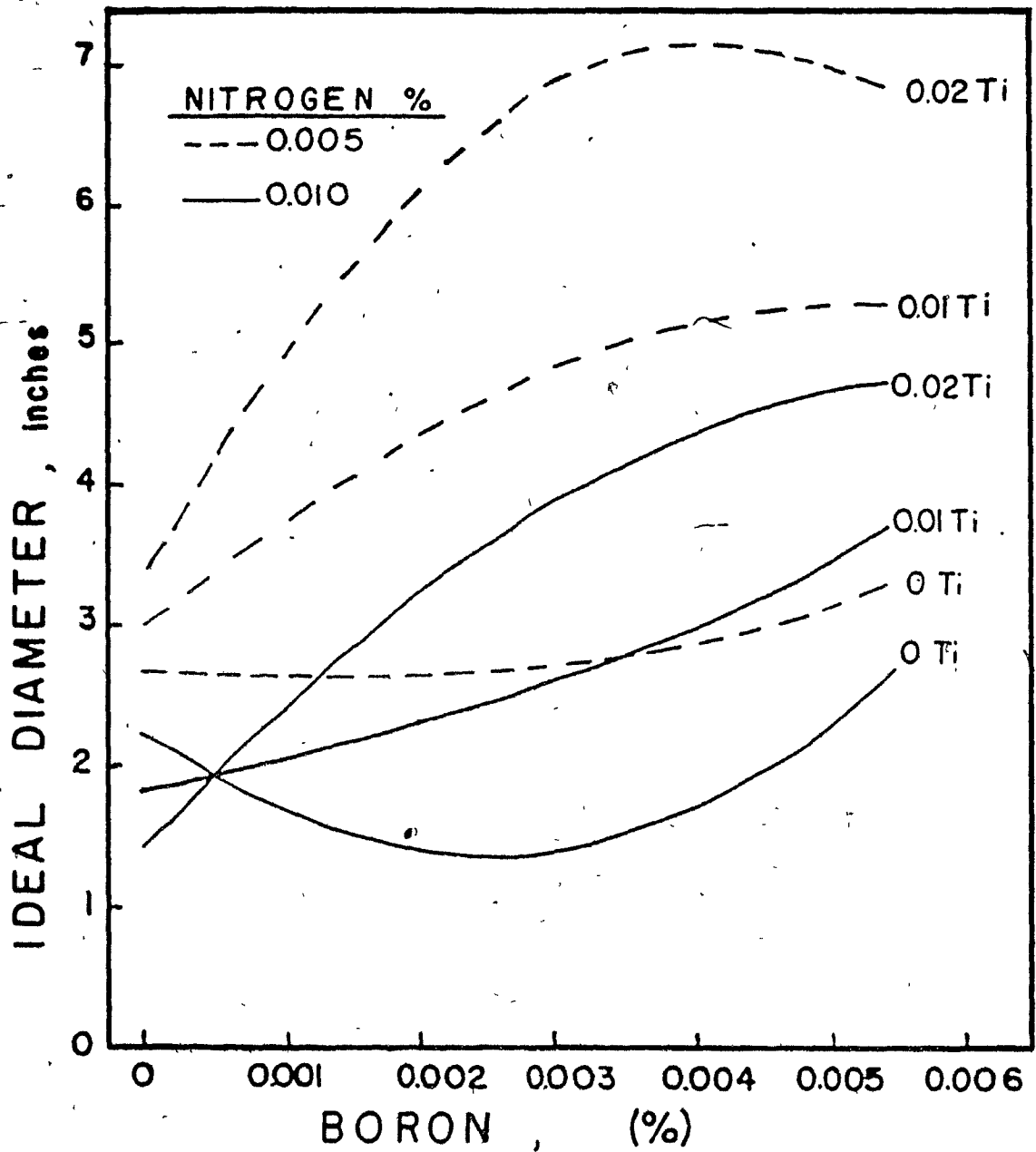


Figure 2.2 Statistically predicted effect of boron on hardenability for various levels of titanium and nitrogen (12).

2.1.2 MECHANISMS OF BORON HARDENABILITY

Because typical boron levels in steels are of the order of 10 ppm by weight, boron does not influence the thermodynamic properties of the bulk austenite or ferrite phases (16). However, since ferrite generally nucleates on austenite grain boundaries, and it has been shown that boron influences the nucleation rate of ferrite (17) (but not the growth rate), most of the interest in boron deals with its effect on the γ to α transformation. There are two reasons why such "small concentrations" of boron can cause significant retardation of the γ to α phase change: the first is that 10 ppm by weight of soluble boron is actually equivalent to 52 ppm atomic, because of the low atomic weight of boron. The second is that for grain sizes greater than 30 μm and for the boron concentration of 10 ppm selected above, there is more than one boron atom in the system for every iron atom in the grain boundary and on the order of 4 billion boron atoms present for every ferrite nucleus (18). A number of mechanisms which explain how boron can retard ferrite nucleation will now be considered.

2.1.2.1 Reduction in Grain Boundary Energy of the Austenite

It has been observed that the segregation of boron to grain boundaries reduces their energy (19) and therefore makes them less favorable sites for ferrite nucleation (Fig. 2.3). The major objection to this proposal is the estimation by Sharma and Purdy (20) which shows that the reduction in energy is of the order of 1% at most and consequently is probably too small to have any significant effect. However, it has been proposed by Morral and Cameron (21) that, depending on the shape of the nucleus, even a 1% reduction in interfacial energy can reduce the nucleation rate by a factor of 10 so that the reduction in austenite grain boundary energy can still be considered a possible mechanism.

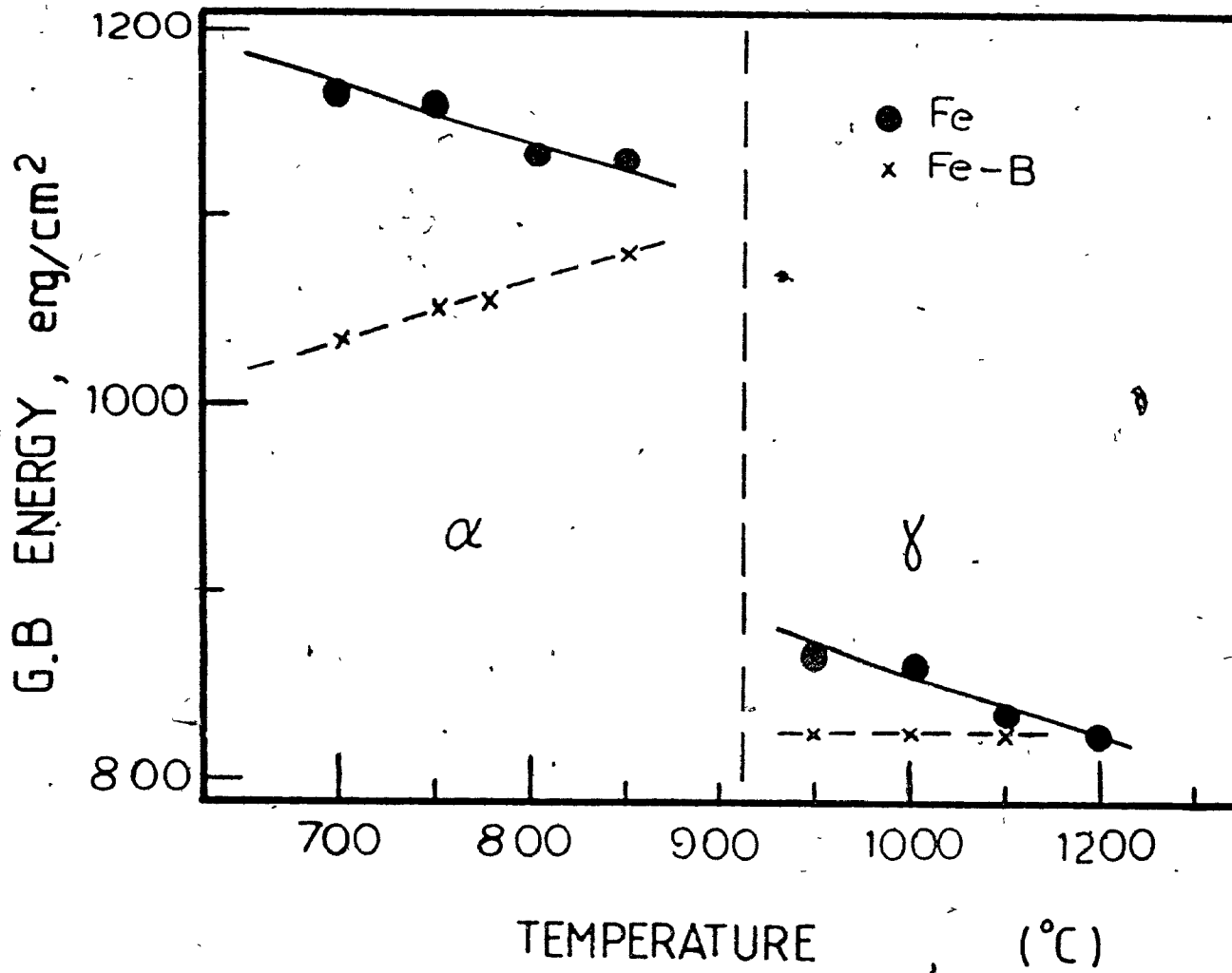


Figure 2.3 Temperature dependence of the grain boundary energy in iron (1) and Fe-B alloy (2),(19).

2.1.2.2 Reduction in Fe Self-Diffusivity

The segregation of boron at the grain boundaries of the austenite can cause reduction of the iron grain boundary self-diffusivity (19, 22) and possibly a reduction in the carbon jump frequency in this region by blocking interstitial sites or by increasing the grain boundary modulus. These mechanisms have been confirmed experimentally. The reduction in the iron grain boundary diffusivity could explain why boron retards the nucleation kinetics of ferrite in a carbon free alloy. In carbon containing alloys, i.e. in steels, carbon jump frequency is rate controlling and a reduction in the latter could explain the retardation of ferrite nucleation. This can also make sense of the observation that boron loses its hardenability potential at carbon concentrations greater than 0.8% by weight, as will be seen later.

2.1.2.3 Reduction in the Number of Nucleation Sites

Studies of the nature of grain boundaries suggest that they cannot be treated as featureless surfaces and that not every grain boundary site can be considered proper for the nucleation of ferrite. However, there are regions of relatively high and low atom density (23). If regions of low density are more favored sites for ferrite nucleation, it is possible that boron can poison them by diffusing there or by precipitating on them as borocarbides (17, 20, 24), forcing ferrite to nucleate elsewhere at a reduced rate.

2.1.2.4 Nucleation on Borocarbides

The presence of boron clearly increases the incubation time for the formation of ferrite and lowers substantially the nucleation rate after the onset of ferrite formation (10). Since the nucleation of ferrite occurs mainly on grain boundaries (25), particular attention must be devoted to the possible role of the grain boundary $M_{23}(B,C)_6$ borocarbides. These precipitates, formed during cooling, have a parallel cubelcube orientation relationship with the parent γ grain on one side of the boundary (17, 26). The interface between the precipitate and the parent grain is therefore of substantially reduced energy

when compared to the energy of the unmodified grain boundary; as a result it is expected that the nucleation of ferrite should be inhibited on that side of the grain boundary (17, 20). Figure 2.4 (27) shows a schematic diagram for the nucleation and growth of primary ferrite at the $\text{Fe}_{23}(\text{B,C})_6$ /austenite interface. Because $\text{Fe}_{23}(\text{B,C})_6$ is in a parallel orientation relationship with austenite grain γ_1 (Fig. 2.4 (a)), primary ferrite will nucleate at the $\text{Fe}_{23}(\text{B,C})_6$ /austenite γ_2 interface, which has no specific orientation relationship (Fig. 2.4 (b)). The primary ferrite will then grow into austenite grain γ_1 (Fig. 2.4 (c)) and eventually enclose the $\text{Fe}_{23}(\text{B,C})_6$ particle completely (Fig. 2.4 (d)), resulting in an asymmetrical shape. Therefore, if the precipitates are small enough so that they do not provide significant areas of incoherent boundaries, the net result is an inhibition of the ferrite nucleation rate with respect to larger precipitates, which have already become incoherent.

No matter which of the above proposed hardenability increase mechanisms is operating, the net result of adding boron to a steel will be a shift of the ferrite "C" curve to longer times, as can be seen from Fig. 2.5 (28).

The modification of the TTT diagram in the presence of boron is clearly affected by the specific composition. A brief discussion of compositional effects is appropriate at this stage.

2.1.3 COMPOSITIONAL EFFECTS

2.1.3.1 Carbon Content

Even when the optimum amount of effective boron is present in a steel, the boron hardenability effect can vary appreciably with the chemical composition of the steel, particularly its carbon content. In one of the early studies on boron steels, Rather and Armstrong (29) investigated the boron effect in a wide variety of commercially produced plain carbon and low alloy steels with carbon concentrations ranging from about 0.1 to 1.0 percent. From an analysis of their own and earlier data in the literature, they calculated that the boron hardenability factor (F_β) in such steels decreases with increasing carbon content according to the following relationship:

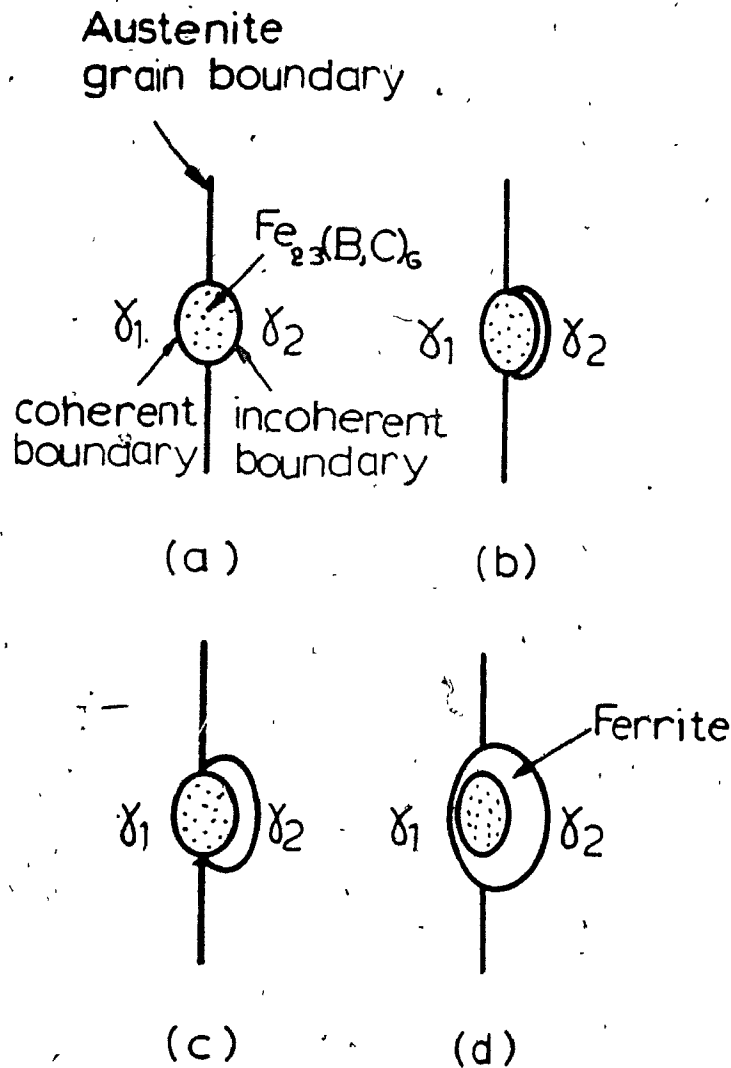


Figure 2.4 Schematic diagram for the nucleation and growth of primary ferrite nucleated adjacent to the $\text{Fe}_{23}(\text{B,C})_6$ /austenite interface (27).

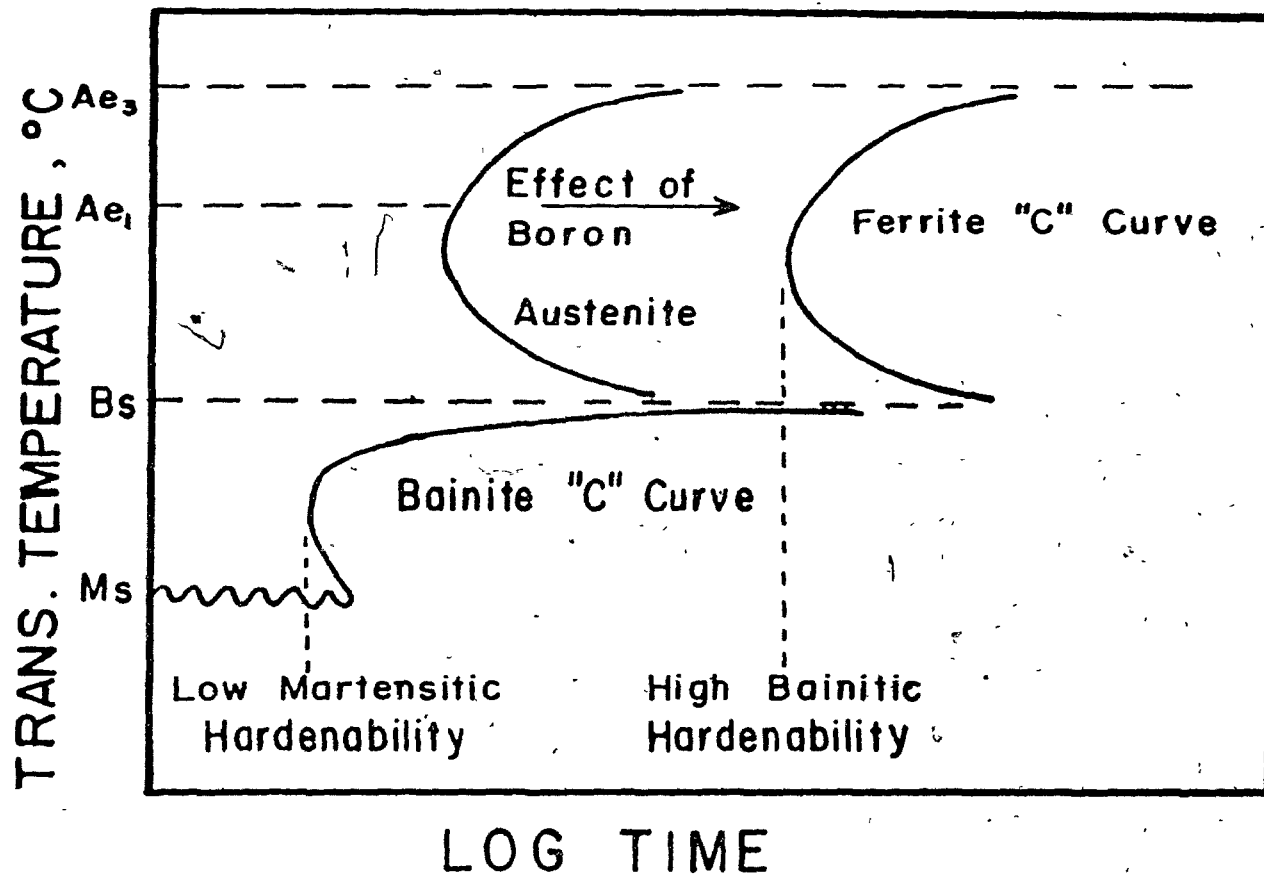


Figure 2.5 Schematic diagram showing the effect of boron on the TTT characteristics of a steel (28).

$$F_{\beta} = 1 + 1.5 (0.9 - \% C) \quad (2.3)$$

The boron factor is defined as the ratio of the ideal diameter measured from Jominy test data over the ideal diameter calculated on the basis of chemical composition (excluding boron) and grain size. Finally, ideal diameter is simply the diameter, in inches, of an infinitely long cylindrical bar which will transform to 50% martensite at its center under the action of an ideal quench.

According to relationship (2.3), boron is very effective in increasing the hardenability of low carbon steels, but is completely ineffective in steels containing more than 0.9% of carbon. The negative interaction between the boron effect and carbon content in hypoeutectoid steels can be explained on the basis that carbon, like boron, retards the proeutectoid ferrite reaction. This is because, when ferrite and pearlite are being produced from austenite, the carbon must partition into the pearlite, i.e. away from the ferrite, a diffusion-controlled process which is time consuming. Therefore, by increasing the carbon content up to the eutectoid level of approximately 0.8% (at which no ferrite is formed), the relative importance of the transformation of austenite to ferrite is decreased progressively. Hayes (30) has reported results similar to those of Rather and Armstrong, but with a slightly steeper linear relationship based on hardenability evaluations of commercial heats of low carbon alloy steels.

The degree of scatter in the boron hardenability factor associated with a particular carbon concentration indicates that the boron hardenability effect in steels of varying composition cannot be explained by a simple correlation with the carbon level. The strength of the boron effect appears to be dependent on the overall austenite transformation characteristics of the base steel rather than on any specific compositional variable. Consideration of the total alloy content is therefore just as significant as the carbon content for predicting the magnitude of this phenomenon.

2.1.3.2 Alloying Elements

The presence of molybdenum strongly enhances the boron effect (31). A synergistic influence on both the nucleation and growth of ferrite has been observed. Microalloying elements now widely used in HSLA steels are particularly interesting when used in conjunction with boron. However, vanadium does not appear to exert any specific effect in the presence of boron, beyond its well known contribution to precipitation hardening. By contrast, niobium exhibits a definite synergistic effect with boron when in solution (10). Finally, it has been reported (32) that the presence of copper in conjunction with boron brings about a significant reduction in the transformation temperature. The lowering of the A_{r3} is nearly 110°C under furnace cooling conditions; even with a very fast cooling rate, the difference is still 42°C .

2.1.4 BORON SEGREGATION

It has been shown previously that boron, whether present as a trace impurity or as an alloying element in low concentrations, segregates to the grain boundaries (14, 17, 33-46). Such boron segregation demonstrates two remarkable features. First, the degree of segregation is enhanced on cooling from higher initial temperatures. This rules out a simple explanation based on binding of the impurity atom to the grain boundary since, if there is a binding energy to the boundary E_s , the degree of equilibrium segregation should vary as $\exp(-E_s/KT)$, leading to a trend with temperature opposite to the one observed. Second, the segregation only occurs during a relatively slow cool and not if the specimen is rapidly quenched. Thus the segregation is a dynamic phenomenon affected by the kinetics of the various processes on an atomic scale. The above two peculiarities classify boron segregation as being part of what is called non-equilibrium segregation.

The theory of non-equilibrium segregation was first discussed by Aust et al. (47, 48) and Anthony (49) and more recently by Williams et al. (39) and Harries and Marwick (50). Qualitatively, the explanation proposed postulates the existence of mobile vacancy-impurity complexes. Segregation is then a consequence of the movement towards overall equilibrium of three species

(vacancies, isolated impurities and complexes) during cooling and the fact that vacancies can be annihilated at free surfaces and grain boundaries.

It is possible to estimate the concentrations of the impurity atoms [I], isolated vacancies [V] and complexes [C] at the initial solution treatment temperature (39). The total impurity concentration is [I] + [C] if there is one impurity atom per complex. The vacancy concentration is:

$$[V] = K_v \exp\left(\frac{-E_F}{KT}\right) \quad (2.4)$$

where E_F is the vacancy formation energy.

The concentration of the complexes is given by:

$$[C] = K_c [I][V] \exp\left(\frac{+E_B}{KT}\right) \quad (2.5)$$

where E_B is the binding energy. Here K_v and K_c are constants and contain various geometric and entropy terms.

After holding at the solution treatment temperature for some time, the concentrations of all three species are uniform ($[I] + [V] \longrightarrow [C]$). During cooling, vacancies are lost at the grain boundaries in order to maintain an equilibrium concentration appropriate to the lower temperature. The reduction in [V] causes a reduction in [C] near the boundaries, where complexes lose their vacancies to become isolated impurities. Meanwhile [C] increases near the centre of the grain. Vacancies cannot be annihilated but can move to impurities to maintain equilibrium at the lower temperature according to Eq. 2.5. Diffusion attempts to even out these inhomogeneous concentrations. When quenching is very rapid, the complexes have insufficient time to diffuse to the boundary. At intermediate quenching rates, the complexes deposit boron at the boundary but the now isolated boron has insufficient time to diffuse back into the matrix, so that grain boundary segregation is produced. Finally, at

very slow quenching rates, the boron deposited at the boundary has sufficient time to diffuse back into the matrix and the segregation is eliminated.

2.1.5 MECHANICAL PROPERTIES AND USES OF BORON STEELS

Boron steels are primarily used in the heat treated state. A certain confusion appears in the literature, however, as to possible detrimental effects of boron on various properties of steels in the tempered state. A brief review of the properties and uses of boron is therefore appropriate.

2.1.5.1 Tempering Response, Formability

When alloying elements such as niobium, vanadium, chromium and molybdenum are added to a carbon steel, they not only improve the hardenability but produce additional strength in the as tempered condition by means of precipitation strengthening. When boron is used as a substitute for these elements, their precipitation hardening effect will be absent. Boron does not produce a secondary hardening effect on its own, so carbon-boron steels will be inherently softer in the tempered condition than the alloy steels they replace, as long as the carbon content remains constant. Boron steels are therefore more sensitive to the tempering conditions and tighter control over these may be needed. However, if compared on the basis of hardenability, boron steels will generally contain less carbon and manganese (and, of course, other alloying elements) than the steels they replace. As a result, boron steels of equivalent hardenability will be considerably softer in the unhardened, as received condition than their higher carbon or alloy counterparts. This can lead to significant energy and production savings because:

- (i) annealing times prior to cold forming can frequently be cut in half compared to those needed for conventional alloy steels(51);

- (ii) boron steels do not require annealing after hot forging and before cold trimming and yet trim die life remains adequate (1). In addition, it has been observed that boron steels have a less adherent scale than conventional alloy steels, so that die life is improved.

2.1.5.2 Considerations Regarding Temper Embrittlement

It has been stated that the use of boron increases the potential of the steel for temper embrittlement, which is a loss in the as-tempered ductility after tempering in a specific range (depending on the composition) or slow cooling through it (7). Closer examination shows, however, that this is only so in certain cases, and exactly the opposite may be true in others. It is known that individual alloying elements either enhance or retard the development of temper embrittlement. Among the common alloying elements, molybdenum is generally added to prevent or diminish this phenomenon; whereas manganese and chromium make the steel more susceptible to it. When boron is added in order to replace molybdenum for hardenability purposes, the protective action of molybdenum will be lost. However, if boron is used to substitute for chromium (which is usually the case), the temper embrittling tendency of the steel remains the same or improves somewhat (7). Boron added to steel not susceptible to embrittlement will have no effect. If a steel is already susceptible without boron and there is no change in composition other than the addition of boron, there will be an increase in susceptibility (7, 52).

2.1.5.3 Hot Workability

Boron steels are easier to hot form than their low alloy counterparts for the reason that most alloying elements strengthen the austenite at hot working temperatures, whereas boron only has a minimal effect. Thus if the former are replaced by the proper amount of boron, the hot workability will improve (7). This has two important energy saving implications in that; (a) less work is required for deformation at a given temperature; and (b) for the same amount of deformation energy, a lower working temperature may be used. There are

certain precautions to be taken in the use of boron, however. Plain carbon and carbon-manganese-boron steels have a tendency toward hot shortness, so the steelmaker must guard against overheating (53). The phenomenon is associated with the formation of a low melting point eutectic between an intermetallic of the form M_2B , austenite and possibly cementite (7). This tendency can be avoided by maintaining the boron concentration within the optimum range and by guarding against high temperatures and excessively long soaking times.

2.1.5.4 Creep Resistance

The beneficial effect of boron on the creep properties of austenitic stainless steels has long been recognized (54). Additions of 0.002 - 0.005% B improve creep resistance and high temperature ductility in these steels, as well as in some superalloys. Adding 50 ppm of boron to types 316, 321, and 347 stainless steel increases the mean stress rupture life by a factor of three or increases the stress to failure in 10000 hours by up to 25% (55). In ferritic steels, such as the heat resisting Cr-Mo grades, boron is claimed to have a detrimental effect on rupture ductility (56), but benefits have been reported in cases where boron is used in combination with titanium, molybdenum or niobium (57).

2.1.5.5 Boron in HSLA Steels

Boron drastically increases the bainite hardenability through its strong inhibiting effect on the ferrite reaction, as described above. This can be used in some cases to reach higher strength levels in steels which would normally exhibit a ferrite-pearlite structure after air cooling. However, the toughness of bainite is intrinsically low. In order to improve the fracture resistance of bainitic steels, it is indispensable to minimize the austenite grain size prior to the bainite transformation. This is because the effective grain size for cleavage fracture of the bainitic steels has a strong dependence on the prior austenite grain size (28). These bainitic steels, which usually have very low carbon contents (less than 0.05% C) and consequently very good toughness and

weldability, need to be controlled rolled, a process which offers significant processing economies in comparison with the alternative of quenching and tempering.

2.2 CONTROLLED ROLLING OF HSLA STEELS

In its most general sense, controlled rolling (or thermomechanical treatment) refers to any combination of deformation and temperature control during the processing of materials which enables the required product properties to be attained without any further heat treatment. The aim of conventional controlled rolling is the production of steels with a combination of high strength and toughness. This can best be achieved with a refined and homogeneous austenite structure which leads to a fine and homogeneous ferrite structure in the final product.

In steels, controlled rolling is often considered to have three (58) or four stages (59). These are: reheating (or soaking), roughing, finishing and, if the product is sufficiently thin, coiling. The basic metallurgical principles of the first three stages are illustrated in Fig. 2.6. The influence of accelerated cooling after reheating is also described below.

2.2.1 REHEATING AND SOAKING

This stage consists of reheating the material at a temperature conventionally between 1200 and 1300°C (60, 61). In order to save energy, lower temperatures are being increasingly used. During soaking, it is desirable to bring all the microalloy carbonitrides into solid solution (with the exception of TiN). The selection of the soaking temperature and time is very important as it is related to both economic and metallurgical aspects of the process. Low soaking temperatures produce relatively small initial austenite grains and consequently smaller reductions are required for recrystallization. Soaking temperatures lower than the carbonitride solution temperature can also be used. However, the undissolved precipitates lead to loss in efficiency of both the

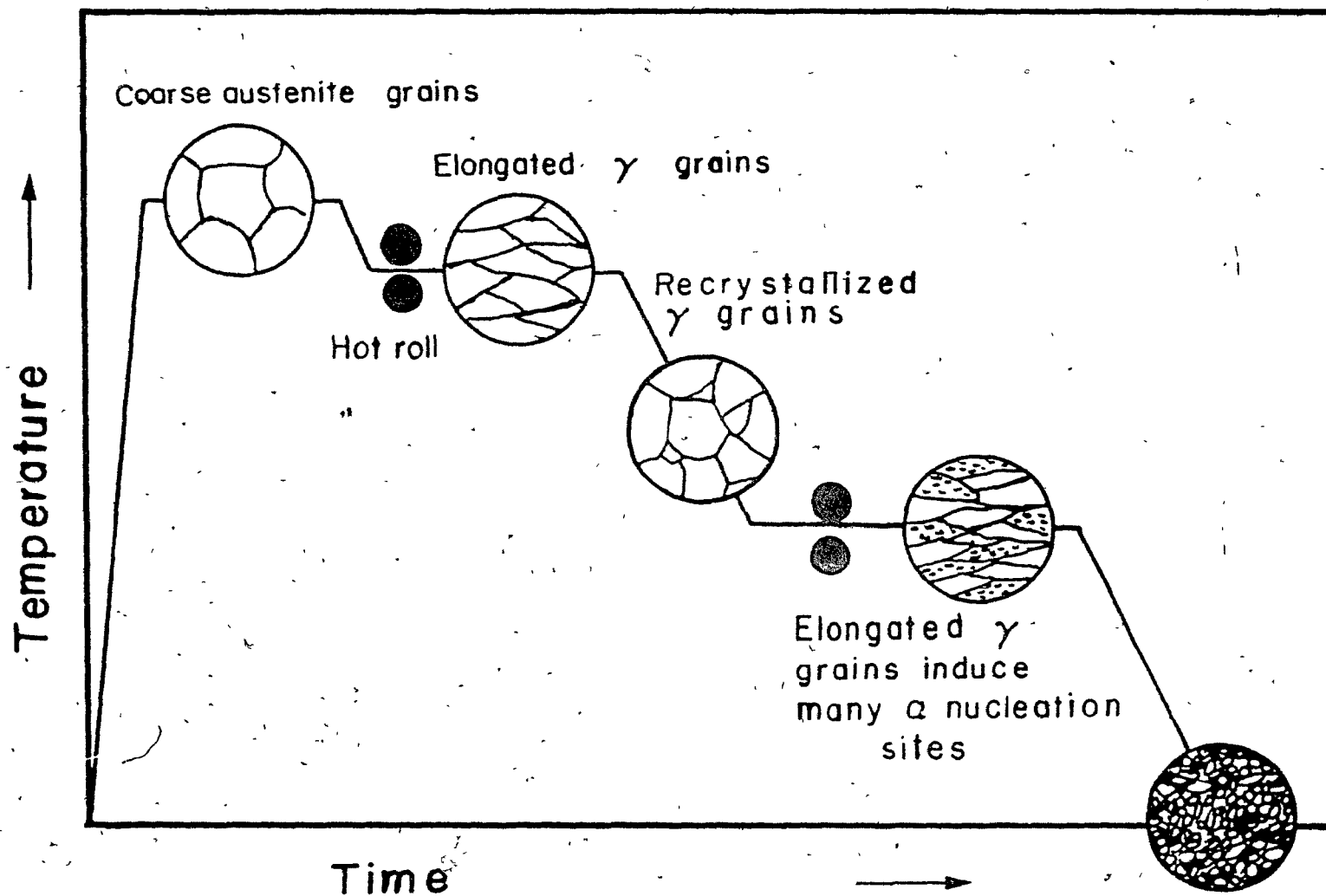


Figure 2.6 Schematic illustration of the controlled rolling process and the resulting microstructures.

solute retardation of recrystallization in the subsequent stages of the process as well as in effectiveness of precipitation strengthening.

2.2.2 CHANGES IN AUSTENITE STRUCTURE DURING HOT ROLLING

It has been mentioned earlier that the state of austenite prior to ferrite formation is very important because it determines the size and morphology of the grains in the final product. These, in turn, are mainly responsible for the mechanical properties of the material. In Fig. 2.7, the three "states" of the austenite are illustrated:

- (i) The range of high temperatures of deformation. Recrystallization in this region is very rapid (within milliseconds or seconds) and is followed by some grain growth, leading to some refinement of the austenite grains. In industry, this region corresponds to roughing and rolling for width.
- (ii) The intermediate temperature range. Provided the strain and strain rate of deformation are properly chosen, complete static recrystallization takes place and small austenite grains are observed (case c). If the conditions are not well chosen, then a sluggish and incomplete recrystallization takes place (case a). Alternatively, static recrystallization can be followed by localized grain growth (case b), leading to mixed grain structures. Roughing is carried out in this region as well, and only structures of the (c) type are desirable in rolling practice.
- (iii) The low temperature region (which is nevertheless above the austenite to ferrite transformation temperature A_{r3}), or no recrystallization region. Here the austenite grains are flattened and strain hardened. The grain volume remains constant but the grain surface to grain volume ratio S_v increases. This results in an increase in the number of

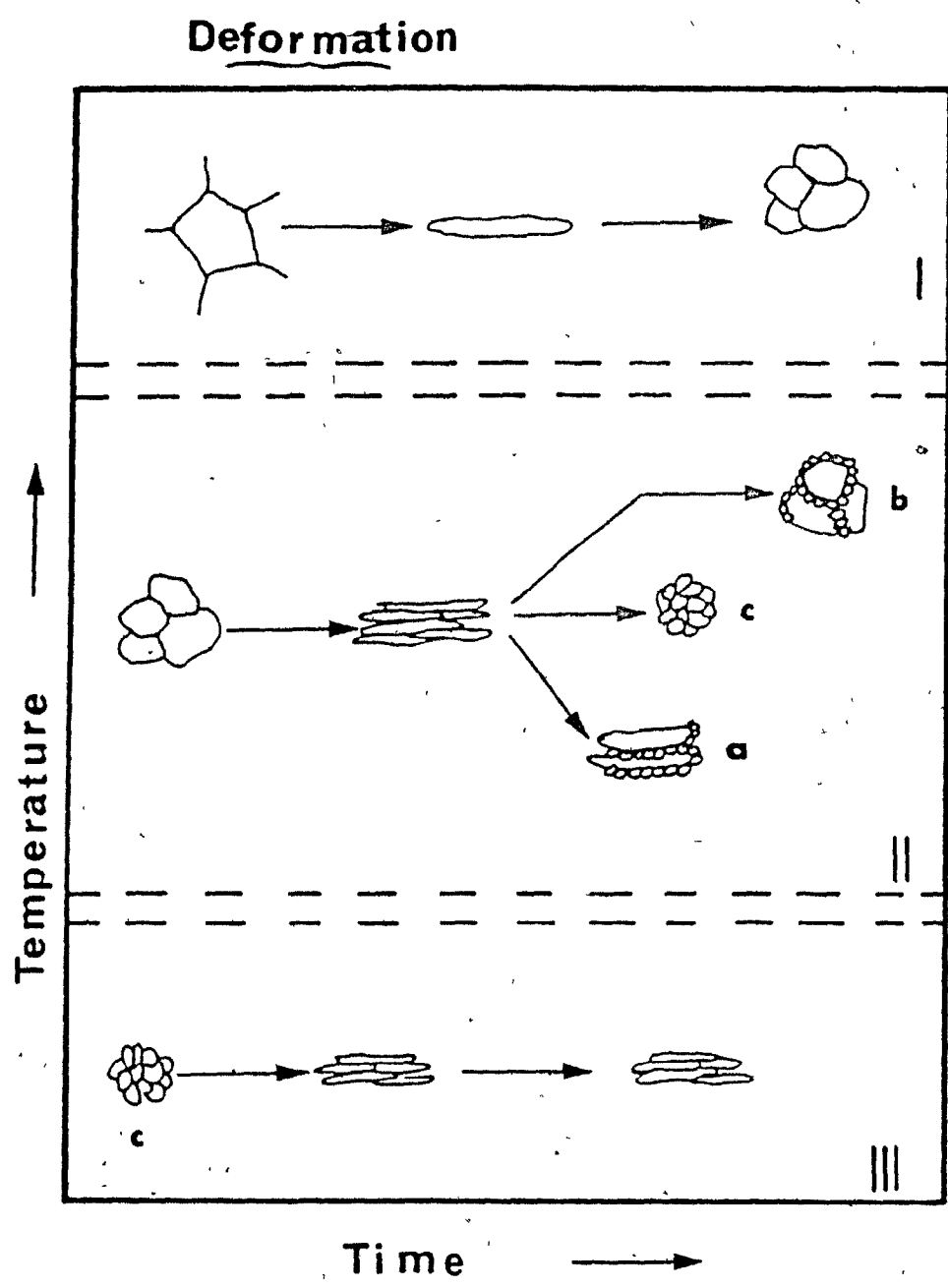


Figure 2.7 Changes in austenite grains during controlled rolling (73).

potential nucleation sites for the $\gamma \rightarrow \alpha$ transformation leading to finer final microstructures (58). Other important nucleation sites are the deformation bands inside the deformed austenite grains (62). Deformation bands are very often formed in this range of temperatures during hot rolling. Sellars et al. (63) have also reported that deformation bands are introduced into the grains and become nucleation sites for recrystallization in nickel when tested in torsion above this temperature range. However, the density of the deformation bands depends mainly on the rolling reduction (above 30%) and is hardly affected by rolling temperature and initial grain size (64). One of the problems associated with the presence of deformation bands is that the frequency of their appearance is rather random and this can lead to mixed structures.

Finally, finish rolling is sometimes extended into the region below the A_{r3} temperature. This is done so as to increase the strength and toughness. The improvement in strength is considered to be mainly due to: 1) further refinement by austenite pancaking; 2) dislocation and substructure hardening; 3) enhancement of precipitation hardening. Toughness, however, correlates with: a) the grain size of the ferrite or bainite, b) the degree of recovery of the deformed ferrite; c) the volume fraction of deformed ferrite; and d) the texture (65, 66). As far as texture is concerned, Tanaka et al. (67) have the view that extensive ferrite deformation develops a (100) texture, causing separation (splitting), which raises the transition temperature and lowers the impact energy. Thus excessive straining in the $\alpha + \gamma$ range is not recommended.

2.2.3 COOLING CONDITIONS

Cooling is a natural and integral part of controlled rolling. Its control can yield excellent results in terms of economy, productivity and material properties. Rapid cooling rates during rolling can lower the transformation temperature A_{r3} , prevent austenite recrystallization prior to transformation, and reduce the extent of carbonitride precipitation in the austenite (28). Lower

At low temperatures increase the extent of the no-recrystallization zone and also decrease the ferrite grain size. This is because ferrite grain growth is limited at lower temperatures. The limitation of precipitation in the austenite region, leaves a large proportion of the microalloying elements in solution and, as a result, leads to enhanced precipitation in the ferrite region. This is both a source of ferrite grain refinement and improved precipitation strengthening due to the formation of finer precipitates at lower temperatures.

Accelerated cooling after rolling can also be used to produce fine ferrite grains. In this way, strength and toughness are improved simultaneously. Nevertheless, when the cooling rate is too high, toughness may be reduced as a result of bainite formation. Optimum cooling rates must therefore be used, selected in connection with the hardenability characteristics of the steel.

2.3 HIGH TEMPERATURE SOFTENING MECHANISMS

The success of thermomechanical processing is largely dependent on appropriate control of the softening and hardening processes. All the above metallurgical aspects are closely related to the temperature. There are two main softening and five main hardening mechanisms; a) recovery and recrystallization; and b) grain size, solute, precipitate, and transformation strengthening as well as work hardening. The roles of the strengthening mechanisms will not be covered in this review.

2.3.1 RECOVERY

The work hardening of crystals during plastic deformation is due to the increase in dislocation density that takes place and to their mutual interaction. The introduction of dislocations produces a large increase in the strain energy of the crystals (stored energy) which can be released when the dislocations either annihilate each other or rearrange themselves into low energy configurations. Some energy is released by the local rearrangement of dislocations into tangles and a further release of energy occurs when low-angle boundaries are formed. Both these processes involve the climb of dislocations

and only occur when there is sufficient thermal activation to allow the local and long-range diffusion of point defects to take place. These changes are accompanied by the pronounced softening of hardened material. The process is called recovery and there are two different types: 1) static and 2) dynamic. Only the static variety is going to be examined here.

2.3.1.1 Static Recovery

Static recovery is involved in the entire rolling process and especially during deformation in the no-recrystallization region. The static recovery process occurs when there is no load applied to the material and it does not involve an incubation time. During the process, the sub-boundaries become sharper and the dislocation density within the subgrains is reduced, with little change in their shape or size. Temperature, strain, strain rate and addition of alloying elements are the main factors affecting the recovery rate. The rate of recovery increases as the temperature, prestrain and strain rate are increased (68).

2.3.2 RECRYSTALLIZATION

When a heavily cold worked metal (with considerable work hardening) is heated above a critical temperature, new grains, relatively free from dislocations, are produced, resulting in a process called recrystallization (69, 70). The main types of recrystallization are: static, dynamic, metadynamic and continuous (or in situ). Only the static case will be described here.

2.3.2.1 Static Recrystallization

This restoration process is the most important of the softening mechanisms involved in controlled rolling. It occurs after a critical amount of hot deformation has been applied to the material. The nucleation and completion of this type of recrystallization takes place in the absence of applied load. The time necessary for this restoration process is a function of the

material properties, the temperature, the amount and rate of prior deformation, as well as the initial grain size. During static recrystallization, the strained grains are replaced by new, strain-free ones. A large number of dislocations is consumed by the grain boundaries as they migrate through the metal (71). Finer recrystallized grains are produced when prior straining is carried out at relatively high strain rates, low temperatures, with large reductions and on material with small initial grain sizes. The incubation time and the rate of static recrystallization are also influenced by the strain, strain rate, temperature and grain size. Smaller initial grain sizes and higher strain rates increase the rate of recrystallization and decrease the incubation time (68). An increase in temperature results in a decrease in incubation time and an increase in the rate of recrystallization (68). This restoration mechanism is very important in controlled rolling practice, because small reductions per pass are frequently followed by interpass times comparable with the times required for static recrystallization. Thus recrystallization may or may not take place, depending on the details of the schedule.

2.4 SOLUTE DRAG

Many investigators agree that the presence of Nb, Ti, Mo and V as solutes in a plain carbon steel is effective in retarding recovery and recrystallization (72-78). The additions also suppress grain growth and increase the high temperature strength of the material as a whole. Similarly, the addition of 0.01% of manganese or iron to high purity aluminum can decrease the rate by a factor of 10^{12} or 10^{16} , respectively (79). Clarification of the role of impurities is therefore absolutely essential for the understanding of recrystallization in deformed materials.

Lücke and Detert (80) were the first to present a quantitative theory of grain boundary mobility in recrystallization which took into account the interaction between grain boundaries and solute impurity atoms. When foreign atoms are introduced into a pure material they occupy different sites depending on their size. If the solute and solvent atoms are roughly similar in size, the solute atoms will occupy sites in the crystal lattice of the solvent atoms, forming a substitutional solid solution. If the atoms are much smaller

than the solvent atoms, they occupy interstitial positions in the solvent lattice. Carbon, nitrogen, oxygen hydrogen, and boron are the elements which commonly form interstitial solid solutions. When the difference in size between the solute and solvent atoms is large, the lattice surrounding a foreign atom will be disturbed, causing expansion or contraction depending on whether the foreign atom is larger or smaller. As a result, solute atoms prefer to segregate to grain boundaries, thereby lowering the energy of the aggregate. Similar considerations apply to differences in elastic modulus or electronic structure. The stress field around a foreign atom within a grain, and therefore the energy E gained by moving a solute atom into the grain boundary, can be estimated from Cottrell's formula (81) if it is assumed that the grain boundary is built up of dislocations:

$$E = \frac{4}{3} r^3 G \frac{1 + \sigma}{1 - \sigma} \eta \quad (2.6)$$

$$\eta = \left| \frac{r - r_f}{r} \right| \quad (2.7)$$

Here G is the shear modulus, σ is Poisson's ratio, r is the atomic radius of the base metal, and r_f is the radius of the solute atom.

In order for the grain boundary to move during recrystallization, a driving force must act upon the boundaries. Here, it will quite simply, be assumed that the line tension of the dislocations ending in the boundary is the driving force ($\sim 10^8$ dynes/cm²). If a grain boundary loaded with foreign atoms starts to move, the solute atoms will tend to be left behind. Because of the attractive force between the boundary and the solutes, however, the latter will jump towards the boundary rather than away from it if the rate of diffusion permits it to do so. This results in a net velocity towards the boundary, so that the solute is able to follow it if the boundary moves slowly enough. Fig. 2.8 (81) shows this schematically. When a boundary moves with constant velocity, the total force acting upon the boundary must be zero; in the absence of other

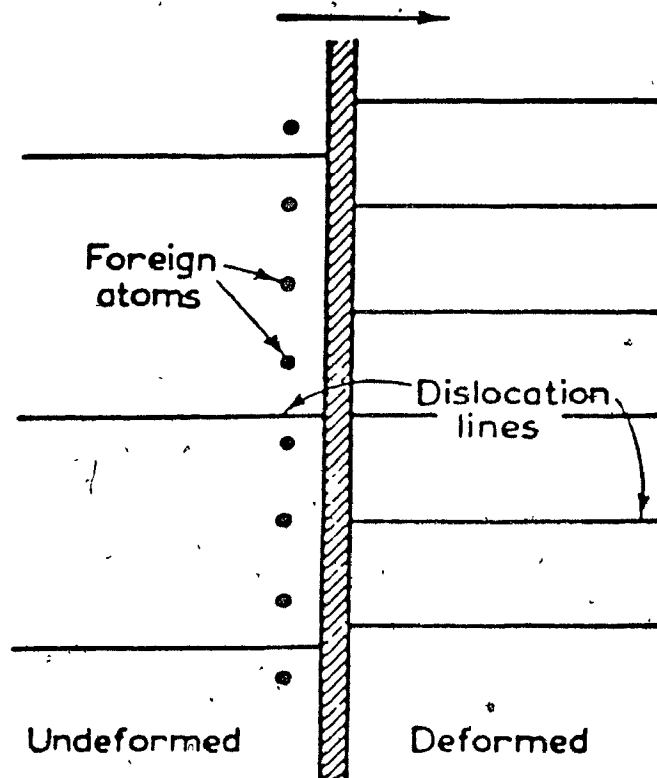


Figure 2.8 Moving grain boundary between deformed and undeformed crystals (schematic). The boundary moves under the influence of the higher density of dislocation lines in the deformed crystal in the direction of the arrow, leaving somewhat behind the atmosphere of foreign atoms (80).

forces, the driving force will just be compensated by the retardation due to the impurity atoms behind the boundary. It is assumed that the rate of boundary motion is the rate determining process and that without impurity atoms the boundary would move very much faster. Because the theory of Lücke and Detert (80) as first proposed failed to explain the results of Aust and Rutter (82) regarding the relative effects of silver, gold and tin in high purity lead, the model proposed by J.W. Cahn (83) was introduced. It will now be described and is employed in the Discussion part of this thesis.

2.4.1 THE COMPOSITION PROFILE

If the grain boundary can be represented by an interaction energy $E(x)$ and a diffusion coefficient $D(x)$ for transport normal to the boundary, both of which are functions of the distance from an arbitrarily chosen center plane of the boundary, the chemical potential of the impurity species can be given by:

$$\mu = KT \ln C(x) + E(x) + \text{Const} \quad (2.8)$$

where K is Boltzmann's constant, T is the temperature, $C(x)$ is the composition and the constant is chosen so that $E(\infty) = 0$.

The flux of atoms is assumed to be given by:

$$-J = \frac{DC}{KT} \frac{\partial \mu}{\partial x} = D \frac{\partial C}{\partial x} + \frac{DC}{KT} \frac{\partial E}{\partial x} \quad (2.9)$$

and

$$\frac{\partial C}{\partial t} = D \frac{\partial^2 C}{\partial x^2} + \left[\frac{\partial D}{\partial x} + \frac{D}{KT} \frac{\partial E}{\partial x} \right] \frac{\partial C}{\partial x} + \frac{1}{KT} \left[\frac{\partial D}{\partial x} \frac{\partial E}{\partial x} + D \frac{\partial^2 E}{\partial x^2} \right] C \quad (2.10)$$

When the velocity of the grain boundary (V) is constant, the composition profile can be expressed as:

$$\frac{\partial C}{\partial t} = -V \frac{\partial C}{\partial x}, \quad V > 0 \quad (2.11)$$

and consequently, by combining Eq. 2.10 and Eq. 2.11, we obtain

$$0 = D \frac{\partial^2 C}{\partial x^2} + \left[\frac{\partial D}{\partial x} + \frac{D}{KT} \frac{\partial E}{\partial x} + V \right] \frac{\partial C}{\partial x} + \frac{C}{KT} \left[\frac{\partial D}{\partial x} \frac{\partial E}{\partial x} + D \frac{\partial^2 E}{\partial x^2} \right] \quad (2.12)$$

Eq. 2.12 was derived under the assumption that we are dealing with dilute solutions everywhere (for Eq. 2.8 to be valid) and that D is defined as the ratio $-JKT/(\partial\mu/\partial x) \cdot C$ (for Eq. 2.9), so that, for a given temperature it is only a function of x .

The solution to Eq. 2.12 is given by:

$$C = C_0 V \exp \left[-\frac{E(x)}{KT} - V \int_{x_0}^x \frac{d\eta}{D(\eta)} \right] * \\ * \int_{-\infty}^x \exp \left[\frac{E(\xi)}{KT} + V \int_{x_0}^{\xi} \frac{d\eta}{D(\eta)} \right] \frac{d\xi}{D(\xi)} \quad (2.13)$$

Equation 2.13 does not hold for $V < 0$ and at $V = 0$ we obtain a singularity. Therefore, for $V = 0$ we can have, from Eq. 2.8:

$$C = C_0 \exp \left[-\frac{E(x)}{KT} \right] \quad (2.14)$$

where C_0 is the matrix composition.

2.4.2 IMPURITY DRAG

The force exerted by a solute atom on the boundary is $-(dE/dx)$ (negative when adsorption is taking place). The total force applied by all impurity atoms on the boundary is given by:

$$P_i = -N_v \int_{-\infty}^{\infty} (C - C_0) \frac{dE}{dx} dx \quad (2.15)$$

where $N_v = 4/a^3$ is the number of atoms per unit volume and a is the lattice parameter.

Because the values of $C(x)$, $E(x)$ and $D(x)$ are difficult to assess in order to evaluate P_i , some approximations must be made.

2.4.2.1 High Velocity Limit

By expanding the functions $E(\xi)$, $D(\xi)$ and $\int_{x_0}^{\xi} d\eta/D(\eta)$ in Eq. 2.13 in a Taylor series about $\xi = x$ and neglecting the higher order terms, we can obtain an approximate expression for $C(x)$, which is:

$$C(x) \approx \frac{C_0}{1 + \frac{DE'}{KTV}} \quad (2.16)$$

This is valid under the condition that $V \gg -D(x)/KT \cdot E'(x)$; the impurity drag is then approximately equal to:

$$P_i = \frac{N_v C_0}{KTV} \int_{-\infty}^{\infty} E^2 D dx \quad (2.17)$$

which indicates that the drag is proportional to the diffusivity and inversely proportional to the velocity.

2.4.2.2 Low Velocity Limit

If it is assumed that there exists a distance Λ from the boundary beyond which $E = 0$ and $D = D(\infty)$, we can, for $V \int_{-\Lambda}^{\Lambda} dx/D(x) < 1$ or $1/V > \int_{-\Lambda}^{\Lambda} dx/D(x)$ expand the part of the exponential involving V in Eq. 2.13 and obtain for $-\Lambda < x < \Lambda$

$$C(x) = C_0 e^{-E/KT} \left\{ 1 + V \int_{-\Lambda}^x \frac{e^{-\frac{E(\xi)}{KT}} - 1}{D(\xi)} d\xi + O(V^2) \right\} \quad (2.18)$$

When Eq. 2.18 is substituted into Eq. 2.15, the drag is given as:

$$P_t = 4 N_0 C_0 V K T \int_{-\infty}^{\infty} \frac{\sinh^2[E(x)/2KT]}{D(x)} dx \quad (2.19)$$

2.4.2.3 Approximate Equation for Impurity Drag

The two equations for the drag (Eqs. 2.17, 2.19) can be combined into one which holds for both the high and low velocity ranges as follows:

$$P_t = \frac{\alpha V C_0}{1 + \beta^2 V^2} \quad (2.20)$$

where

$$\alpha = 4 N_v K T \int_{-\infty}^{\infty} \frac{\sinh^2 \frac{E(x)}{2 K T}}{D(x)} dx \quad (2.21)$$

$$\frac{\alpha}{\beta^2} = \frac{N_v}{K T} \int_{-\infty}^{\infty} \left(\frac{dE}{dx} \right)^2 D(x) dx \quad (2.22)$$

Both α and β are inversely proportional to the diffusivity.

The drag first increases with velocity, then it reaches a maximum at $V\beta = 1$ and finally decreases. It has an inflection point at $V\beta = \sqrt{3}$ for which the slope is $dP_i/dV = -\alpha C_0/8$ and at which the drag has the value $P_i = \sqrt{3} \alpha C_0/4\beta$. For an assumed interaction energy profile as shown in Fig. 2.9, the values of α and β can be given as:

$$\alpha = N_v (K T)^2 \delta \left(\sinh \frac{E_0}{K T} - \frac{E_0}{K T} \right) \quad (2.23)$$

$$\beta^2 = \frac{\alpha K T \delta}{2 N_v E_0^2 D} \quad (2.24)$$

where δ is the width of the grain boundary. Fig. 2.10 gives the corresponding impurity drag for various velocities.

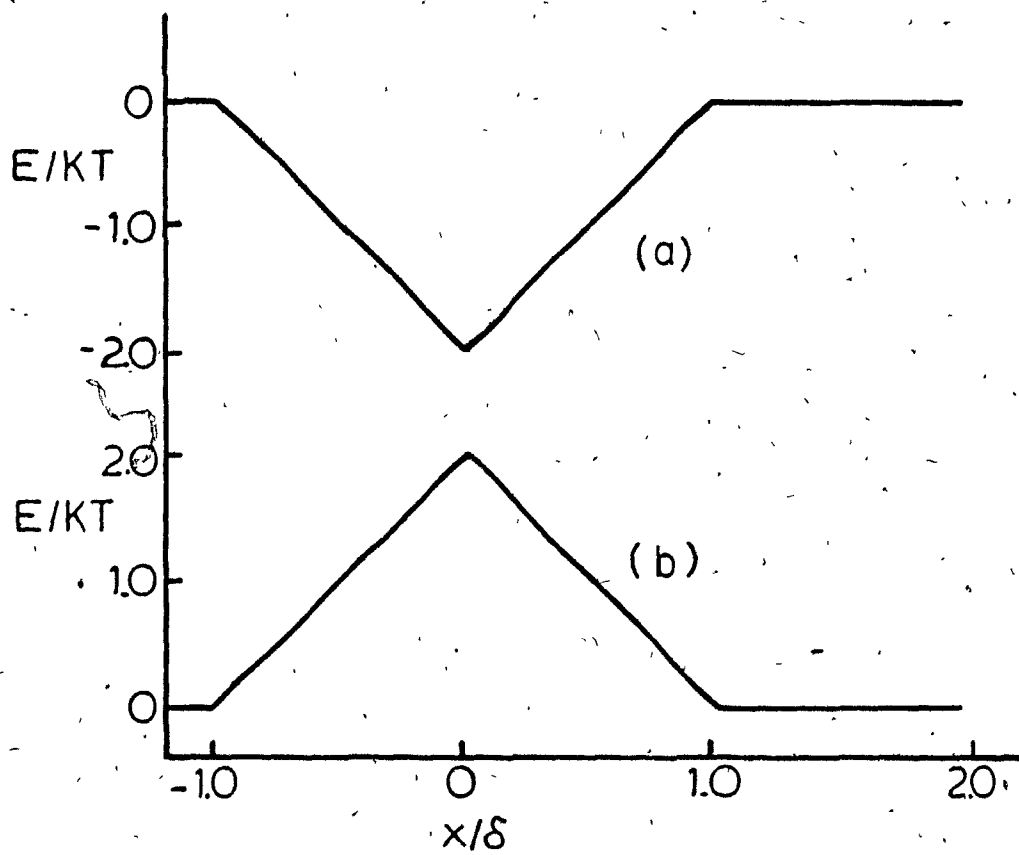


Figure 2.9 The interaction energy profile $E(x)$ used.
(a) $E < 0$; (b) $E > 0$.

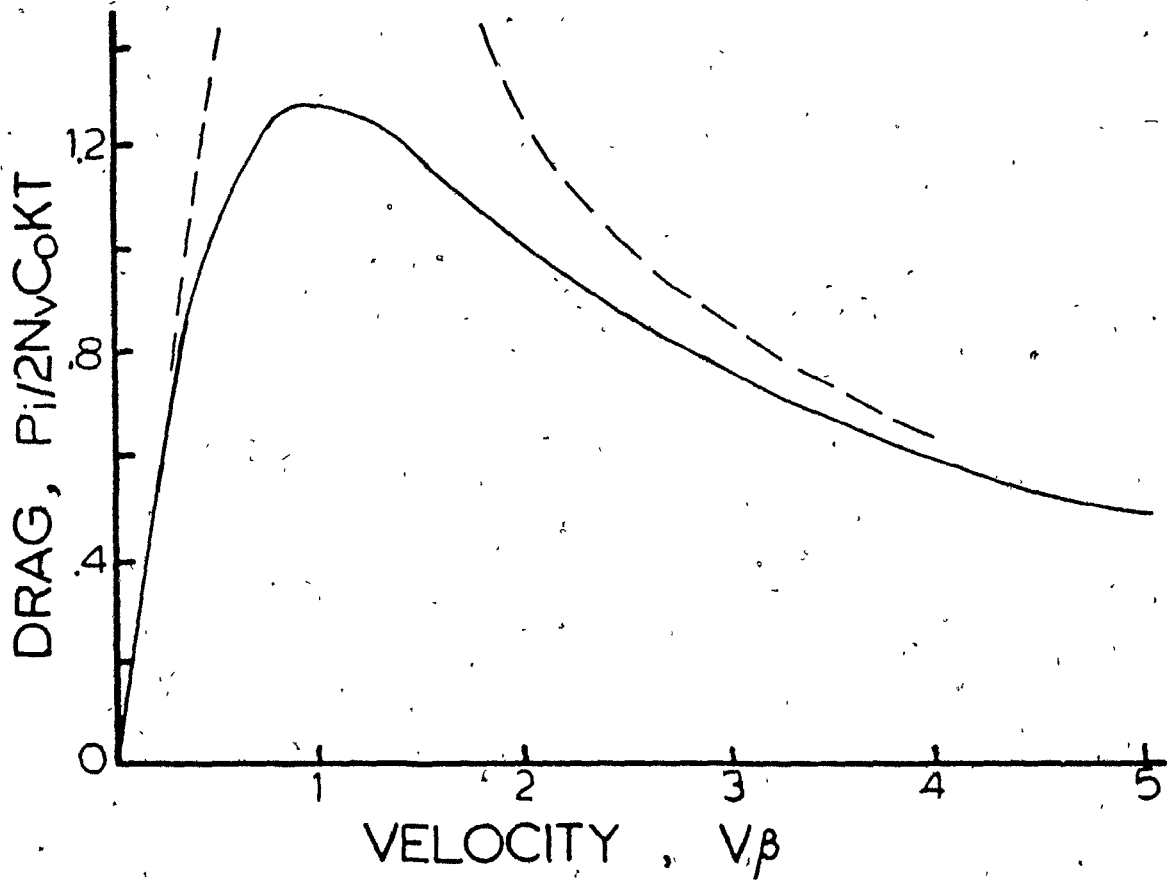


Figure 2.10 Impurity drag for various velocities (83).

CHAPTER 3

EXPERIMENTAL MATERIALS AND PROCEDURE

3.1 EXPERIMENTAL MATERIALS

Four steels were used in the present work, with the purpose of investigating the effect of boron addition on the recrystallization behaviour of ultra low carbon steels. These steels were prepared in the Physical Metallurgy Research Laboratories of the Department of Energy, Mines and Resources (Ottawa), and their chemical compositions are listed in Table 3.1. The low carbon content was selected as being representative of the ULCB (ultra low carbon bainitic) steels being made for pipeline applications. The titanium addition was made to prevent boron nitride formation, which would have eliminated boron in solution, and thus have interfered with its role in promoting bainite formation. The aluminum, in turn, was added to protect the titanium from oxidation. Finally the niobium addition was designed to provide precipitation strengthening and to improve the hardenability by acting in conjunction with the boron.

The preparation of compression specimens was based on that used in previous investigations (84, 85). Cylindrical samples were machined from the as-received plates with the compression axes aligned parallel to the rolling direction. An aspect ratio (height-to-diameter) of 1.5 was selected to promote homogeneous deformation (84). The end surfaces of the specimens were grooved (86) to allow for maximum retention of the glass powder lubricant. The sample and groove geometries are illustrated in Fig. 3.1.

All samples were heat treated at 1000°C for 1 hour under vacuum, and then air cooled. This normalization heat treatment was applied in order to eliminate the rolling textures present in the as-received material; such textures frequently lead to the production of elliptical cross-sections in deformed samples.

TABLE 3.1 - Chemical Compositions of the Steels Investigated (wt.%)

	<u>C</u>	<u>Mn</u>	<u>Si</u>	<u>P</u>	<u>S</u>	<u>Ti</u>	<u>Nb</u>	<u>B</u>	<u>Al</u>	<u>N</u>
Base	.03	1.54	.19	.008	.005	.02	----	----	.02	.0048
Boron	.03	1.55	.18	.007	.006	.02	----	.0033	.02	.0043
Nb	.026	1.42	.156	.007	.007	.02	.055	----	.02	.0063
Nb + B	.026	1.56	.150	.006	.007	.02	.055	.0030	.025	.0064

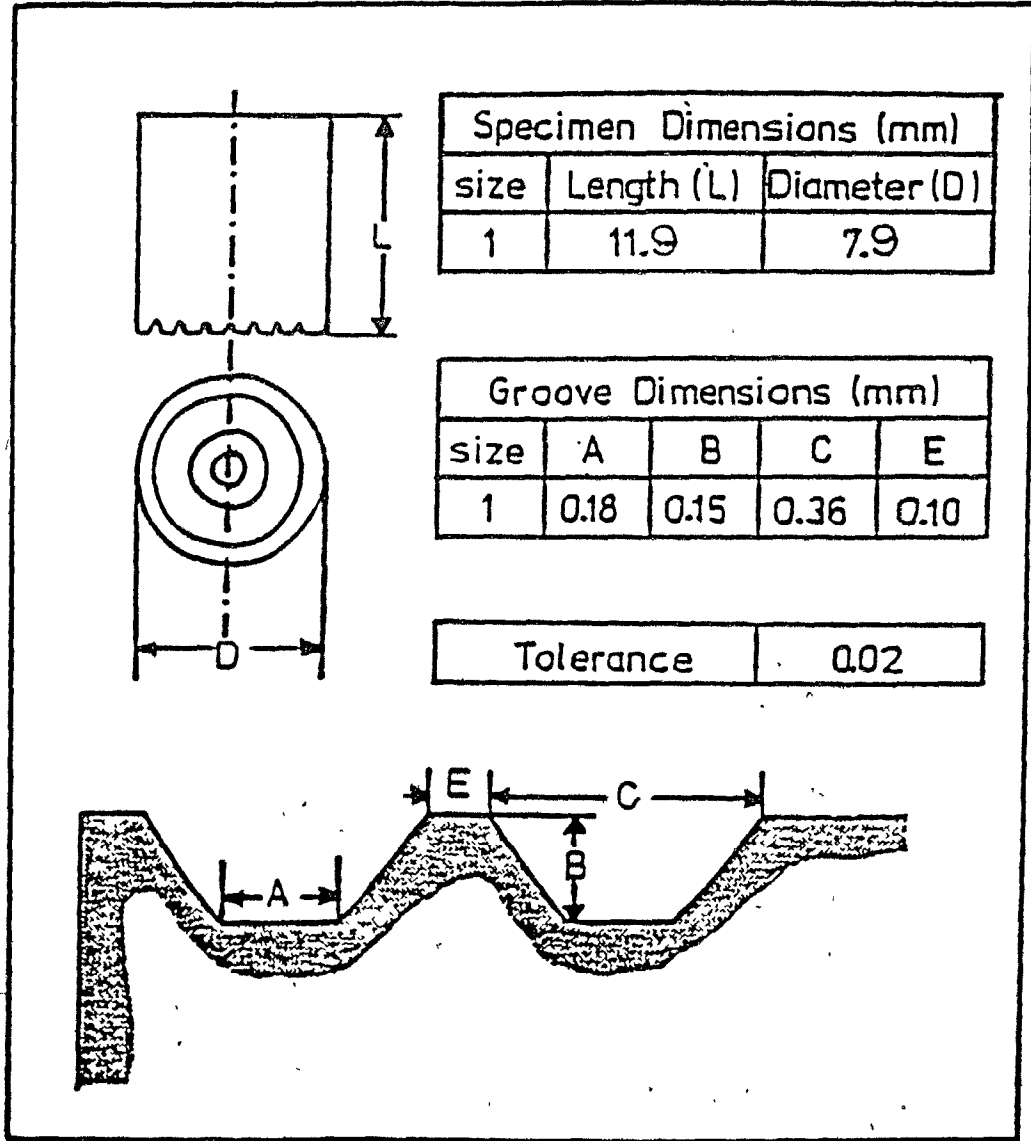


Figure 3.1 Compression test sample geometry and groove design (84).

3.2 EXPERIMENTAL EQUIPMENT

The hot compression tests were carried out on a 100 kN MTS closed loop electrohydraulic testing machine. A CENTORR model M60 front loading high temperature high vacuum furnace was used to provide the temperature requirements for the experiments. For purposes of performing constant true strain rate compression tests and of data acquisition, the MTS testing machine is interfaced to a PDP-11/04 minicomputer by means of an MTS 433 unit. The loads and displacements were stored by the computer during the compression of the sample, and were subsequently displayed on a Tektronix 4010 graphics terminal immediately after each test.

Flow curves were plotted using the same terminal and permanent copies were provided by a Tektronix 4613 hard copy device. Following that, the test data were transferred to a floppy disk for permanent storage; they could be recalled at will at later times.

External views of the test assembly can be seen in Figs. 3.2 and 3.3; these include the MTS machine (a), the furnace (b), the PDP-11/04 computer (c), the Tektronix terminal (d) and hard copier (e), as well as the control consoles for the vacuum system and temperature regulation for the MTS machine (f).

The compression tooling was comprised of upper and lower anvils (tungsten) tightly screwed to stainless steel extension rods. The top extension rod is fixed to the ram of the MTS machine, whereas the lower one is attached to the load cell. An interior view of the furnace chamber, the compression tools and heating system is given in Fig. 3.4. (The heating elements are of tungsten mesh). The experiments were carried out in a vacuum of 10^{-5} torr or better.

3.3 EXPERIMENTAL METHOD AND CONDITIONS

3.3.1 STATIC RECRYSTALLIZATION

The experimental technique for following the static recrystallization of hot worked austenite used in this investigation was the interrupted

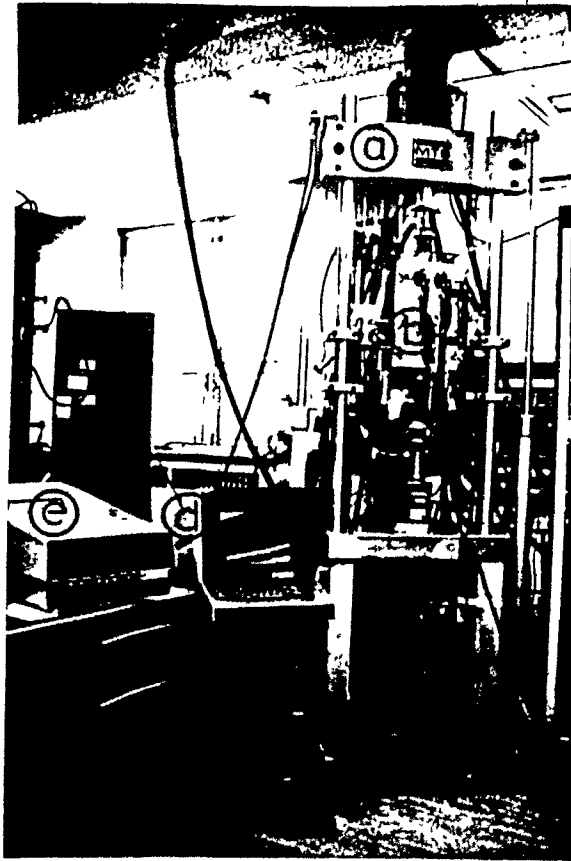


Figure 3.2 External view of the high temperature compression testing equipment.

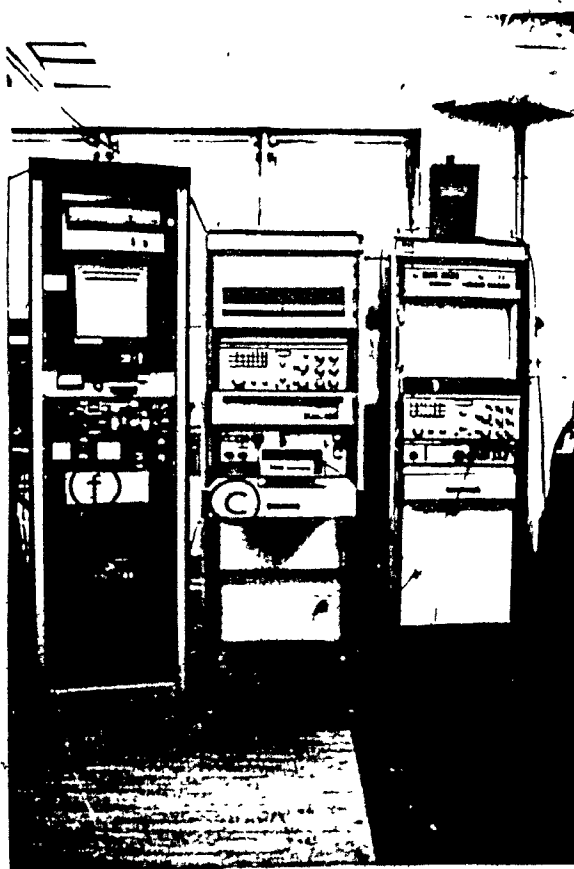


Figure 3.3 External view of the computer and control consoles for vacuum and temperature regulation.

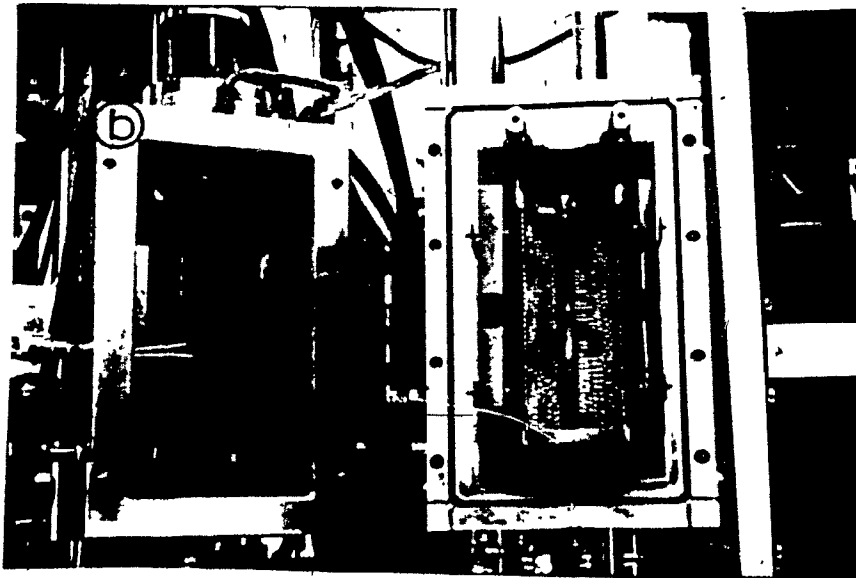


Figure 3.4 Interior view of the CENTORR high temperature furnace and compression tools.

compression test method developed by Petkovic (87). This technique is based on the principle that the yield stress at high temperatures is a sensitive measure of the structural state of the material. Examples of the two experimental curves are presented in Fig. 3.5. These samples were loaded at a constant strain rate of 2 s^{-1} to a prescribed strain of 0.25, unloaded, and held at zero load for time intervals of 1.5 and 10 s. After the interruption, the samples were reloaded at the same strain rate for an additional strain of 0.25. As can be seen from Fig. 3.5, after an interruption of 1.5 s, the flow curve on reloading rises rapidly to a stress level comparable with the loading curve. By contrast, when the interruption time is longer (e.g. 10 s), the reloading flow curve approaches that observed during the initial loading of the annealed material.

The degree of softening, X , taking place during the unloading period can be estimated from the expression

$$X = \frac{\sigma_m - \sigma_r}{\sigma_m - \sigma_0} \quad (3.1)$$

Here σ_m is the flow stress immediately before unloading and σ_0 and σ_r are the yield stresses pertaining to the first and second cycles of loading, respectively (Fig. 3.6). An offset strain of 0.2% was used to define the initial flow (yield) stresses on loading and reloading.

All the samples were subjected to an austenitization heat treatment immediately prior to testing for the following two reasons:

- The complete dissolution of all the microalloy carbides was desired; and
- It was considered useful to have approximately the same austenite grain size in all the steels.

The equilibrium solution temperature of NbC was calculated from the relation given by Cordea (88):

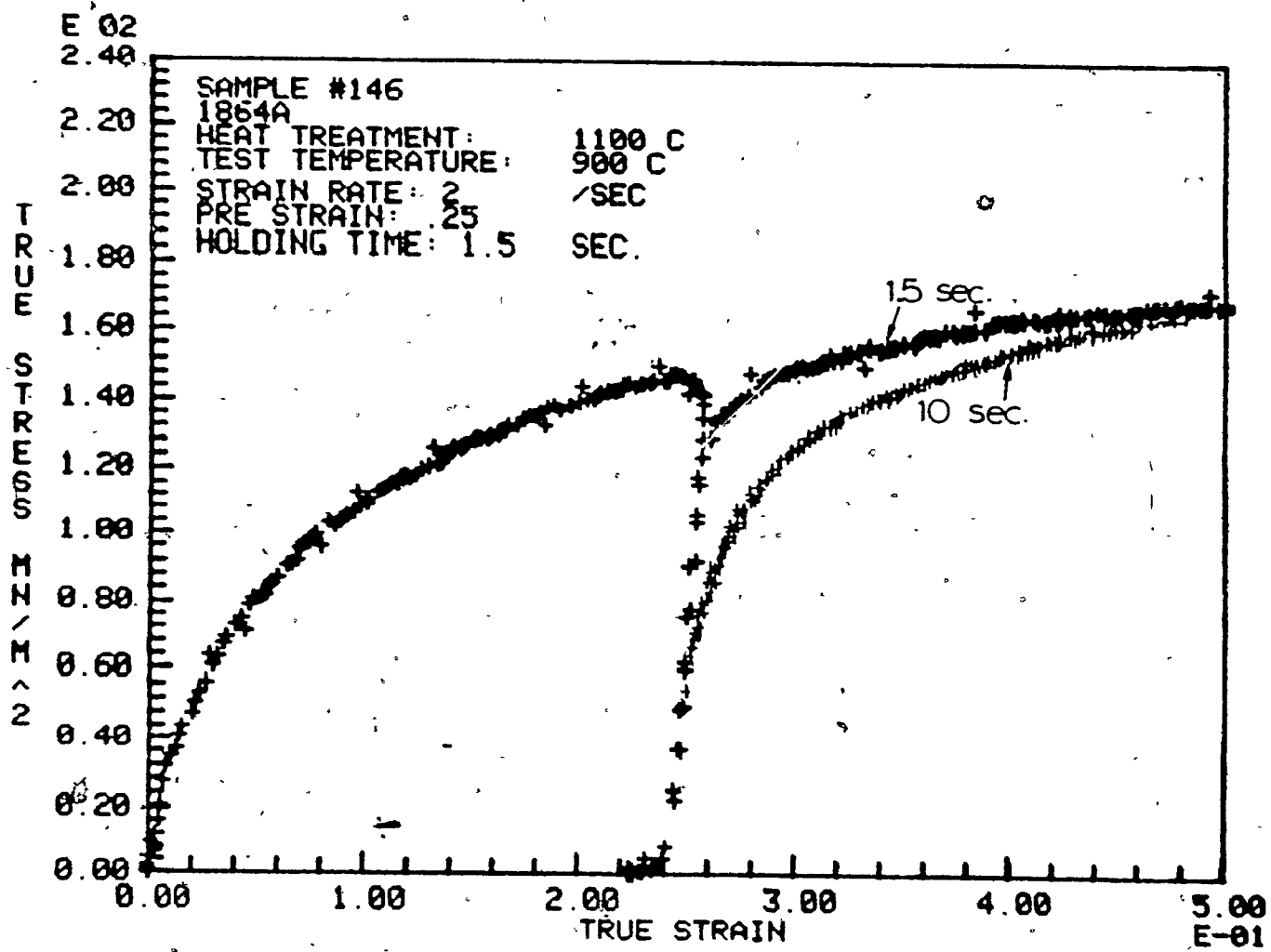


Figure 3.5 Typical experimental flow curves for interruption times of 1.5 and 10 seconds.

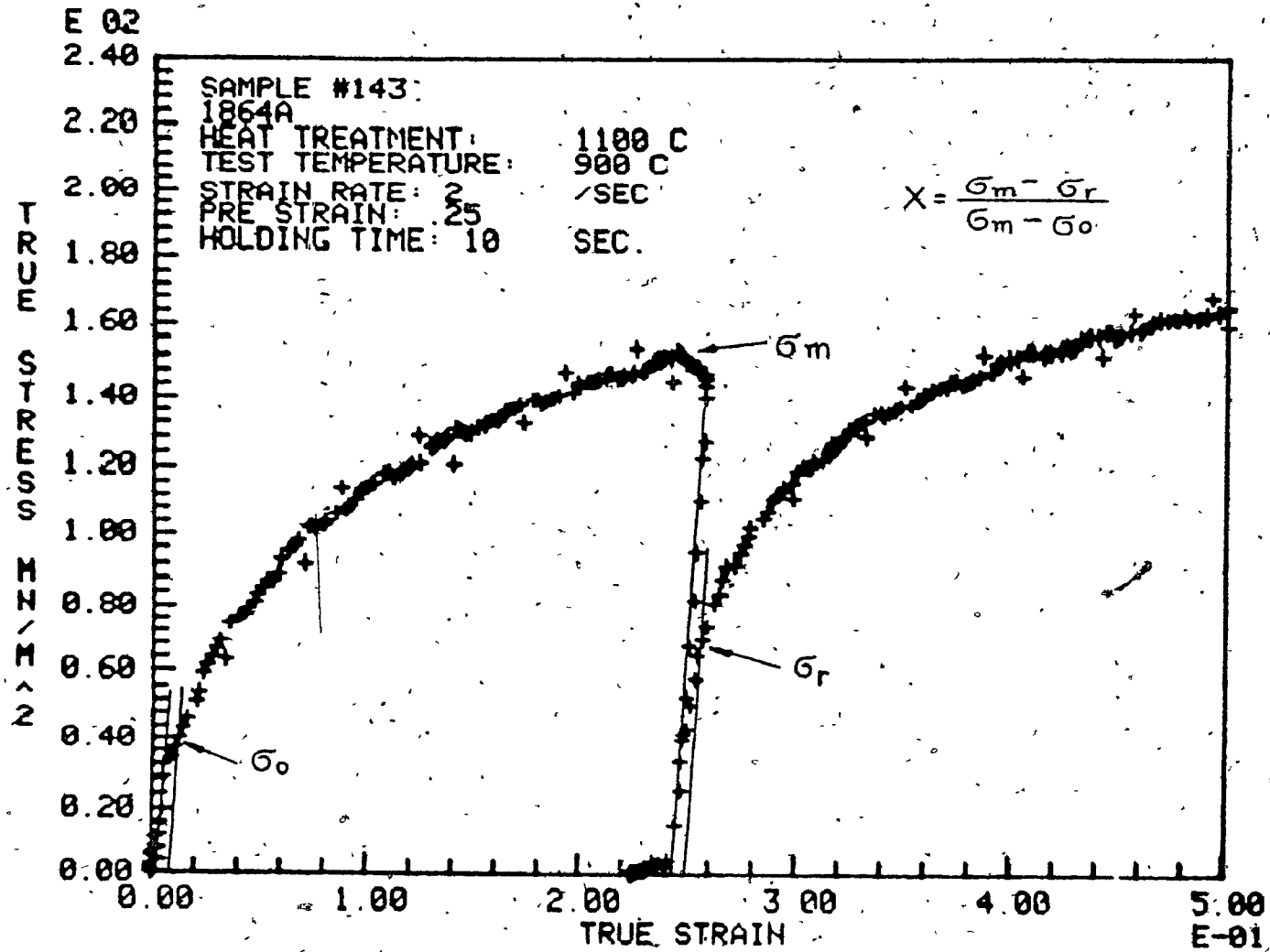


Figure 3.6 Determination of the percentage softening by the offset method.

$$\log[(Nb)(C)] = -\frac{7510}{T} + 2.96 \quad (3.2)$$

In the above equation, (Nb) and (C) are the concentrations in weight percent of Nb and C, respectively, and T is the absolute temperature. The solution temperature was estimated to be approximately 1020°C. In order to ensure complete dissolution, the austenitization temperature was raised approximately 75°C above the estimated one. In this way the austenitization temperature was selected to be 1100°C, a temperature high enough to dissolve the Fe₂₃(B, C)₆ precipitates as well. Finally, some large precipitates (TiN and MnS) were detected at 1100°C. These were formed at much higher temperatures and also act as grain refiners in the present case because they prevent grain coarsening during austenitization.

3.3.2 DYNAMIC RECRYSTALLIZATION

The parameters associated with dynamic recrystallization were obtained from interrupted stress-strain curves, as indicated in Fig. 3.7. The peak strain ϵ_p was taken as a measure of the onset of dynamic recrystallization, i.e. of the nucleation strain, even though the actual onset is known to occur somewhat earlier. In a similar manner, the recrystallization strain ϵ_x was considered to be defined by the distance between the first peak (ϵ_p) and the first valley or minimum (see Fig. 3.7).

These two quantities can be divided by the testing strain rate, $\dot{\epsilon}$, to give the nucleation time and recrystallization time, respectively, from which the corresponding rates can be calculated in turn. The austenitization and test temperatures as well as the strain rates used were selected in such a way as to provide flow curves with at least one peak and one valley for the appropriate definition of ϵ_p and ϵ_x .

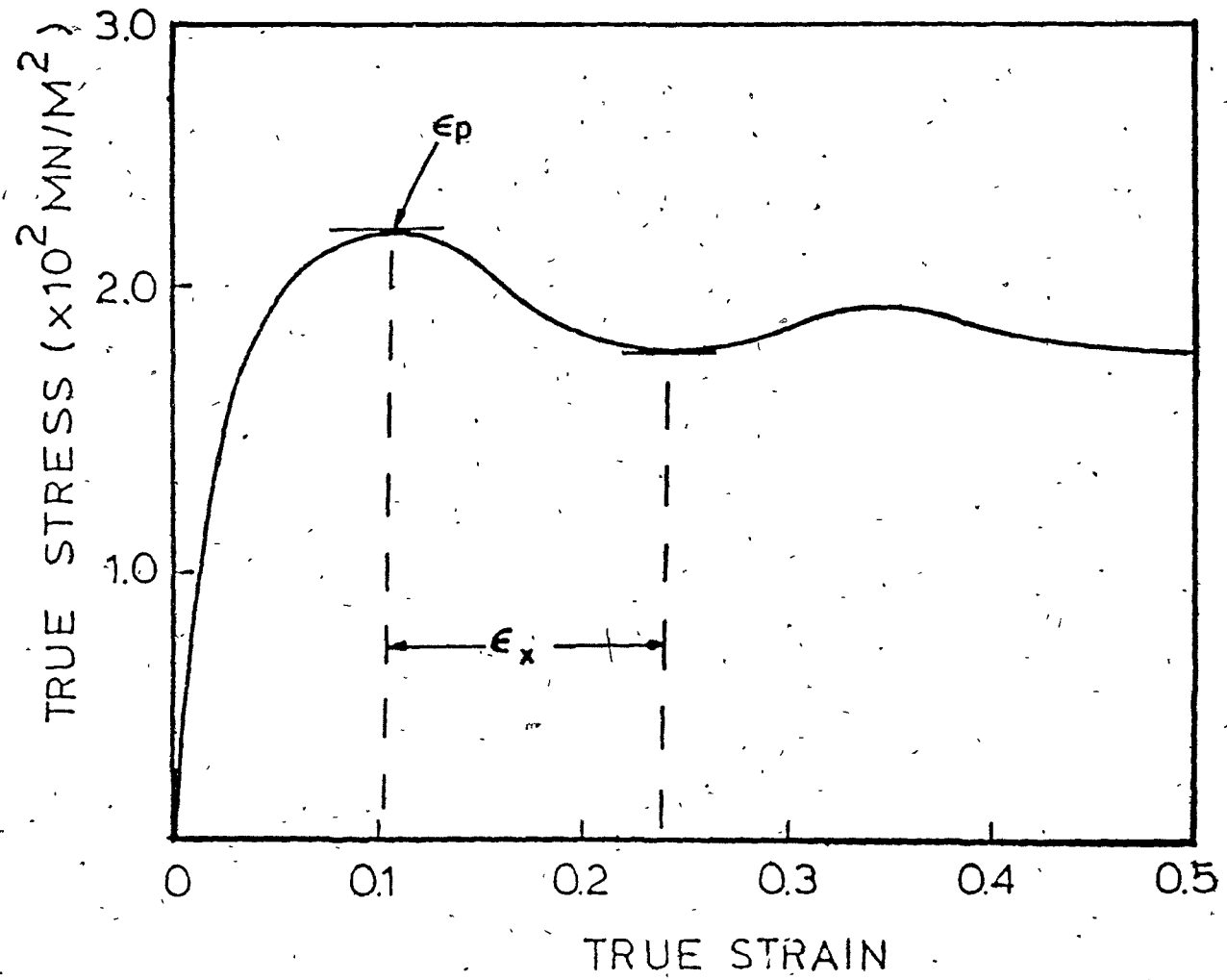


Figure 3.7 Typical stress/strain curve and the values of ϵ_p and ϵ_x .

3.4 METALLOGRAPHY

Three different types of metallography were employed in the present investigation; the sample preparation routines involved are described below.

3.4.1 OPTICAL MICROSCOPY

The quenched samples were first cut along the compression direction with a 11-1180 Buehler Isomet low speed diamond saw operated with coolant so as to protect the specimen from overheating. One of the resulting pieces was mounted in black bakelite MM 112. Then the sectioned surface was ground using 120, 240, 400 and 600 grit silicon carbide papers in sequence, polished with 6 and 1 μm diamond pastes, and finally with 0.3 and 0.05 μm alumina to finish. Etching was the last stage of sample preparation. For the quenched samples, hot saturated aqueous picric acid solutions at 60 to 90°C were used with the addition of some Teepol 601. This etchant revealed the prior austenite grain boundaries.

3.4.2 ELECTRON MICROSCOPY

The initial stage of preparation of carbon extraction replicas, used for the detection of precipitates in electron microscopy, was the same as in the case of optical microscopy. Then the polished samples were lightly etched in nital (3% HNO_3 in 95% methanol). After that, a thin and even film of carbon was deposited on the surface of the samples using a standard carbon evaporation unit. The carbon coated surfaces of the samples were scribed with a scalpel blade to produce replicas 3 x 3 mm in size.

The extraction replicas were released by electropolishing using a very low initial current for approximately 5 min., which was later increased gradually. The positive electrode of the DC power supply used was always in contact with the surface of the specimen. The composition of the electrolyte employed was the following:

78 ml perchloric acid

120 ml distilled water

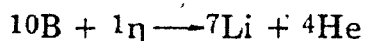
700 ml ethanol

100 ml butanol

Subsequent to that, the replicas were washed gently in alcohol first and then in a 50/50 mixture of alcohol and water and finally placed on copper grids (Cu, 3mm, 200 mesh) and dried. The grids were observed in the transmission mode (80 kV) in a JEOL-100 CX electron microscope fitted with a PGT System IV energy dispersive x-ray spectrometer (EDS) for the chemical analysis of individual particles.

3.4.3 BORON AUTORADIOGRAPHY

The technique of boron autoradiography is relatively new and it has been applied to pinpoint the location of boron in the microstructure (89, 90). Autoradiography takes advantage of the fact that naturally occurring boron consists of 18.8% ^{10}B and 81.2% ^{11}B , and when this is exposed to neutron irradiation, the ^{10}B decomposes according to:



The alpha particles (He nuclei) generated in this fashion can leave distinctive tracks on a sensitive film or emulsion placed on the steel surface to be examined. When studied under phase contrast microscopy, the film clearly delineates concentrations of boron in the microstructure.

The first stage of sample preparation was the same as for optical microscopy. Then a strip of sensitive film (Kodak LR115) was squeezed against the top of each sample. The samples were placed in an aluminum holder and then inserted into the neutron radiography facility of the NRX nuclear reactor

at AECL in Chalk River (Fig. 3.8 (91)). The samples were exposed for 385 hours to a fluence of 5×10^{14} neutrons/cm². After the above treatment, the samples were removed from the reactor and the film was etched for 5 min. in a basic solution (10% NaOH and 90% distilled water) at 65°C. Then the film was examined under top illumination in an optical microscope. Finally, the photographs were taken with a Polaroid type 55 film.

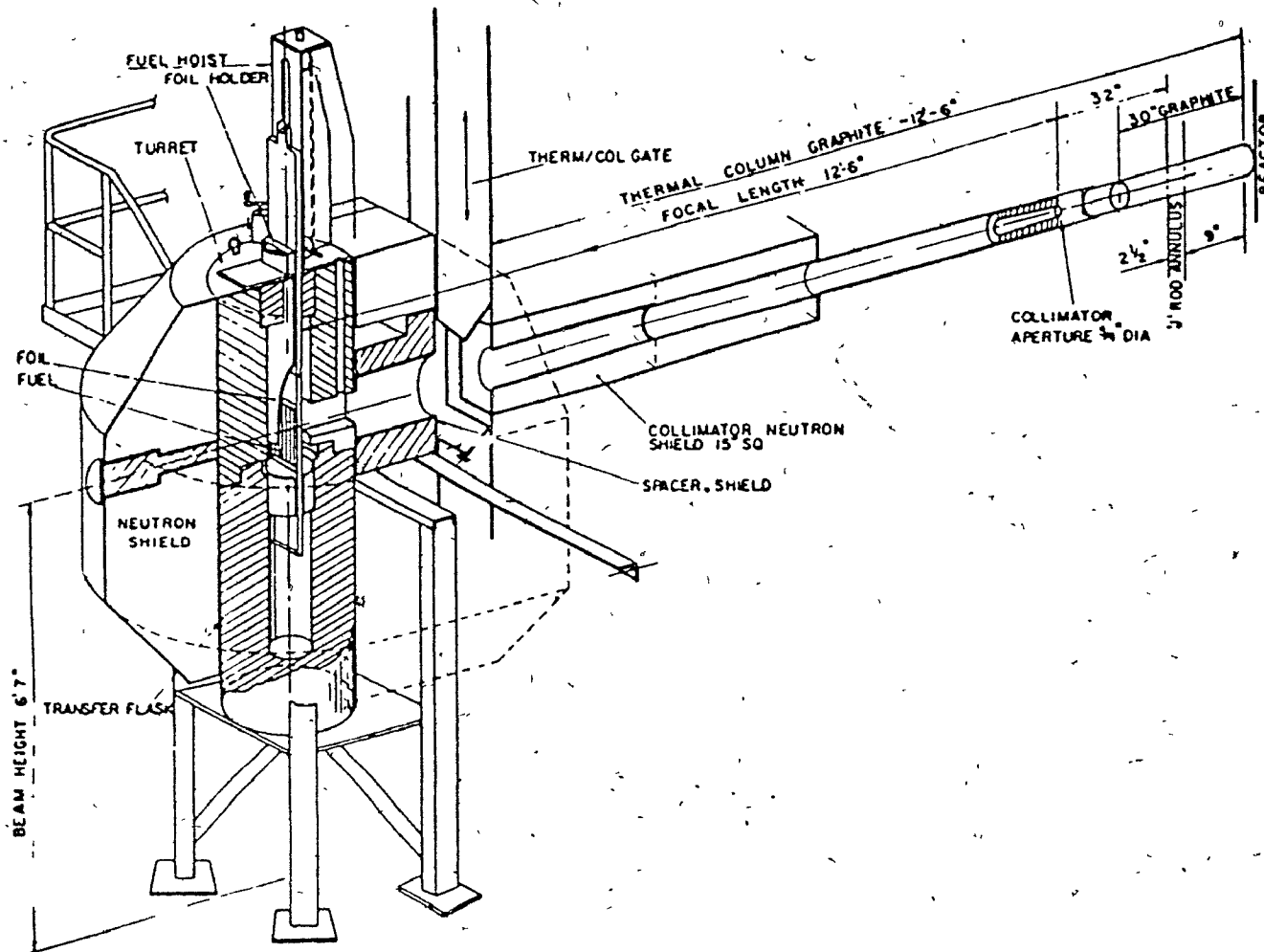


Figure 3.8 Neutron radiography unit at NRX south thermal column (91).

CHAPTER 4

EXPERIMENTAL RESULTS

The aim of the present research in its broadest interpretation was the investigation of the influence of boron on the softening processes taking place in hot worked austenite under both static and dynamic conditions. In particular, there were three detailed objectives to be dealt with, namely:

- 1) To determine the effect of boron addition on the recrystallization behaviour of hot worked austenite.
- 2) To investigate the possible synergistic influence of niobium plus boron when added jointly and to explain the roles of niobium and boron in this phenomenon.
- 3) To consider the implications of the niobium plus boron interaction on the rolling schedules appropriate to ultra low carbon bainitic (ULCB) steels.

In order to fulfil the above goals, two distinctly different sets of experiments were carried out on the four steels listed in Table 3.1. The first set of experiments was comprised of interrupted hot compression tests always performed at a constant true strain rate of 2 s^{-1} in the temperature range 900 to 1100°C .

The amount of prestrain was varied from 12 to 50% and the load-free time following the prestraining was increased from very small values (fractions of a second) to the time required for the steel to recrystallize completely. In this way the progress of static softening vs. time was studied under three different predeformation conditions (12, 25 and 50%). In order to study the influence of boron on softening under dynamic conditions, uninterrupted stress/strain curves were also employed. The basic criterion for the selection of the experimental conditions in this case was the appearance of at least one peak and one valley in the flow curves. The experimental

parameters varied in this part were: the austenitization temperature (in the range of 1050 to 1250°C), the test temperature (in the range of 1000 to 1100°C), and the strain rate (in the range of 10^{-3} to 0.5 s⁻¹).

4.1 STATIC SOFTENING RESULTS

4.1.1 FLOW CURVES OBTAINED IN INTERRUPTED COMPRESSION TESTS

Selected sets of true stress-true strain curves are presented in Figures 4.1 to 4.4. These were produced by the computer after interrupted compression tests performed at 1000°C on the plain carbon, boron, niobium, and niobium plus boron steels, respectively. In order to keep the diagrams simple, a single curve was selected as representative for the plain carbon and boron steels, and two curves for the niobium and niobium plus boron steels. Nevertheless, 5 to 12 tests were carried out on each steel at a given temperature. The type of steel, the austenitization and test temperatures, the prestrain and strain rate as well as the holding or load free times are indicated on each figure.

Comparison of the flow curves for the base (Fig. 4.1) and boron (Fig. 4.2) steels reveals two important observations:

- (i) The stress-strain curve for the first compression is the same for both steels (unloading stress of about 120 MPa). This suggests that there is little strengthening of the base steel when boron is added.
- (ii) The difference in the amount of softening after the same holding time during the load-free interval (2 seconds) is not very large, indicating that the single addition of boron to the base steel retards the softening process only slightly.

Similarly comparison between the niobium (Fig. 4.3) and niobium plus boron steels reveals the following:

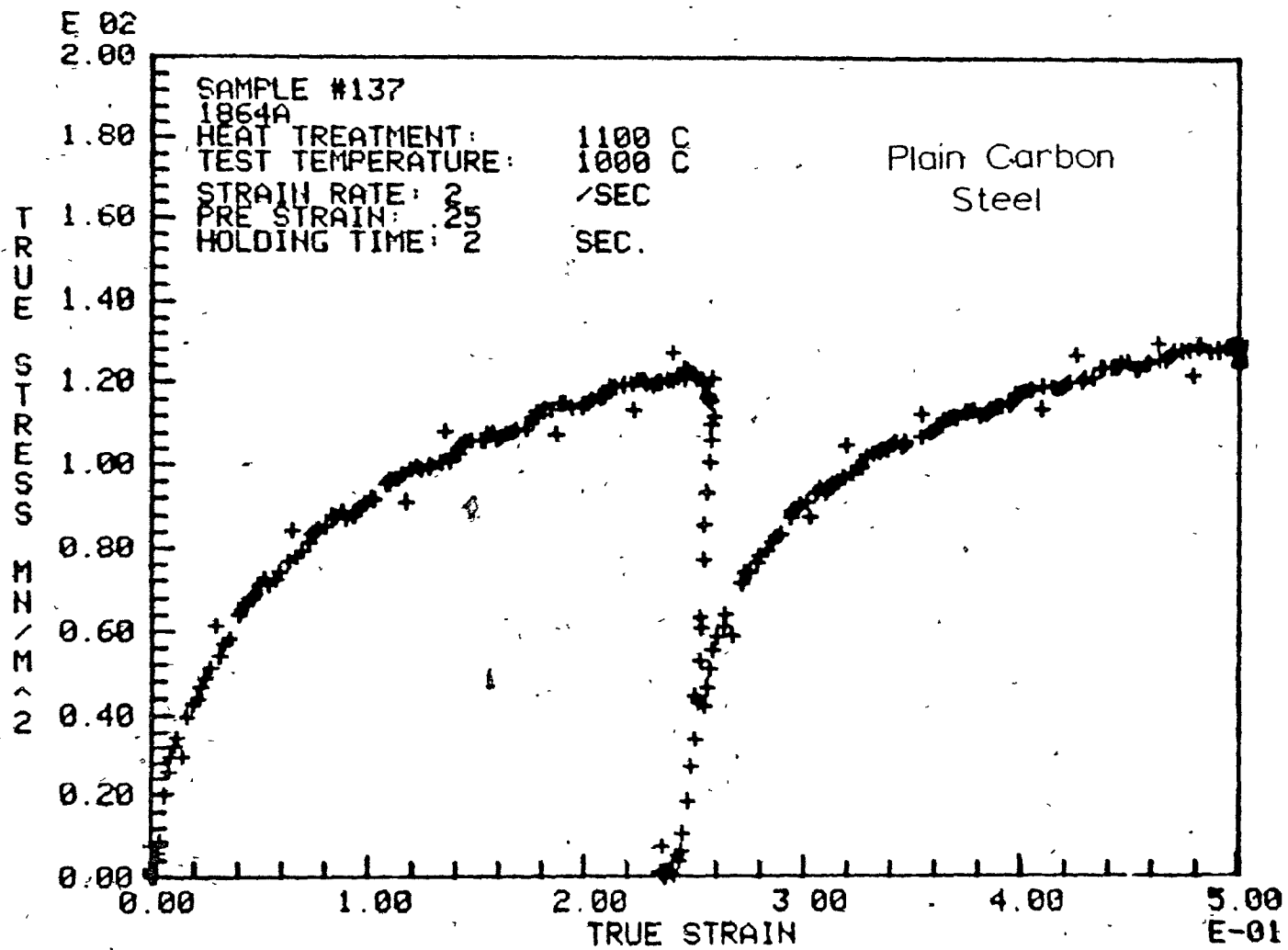


Figure 4.1 Interrupted flow curve for the plain C steel tested at 1000°C, after a holding time of 2 seconds.

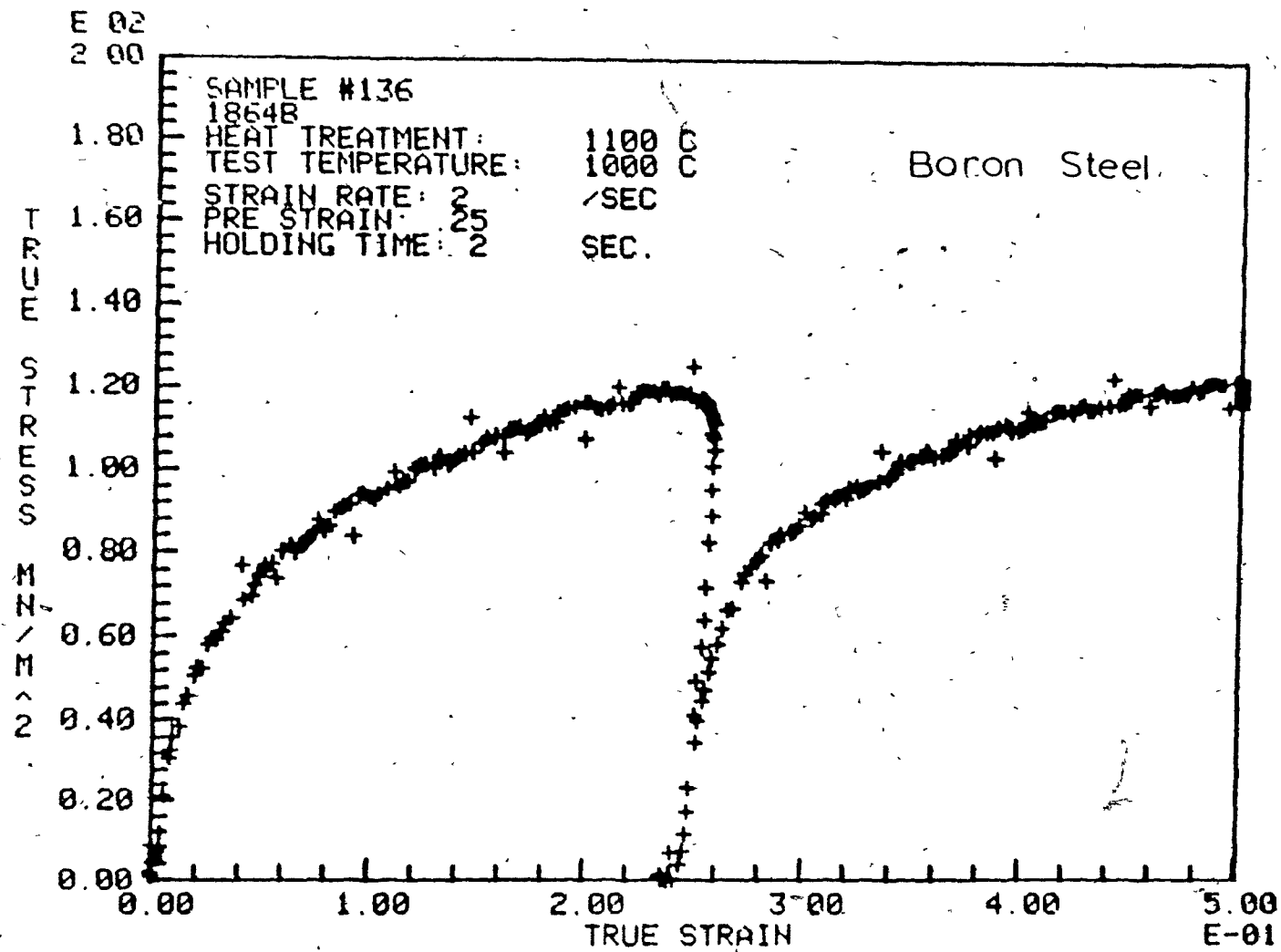


Figure 4.2 Interrupted flow curve for the plain C plus boron steel tested at 1000°C, after a holding time of 2 seconds.

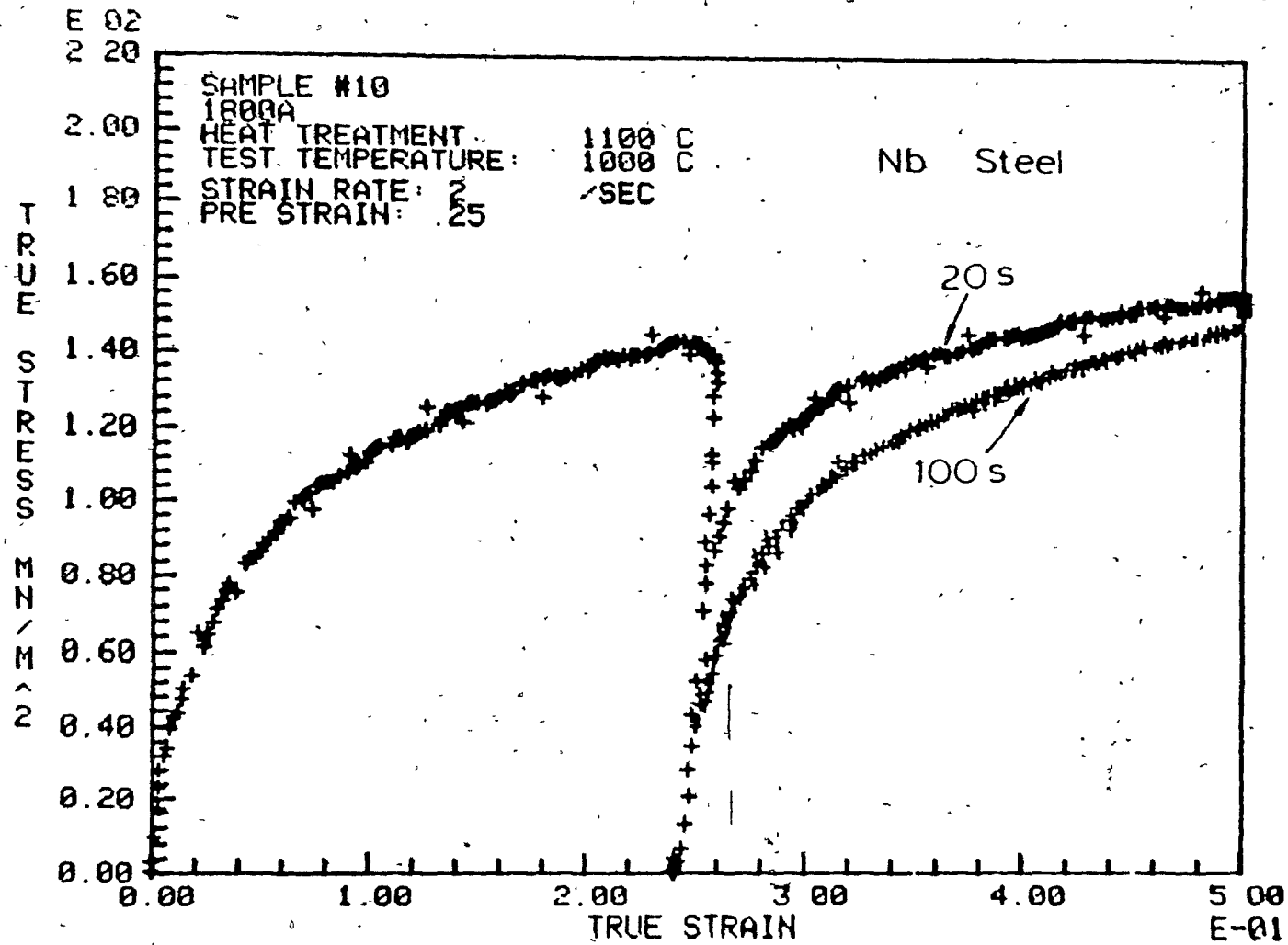


Figure 4.3 Interrupted flow curves for the Nb steel tested at 1000°C after two different holding times.

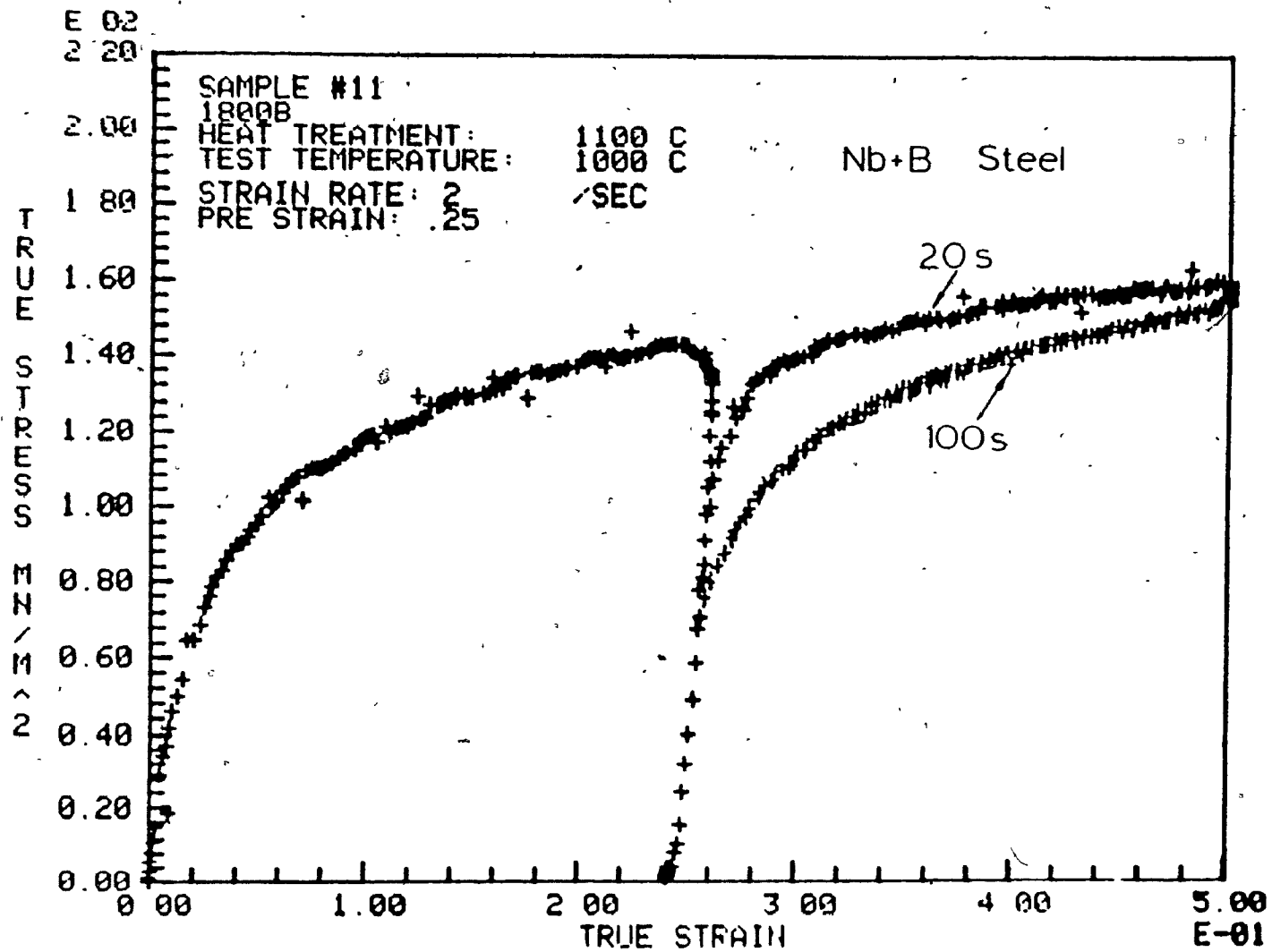


Figure 4.4 Interrupted flow curves for the Nb + B steel tested at 1000°C after two different holding times.

- (i) The stress-strain curve for the first compression is almost the same (unloading stress of about 144 MPa) and again the addition of boron (to the niobium steel in this case) does not significantly influence the stress level. The difference in unloading flow stress between the base and niobium steels (about 24 MPa) can therefore be attributed solely to the addition of the Nb.
- (ii) After increasing holding times (from 20 to 100 seconds) and for the same steel (Nb or Nb + B), larger amounts of softening are observed.
- (iii) For the same holding times (20 or 100 seconds), there is a considerable difference in softening between the two steels, indicating that boron has a strong retarding action when niobium is present.

The above results represent only a small fraction of the experimental work conducted in this part of the investigation. Readers interested in the effect of temperature, prestrain and alloy composition on the actual shape of the flow curve and on the values of the flow stresses developed are referred to Appendix I. Here about one third of the compression curves are presented in the form of a single set per experimental condition. In the next chapter, the influence of the experimental conditions on the softening behaviour of the different steels will be examined in much more detail.

4.1.2 FRACTIONAL SOFTENING DETERMINED BY THE OFFSET METHOD

The complete fractional softening vs. holding time curves for all the experimental conditions are presented in Figures 4.5 to 4.8. These results were determined by the offset method and the conditions and materials employed are indicated on each diagram. Two regions can be distinguished in all the curves: the static recovery region, which corresponds to small amounts of softening (usually about 20%), and the static recrystallization region (from 20 to 100%

softening). The two softening processes overlap at around 20% and the transition from one mechanism to the other is marked by an acceleration of the softening process. For a better appreciation of the early softening behaviour, the static recovery results for the Nb and Nb + B steels are presented in amplified form in Figs. 4.5(b) and 4.7(b) for prestrains of 0.25 and 0.50, respectively.

In Figure 4.5(a), the amount of softening taking place during the unloading interval is shown as a function of the time of the unloading for a prestrain of 0.25 for the Nb (open symbols) and the Nb + B (full symbols) steels. It is evident from the results that: (i) the presence of boron in solution leads to a retardation in the rate of austenite recrystallization compared to that obtained in the unmodified niobium steel; (ii) the maximum retardation is observed at a test temperature of 1000°C; (iii) there is only limited retardation of recrystallization due to boron addition at 1100 and 900°C; (iv) at test temperatures of 1050 and 950°C, there is an appreciable difference between the behaviour of the two steels, although the magnitude of the effect is less than that observed at 1000°C. It should be noted that at 900°C, softening is very slow and there is a possibility that the precipitation of NbC (in the two steels) and $\text{Fe}_{23}(\text{B,C})_6$ (in the Nb + B steel) takes place.

In Figure 4.5(b), the fractional softening associated with the static recovery process is plotted for very short times. Clearly the recovery part is retarded at the earliest times, as is the overall recrystallization behaviour.

The softening behaviour of the base and base plus boron steels tested at 900 and 1000°C after a prestrain of 0.25 applied at a strain rate of 2 s^{-1} can be seen in Figure 4.6. For comparison reasons, the results presented in Figure 4.5(a) for the Nb and Nb + B steels are also included. From this comparison, the following conclusions can be drawn: (i) the softening process in the base and base plus boron steels proceeds much more quickly than in the Nb and Nb + B steels; (ii) the sole addition of boron to the base steel does not appreciably retard the softening process; (iii) the niobium addition to the base steel causes a very large retardation; (iv) the presence of boron in the niobium steel results in a further retardation which is larger than the sum of the retardations produced by the single additions of boron and niobium to the base steel. It is

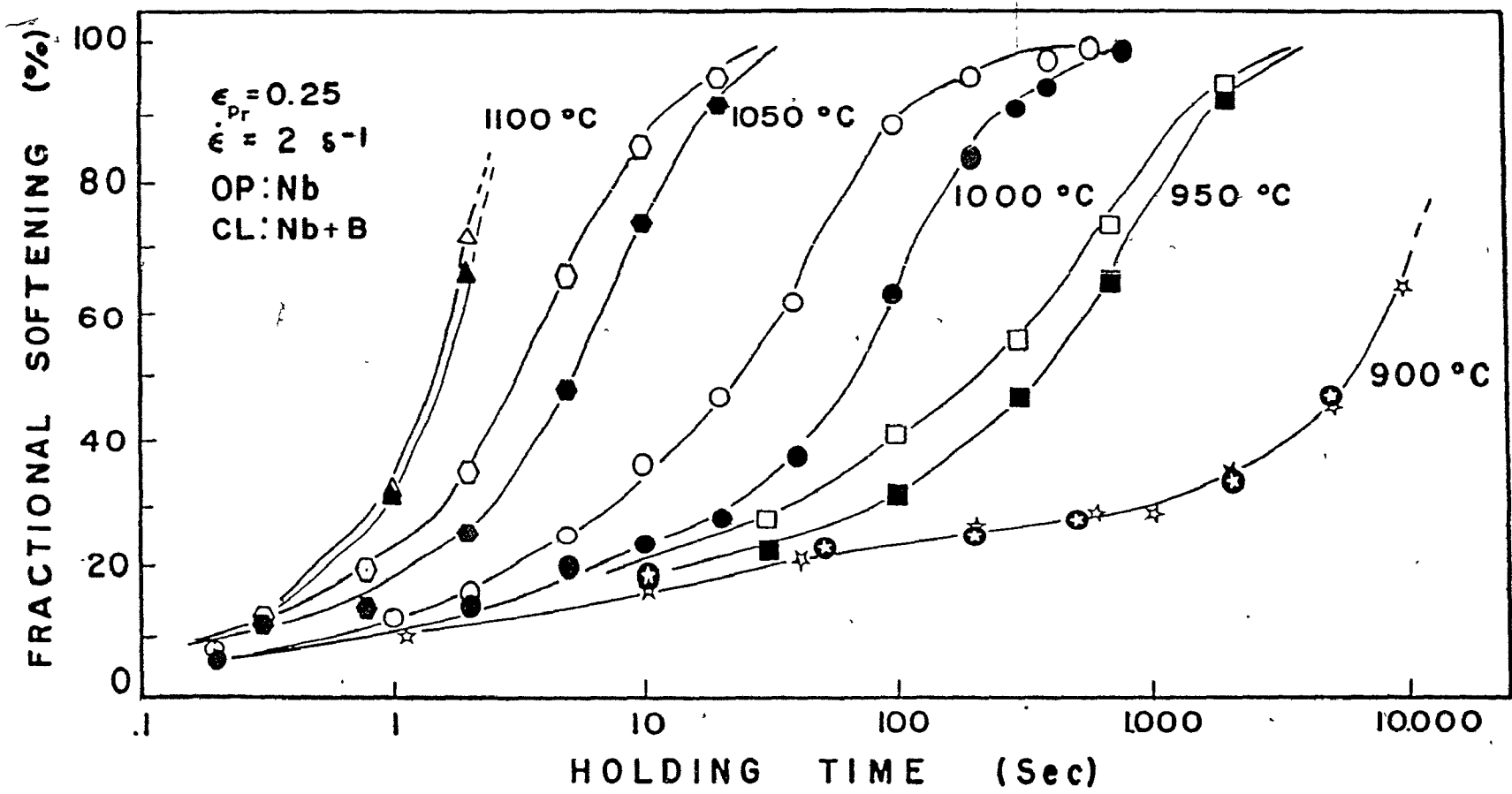


Figure 4.5(a) Static recovery and recrystallization of the Nb and Nb + B steels after a predeformation of 0.25.

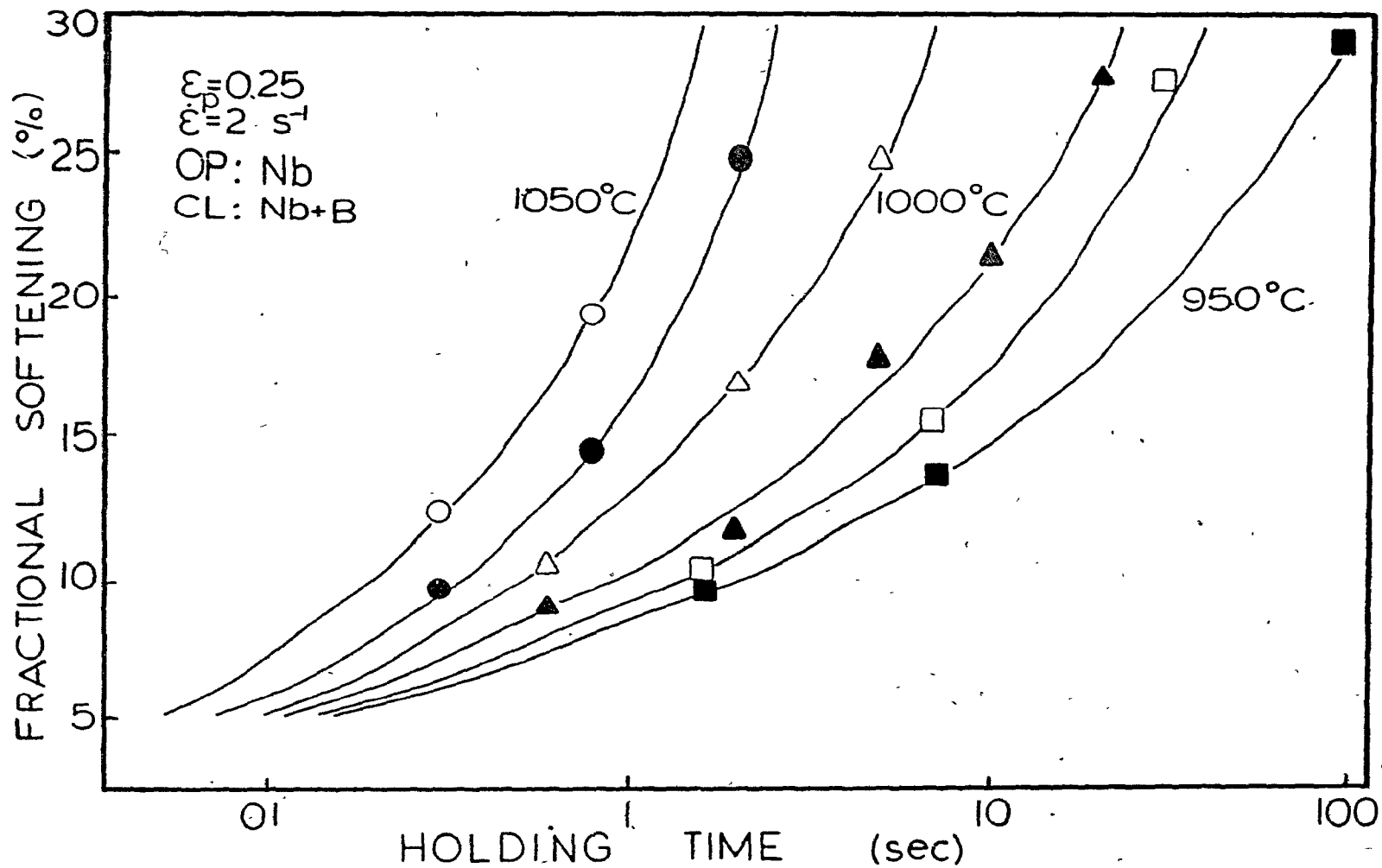


Figure 4.5(b) Static recovery in the Nb and Nb + B steels after a predeformation of 0.25.

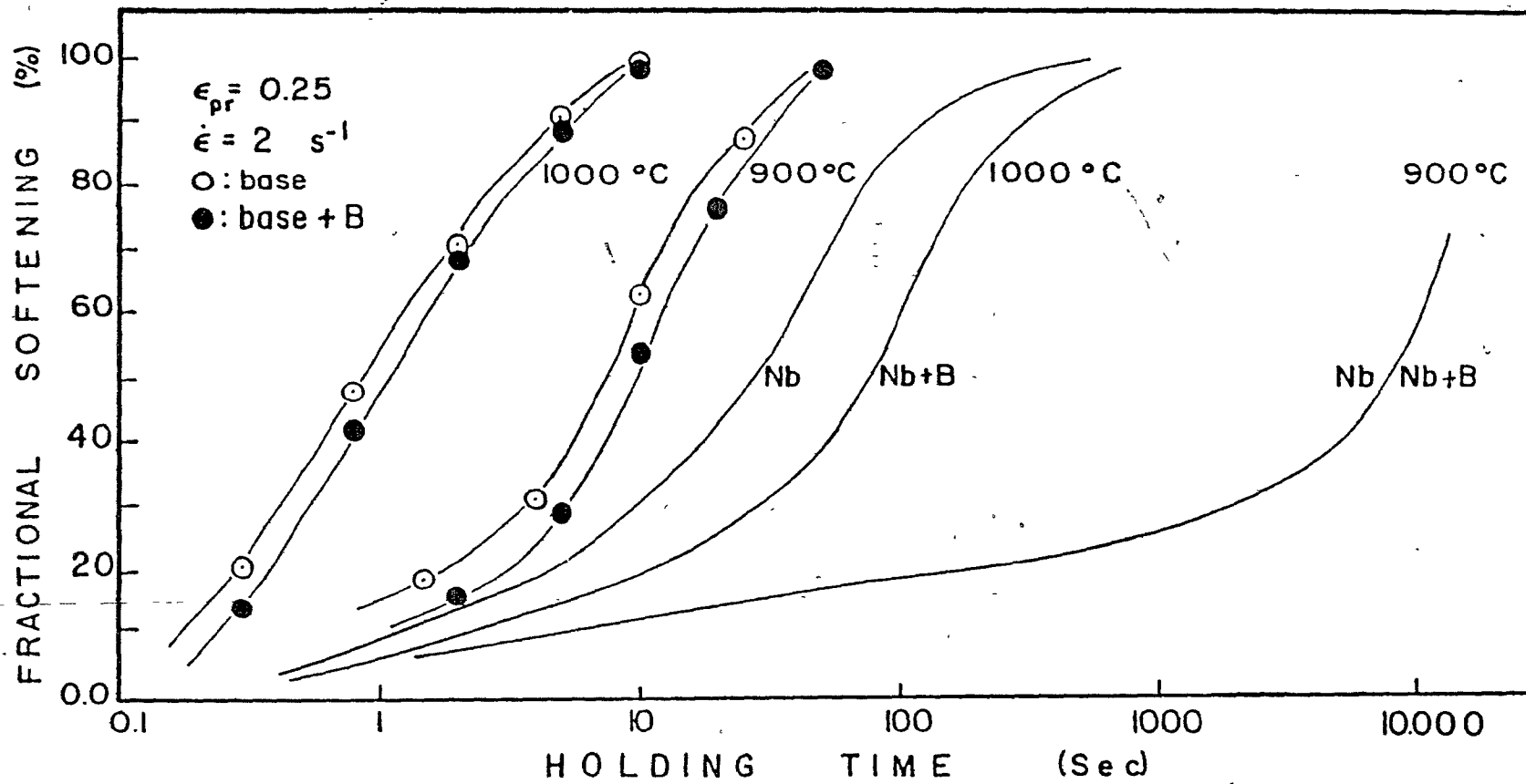


Figure 4.6 Comparison of the softening behaviour of the plain C, plain C plus B and Nb, Nb + B steels deformed 0.25 at 1000 and 900°C.

readily apparent from the above that the combined addition of niobium and boron produces a synergistic retarding effect.

The above observations clearly suggest the presence of a solute-drag effect. If this interpretation is valid, the retardation of recrystallization depends on: (i) the velocity of the moving grain boundaries; and (ii) the diffusivity of the relevant solute atoms. For a better understanding of this phenomenon, experiments were conducted with different amounts of predeformation, namely 0.5 and 0.12. Increasing the amount of the prestrain increases the velocity of the recrystallizing grain boundaries through its effect on the dislocation density and hence the driving force. Decreasing the amount of the prestraining, by contrast, has the reverse effect.

From Figure 4.7(a) it is evident that, with increased prestrain, boron still retards recrystallization but now the effect is greatest at 950 instead of 1000°C. It is also apparent that the time for 60 percent softening (equivalent to 50% recrystallization because of the occurrence of about 20% softening by recovery) for the niobium plus boron steel at the temperature of greatest retardation is approximately 100 seconds, as in the previous case of the 0.25 predeformation. The softening curves also indicate that: (i) NbC precipitation may begin at about 200 seconds in the Nb steel at this temperature; and (ii) the addition of boron appears to accelerate the precipitation kinetics by as much as an order of magnitude. If the precipitation did not take place at 900°C, the relative difference between the Nb and Nb + B steels would follow the pattern observed in Fig. 4.5(a). The recovery parts of the softening curves can be seen in Figure 4.7(b), indicating that recovery is retarded in the same fashion as in the case of $\epsilon = 0.25$.

The softening curves obtained from the experiments with 12 percent predeformation (and therefore with decreased grain boundary velocity) are shown in Figure 4.8. Once again, there is a condition of maximum retardation, at 1050°C in this case, and the time for 60 percent softening for the Nb + B steel is again at about 100 seconds. Furthermore, because the temperature range of these experiments is relatively high, the retarding effect is unlikely to be due to the occurrence of precipitation, but is more likely to involve some kind of solute drag.

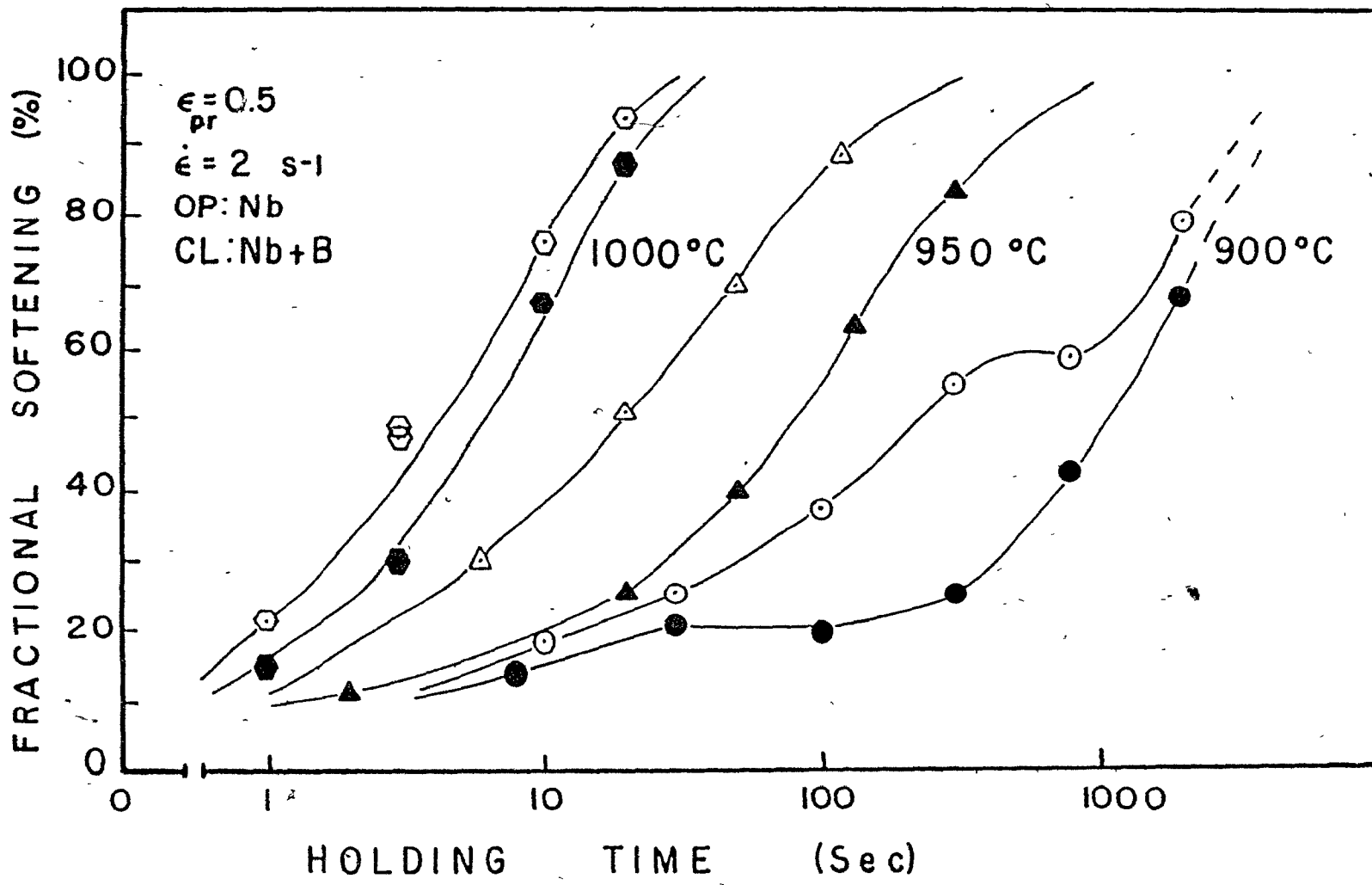


Figure 4.7(a) Static recovery and recrystallization of the Nb and Nb + B steels after a predeformation of 0.5.

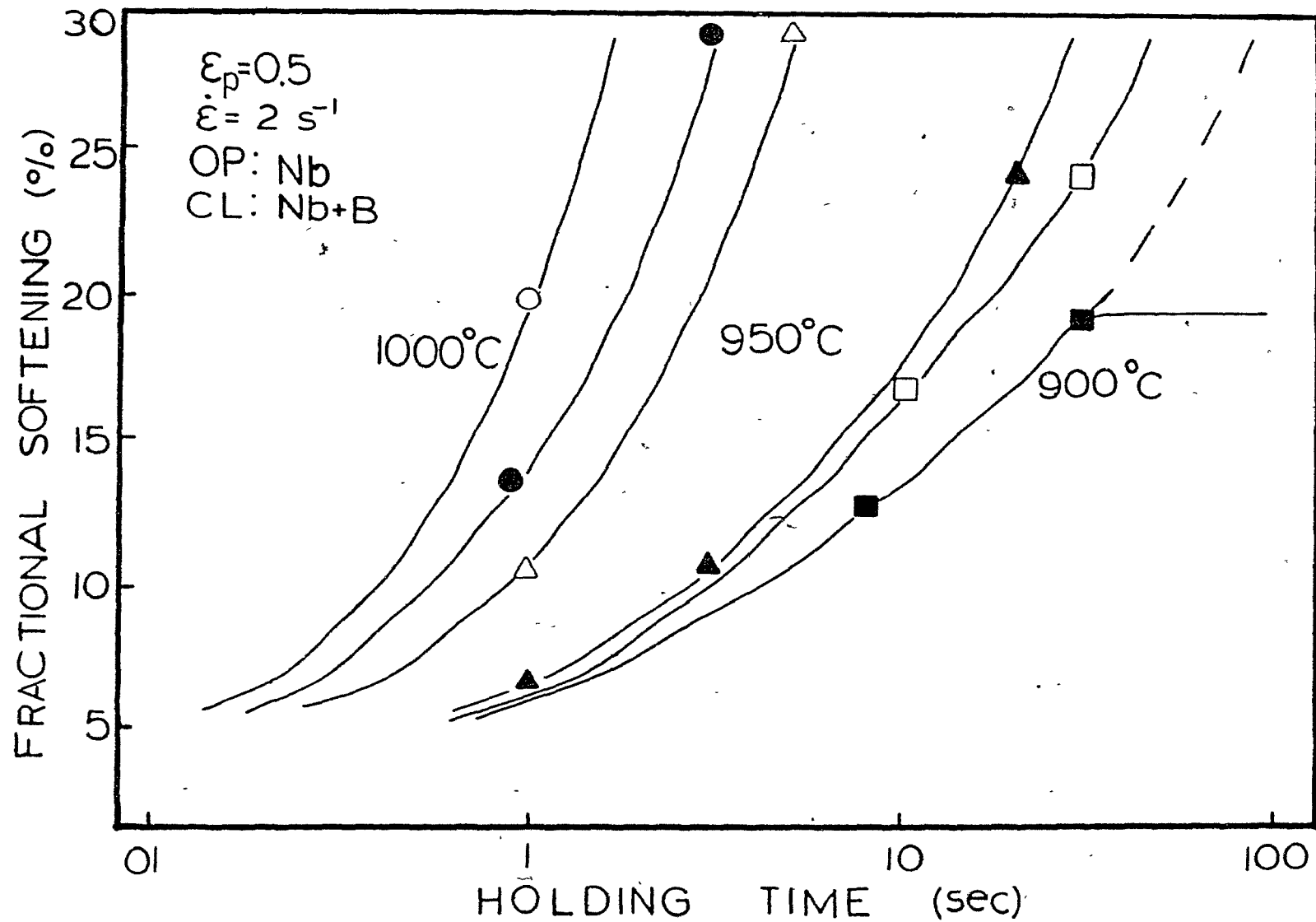


Figure 4.7(b) Static recovery in the Nb and Nb + B steels after a predeformation of 0.5.

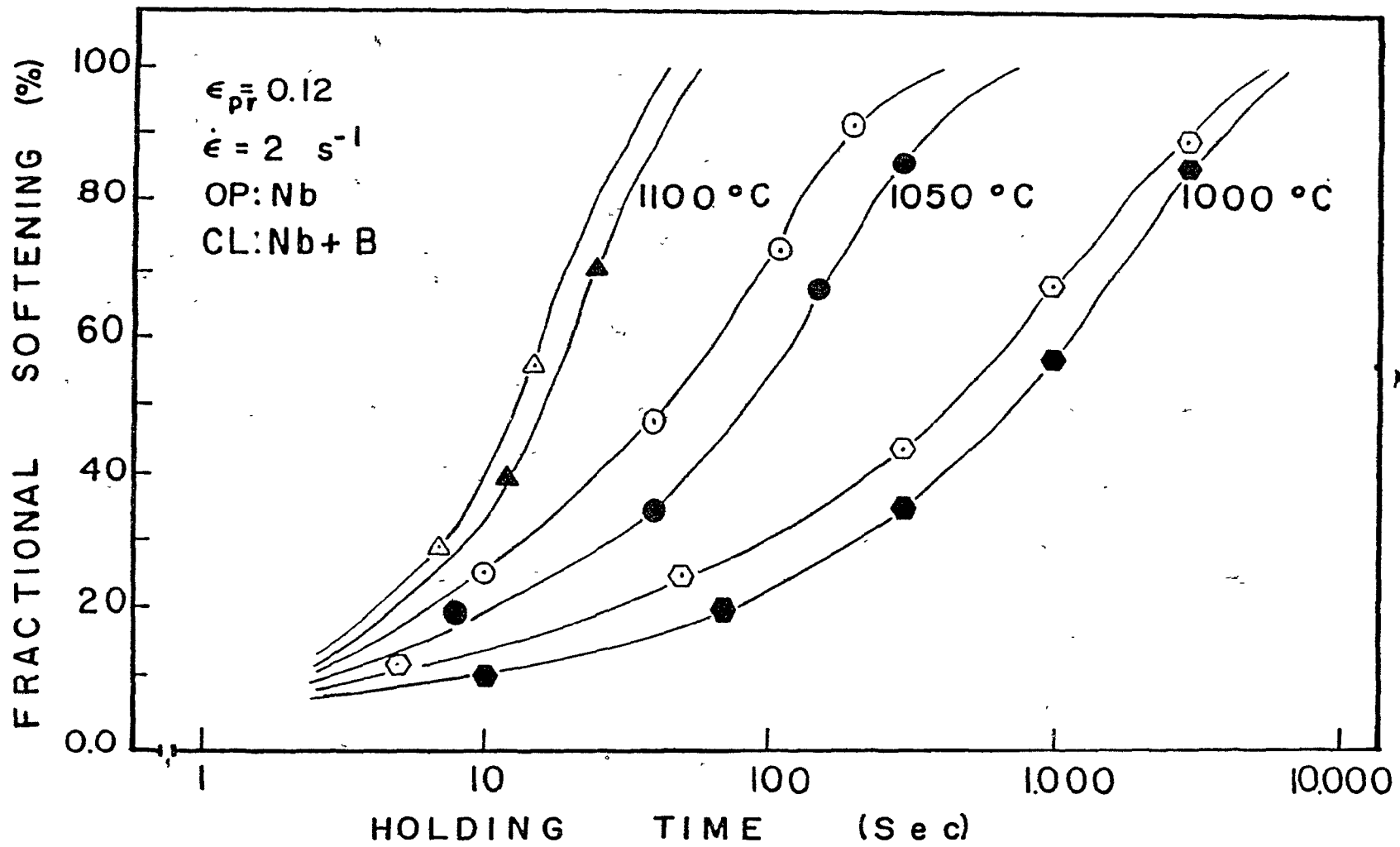


Figure 4.8 Static recovery and recrystallization of the Nb and Nb + B steels after a predeformation of 0.12.

4.2 DYNAMIC SOFTENING RESULTS

4.2.1 FLOW CURVES OBTAINED IN COMPRESSION

Typical sets of compression flow curves are presented in Figures 4.9 through 4.11. These curves represent a small portion of the work conducted in the full investigation and are selected so as to illustrate the effect of different parameters on the shape of the curves. More complete sets of the curves are collected and displayed in Appendix II. In Figure 4.9, four steels tested under identical conditions are compared. The shapes of these curves are typical of materials that recrystallize dynamically. After macroscopic yielding, the material work hardens. As the rate of recovery increases with strain, the net rate of work hardening decreases with strain. Finally, dynamic recrystallization is initiated just before the peak stress is attained, and the subsequent drop in flow stress is due to the progress of dynamic recrystallization. This softening process involves both nucleation and growth, and therefore requires time.

From a comparison of these flow curves, the following observations can be made: (i) the addition of Nb to the base steel increases the peak stress of the flow curve; (ii) the addition of boron to the base and Nb steels does not increase the peak stress; (iii) the peak strain (ϵ_p) pertaining to the Nb flow curve is much larger than the peak strain for the base material, so that Nb in solution apparently retards the softening process; and (iv) the presence of boron increases the peak strain (mainly in the Nb steel), and also increases the recrystallization strain (ϵ_x). (Note that the time, t , to reach a selected strain, ϵ , at a given strain rate, $\dot{\epsilon}$, is $t = \epsilon/\dot{\epsilon}$). The presence of boron therefore also appears to retard the softening process.

In Figure 4.10, flow curves determined on the Nb + B steel at three different strain rates are depicted. As the strain rate is increased from 0.001 to 0.1 s⁻¹, the following changes in the shape of the flow curve can be observed: (i) higher strain rates produce flow curves with higher stress levels; (ii) when the strain rate is increased, the peak strain and recrystallization strain both increase; and (iii) the flow curve displays a single peak at a strain rate of 0.1 s⁻¹ and multiple peaks at a strain rate of 0.001 s⁻¹.

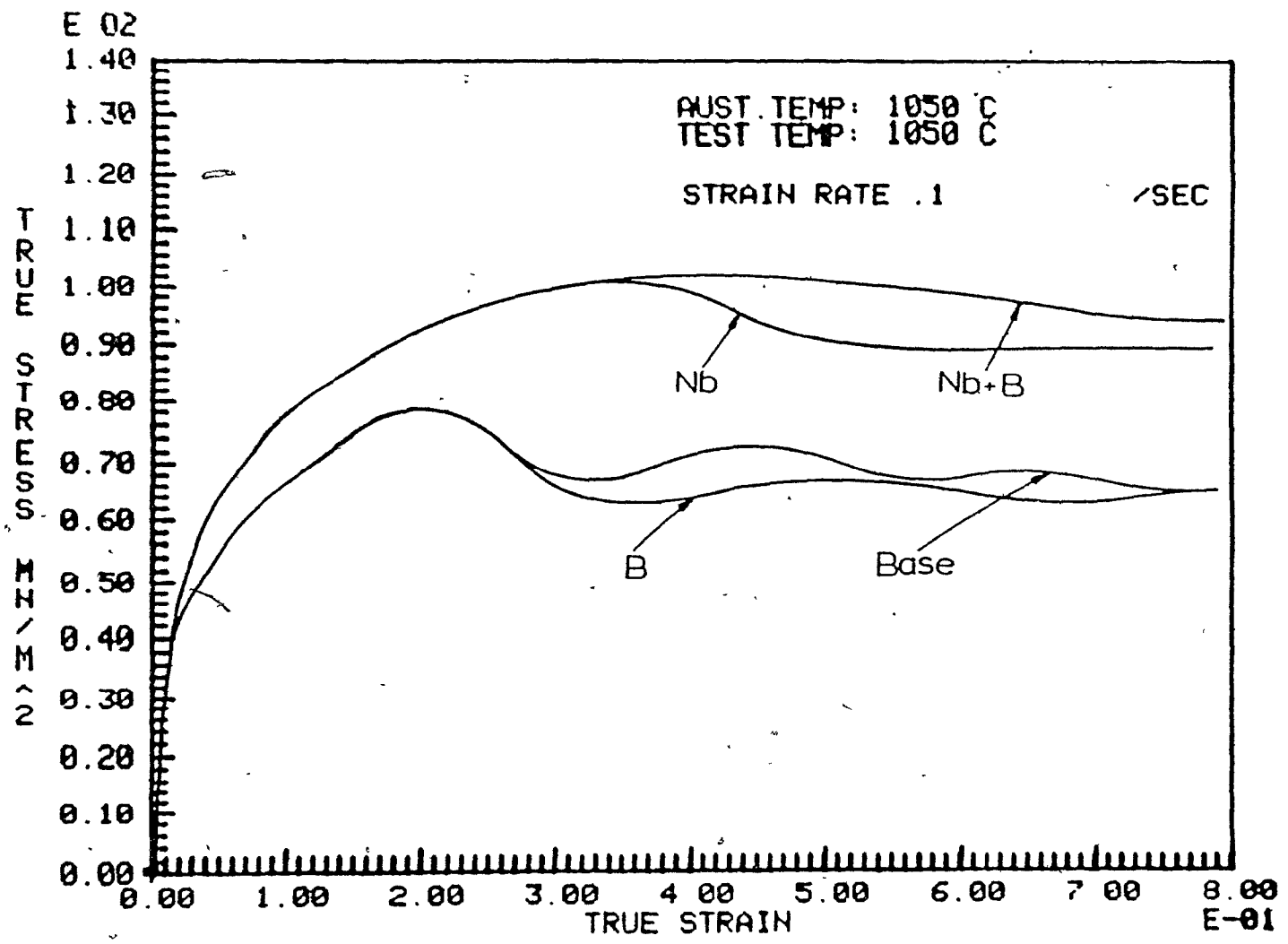


Figure 4.9 Effect of microalloying additions on the shapes of the dynamic recrystallization flow curves.

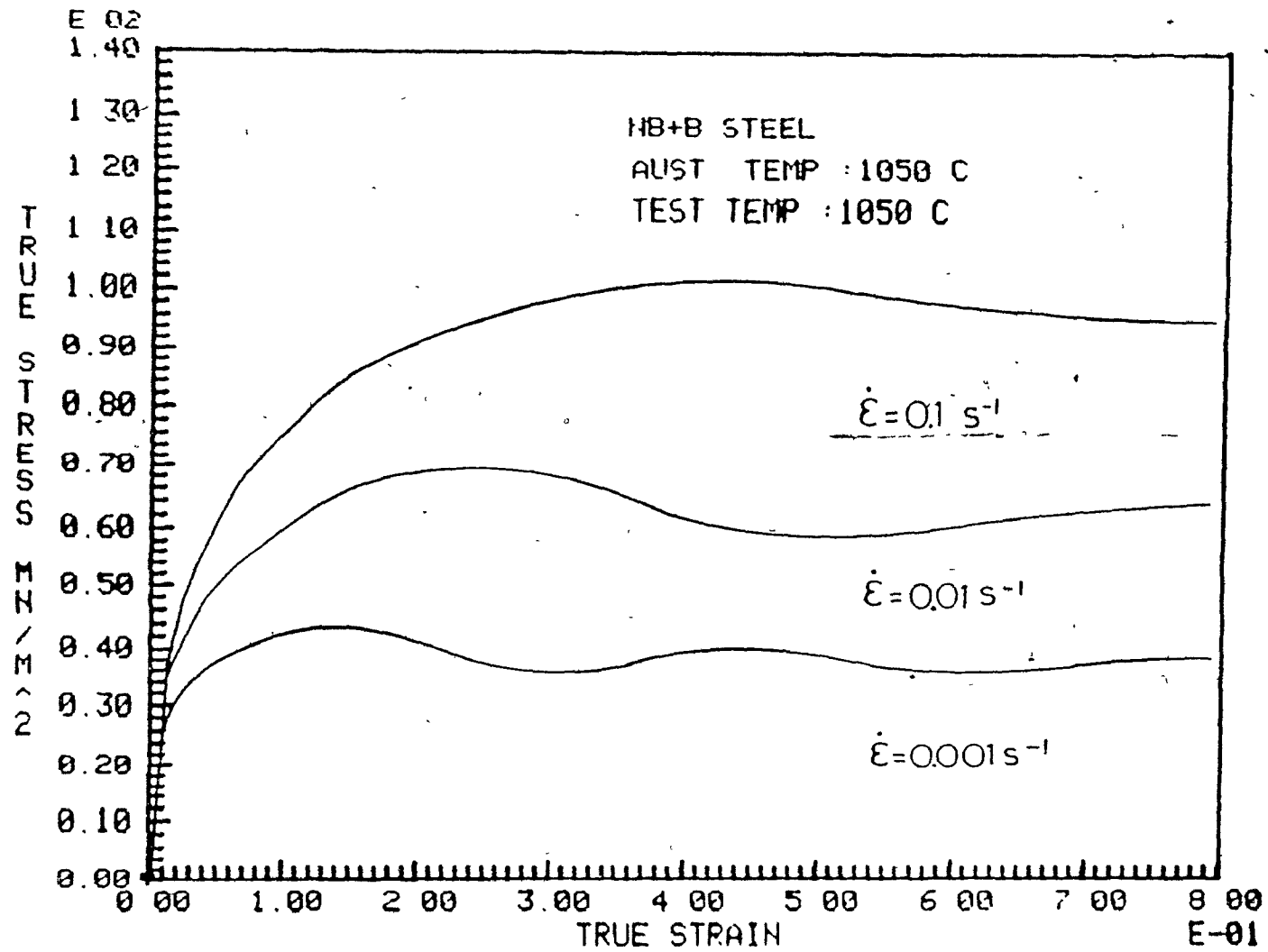


Figure 4.10 Effect of strain rate on the shapes of the dynamic recrystallization flow curves.

The effect of austenitizing temperature is illustrated in Figure 4.11. The Nb steel selected for these experiments was austenitized at 1050, 1100, and 1150°C for the same time (10 minutes); it was then deformed at 1050°C to a strain of 0.8. The austenitization temperature clearly influences the initial austenite grain size (higher austenitization temperature leads to larger grain size) and the dissolution of precipitates. High temperatures can also be expected to decrease the degree of segregation of the solute atoms within the material. The differences in the flow curves, which are not great, can be attributed mainly to the differences in initial grain size and are the following: (i) there is little difference in the stress levels of the three flow curves; (ii) when a higher austenitization temperature is employed, leading to a larger initial grain size, larger peak and recrystallization strains are produced; and (iii) small initial grain size (about 35 μm at 1050°C) leads to a multiple peak flow curve, indicating grain coarsening (92), while a large initial grain size (about 52 μm at 1150°C) results in a single peak (grain refinement) flow curve.

4.2.2 DEPENDENCE OF ϵ_p AND ϵ_x ON DEFORMATION CONDITIONS

The effect of deformation parameters such as strain rate and the test and austenitization temperatures on ϵ_p and ϵ_x (onset and duration of recrystallization) is illustrated in Figures 4.12 to 4.14. Figures 4.12(a) and (b) depict the effects of test temperature on the critical strain ϵ_p (Fig. 4.12(a)) and on the recrystallization strain ϵ_x (Fig. 4.12(b)). For all four steels, ϵ_p and ϵ_x decrease as the test temperature is increased indicating that the onset of recrystallization takes place earlier at higher temperatures. Boron addition to the base steel does not significantly affect the onset of recrystallization, whereas the presence of Nb results in a very large increase. The retarding effect of B when added to the Nb steel is largest at 1000°C and decreases with increasing temperature. This result is consistent with the effects of B addition on the static recrystallization behaviour which were described above. Because the peak and recrystallization strains were too large for determination by compression testing at 950 and 900°C, the temperature condition associated with maximum retardation could not, unfortunately, be established.

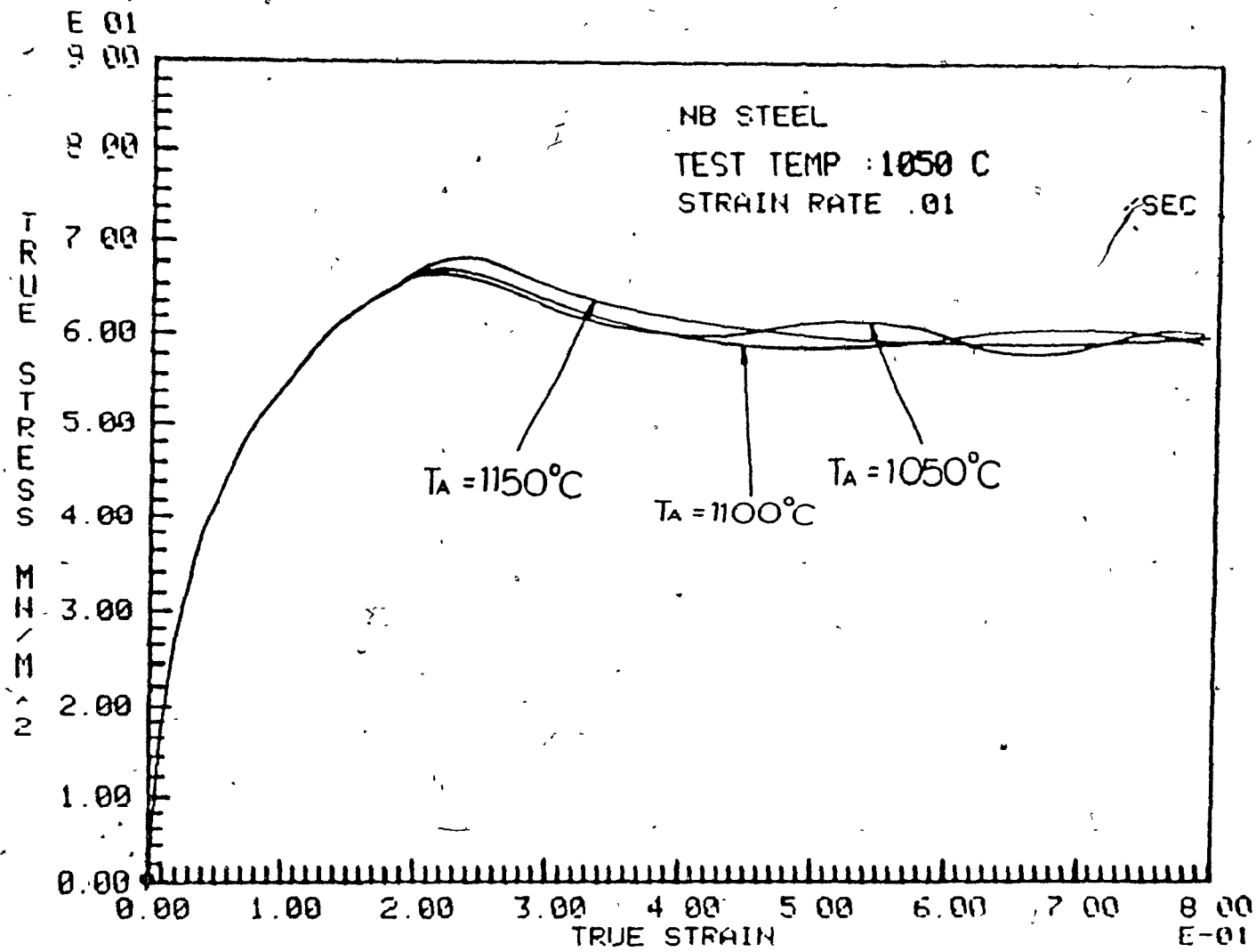


Figure 4.11 Effect of austenitizing temperature on the shapes of the dynamic recrystallization flow curves.

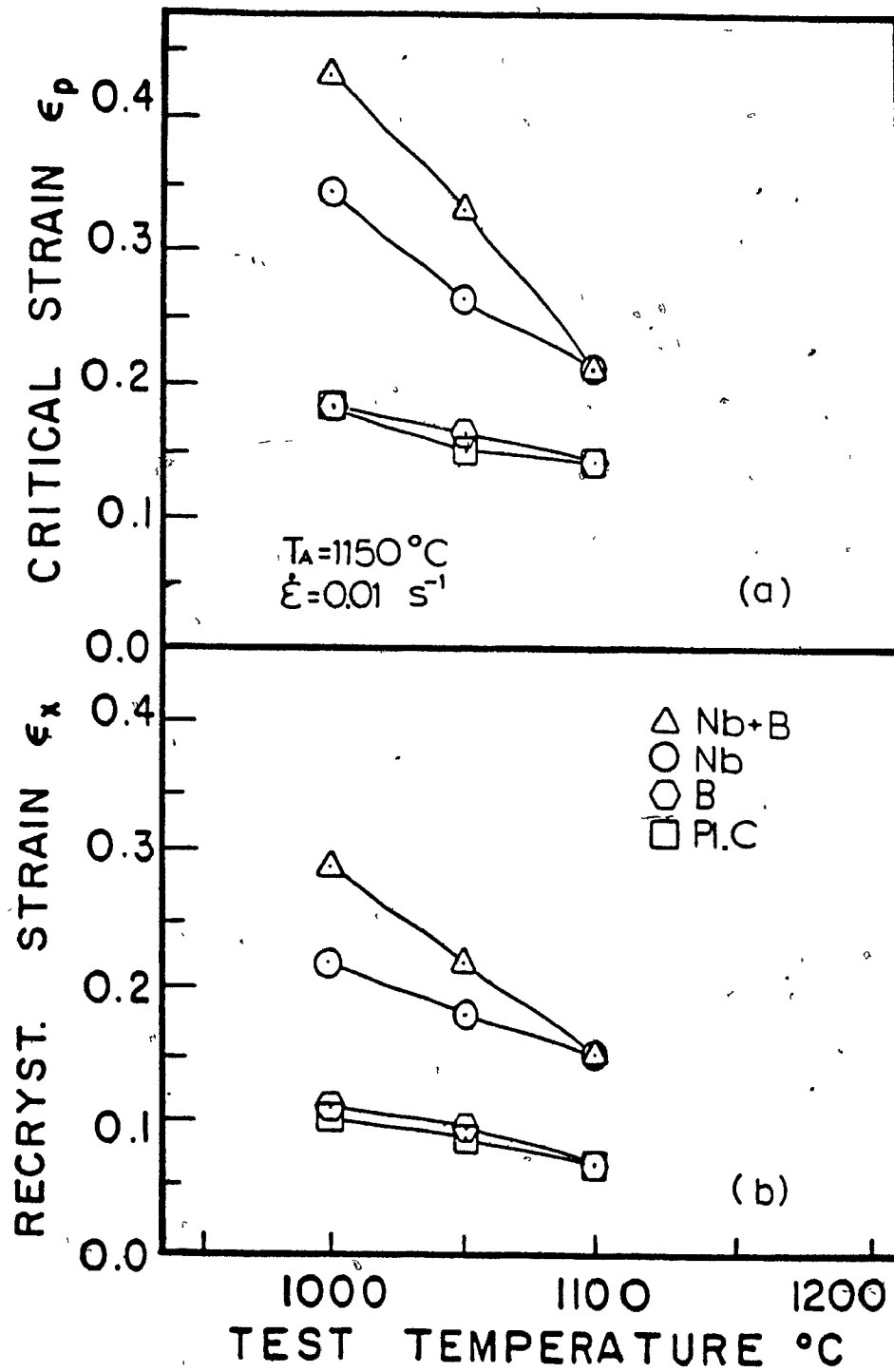


Figure 4.12 Effect of test temperature on ϵ_p and ϵ_x .

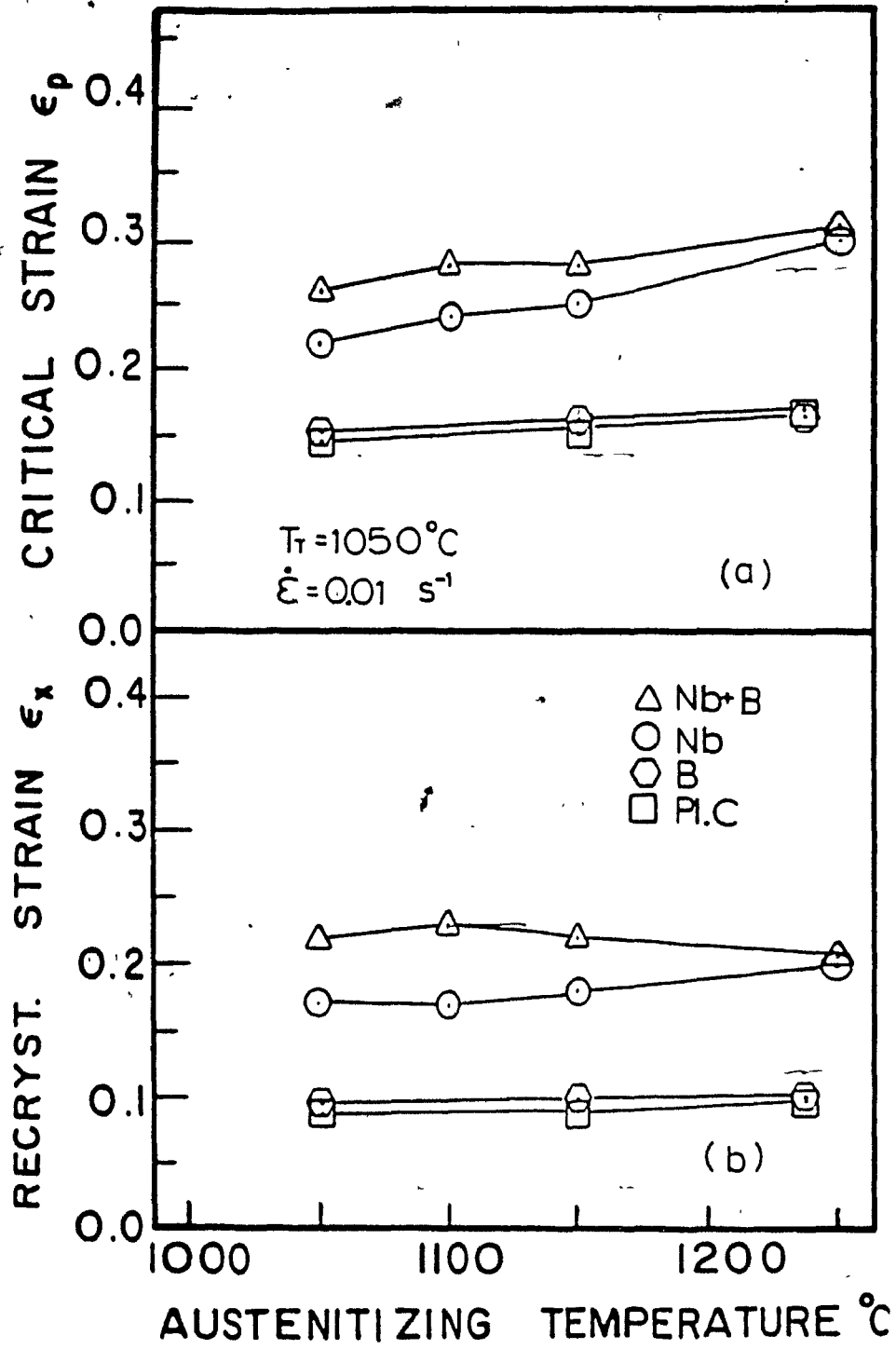


Figure 4.13 Effect of austenitization temperature on ϵ_p and ϵ_x .

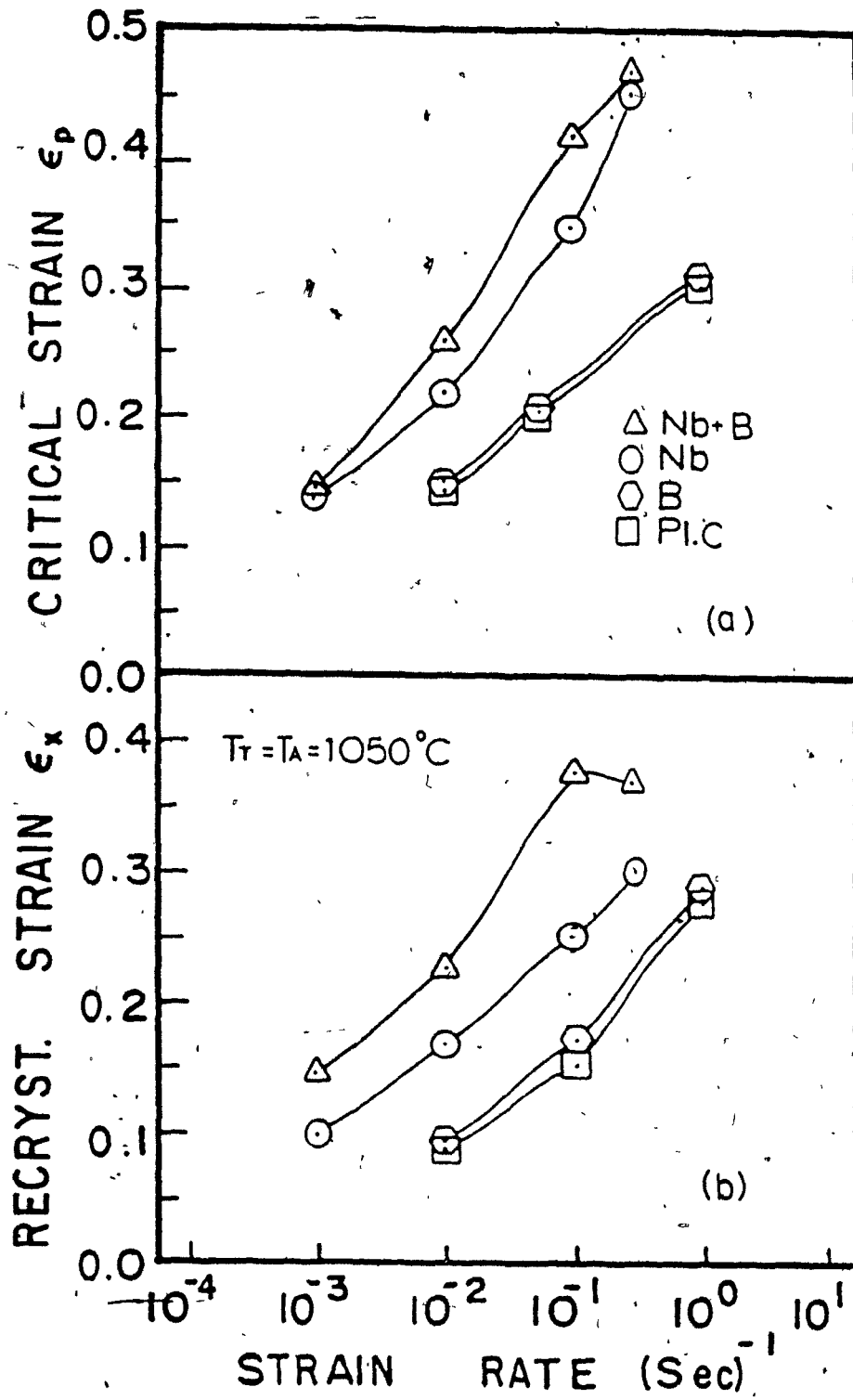


Figure 4.14 Effect of testing strain rate on ϵ_p and ϵ_x .

The influence of austenitization temperature on the onset strain for dynamic recrystallization as well as on the recrystallization strain can be seen in Figures 4.13(a) and 4.13(b), respectively. For all steels tested, the values of ϵ_p increase with austenitizing temperature. This is probably related to the differences in initial austenite grain size. Higher austenitization temperatures produce larger grain sizes and, therefore, fewer nuclei for recrystallization. (Recrystallization is usually nucleated on the prior austenite grain boundaries.) The detailed results showing the influence of austenitization temperature on grain size will be presented later.

The base and base plus boron materials have closely similar behaviour, whereas the Nb and Nb + B steels display considerable differences at 1050°C and much less at 1250°C. Lower reheating temperatures than 1050°C were not employed because the NbC precipitates would have remained undissolved.

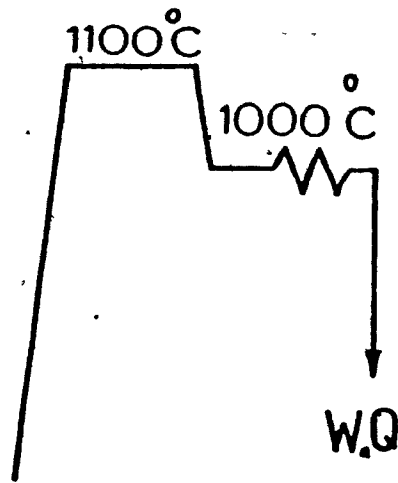
Finally the dependence of ϵ_p and ϵ_x on testing strain rate is shown in Figures 4.14(a) and 4.14(b). Here it is evident that whereas there is little difference between the base and base plus boron steels, the difference in ϵ_p and ϵ_x between the Nb and Nb + B steels are strain rate dependent and that the retardation due to boron addition is at a maximum at strain rate of 0.1 s⁻¹. The difference decreases as the strain rate is increased to 0.5 or decreased to 0.001 s⁻¹.

4.3 METALLOGRAPHIC RESULTS

4.3.1 OCCURRENCE OF PRECIPITATION DURING STATIC RECRYSTALLIZATION

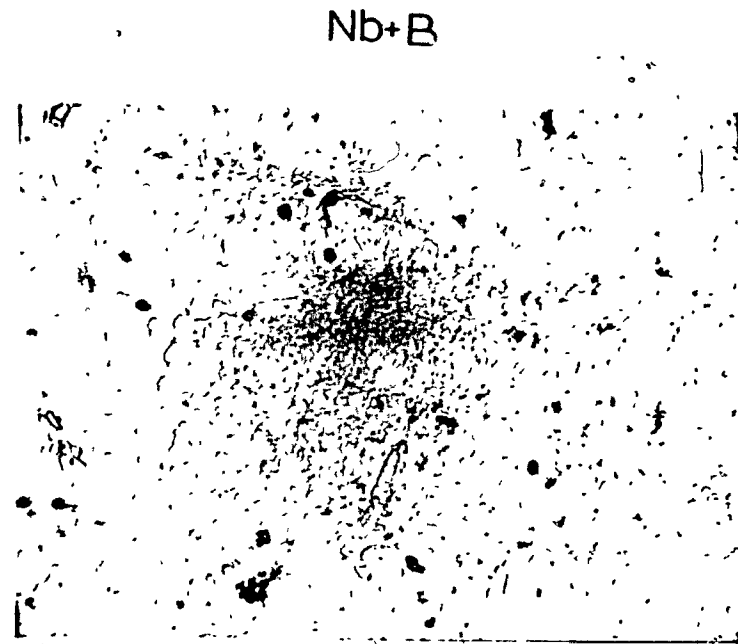
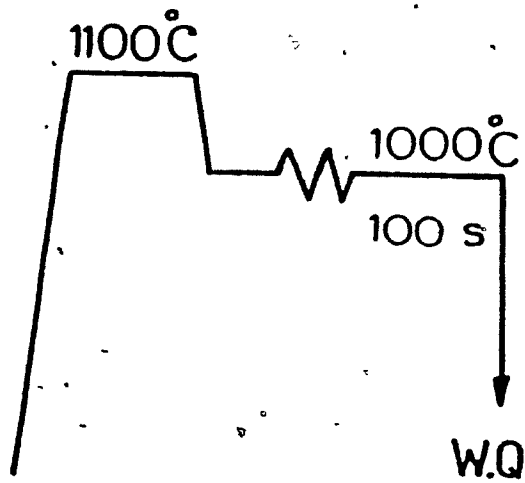
In order to investigate in what form (solute or precipitate) boron influences the recrystallization process, carbon extraction replicas were prepared for the Nb and Nb plus boron steels tested under the experimental conditions described above. Examples of the results obtained are presented in Figures 4.15 to 4.22. The sample shown in Figure 4.15 was austenitized at 1100°C for 15 minutes; the temperature was then lowered to 1000°C, the sample deformed 25% and quenched immediately after deformation. The

Nb+B



x 33.000

Figure 4.15 Undissolved TiN precipitates in a Nb + B steel solution treated and then deformed 25% at 1000°C and immediately quenched.



x 33,000

Figure 4.16 Undissolved TiN precipitates in a solution treated Nb + B steel deformed 25% at 1000°C and quenched 100 seconds after deformation.

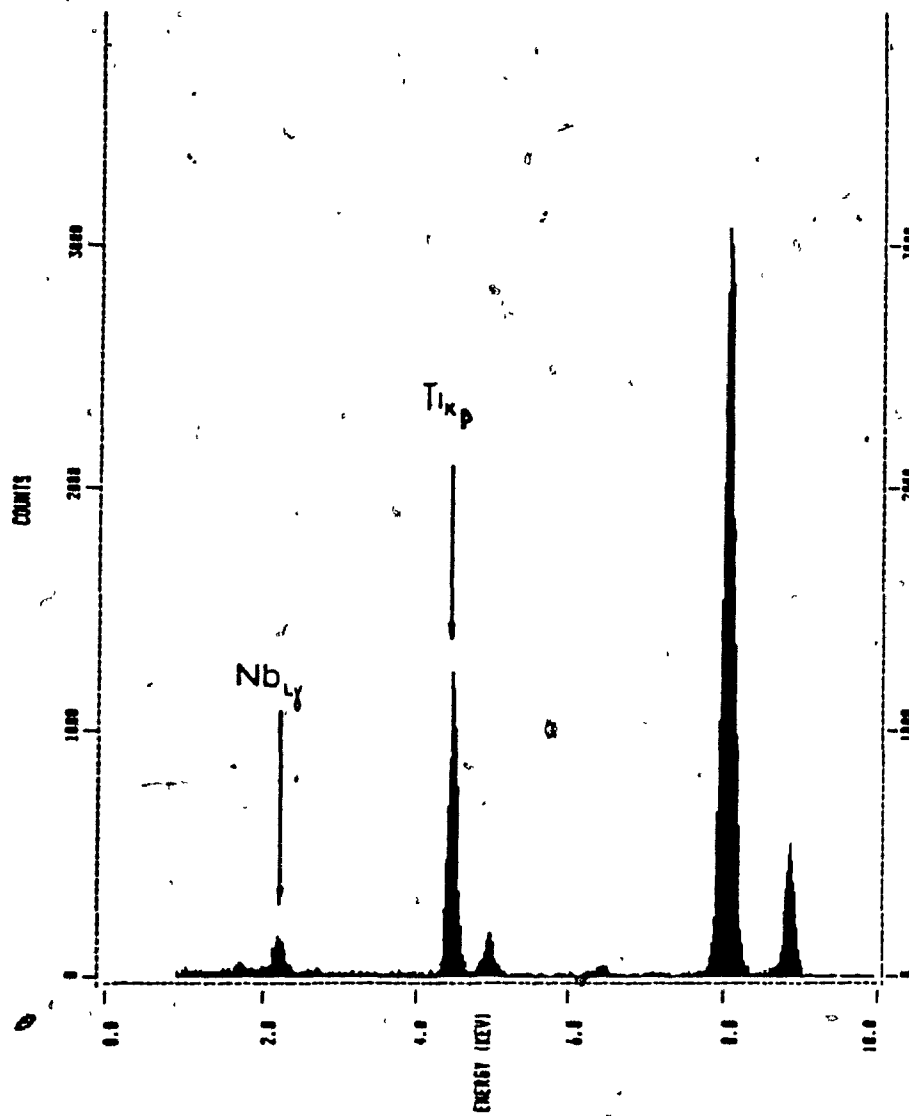


Figure 4.17 X-ray spectrum analysis of the TiN precipitates shown in Figs. 4.15 and 4.16.

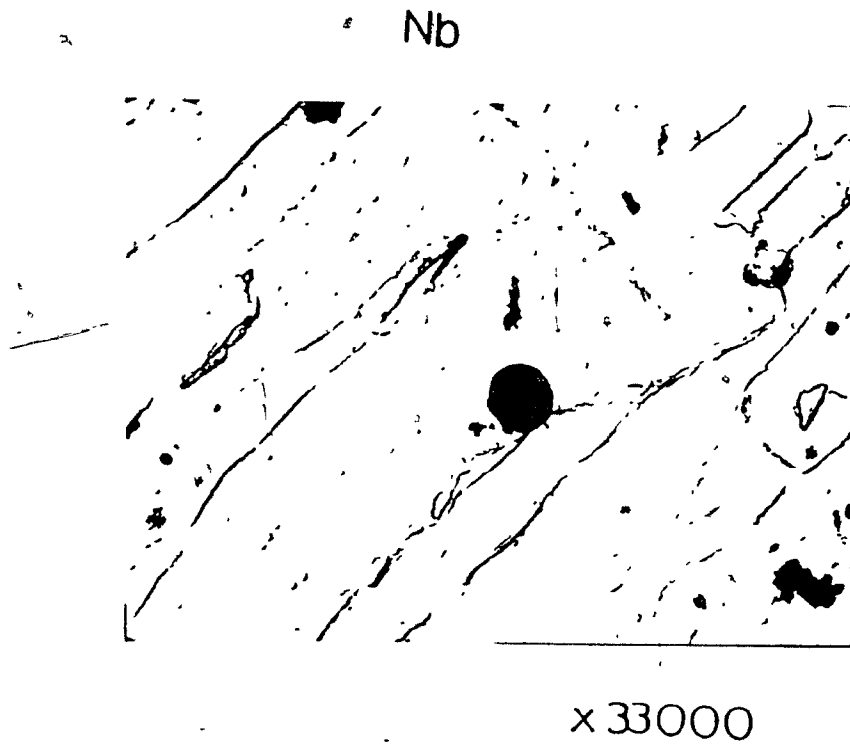
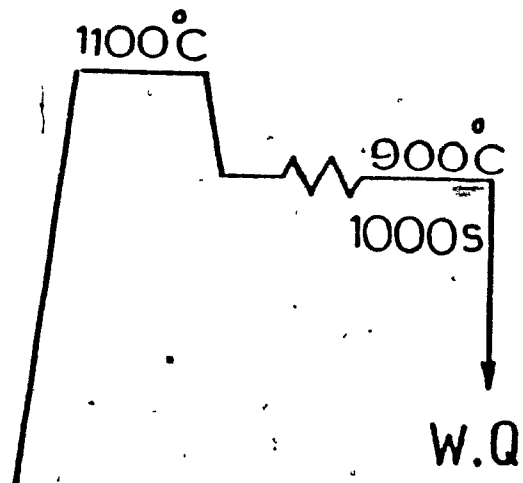


Figure 4.18 Undissolved MnS precipitates in a solution treated Nb steel deformed 25% at 900°C and quenched after 100 seconds.

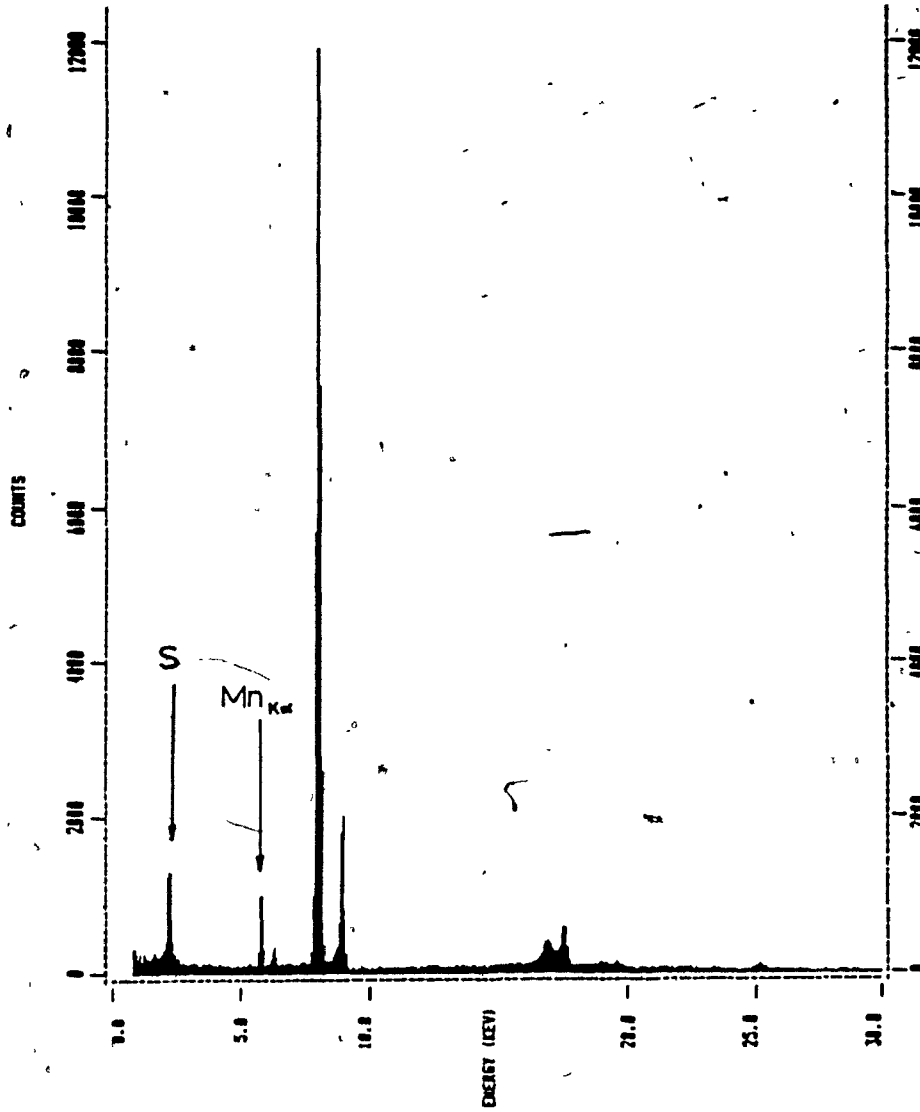


Figure 4.19 X-ray spectrum analysis of the MnS precipitates shown in Fig. 4.18.

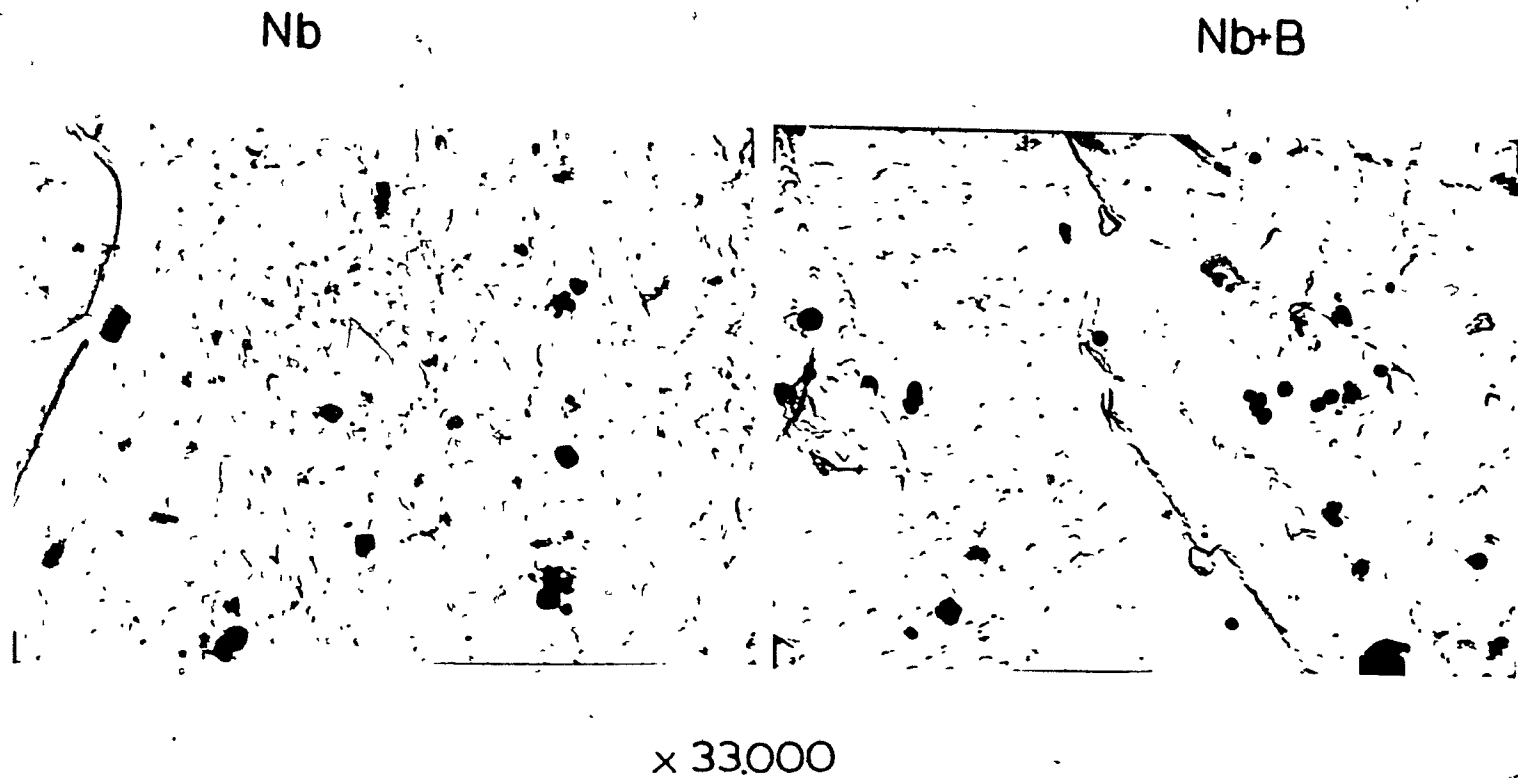


Figure 4.20 Comparison of the precipitates in solution treated Nb and Nb + B steels deformed 25% at 900°C and quenched after 1000 seconds.

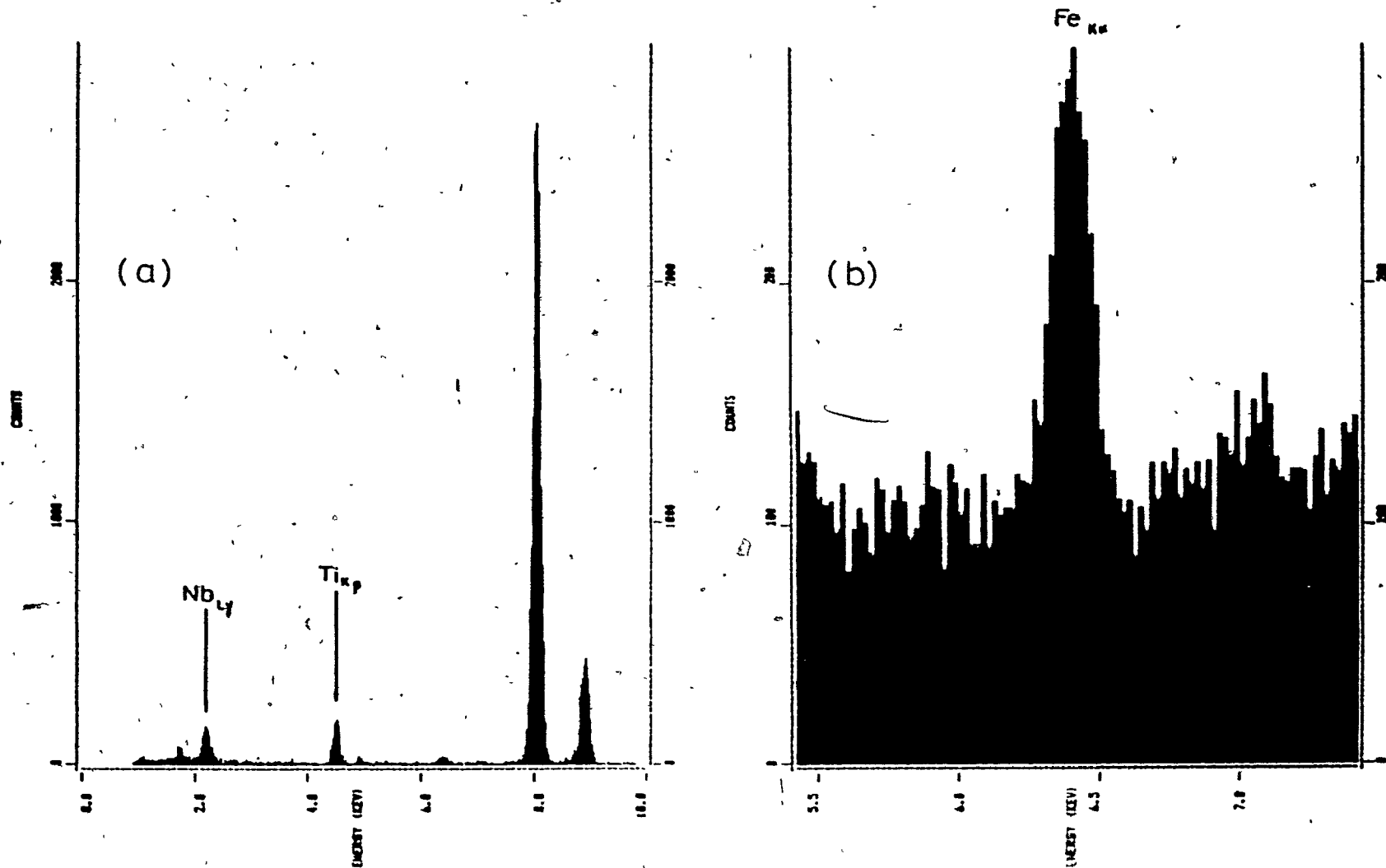


Figure 4.21 X-ray spectrum analysis of the precipitates in solution treated Nb (a) and Nb + B (b) steels deformed 25% at 900°C and quenched after 1000 seconds.

micrograph reveals the existence of a small number of large precipitates which remained undissolved. Similar coarse precipitates were observed when the sample was quenched 100 seconds after the deformation (Fig. 4.16). As can be seen from the spectral analysis of these precipitates (Fig. 4.17), they consist mainly of TiN, which forms at very high temperatures; sometimes there was a small additional peak indicating the presence of some undissolved NbC close to but separate from the TiN. The appearance of the Nb samples (i.e. those not containing B) pertaining to the same conditions was similar to that shown in Figs. 4.15 and 4.16; no examples are therefore included here.

The remaining diagrams, Figures 4.18 to 4.22, pertain to Nb and Nb + B steels deformed at 900°C and quenched after 1000 seconds. The large round particles shown in Figure 4.18 were found to be MnS (Fig. 4.19). This type of precipitate also forms at high temperatures and several examples were detected in the 1000°C samples as well. In Figure 4.20, a Nb and a Nb + B sample are compared; the spectral analyses of the precipitates shown indicate that NbC particles of considerable size are present close to the TiN particles (Figure 4.21(a)).

In the Nb + B sample, there are more precipitates per unit area and there are also some additional fine particles. The micrographs in Figure 4.22 depict the same area of the Nb + B steel at two different magnifications and the spectral analysis of the large grain boundary precipitates indicates an Fe peak (Fig. 4.21(b)). The above finding confirms that the grain boundary precipitates are $\text{Fe}_{23}(\text{B,C})_6$, an observation that is consistent with similar reports in the literature (26, 31).

4.3.2 BORON AUTORADIOGRAPHY RESULTS

The location of boron inside the microstructure after different experimental pretreatments is illustrated in Figures 4.23 to 4.26. Here the autoradiographs can be compared with the photomicrograph for the steel (Nb + B) in the same condition. The sample shown in Figure 4.23 was quenched in water from 1000°C after austenitization at 1100°C. The autoradiograph (Figure 4.23(b)) shows no clear evidence of boron segregation

Nb+B



x16,000

x 66,000

Figure 4.22 $\text{Fe}_{23}(\text{B}, \text{C})_6$ precipitates at a γ -grain boundary in a solution treated Nb + B steel deformed 25% at 900°C and quenched after 1000 seconds.

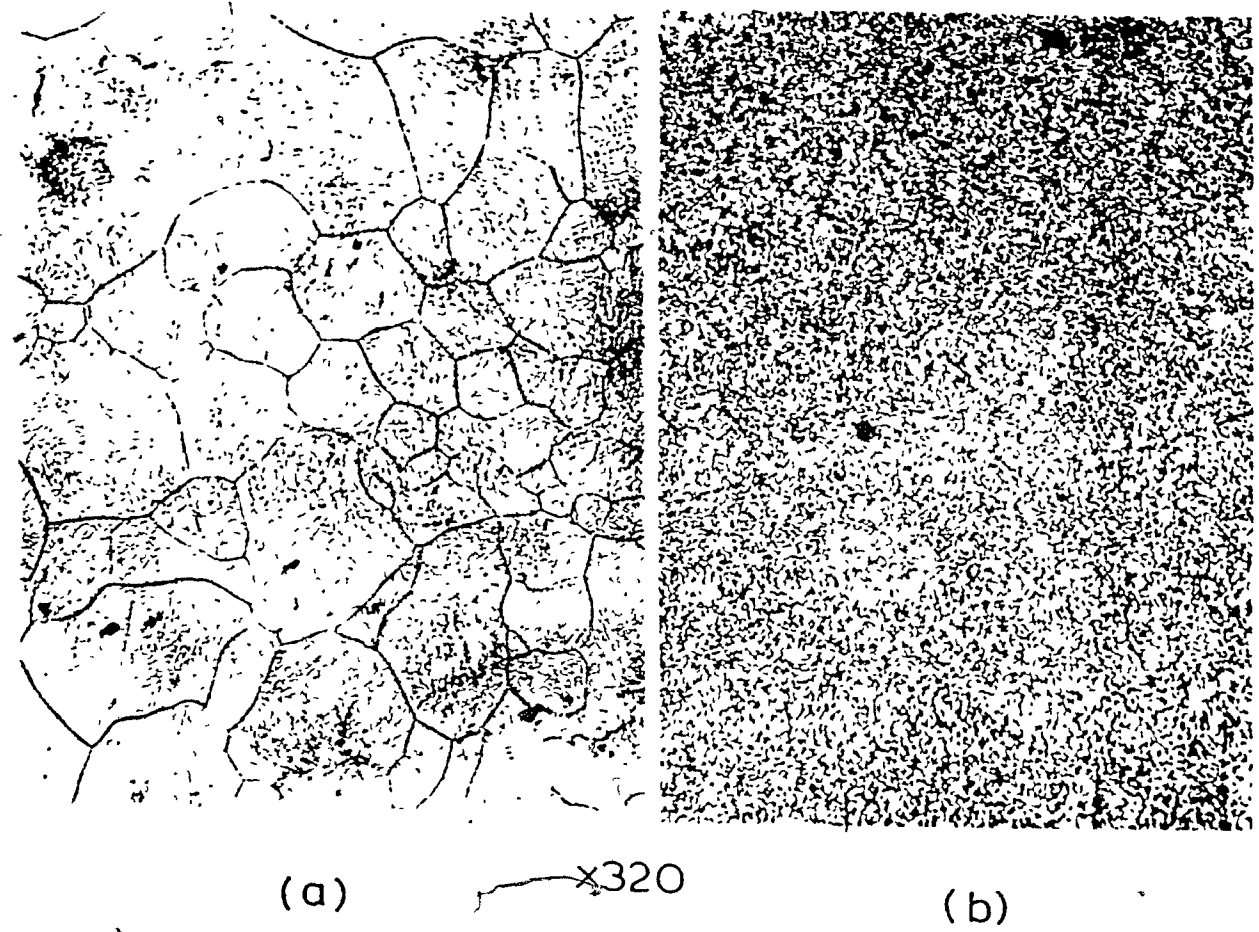
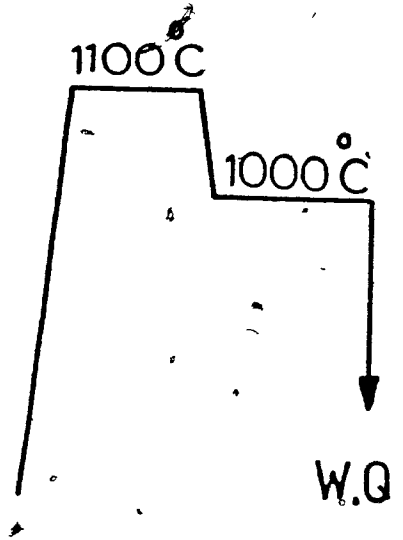
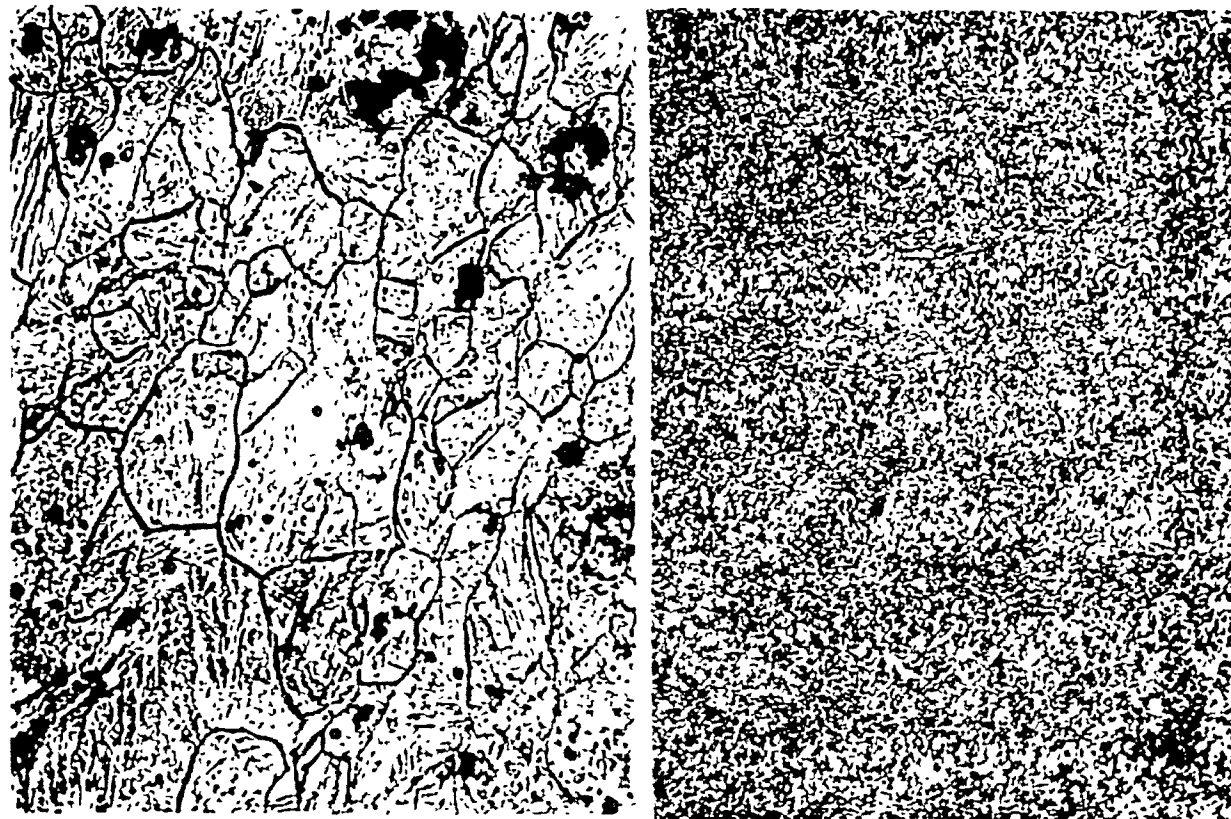
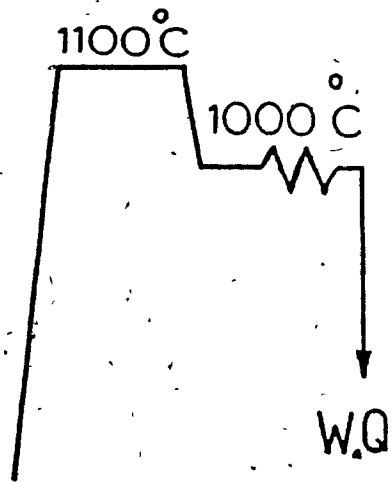


Figure 4.23 Photomicrograph (a) and boron autoradiograph (b) of a Nb + B steel quenched from 1000°C after austenitization at 1100°C. No segregation of boron can be seen (thermal neutron dose: 5×10^{14} n/cm²).

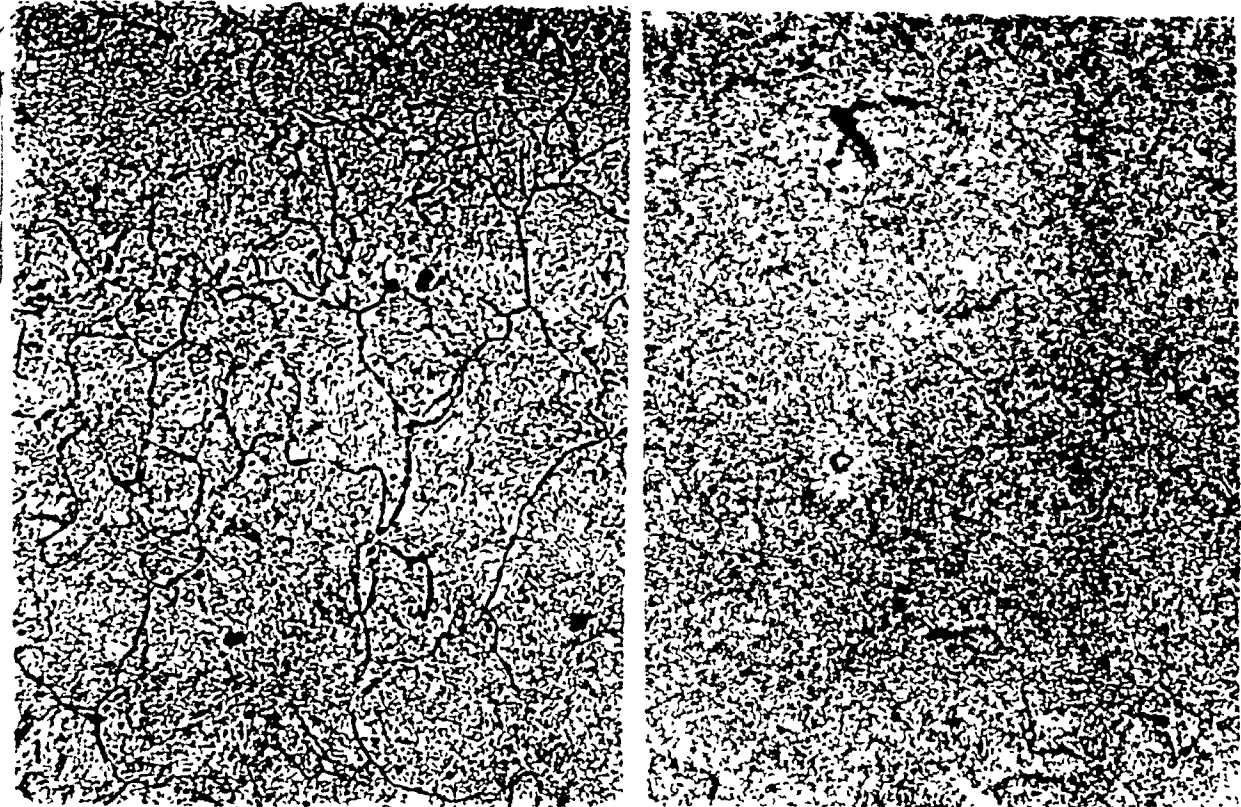
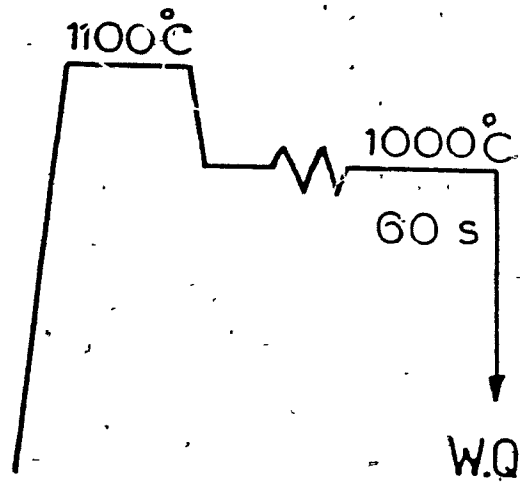


(a)

x320

(b)

Figure 4.24 Photomicrograph (a) and boron autoradiograph (b) of a Nb + B steel quenched immediately after a deformation of 25% at 1000°C showing no segregation of boron (thermal neutron dose: 5×10^{14} n/cm²).

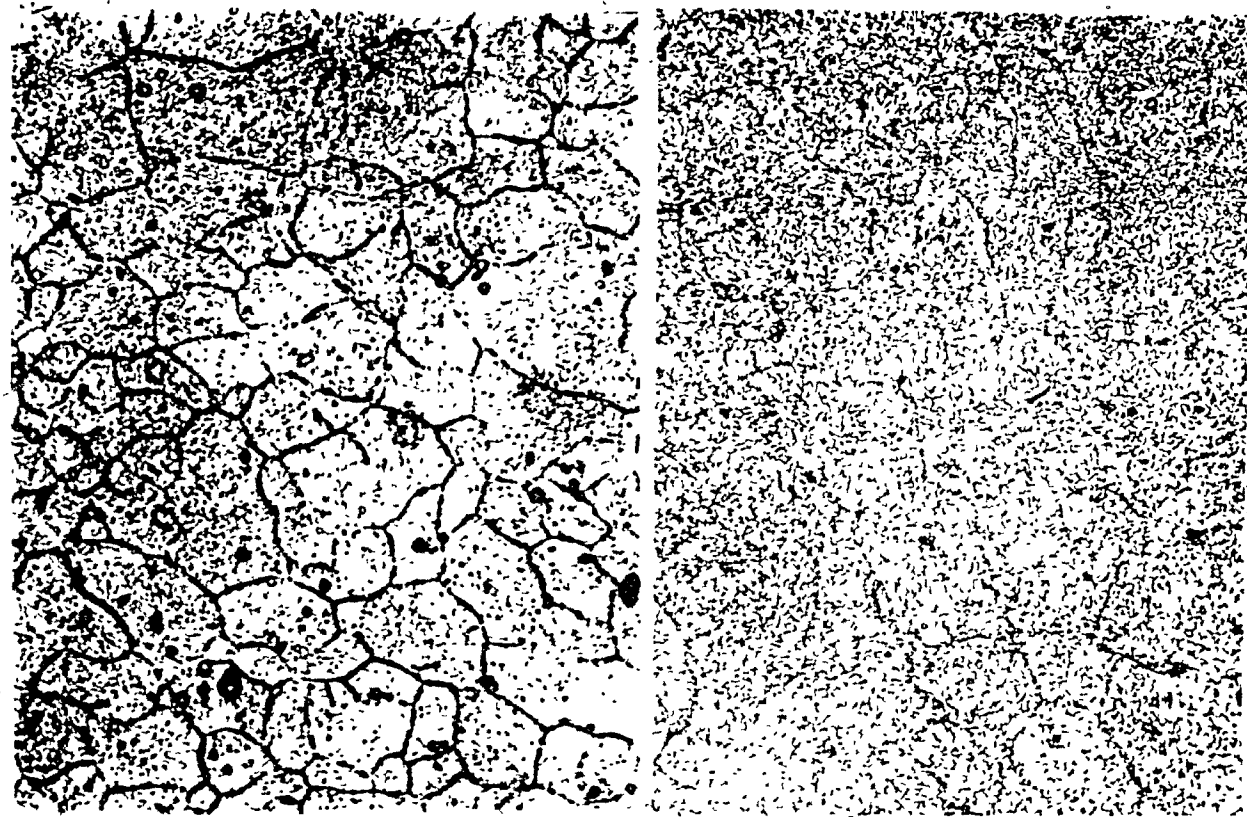
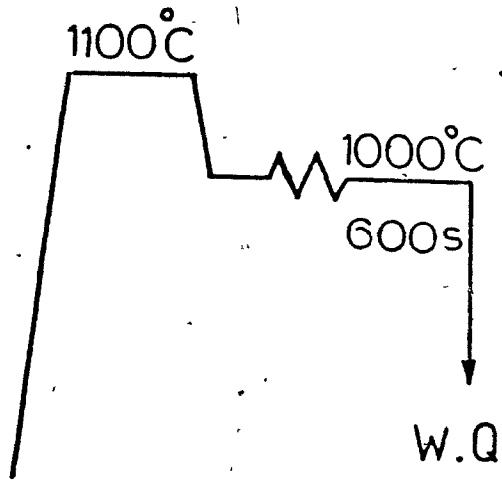


(a)

x320

(b)

Figure 4.25 Photomicrograph (a) and boron autoradiograph (b) of a Nb + B steel deformed 25% at 1000°C and quenched after 60 seconds. Some boron segregation can be seen at the recrystallizing grain boundaries (thermal neutron dose: $5 \times 10^{14} \text{ n/cm}^2$).



(a)

x320

(b)

Figure 4.26 Photomicrograph (a) and boron autoradiograph (b) of a Nb + B steel deformed 25% at 1000°C and quenched after 600 seconds showing considerable segregation of boron (thermal neutron dose: 5×10^{14} n/cm²).

at the grain boundaries. In Figure 4.24(a), the sample was first austenitized at 1100°C, then deformed 25% at 1000°C and immediately quenched. The grains are evidently flattened and the corresponding autoradiograph (Figure 4.25(b)) indicates that boron segregation has not taken place at the grain boundaries. Figure 4.25(a) shows the microstructure of a sample austenitized at 1100°C and deformed at 1000°C to a strain of 25%. The sample was quenched after an isothermal holding time of 60 seconds. The process of static recrystallization is almost at its beginning and clearly there is some boron segregated at the grain boundaries (Figure 25(b)). Finally, when the isothermal holding time was increased to 600 seconds (almost at the end of recrystallization) a considerable amount of boron segregated at the recrystallizing grain boundaries can be observed (Fig. 4.26(b)).

4.3.3 DETERMINATION OF INITIAL GRAIN SIZE

In order to determine the initial austenite grain size, a series of Nb + B steels was (i) heat treated for one hour at 1000°C and air cooled; (ii) austenitized for 15 minutes at 1250, 1150, 1100 and 1050°C and water quenched. As the austenitization temperature is increased, the initial grain size increases, as can be seen in Figure. 4.27.

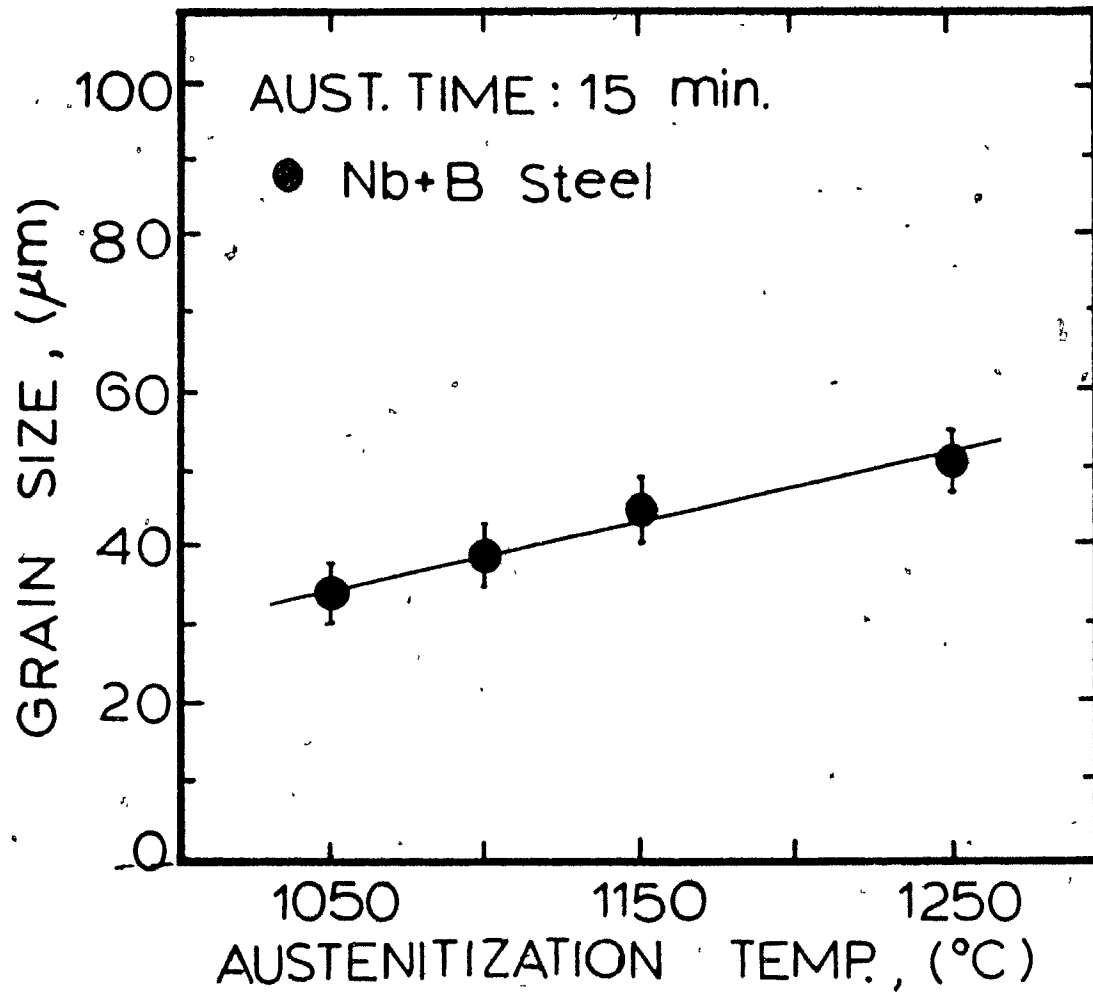


Figure 4.27 Austenite grain size as a function of austenitization temperature.

CHAPTER 5

DISCUSSION

During deformation at a strain rate and temperature of interest in hot working operations, all metals undergo work hardening and dynamic recovery, and some may undergo dynamic recrystallization as well. Most metals and alloys are hot worked under interrupted, non-isothermal deformation conditions, such as in commercial forging or hot rolling, where the incremental strains are small and generally do not reach those required to attain steady state conditions. In such interrupted operations (where the strain involved in a single pass ϵ very seldom exceeds the critical value for dynamic recrystallization and consequently dynamic recrystallization nuclei are not formed), softening by static recovery is followed by static recrystallization during the interpass times. The rate of classical recrystallization is a function of temperature T , driving force and density of nucleation sites. The latter two in turn depend respectively on (i) the local difference in dislocation density and (ii) on the grain size d_0 , since nucleation occurs preferentially at grain boundaries. The dislocation density differences are proportional to the dislocation density itself, which depends on the Zener-Hollomon parameter Z and the predeformation ϵ_p . The effects of temperature, prestrain and initial grain size on the rate of recrystallization were investigated in the present work and, for ease of presentation, the results obtained under static and dynamic conditions will now be discussed separately.

5.1 STATIC STRUCTURAL CHANGES

In the present investigation, the influence of two out of the above three parameters, namely the temperature and prestrain, was investigated under static conditions. The results were presented (Chapter 4) as percentage softening versus log of the holding time and the softening curves had a sigmoidal shape. The same type of sigmoidal curve also appears when the isothermal transformation of austenite to pearlite is followed as a function of (log) time. Such dependences are characteristic of processes involving

nucleation and growth, and under these conditions the results can be fitted to the Avrami equation (93, 94)

$$x = 1 - \exp(-kt^n) \quad (5.1)$$

where x is the fraction of the material transformed or recrystallized, t is the time, k is the rate constant and n is an exponent.

5.1.1 CALCULATION OF THE PARAMETERS k AND n

Equation 5.1 can be rewritten as follows:

$$1 - x = \exp(-kt^n)$$

$$-\ln(1 - x) = kt^n$$

$$\log_{10} \ln\left(\frac{1}{1-x}\right) = \log_{10} k + n \log_{10} t \quad (5.2)$$

From Equation 5.2 it is apparent that the slope of the $\log_{10} \ln(1/1 - x)$ versus $\log_{10} t$ plot will be equal to n and that the value of the ordinate at $t = 1$ is $\log k$, from which the value of k can be derived. Such a plot is displayed in Figure 5.1, where the experimental data were obtained from the Nb and Nb + B steels deformed to $\epsilon = 0.25$ at 1050, 1000 and 950°C. The most interesting feature of this plot is that, instead of obtaining a single straight line for each steel tested at a given temperature, there are two segments to each fit. Also the slopes of the two linear parts change at values of softening of about 25%. The above indicates that there are two softening processes taking place: (i) static recovery, (from 0 to 25% softening) and; (ii) static recrystallization (from 25 to 100% softening). The values of k and n for recovery and recrystallization were therefore measured separately, by following the method introduced by Luton (95).

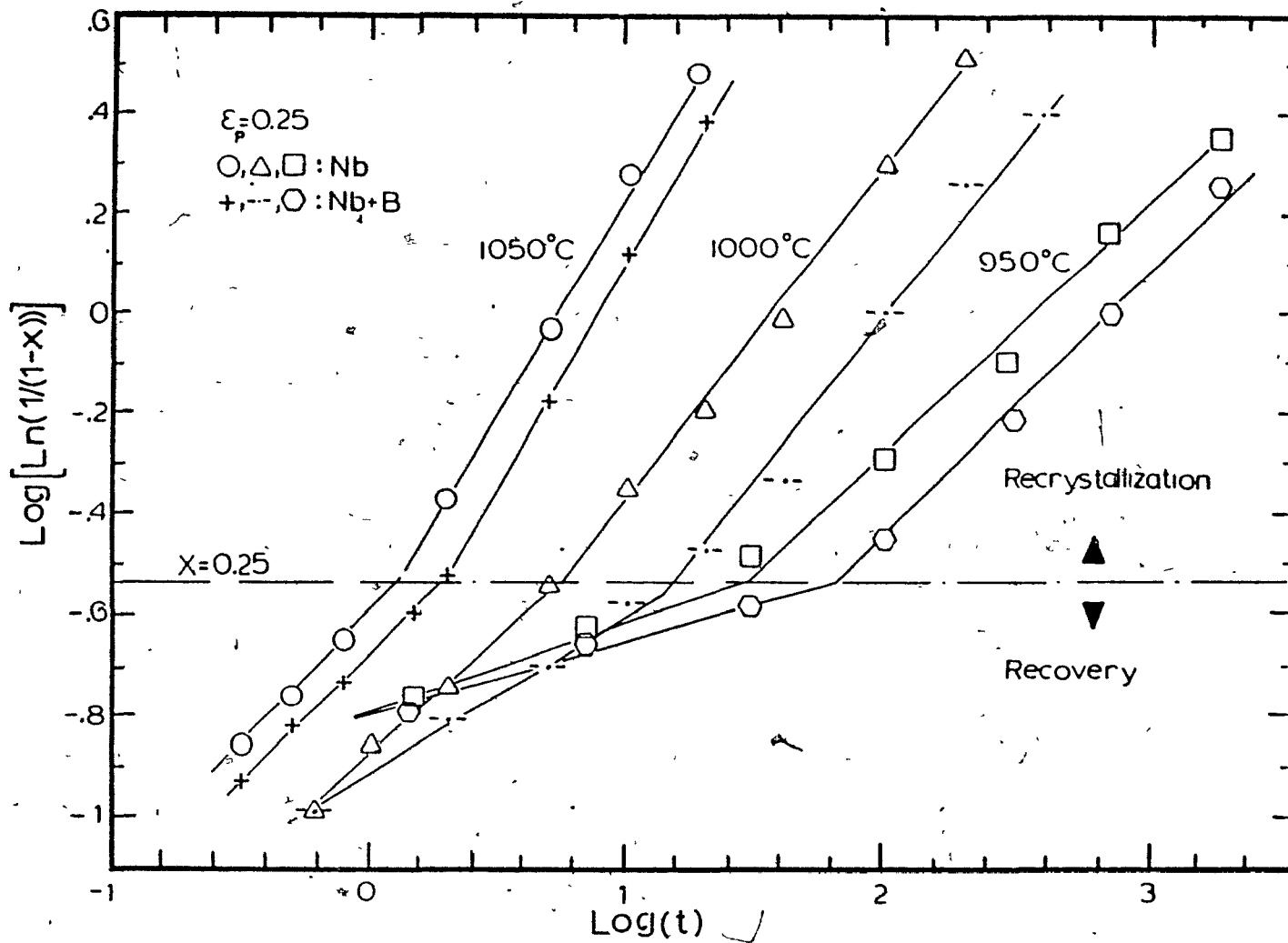


Figure 5.1 Dependence of $\log \ln(1/1 - x)$ on $\log t$ at three different temperatures in the Nb and Nb + B steels.

For the analysis of recovery, it is useful to define an expression for the fractional recovery in which full recovery is represented by the reloading stress σ_∞ . When only recovery is taking place, the fractional softening is given by

$$X^r = \frac{\sigma_m - \sigma_r}{\sigma_m - \sigma_0} \quad (5.3)$$

Here σ_m is the flow stress immediately before unloading and σ_0 and σ_r are the initial flow stresses recorded during prestraining and reloading, respectively. The superscript r is used here to denote the softening fraction attributable to recovery only. It follows that the fractional softening at the completion of recovery X_∞^r , is given by

$$X_\infty^r = \frac{\sigma_m - \sigma_\infty}{\sigma_m - \sigma_0} \quad (5.4)$$

and the degree of recovery x^r by

$$x^r = \frac{X^r}{X_\infty^r} = \frac{\sigma_m - \sigma_r}{\sigma_m - \sigma_\infty} \quad (5.5)$$

The experimental quantities X^r and X_∞^r can be substituted into equation (5.1) to yield the following equation

$$X^r = X_\infty^r (1 - \exp(-k^r t^{n^r})) \quad (5.6)$$

The values of the time exponent n^r and the rate constant k^r for recovery only can be obtained from plots of $\log_{10} \ln(X_\infty^r / X_\infty^r - X^r)$ vs. $\log_{10} t$. The saturation level of X_∞^r was chosen to be 0.25 for this purpose.

A similar approach was followed for the case of recrystallization and the equation that resulted is given by

$$X^R = X_{\infty}^R (1 - \exp(-k^R t^{n^R})) \quad (5.7)$$

where $X_{\infty}^R = 0.75$, $t = t - t_0$ and t_0 is the time for 25% softening in this case.

The overall softening produced when the two restoration processes occur together is in general given by the sum of the individual components as:

$$X = X^r + X^R \quad (5.8)$$

5.1.1.1 Static Recovery

In Figures 5.2 to 5.4, plots of $\log_{10} \ln(X_{\infty}^r / X_{\infty}^R - X^r)$ versus $\log(t)$ are presented calculated from the experimental softening curves for prestrains of 12, 25 and 50%, respectively.

A number of observations can be made from these plots: (i) for a given predeformation, material and test temperature, the data are well represented by straight lines; (ii) the slopes of the lines (when ε_p is constant) are similar and do not depend on the material chemistry or test temperature; and (iii) as the predeformation is increased from 12 to 25 to 50%, the average slope (n^r) increases from 0.46 to 0.61 to 0.77, respectively. Clearly the intersections of these lines with the vertical corresponding to $t = 1$ are changing and the values of k^r obtained in this way increase with temperature.

Furthermore, k^r is seen to increase from 0.33 to 0.72 to 1.40 as the predeformation of the Nb steel tested at 1000°C is increased from 12 to 25 to 50% (Table 5.1). A similar dependence of the rate constant (k^r) on temperature and strain was reported by Luton and Jonas (95) for ETP copper, but the numerical values were different. However, in contrast to the results of the above investigators, the time exponent n^r in the present work depends on deformation (Table 5.1).

Figure 5.5 shows the dependence of the time exponent n^r on the strain, and this dependence can be expressed by an empirical formula as:

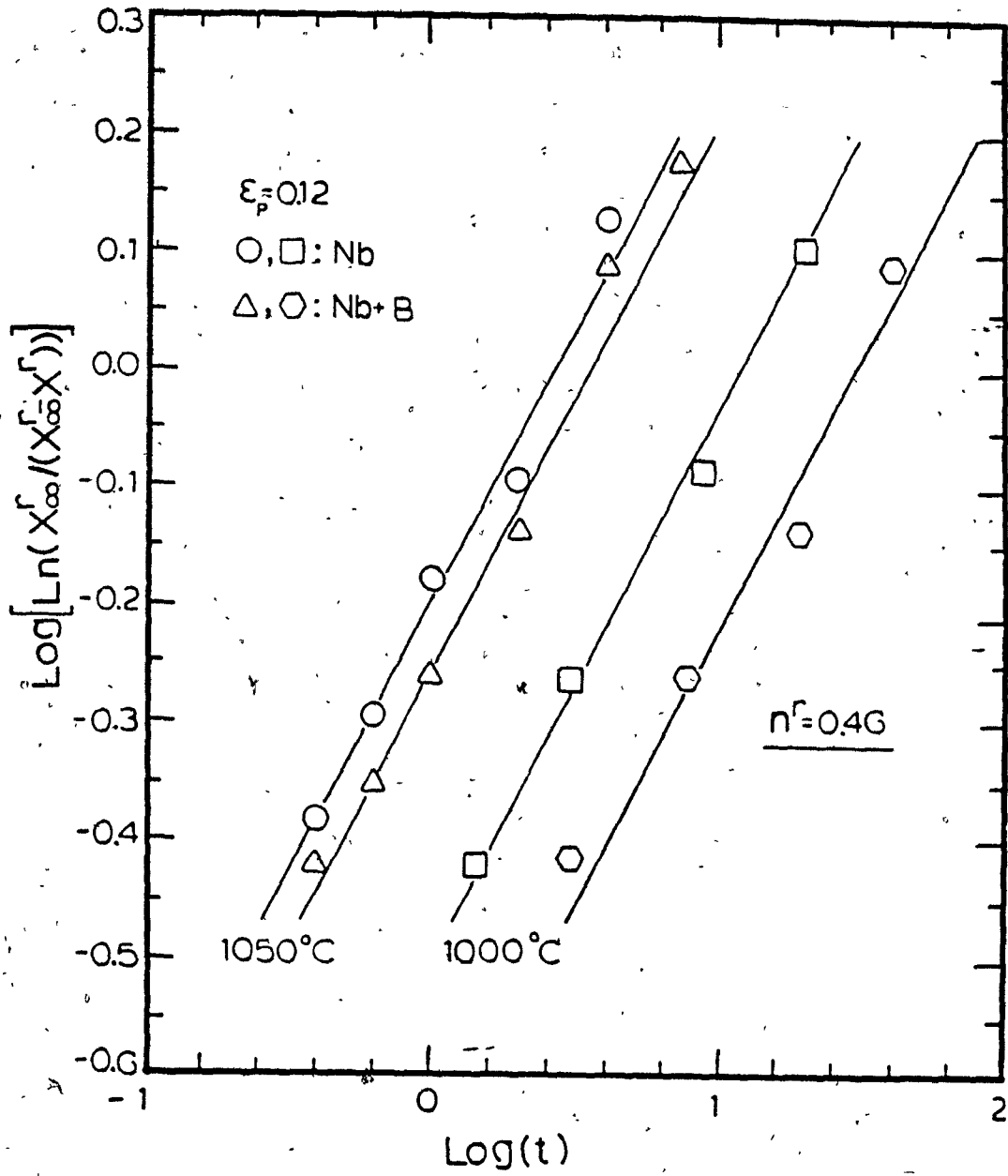


Figure 5.2 Dependence of $\log \ln (X_\infty^r / X_\infty^r - X^r)$ on $\log(t)$ for $\epsilon = 0.12$.

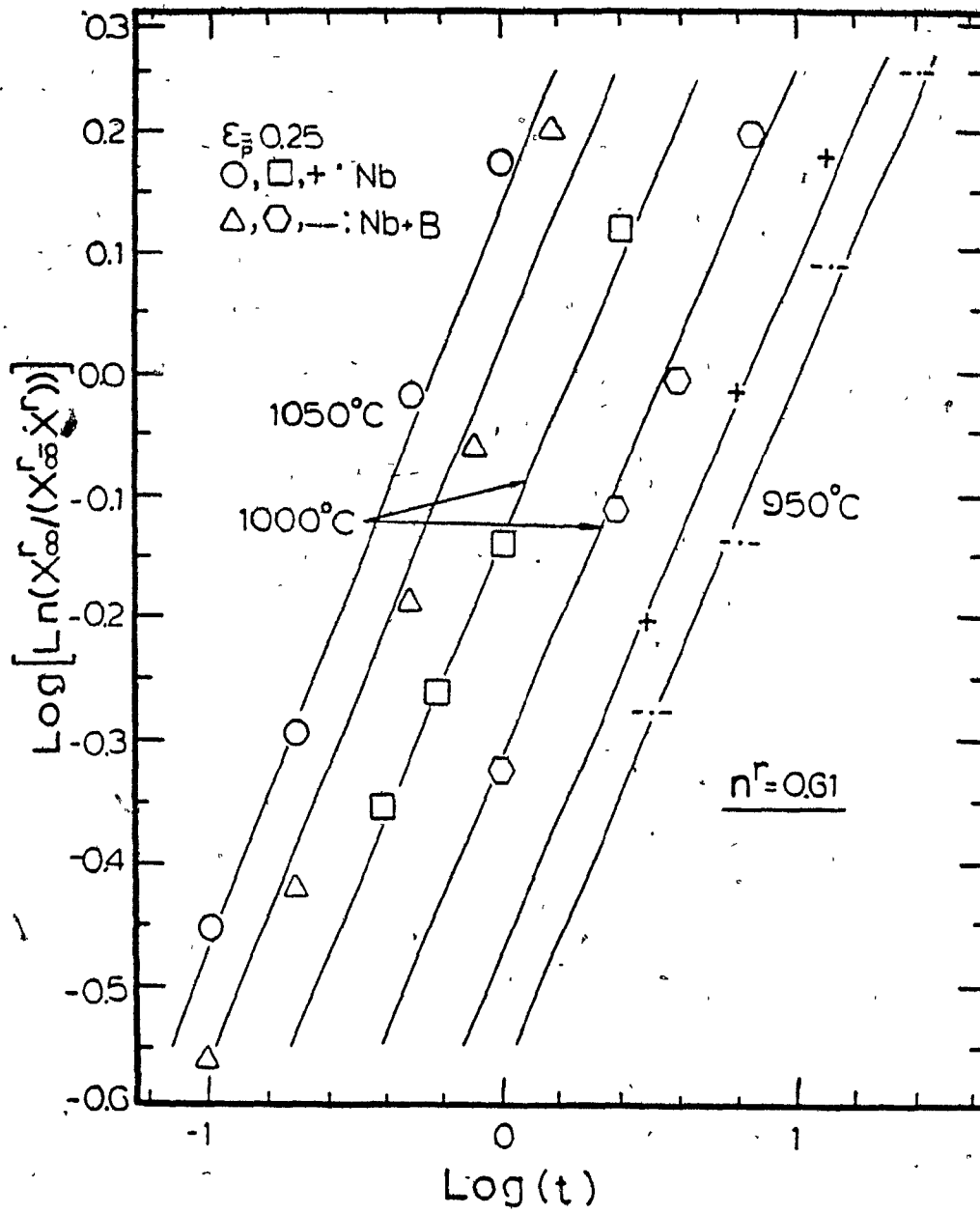


Figure 5.3 Dependence of $\log \ln(X_\infty^r / X_\infty^r - X^r)$ on $\log(t)$ for $\epsilon = 0.25$.

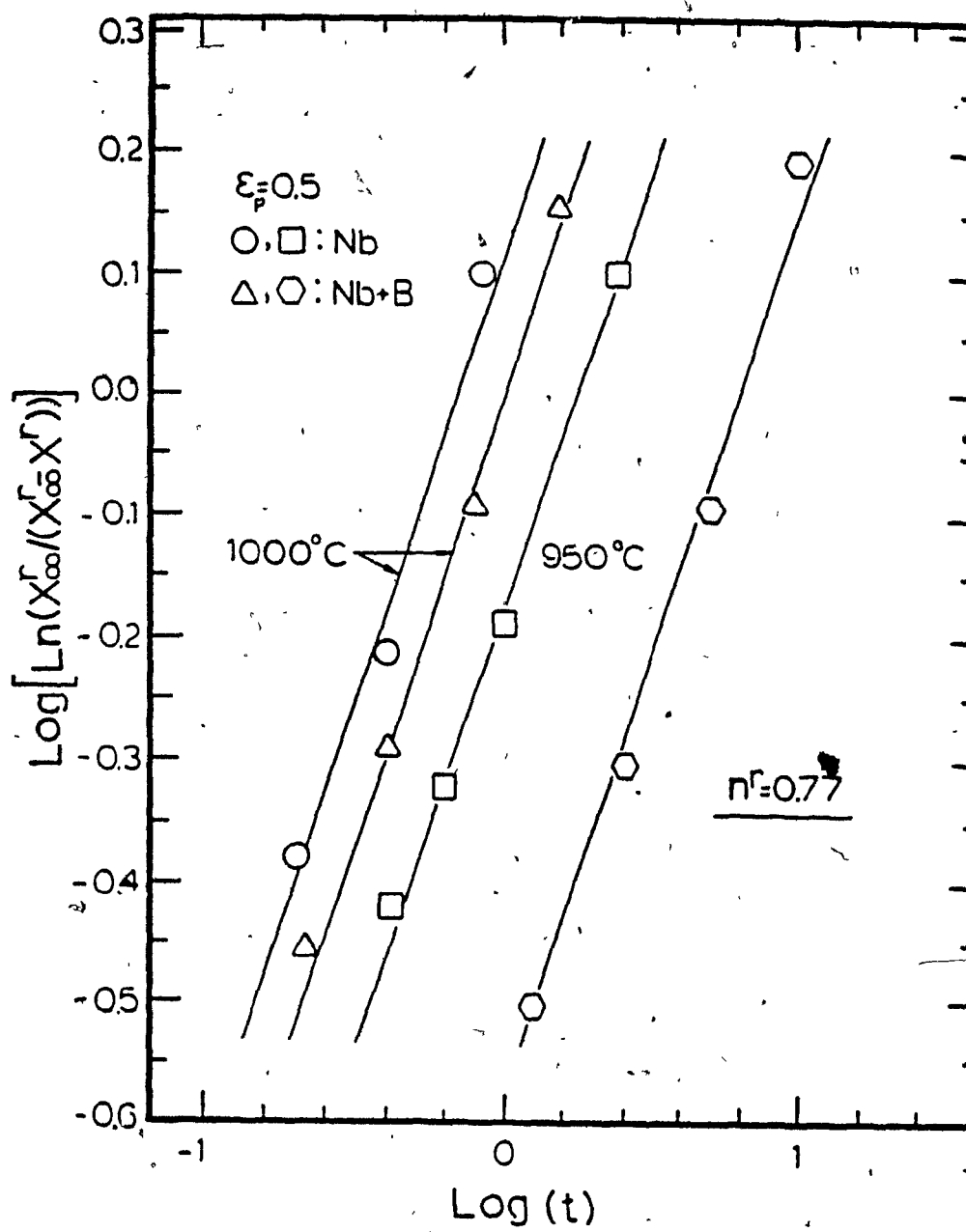


Figure 5.4 Dependence of $\log \ln(X_{\infty}^r / (X_{\infty}^r - X^r))$ on $\log(t)$ for $\epsilon = 0.5$.

TABLE 5.1 - Empirical Constants k^r and n^r Obtained from the Softening Data

Recovery

Prestrain 0.12, Strain Rate 2 s ⁻¹					
Temperature °C	Nb		Nb + B		n ^r average
	k ^r	n ^r	k ^r	n ^r	
1050	0.65	0.49	0.57	0.48	0.46
1000	0.33	0.44	0.24	0.44	
Prestrain 0.25, Strain Rate 2 s ⁻¹					
Temperature °C	Nb		Nb + B		n ^r average
	k ^r	n ^r	k ^r	n ^r	
1050	1.50	0.64	1.10	0.63	0.61
1000	0.72	0.60	0.47	0.60	
950	0.32	0.60	0.27	0.59	
Prestrain 0.50, Strain Rate 2 s ⁻¹					
Temperature °C	Nb		Nb + B		n ^r average
	k ^r	n ^r	k ^r	n ^r	
1000	1.40	0.80	1.00	0.77	0.77
950	0.72	0.74	0.26	0.77	

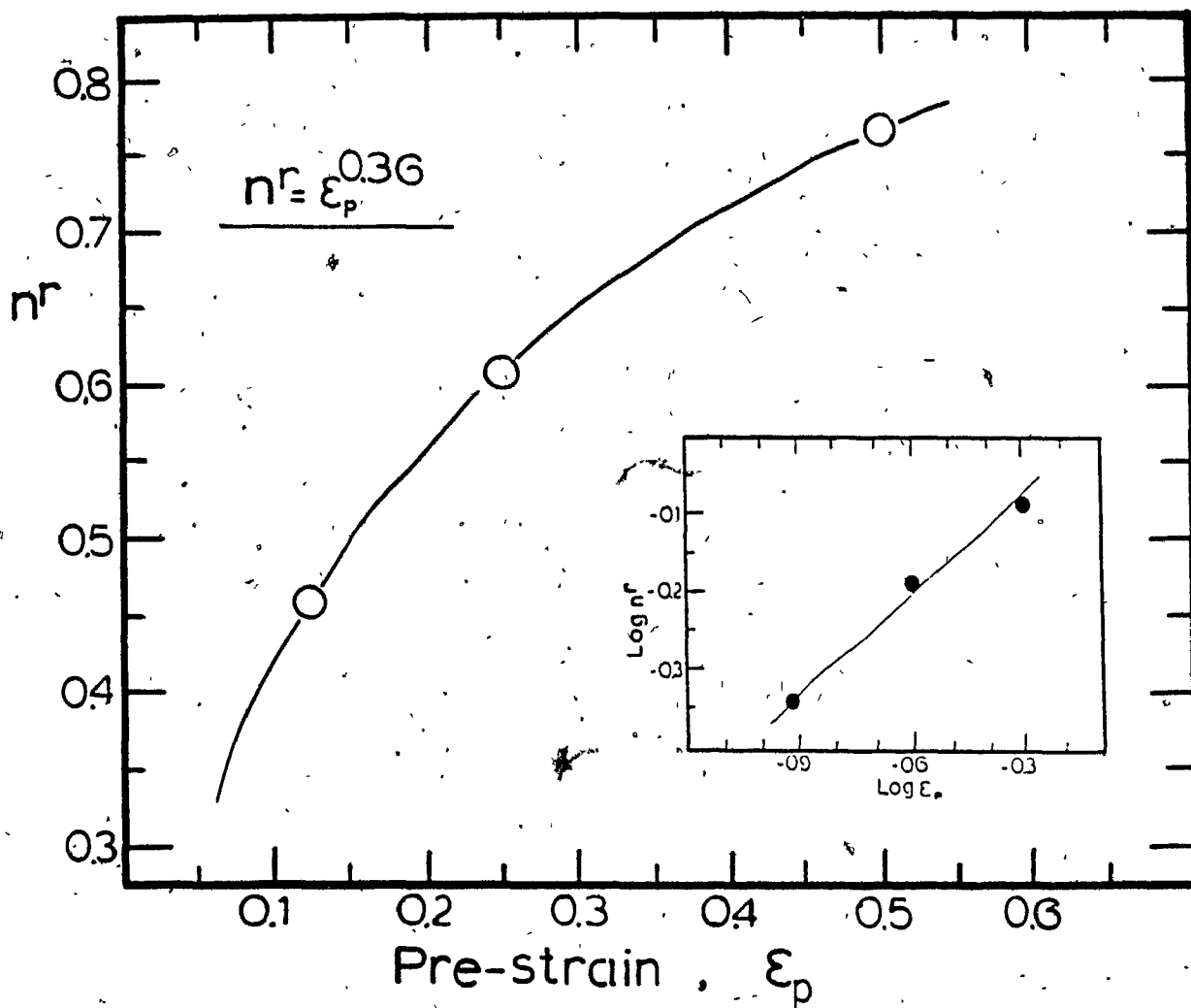


Figure 5.5 Dependence of time exponent n^r on the prestrain ϵ_p .

$$n^r = \varepsilon_p^{0.36} \quad (5.9)$$

The rate coefficient was found to depend on both temperature and strain through an empirical expression of the form

$$K^r = A^r(\varepsilon) \exp\left(-\frac{Q^r}{RT}\right) \quad (5.10)$$

where $A^r(\varepsilon)$ is a constant depending on the strain. The slopes of the $\ln K^r$ versus inverse absolute temperature curves for the Nb and Nb + B steels tested at prestrains of 12, 25 and 50% (Fig. 5.6) provided the values of the activation energies for the two steels ($Q^r_{\text{Nb}} = 193$ KJ/mole, $Q^r_{\text{Nb+B}} = 249$ KJ/mole). The intersection of the above lines with the vertical axis provided the values of the pre-exponential term (A^r). By plotting $\ln A^r$ and $\log_{10} \ln A^r$ versus ε_p and $\log_{10} \varepsilon_p$ (Fig. 5.7), respectively, empirical expressions for $\ln A^r$ were obtained for the Nb and Nb + B steels as follows.

$$\ln A^r_{\text{Nb}} = 19.46 \cdot \varepsilon_p^{0.0645} \quad (5.11)$$

$$\ln A^r_{\text{Nb+B}} = 25.10 \cdot \varepsilon_p^{0.0645} \quad (5.12)$$

5.1.1.2 Static Recrystallization

By using an approach similar to that of the static recovery case, $\log_{10} \ln(X^R_\infty/X^R_\infty - X^R)$ data were plotted versus $\log_{10} (t - t_0)$ for the determination of n^R (see Figs. 5.8 to 5.10). Here t_0 is the incubation time (time for 25% softening). The values of K^R obtained in this way are listed in Table 5.2. The only new observation which can be made here is that the average value of n^R does not vary much with predeformation and temperature and has a value of approximately 0.9. A similar overall dependence was reported by Luton et al. (95) for ETP Cu, but their value of n^R was 2.2.

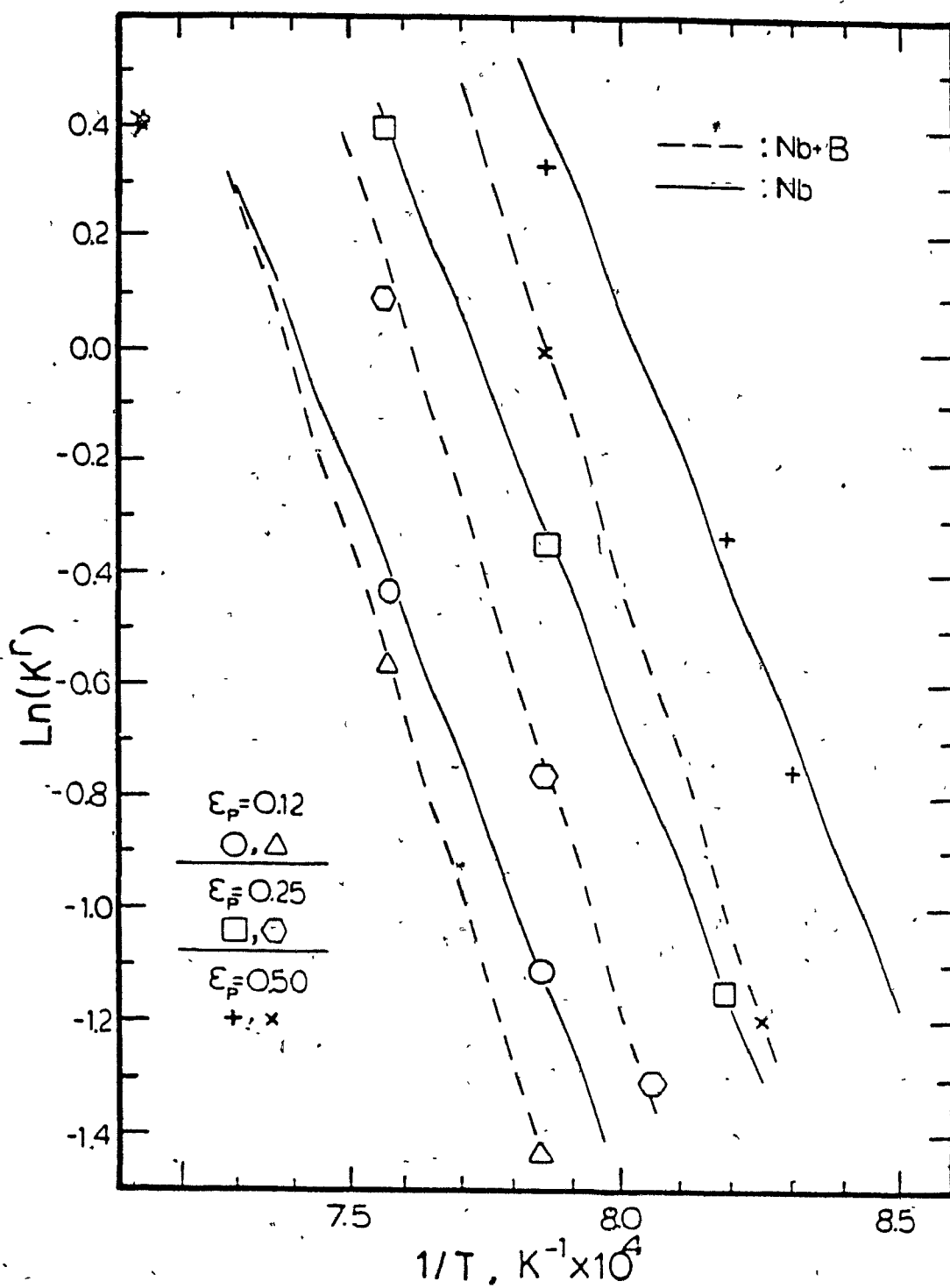


Figure 5.6 Dependence of the rate constant k^r on the inverse absolute temperature.

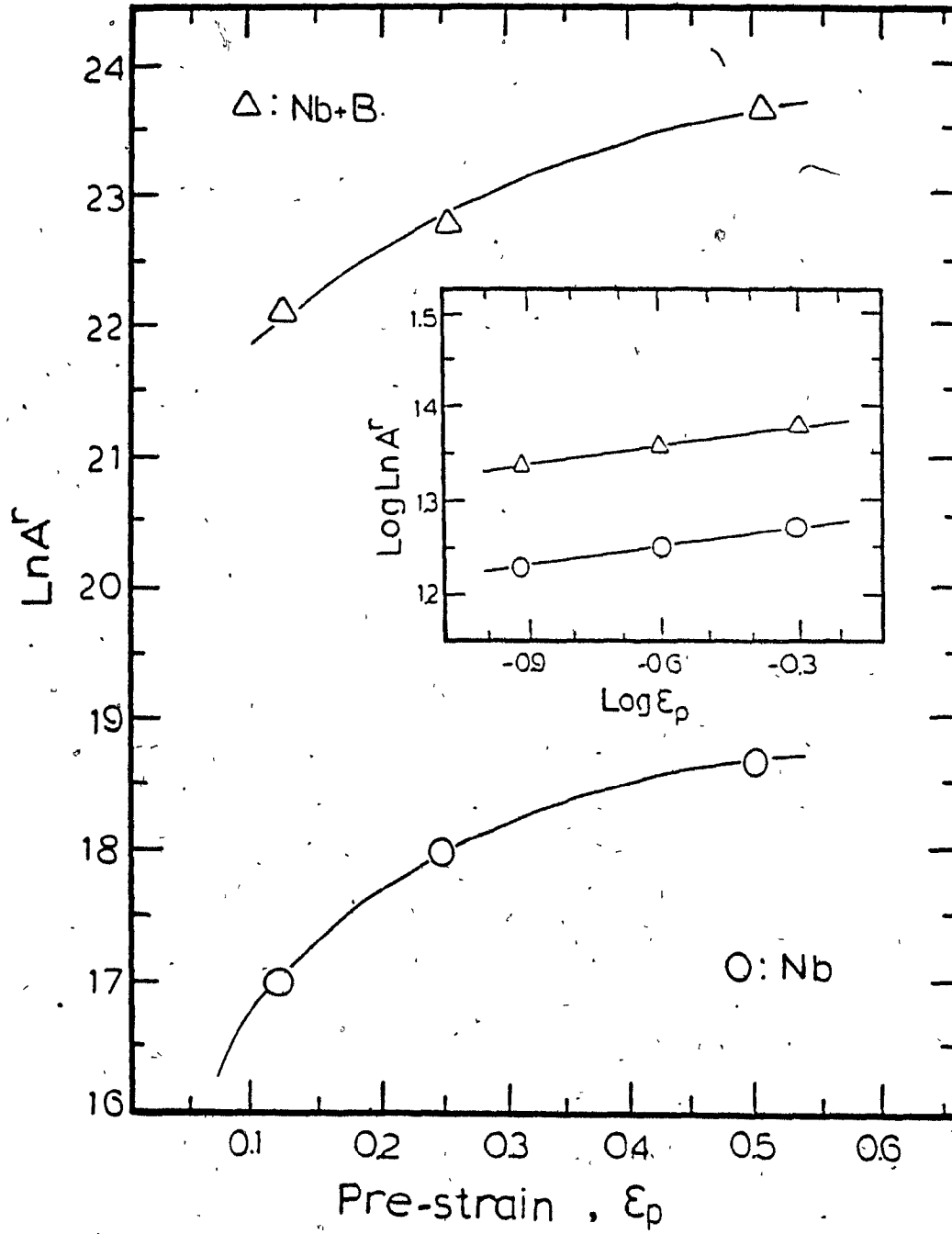


Figure 5.7 Dependence of A^r on the prestrain ϵ_p .

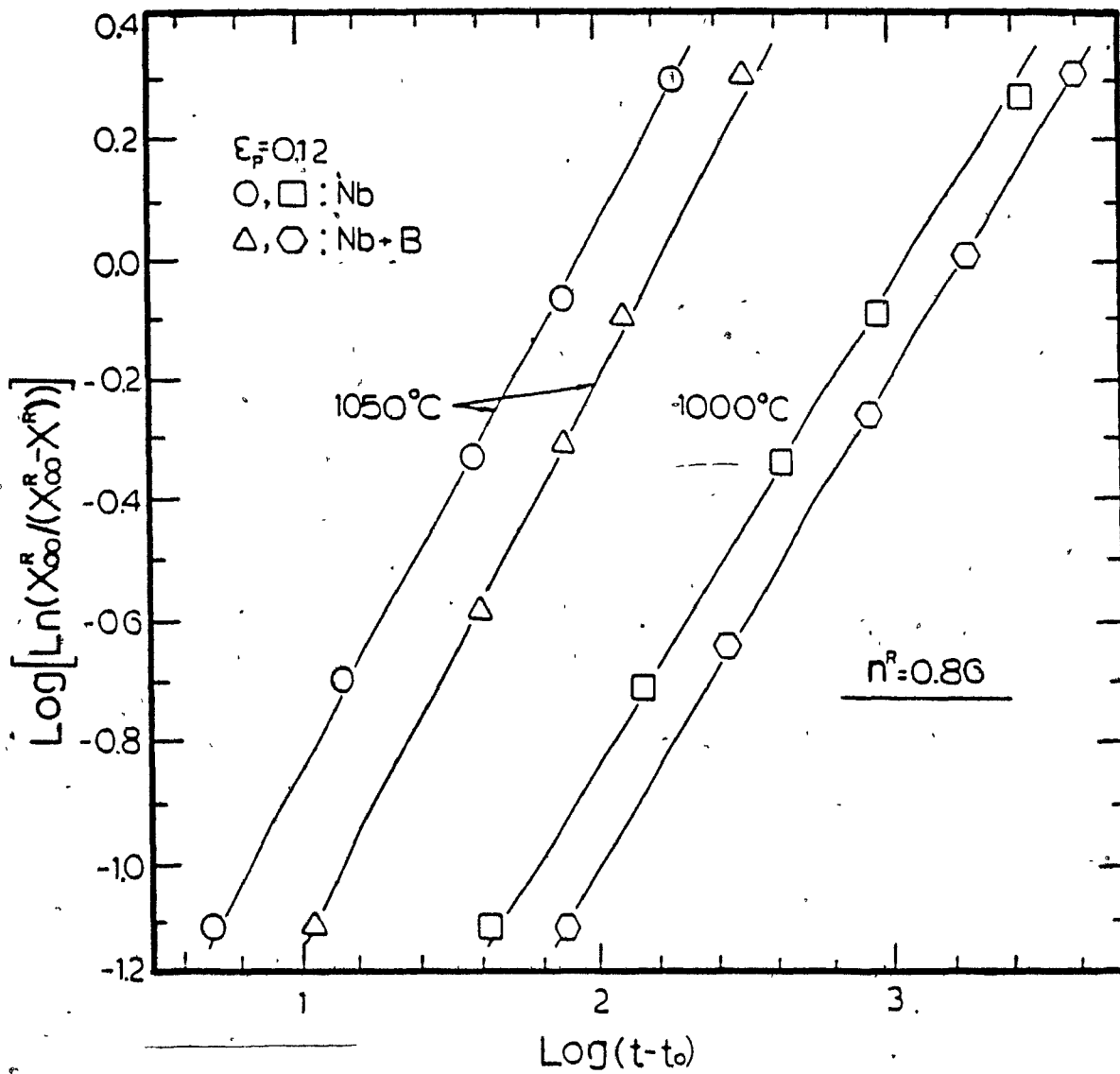


Figure 5.8 Dependence of $\log \ln(X_{\infty}^R / X_{\infty}^R - X^R)$ on $\log(t - t_0)$ for $\epsilon = 0.12$.

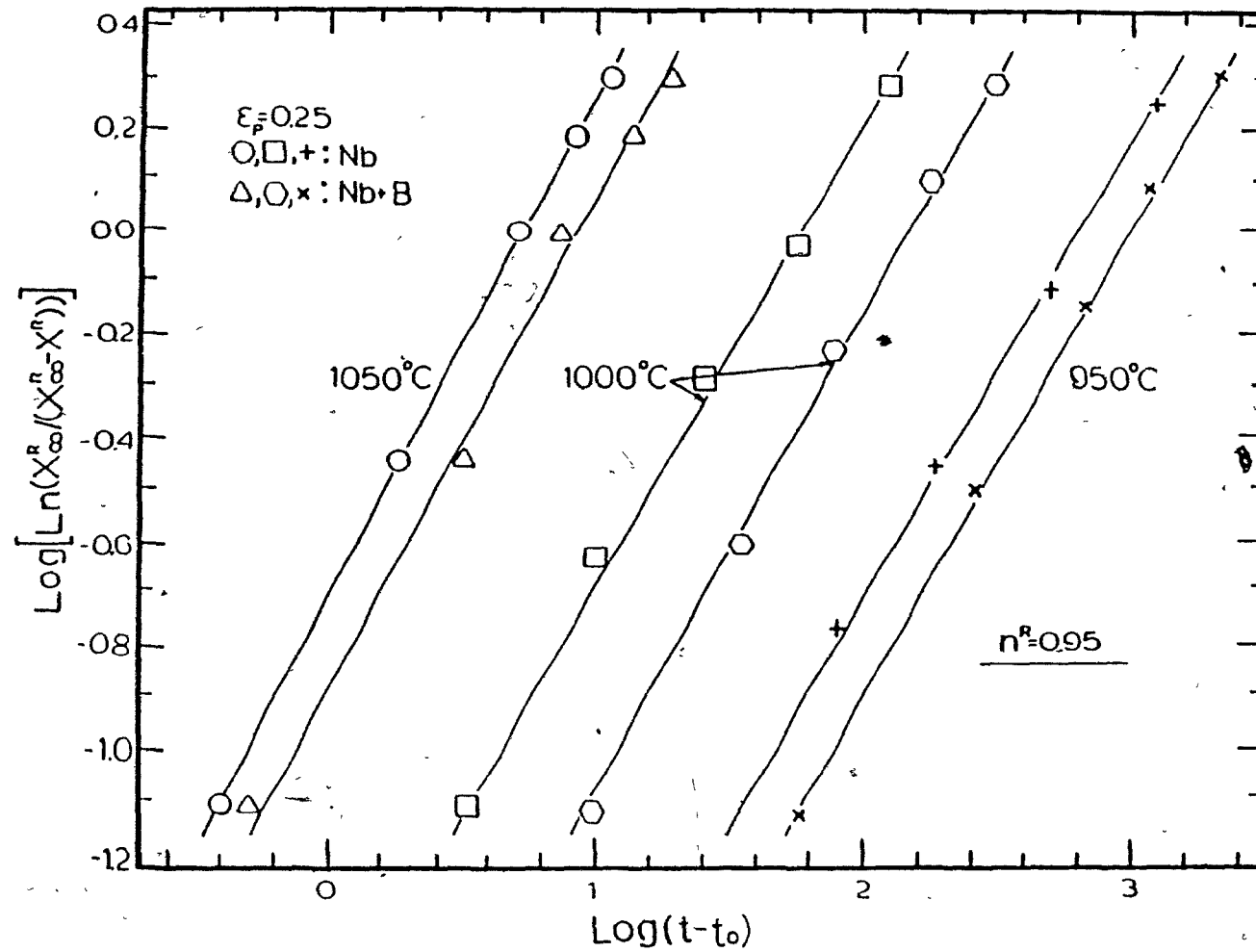


Figure 5.9 Dependence of $\log \ln(X_\infty^R / X_\infty^R - X^R)$ on $\log(t - t_0)$ for $\epsilon = 0.25$.

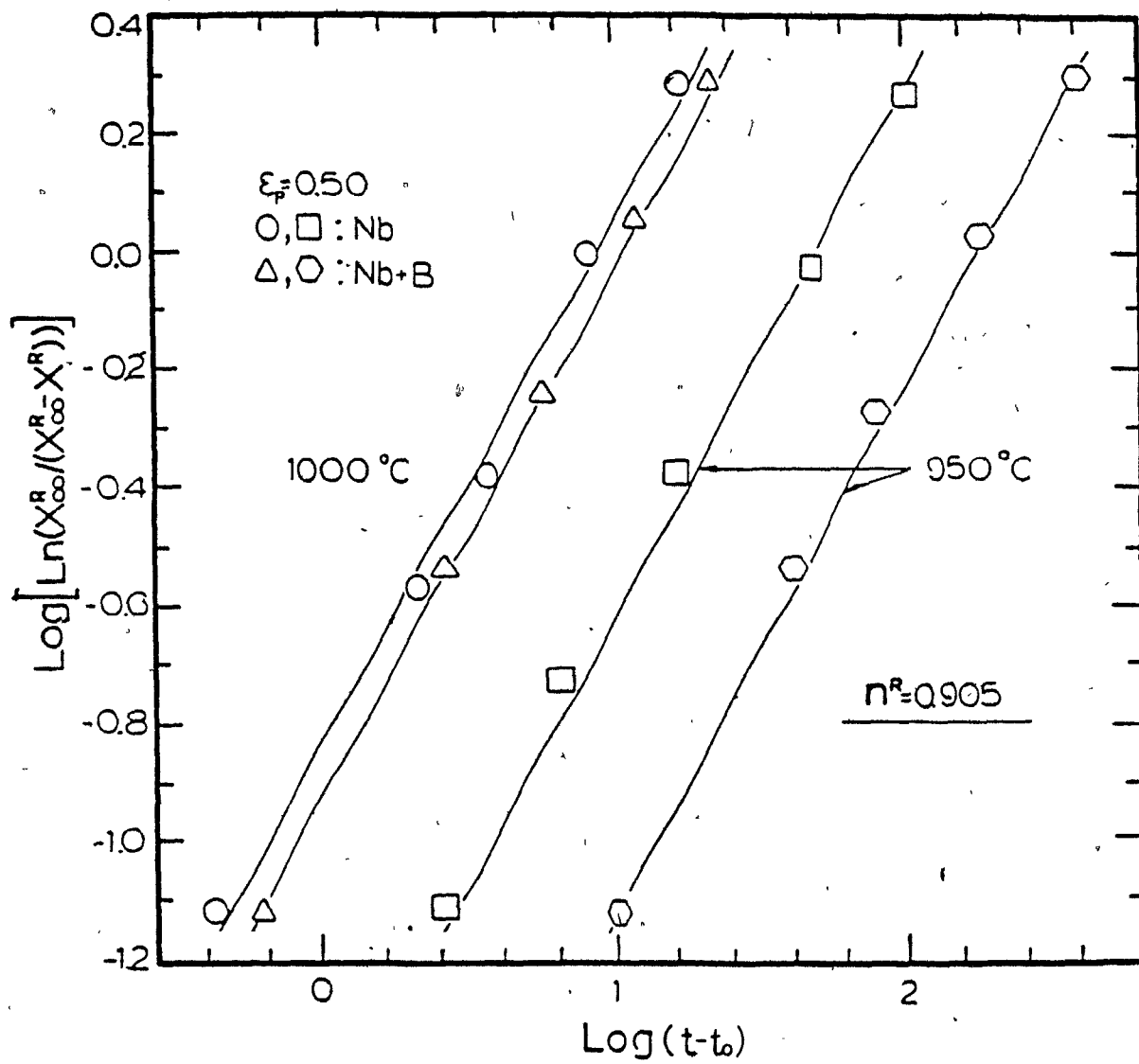


Figure 5.10 Dependence of $\log \ln(X_{\infty}^R / X_{\infty}^R - X^R)$ on $\log(t - t_0)$ for $\epsilon = 0.5$.

TABLE 5.2 - Empirical Constants k^R and n^R Obtained from the Softening Data

Recrystallization

Prestrain 0.12, Strain Rate 2 s^{-1}					
Temperature $^{\circ}\text{C}$	Nb		Nb + B		n^R average
	k^R	n^R	k^R	n^R	
1050	0.017	0.9	0.056	0.91	0.86
1000	0.004	0.8	0.002	0.82	
Prestrain 0.25, Strain Rate 2 s^{-1}					
Temperature $^{\circ}\text{C}$	Nb		Nb + B		n^R average
	k^R	n^R	k^R	n^R	
1050	0.180	1.00	0.13	0.95	0.95
1000	0.030	0.91	0.07	1.00	
950	0.004	0.85	0.0012	0.99	
Prestrain 0.5, Strain Rate 2 s^{-1}					
Temperature $^{\circ}\text{C}$	Nb		Nb + B		n^R average
	k^R	n^R	k^R	n^R	
1000	0.16	0.91	0.11	0.95	0.90
950	0.04	0.85	0.01	0.91	

The rate coefficient for recrystallization (k^R) was found to vary, as in the recovery case, with temperature and predeformation. k^R can therefore be related to inverse temperature and prestrain by the expression:

$$K^R = A^R(\epsilon) \exp\left(-\frac{Q^R}{RT}\right) \quad (5.13)$$

where the constant A^R again depends on prestrain.

From the plots of Figs. 5.11 and 5.12, the values of the activation energy (Q^R ($Q^R_{Nb} = 509$ KJ/mole, $Q^R_{Nb+B} = 638$ KJ/mole) and A^R were calculated to be

$$\ln A^R_{Nb} = 49.60 \cdot \epsilon_p^{0.08} \quad (5.14)$$

$$\ln A^R_{Nb+B} = 60.30 \cdot \epsilon_p^{0.05} \quad (5.15)$$

The validity of the above empirical expressions was tested for the Nb and Nb + B steels as follows. A test temperature of 1000°C was selected, with predeformations of 0.12, 0.25 and 0.5, and a strain rate of 2 s⁻¹. Equations 5.9 to 5.12 provided the values of the parameters n^r and k^r from which the softening due to recovery x^r ($x^r_{\infty} = 0.25$) was estimated from Equation 5.6. Similarly Equations 5.13 to 5.15 provided the value of the parameter k^R ($n^R \approx 0.9$, see Fig. 5.13(a) for incubation time t_0) and, with the aid of equation 5.7, the softening due to recrystallization X^R ($X^R_{\infty} = 0.75$) was estimated. The total softening is the sum of these two softening components (Eq. 5.8). In Figure 5.13(b), the individual values of X^r and X^R are plotted, as well as the total softening X , and these are compared with the experimental data (open symbols). In addition, from Figs. 5.13(c) and 5.13(d), it can be seen that there is good agreement between the experimental and calculated softening curves.

By means of the above analysis, the progress of static softening for any temperature and for deformation in the range of 0.10 to about 0.60 can be readily estimated.

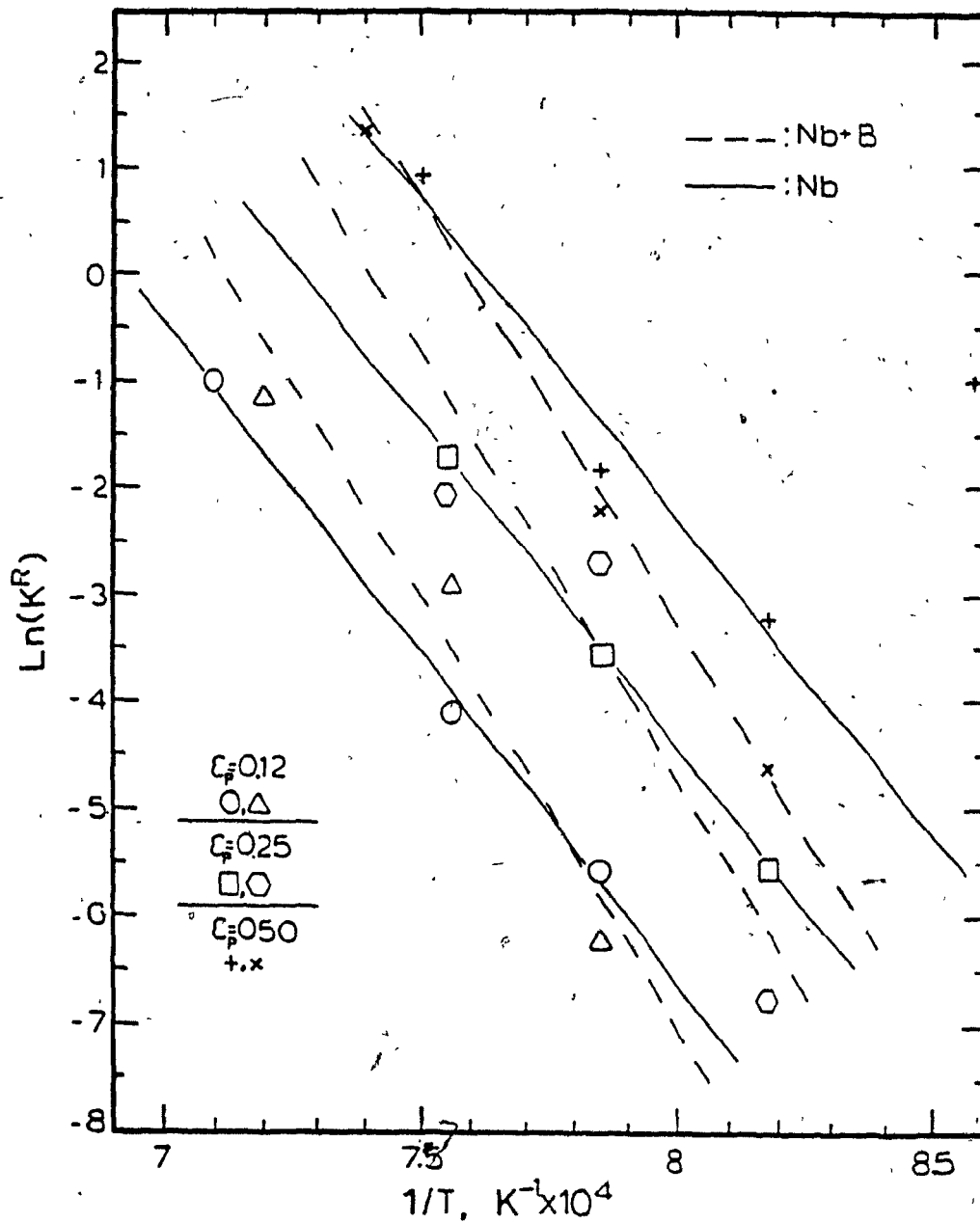


Figure 5.11 Dependence of k^R on temperature at constant prestrain ϵ_p .

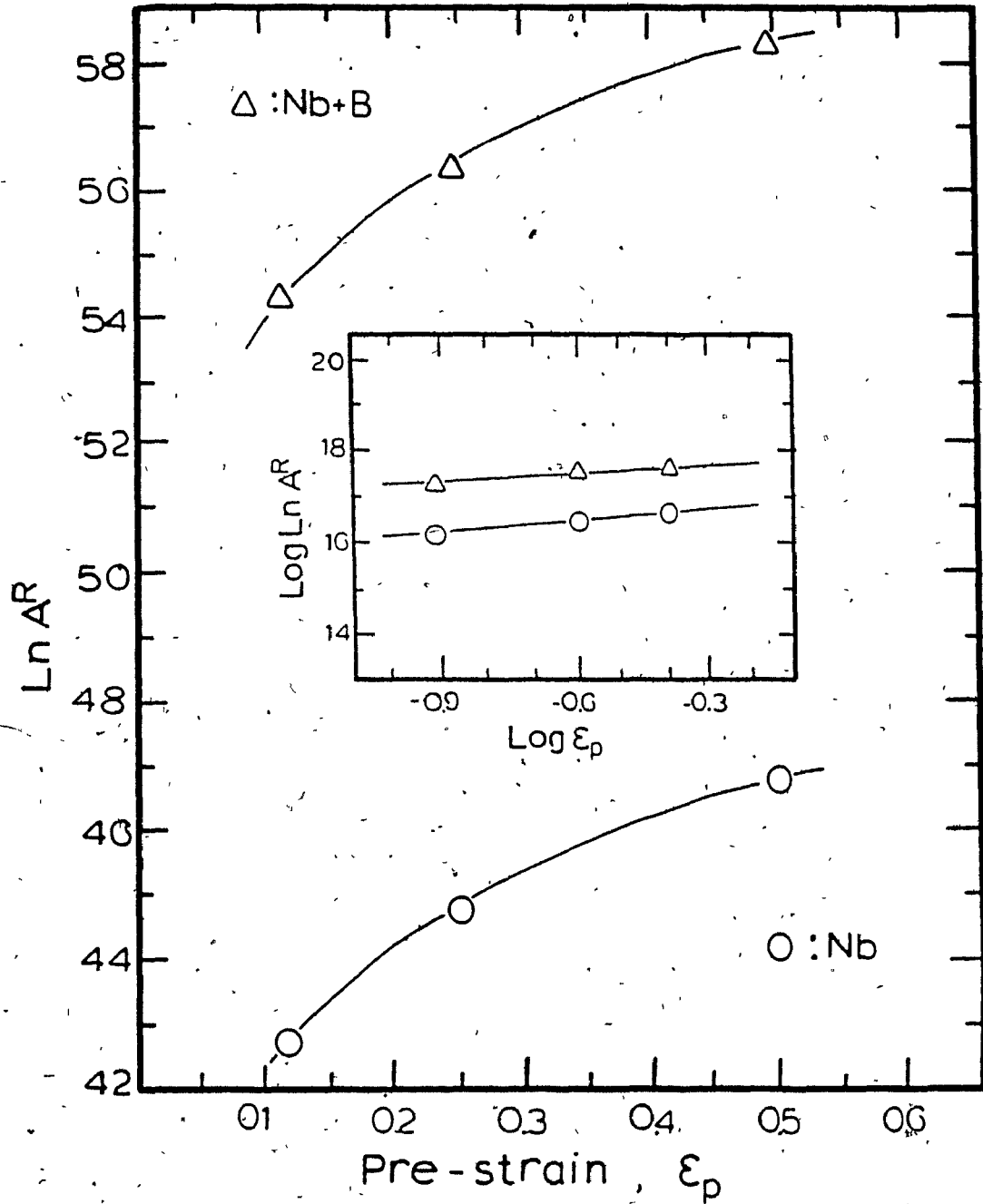


Figure 5.12 Dependence of A^R on prestrain ϵ_p .

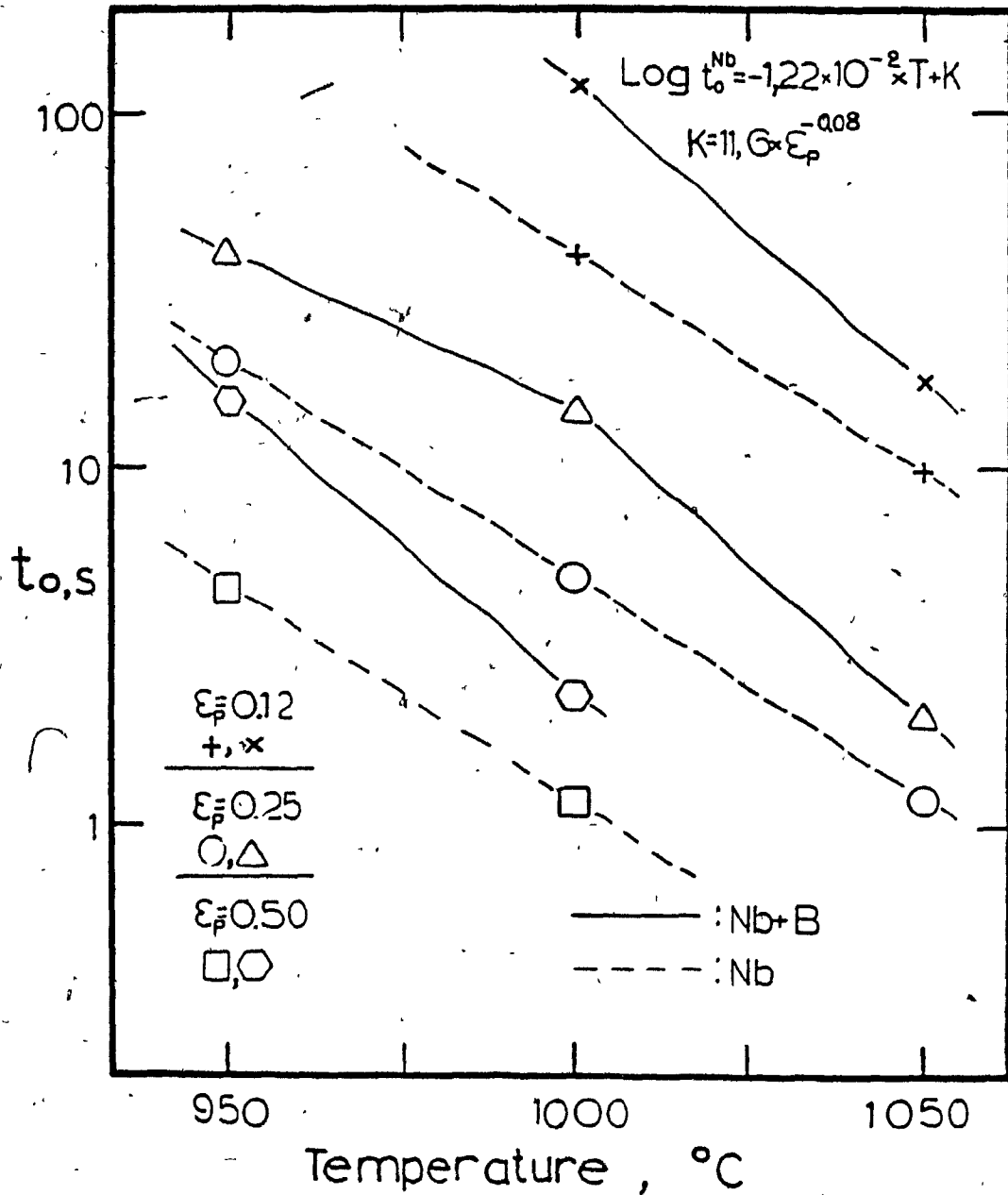


Figure 5.13(a) Dependence of incubation time (t_0) on the temperature for the Nb and Nb + B steels at constant prestrain ϵ_p .

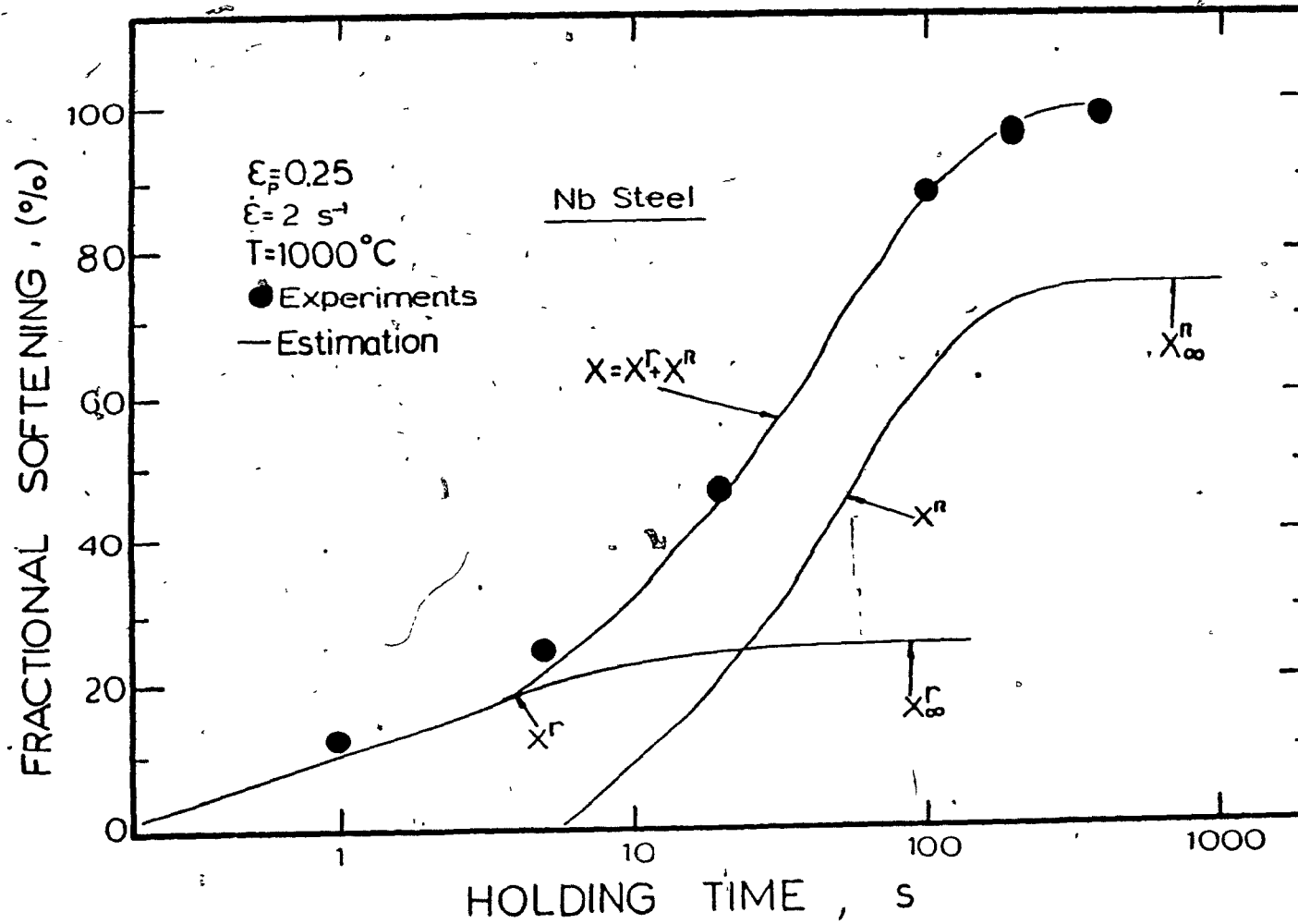


Figure 5.13(b) Comparison of the two-component softening curves and the experimental data points.

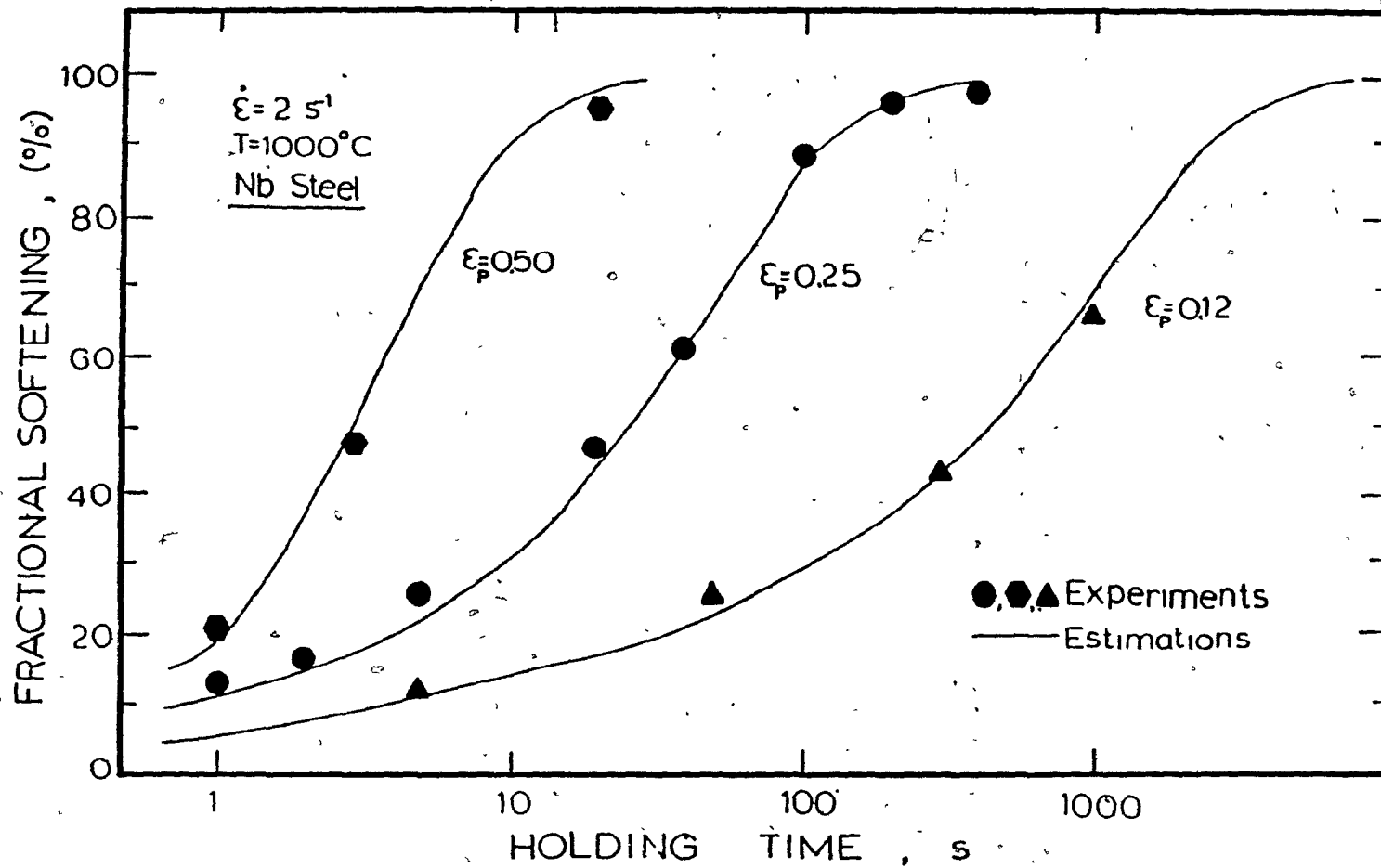


Figure 5.13(c). Comparison of the softening curves derived from the experimental data with the data points themselves (Nb steel).

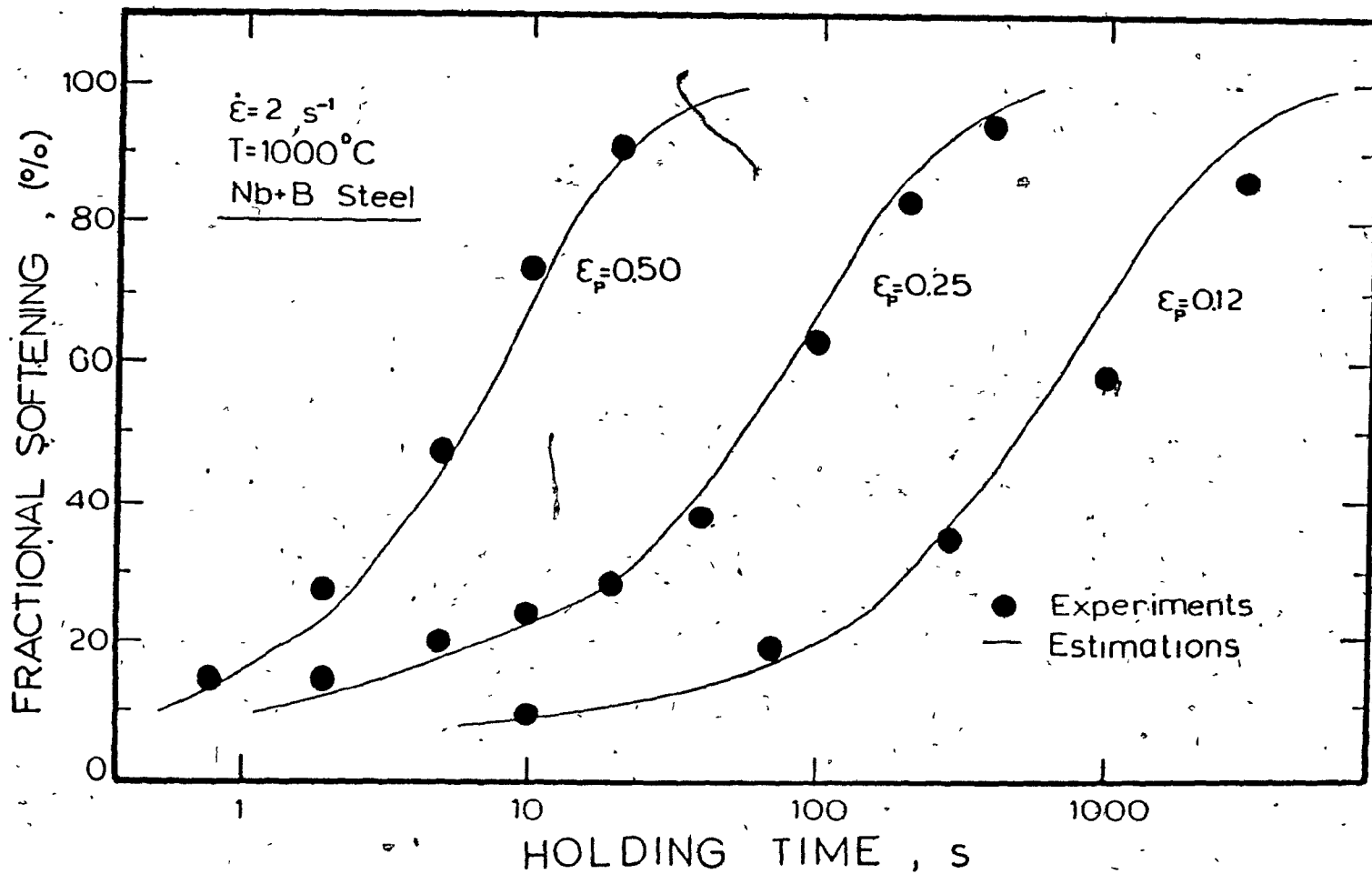


Figure 5.13(d) Comparison of the softening curves derived from the experimental data with the data points themselves (Nb + B steel).

5.1.2 STRAIN DEPENDENCE OF STATIC RECRYSTALLIZATION

The effect of strain on static recrystallization can be seen in Figure 5.14, where the results for the Nb and Nb + B steels held at 1000°C after different prestrains are presented.

Clearly, the process of recrystallization is speeded up as the prestrain is increased from 0.12 to 0.25 to 0.50. The effect of prestraining can also be evaluated from the time for 50% recrystallization (approximately 62.5% softening) $t_{0.5}$. The present data were plotted in this way for several temperatures and the results are shown in Figure 5.15. The points for the various temperatures can be fitted by straight lines and these are approximately parallel.

Estimates of the slopes of these lines give values that vary from - 3.4 to - 4.0. Thus $t_{0.5}$ can be expressed as

$$t_{0.5} = A \varepsilon_p^m \quad (5.16)$$

where A is a constant and m is the slope.

Barraclough and Sellars (96) found a similar effect of strain at small strains, which they reported as

$$t_{0.5} \propto \varepsilon_p^{-4} \quad (5.17)$$

for C-Mn steels.

It should be noted that the above strain dependences are only valid well before the peak in the stress/strain curve is attained. As the peak is approached, the strain dependence decreases and approaches zero by the onset of steady state deformation. Similarly there is a lower limit of strain to which this relationship (Eq. 5.16) is applicable and which is uncertain as the critical strain for static recrystallization has not received systematic study. The data of

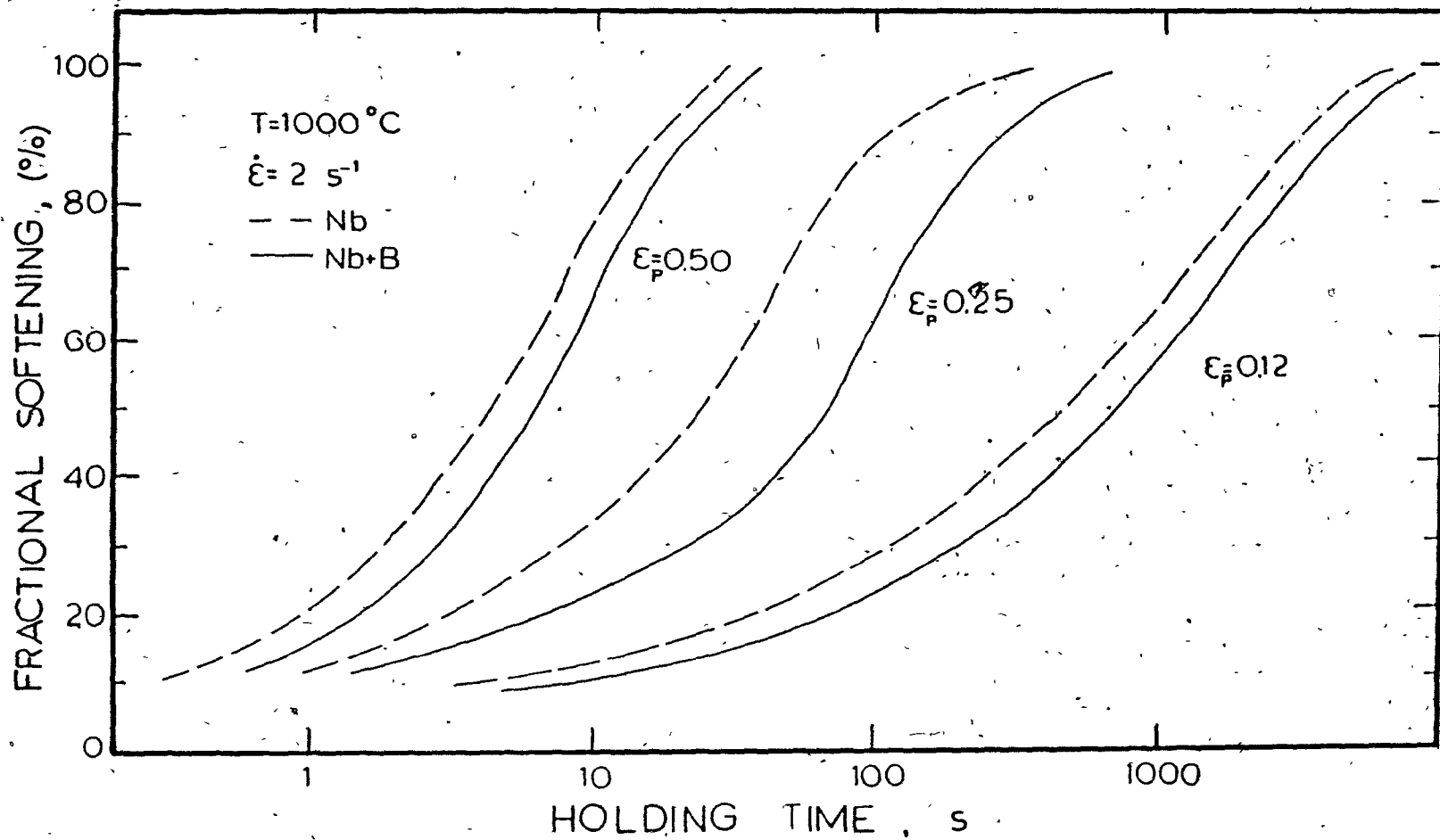


Figure 5.14 Fractional softening vs. holding time at 1000°C for strains of 0.12, 0.25 and 0.5.

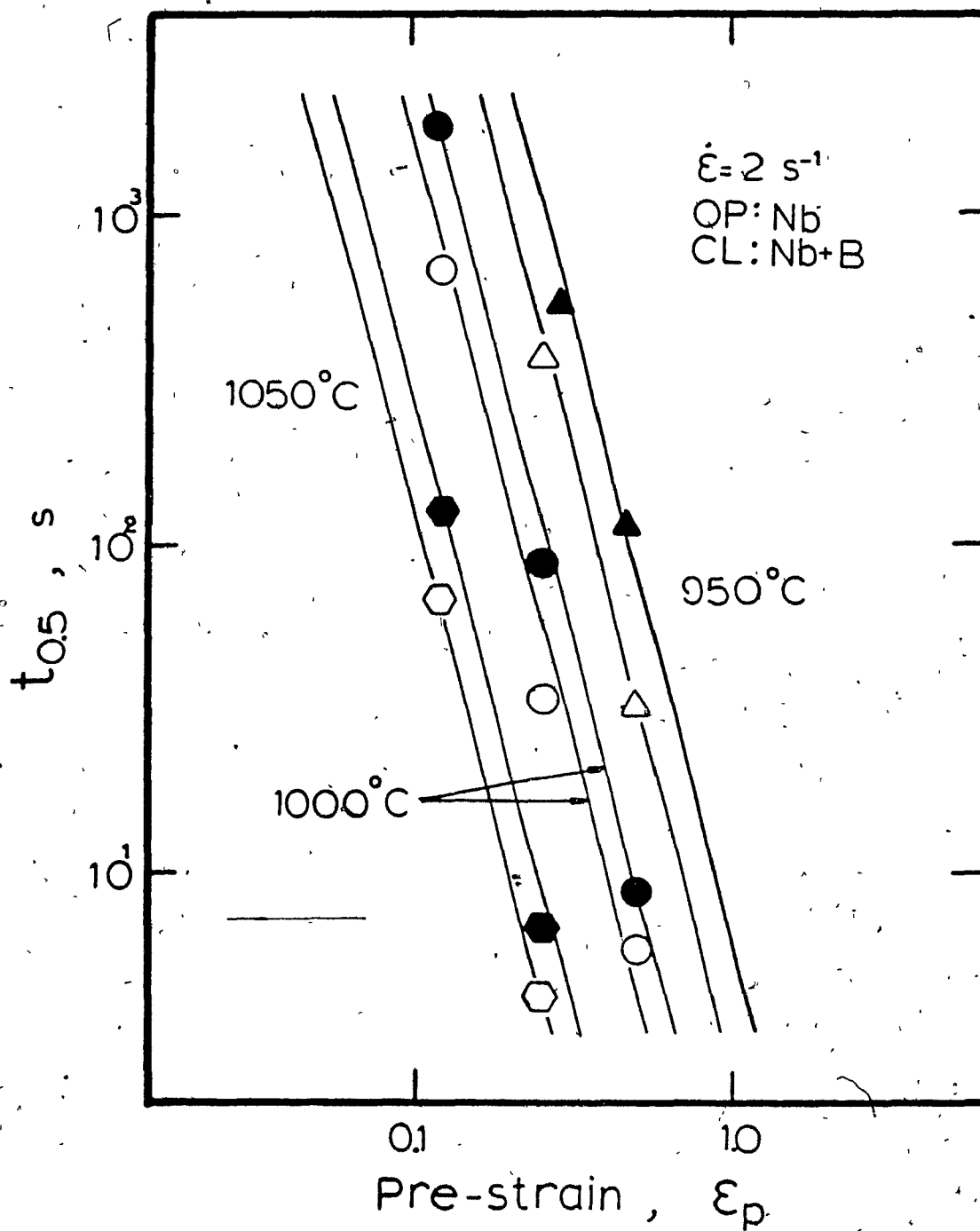


Figure 5.15 Dependence of time for 50% recrystallization (62.5% softening) on the prestrain ϵ_p .

Morrison (97), for example, indicate that it is less than 0.05 for low carbon steel at 950°C whereas the observations of Djaic and Jonas (98) indicate a value greater than 0.055 for high carbon steel at 780°C. The above subject merits further study because low strains are frequently applied in the final passes of plate rolling and these could have significant effects on the final grain size if they are in the vicinity of the critical strain for static recrystallization.

5.1.3 TEMPERATURE DEPENDENCE OF STATIC RECRYSTALLIZATION

Static recrystallization is clearly a thermally activated process and the effect of temperature can be seen from the softening curves presented in Chapter 4 (Figs. 4.5(a), 4.6, 4.7(a) and 4.8). Obviously, as the temperature is increased, the time for the completion of recrystallization is reduced. The temperature dependence can also be described in terms of the time for half recrystallization ($t_{0.5}$), which can be plotted against the inverse absolute temperature. This is done in Figure 5.16 for the plain carbon, boron, niobium and niobium plus boron steels submitted to a prestrain of 0.25. For comparison purposes, the data for the Nb and Nb + B steels tested to prestrains of 0.12 and 0.5 are also plotted. The data points for each steel pertaining to a single prestrain fall on straight lines. The recrystallization data can therefore be expressed as an empirical equation of the form

$$t_{0.5} = A e^{\frac{Q^R}{RT}} \quad (5.18)$$

where R is the gas constant (8.31 J/mole-K) and Q^R an activation energy associated with recrystallization.

The physical significance of Q^R is not completely understood. There is good reason to believe that more than one process is involved in recrystallization, so that Q^R cannot be related to a single simple process. Furthermore, for the 'activation energy' to be strictly valid, the microstructure

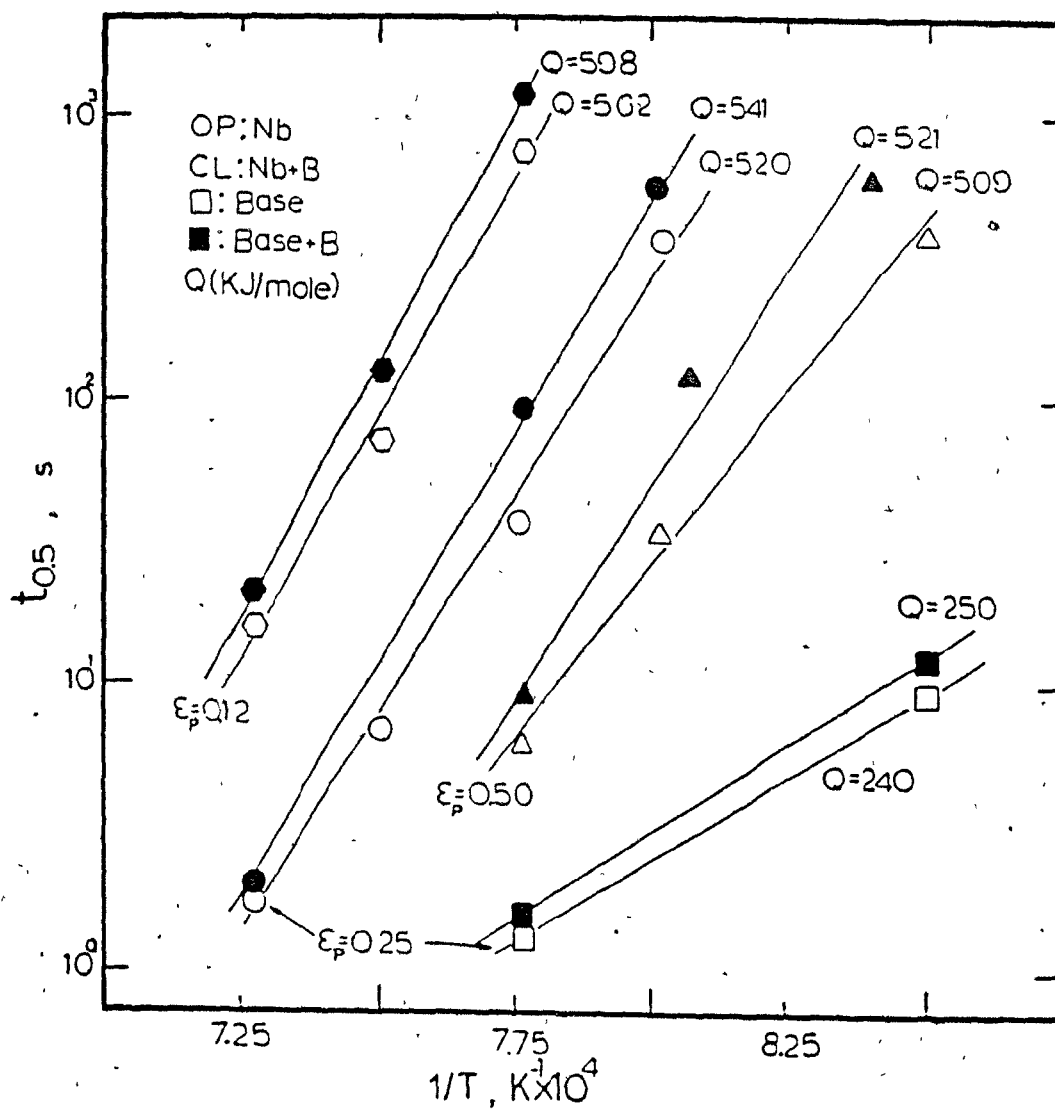


Figure 5.16 Dependence of time for 50% recrystallization (62.5% softening) on the inverse absolute temperature.

(particularly the dislocation density and substructure) must be identical at the start of each experiment carried out over the full temperature range. This can be done by using a different strain rate at each temperature so as to keep the value of $Z = \dot{\epsilon} \exp(Q/RT)$ constant (87). Due to the complexities involved, this approach was not employed in the present investigation. It is best, therefore, to consider the measured recrystallization activation energy as an empirical constant the magnitude of which simply characterizes the ease of recrystallization. Average values of the activation energies determined in the present experiments (slopes of the lines in Fig. 5.16) are presented in Table 5.3. It can be seen that the activation energy increases from 240 for the base steel to 541 KJ/mole for the Nb + B steel when deformed to $\epsilon_p = 0.25$. The addition of boron to the base steel has a very small effect on Q^R , while that of Nb raises it by more than a factor of two.

TABLE 5.3 - Measured Activation Energies for Static Recrystallization (KJ/mole)

Prestrain	Base	B	Nb	Nb + B	Strain Rate (s ⁻¹)
0.12	—	—	562	598	2
0.25	240	250	520	541	2
0.5	—	—	509	521	2

The activation energy for the base steel is somewhat smaller than a previously reported value (272 KJ/mole) (99), but this can be attributed in part to the smaller initial grain sizes used in this work, which are in turn linked with the influence of the TiN particles which are present during reheating.

Finally, when the predeformation is increased from 0.12 to 0.5, the activation energies for the Nb and Nb + B steels decrease from 562 to 509 and

598 to 521 KJ/mole, respectively. This is accounted for most simply by the increase in the driving force with increased prestrain.

5.1.4 STATIC RECRYSTALLIZATION-TIME-TEMPERATURE (RTT) CURVES

The construction of RTT diagrams is very important because they provide information useful to industrial metallurgists about the start and the end of recrystallization.

To signify the start and finish of static recrystallization at each temperature, the amounts of 30 and 90% softening have been selected from the softening curves presented in Chapter 4. The recrystallization start (R_s) and finish (R_f) times can be seen in Figures 5.17 and 5.18 displayed as functions of the holding temperature. Clearly, the single addition of boron to the plain carbon steel retards the start and finish of recrystallization, but only by a small amount. The addition of Nb produces a large retardation in both the R_s and R_f times and the above finding is, of course, in general agreement with many observations in the literature. The combined addition of Nb and B produces the greatest retardations, and these are larger than the sum of the individual retardations attributable to each element. Furthermore, the relative difference between the Nb and Nb + B steel first increases as the temperature is decreased, reaches a maximum, and then decreases again. The location of this "knee" depends on the predeformation condition, but it has nothing to do with the process of precipitation which is discussed in more detail below. Nevertheless, the precipitation of NbC does take place at lower temperatures, as was demonstrated in Chapter 4, and the dashed lines in Figures 5.17 and 5.18 indicate the recrystallization kinetics expected in the absence of second phase particles.

5.1.5 INFLUENCE OF BORON ON CARBIDE PRECIPITATION

In a literature review by Thomas and Henry (55) on austenitic steels, it was demonstrated that the presence of boron modifies the characteristics of

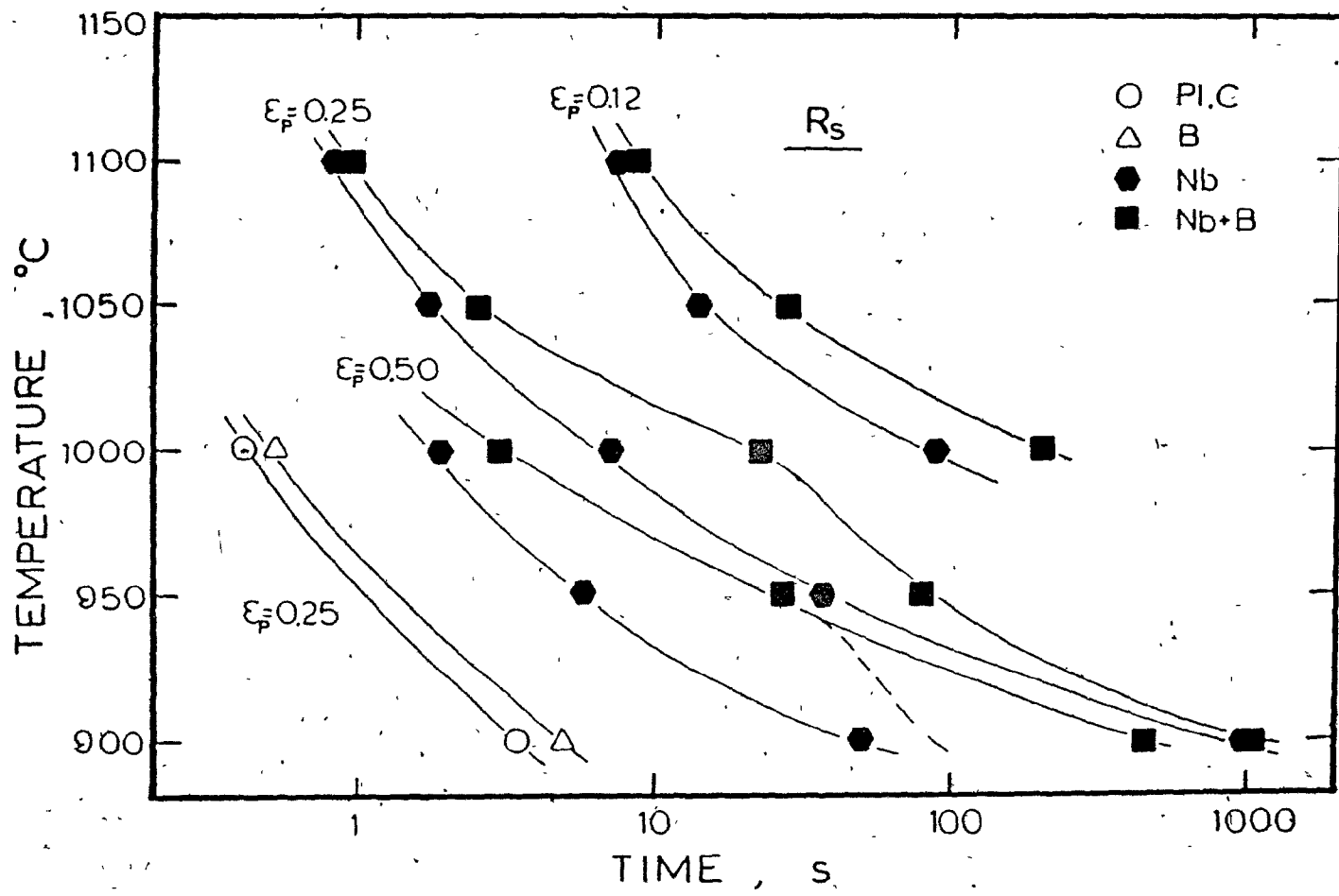


Figure 5.17 Recrystallization start times (R_s) as a function of temperature.

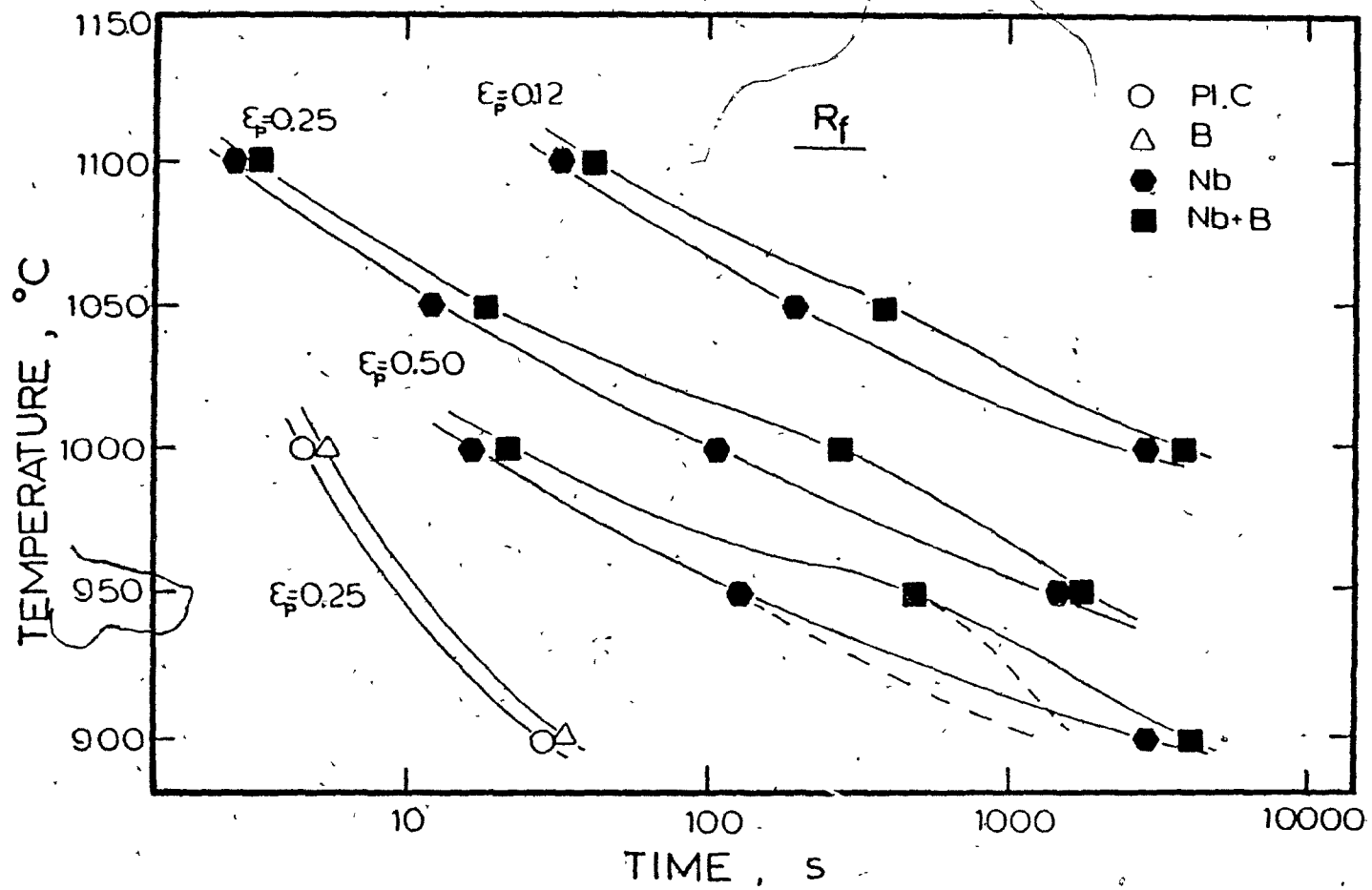


Figure 5.18 Recrystallization finish times (R_f) as a function of temperature.

both grain boundary and intracrystalline carbide precipitation. The modification they described consisted of changes in the number and spatial distribution of the particles. There were also indications of accelerated precipitation, suggesting that boron intervenes in the nucleation process. More recently, clear evidence has been published that boron segregates at the grain boundaries prior to or simultaneously with carbide precipitation and that there is boron present within the carbides (100). It is therefore of interest to examine the role of boron in modifying the various factors that control the nucleation of carbides.

One possible way in which boron may influence nucleation is by lowering the activity of carbon in the matrix or in the precipitate (101). The latter would decrease the chemical free energy term in the nucleation activation energy for precipitation. The influence of small quantities of boron on the surface energy term do not appear to be very plausible and the estimated change in austenite grain boundary energy due to presence of boron is indeed very small (18). The most interesting possible explanation comes from the indication that boron reacts with vacancies to form boron-vacancy complexes (45, 46). These are faster diffusing species than single vacancies and can therefore reach the nucleation site more quickly. The enriched supply of vacancies at the nucleus can then accelerate the process of nucleation.

If the above proposal is correct, experimental variables such as the amount of prior deformation, the preceding heat treatment and cooling rate which strongly influence the number of vacancies and consequently of boron-vacancy pairs, will have a large effect on the morphology and kinetics of precipitation.

5.1.6 THE ROLE OF BORON IN THE SOFTENING PROCESS

The present investigation has shown that single B addition to a base steel is of only small significance in retarding austenite softening, while the combined addition of Nb and B leads, through a synergistic effect, to large retardations. Furthermore, the relative difference in retardation between such Nb and Nb + B steels is not constant, but depends on the amount and

temperature of the deformation. The above observations lead to the following questions: (i) In what state (as precipitates, clusters or in solid solution) are the solute atoms when they retard the softening process? (ii) What is the mechanism responsible for the synergistic action? (iii) Why does the relative difference in retardation between the Nb and Nb + B steels depend on the prior deformation conditions?

Well substantiated answers to the above questions are difficult to provide; nevertheless, some explanations consistent with the results of the present investigation and with results reported in the literature will now be examined in turn.

5.1.6.1 State of Solute Atoms During Retardation of the Softening Process

It is well known that foreign atoms within the host material can be found in three different states, depending on the composition and experimental conditions. The first state involves foreign atoms which combine to form second phase particles or precipitates. These particles are able to retard or even arrest recrystallization completely if they are fine enough (less than 100 Å) and are finely dispersed within the matrix. Under these conditions they exert drag forces on the moving grain boundaries which oppose the driving force. If, on the other hand, they are sufficiently coarse, they have no effect at all.

The second state has to do with "associated solutes", a concept introduced by W.C. Leslie (102). According to this idea, two or more solutes, which display a strong attraction for each other, can be associated in solution, forming a type of cluster. Such clusters can interact strongly with dislocations, retarding recrystallization or strengthening the material to a greater degree than in the absence of such aggregation. The relevant solute may be any combination of interstitial or substitutional elements and the results are most pronounced when these are present in very low concentrations.

Finally, the third state is that of solid solution, where the solutes remain dissolved in the lattice of the material. Solute atoms can also interact with dislocations and grain boundaries, causing both solute strengthening as well as

the retardation of recrystallization, as discussed in the literature review chapter.

The possible presence of precipitates was investigated as described above with the aid of carbon extraction replicas. For this purpose Nb + B samples were austenitized at 1100°C for 15 minutes, deformed at 1000°C at a strain rate of 2 s⁻¹ to a strain of 0.25 and then quenched immediately after deformation. A second set of samples was held isothermally for 100 seconds after deformation prior to quenching (see Figs. 4.15 and 4.16). The examination of these replicas by electron microscopy revealed the presence of coarse TiN and MnS particles which were judged to have formed at high temperatures. Because of their size and distribution, they were considered not to be able to interfere with recrystallization.

Although verification of the existence (or absence) of associated solutes is difficult, the results of the present investigation suggest that the above state did not play a role for two reasons. The first involves a comparison of the prestraining parts of the Nb and Nb + B flow curves (Figs. 4.3 and 4.4). If ordering or clustering had taken place as a result of the addition of boron to the Nb steel, higher work hardening rates and stress levels would be expected to be displayed by the Nb + B steel. The second argument is based on a comparison of the softening curves presented in Chapter 4 (i.e. Fig. 4.5(a)). Clearly, as the test temperature is decreased from 1100 to 900°C, the relative difference in retardation first increases and then decreases. If clustering is taking place, the relative difference would be expected to increase *monotonically*; this is because the undercooling or driving force for precipitation (and therefore for clustering as well) should increase as the temperature is decreased. In other words, more clustering should take place at 950 than at 1000°C, and consequently, the relative difference in softening should be greater at 950 than at 1000°C.

Two of the three possible states of foreign atoms can therefore be rejected, leading us to the conclusion that the foreign atoms are most likely to be acting as solutes in the temperature range of interest (1100 to 950°C).

5.1.6.2 The Solute Drag Theory and Substitutional Solutes

An explanation of the results of the present investigation requires a more detailed familiarity with the solute drag theory than can be gained from the literature review presented above. This model will therefore be examined more closely below. According to the theory, the drag exerted on a moving boundary by the atmosphere of solute atoms trailing it is not a linear function of its velocity. Instead, the drag first increases with the velocity, reaches a maximum and then decreases. When the velocity of the grain boundary is relatively high, the solute atoms can no longer follow the boundary. It breaks away at this point and recrystallization occurs very quickly, almost as fast as in a pure material. This theory was originally developed for pure materials with small amounts of a single impurity. However, here we will assume that it is at least qualitatively valid in the present types of materials.

The mathematical formulation of the drag force P_i as a function of the velocity V is given by Cahn as:

$$P_i = \frac{N_v C_o}{KTV} \int_{-\infty}^{\infty} E^2(x) D(x) dx \quad (5.19)$$

and

$$P_i = 4 N_v C_o VKT \int_{-\infty}^{\infty} \frac{\sinh^2[E(x)/2KT]}{D(x)} dx \quad (5.20)$$

(the symbols N_v , C_o , K , T , $E(x)$ and $D(x)$ have been defined in section 2.4) for the high and low velocity regions respectively. In the high velocity region ($V\beta > \sqrt{3}$ in Figure 2.10), the drag increases with the diffusivity of the impurity; in the low velocity region ($V\beta < \frac{1}{3}$ in Figure 2.10), by contrast, the opposite is true. In both cases, the drag force increases rapidly with the interaction energy $E(x)$.

A critical question at this point is the following. How is it determined whether a specific problem involves high or low drag forces or velocities? For this purpose, we must rely on the experimental results of Aust and Rutter (82) obtained on lead doped with silver, gold and tin. They noted that the faster diffusing species exerted the greater drag. Consequently, it can be concluded that they were dealing, according to Eq. 5.19, with the high velocity extreme. Furthermore, John Cahn (83) has also suggested that almost all work involving the recrystallization of plastically strained crystals is comfortably in the high driving force (high velocity) extreme.

In the case of the recrystallization of hot worked HSLA steels, most specifically when precipitation is not taking place, it has been reported (103, 104) that the retarding ability of the main microalloying elements (Nb, Ti, Mo, V, Mn, Cr, Ni) per atomic percent at 900°C increases in the following ascending order: Ni < Cr < Mn < V < Mo < Ti < Nb. The impurity diffusion parameters of the above elements in FCC iron are presented in Table 5.4. Their diffusivities at 900, 1000 and 1100°C are listed in Table 5.5. It is of considerable interest that the order of the diffusivities of these solute elements follows the order of their retarding abilities. This observation leads us to two important conclusions: (i) first that if the solute drag theory proposed by Cahn is valid for pure metals, it is likely to be at least qualitatively applicable to HSLA steels at high temperatures; (ii) second, that the driving forces and velocities of the recrystallizing grains lie in the high velocity regime.

5.1.6.2.1 A Qualitative Look at Solute Drag

The above two equations for the drag can be combined, as described in Chapter 2, to produce a more comprehensive expression valid for all velocities. This is:

$$P_t = \frac{\alpha VC_o}{1 + \beta^2 V^2} \quad (5.21)$$

TABLE 5.4 - Impurity Diffusion Parameters in γ -Iron

Solute	$D_0(10^{-4} \text{ m}^2/\text{s})$	$Q(\text{KJ/mole})$	References
Fe	0.89	291.3	105
Ni	0.108	273	106-109
Cr	0.169	263.9	110, 111
Mn	0.178	264	112, 113
V	0.28	264	114
Mo	0.036	239.8	111, 115, 116
Ti	0.15	251	117
Nb	5.6	286	118, 119

TABLE 5.5 - Impurity Diffusivities in γ -Iron

Solute	900°C $\times 10^{-14}(\text{cm}^2/\text{sec})$	1000°C $\times 10^{-13}(\text{cm}^2/\text{sec})$	1100°C $\times 10^{-12}(\text{cm}^2/\text{sec})$
Fe	9.35	9.78	7.26
Ni	7.41	6.69	4.38
Cr	29.5	24.7	15.2
Mn	30.7	25.8	15.9
V	48.4	40.6	25.0
Mo	74.5	51.4	26.8
Ti	98.4	74.4	41.8
Nb	101.0	101.5	72.7

where

$$\alpha = \frac{N_v (KT)^2 \delta}{E_o D} \left(\sinh \frac{E_o}{KT} - \frac{E_o}{KT} \right) \quad (5.21(a))$$

$$\beta^2 = \frac{\alpha KT \delta}{2 N_v E_o^2 D} \quad (5.21(b))$$

and δ is the grain boundary width (about 5 Å). Note that the constants α and β are inversely proportional to diffusivity D . The value of the interaction energy E_o can be calculated, as shown in section 2.4, from the equation

$$E_o = \frac{4}{3} r_{Fe}^3 G \frac{1 + \sigma}{1 - \sigma} n \quad (5.22)$$

where

$$n = \left| \frac{r_{Fe} - r}{r_{Fe}} \right|$$

$$\sigma_{\gamma\text{-iron}} = 0.286,$$

and

$$G = 8.1 \times 10^4 \left(1 - \frac{0.91(T - 300)}{1810} \right) \text{MPa} \quad (5.23)$$

($\sigma_{\gamma\text{-iron}}$ = Poisson's ratio, G = shear modulus for γ -iron (120) at a given temperature T (K)). The atomic radii (r) for several common alloying elements are listed in Table 5.6.

TABLE 5.6 - Atomic Radii of Common Alloying Elements* (Å) (121)

Element	γ -Fe	Nb	Ti	Al	Mo	V	Mn	Si
Radius	1.274	1.468	1.462	1.432	1.400	1.346	1.312	1.319

*For coordination number 12

By substituting the data presented earlier into the above equations, the drag force versus normalized velocity relation was obtained for pure iron doped with the various addition agents in turn. The set of relations is presented in Figure 5.19(a). Furthermore, in Fig. 5.19(b), the drag force versus velocity profiles can be seen (i.e. without normalization). The values of the constants α and β and of the interaction energies E_0 employed are given in Table 5.7 as calculated from Eqs. 5.21(a) to 5.23. For these results to apply to steel in a qualitative way, it must be assumed at this point that the responses of pure iron doped with a single impurity and of the present base steel doped with the same element are similar. The kinetics of recrystallization of the pure iron will of course be much faster than those of the base steel under the same deformation conditions.

Bearing in mind the above assumptions and qualifications, the profiles of Figure 5.19 show that the addition of Nb to steel should produce a much higher drag force (and therefore retard recrystallization to a greater degree) than the addition of the same concentration of V.

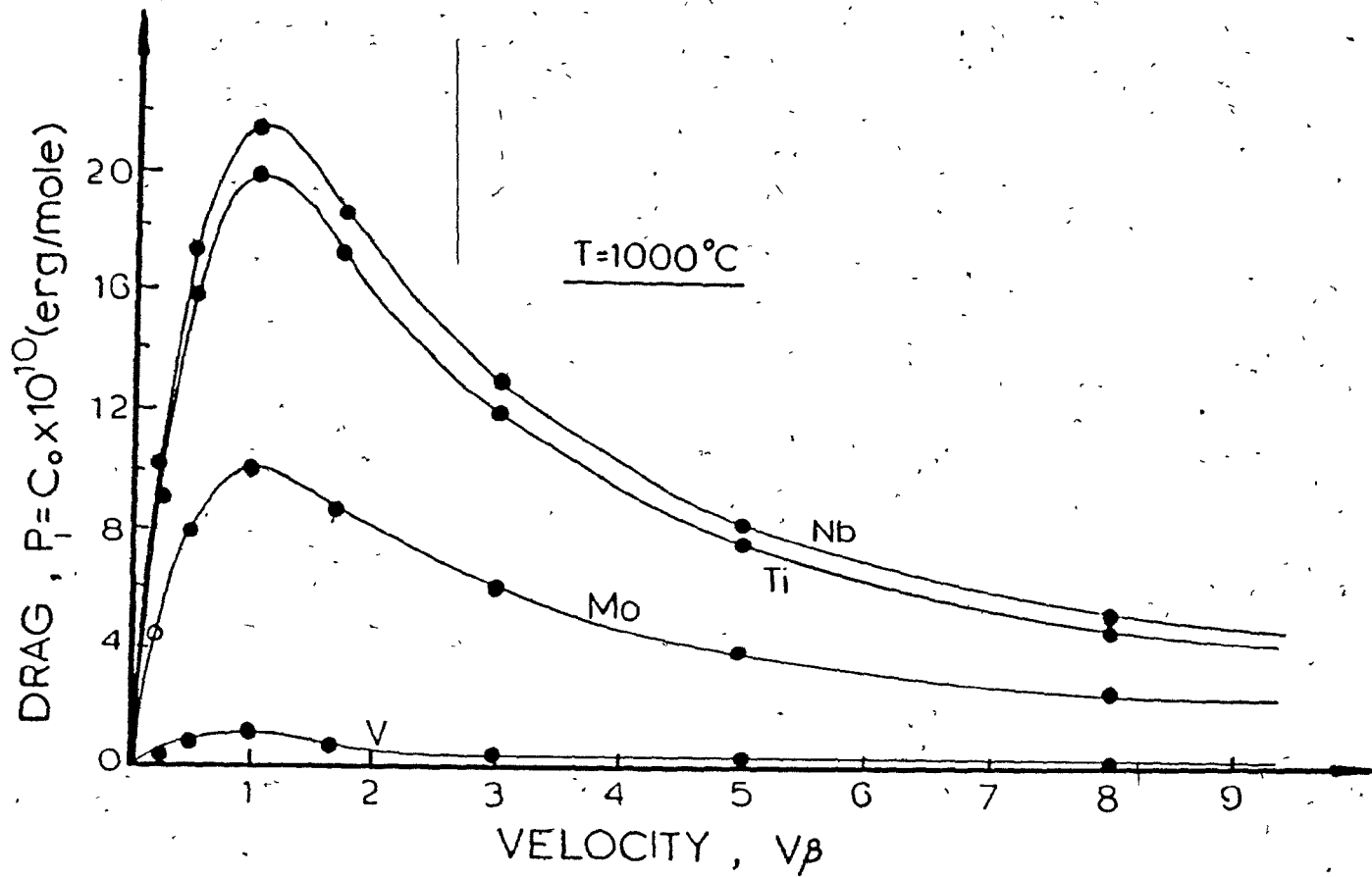


Figure 5.19(a) Impurity drag vs. normalized velocity profiles for various elements in γ -iron.

TABLE 5.7 - Calculated Values of α , β and E_0 at 1000°C

Solute	α (erg sec/mole cm)	β (sec/cm)	E_0 (erg)
Nb	6.43×10^{14}	1.5×10^3	3.05×10^{-13}
Ti	8.32×10^{14}	2.1×10^3	2.99×10^{-13}
Mo	5.83×10^{14}	2.9×10^3	2.03×10^{-13}
V	2.5×10^{15}	1.45×10^5	1.14×10^{-14}
Mn	1.21×10^{15}	1.82×10^5	6.10×10^{-15}

This is, of course, consistent with a great deal of experimental observations. The magnitude of the maximum drag force depends only on the interaction energy E_0 , while the *position* of the maximum is a function of the interaction energy and diffusivity D of the alloying elements. An increase in interaction energy and/or diffusivity (both increase with size of the substitutional element) will move the drag force versus velocity profile towards the region of higher velocity (Fig. 5.19(b)). For elements which are similar in size, e.g. Nb and Ti, the faster diffusing element (Nb) is expected to exert the larger drag.

The effect of temperature on the drag force vs. velocity curve for Nb can be seen in Fig. 5.20. As the temperature is increased from 1000 to 1100°C, the profile shifts downwards to lower drag forces, but does not change shape. This suggests that, as the temperature is increased, the velocity of a grain boundary moving under a constant driving force will increase, a prediction which again is well documented experimentally.

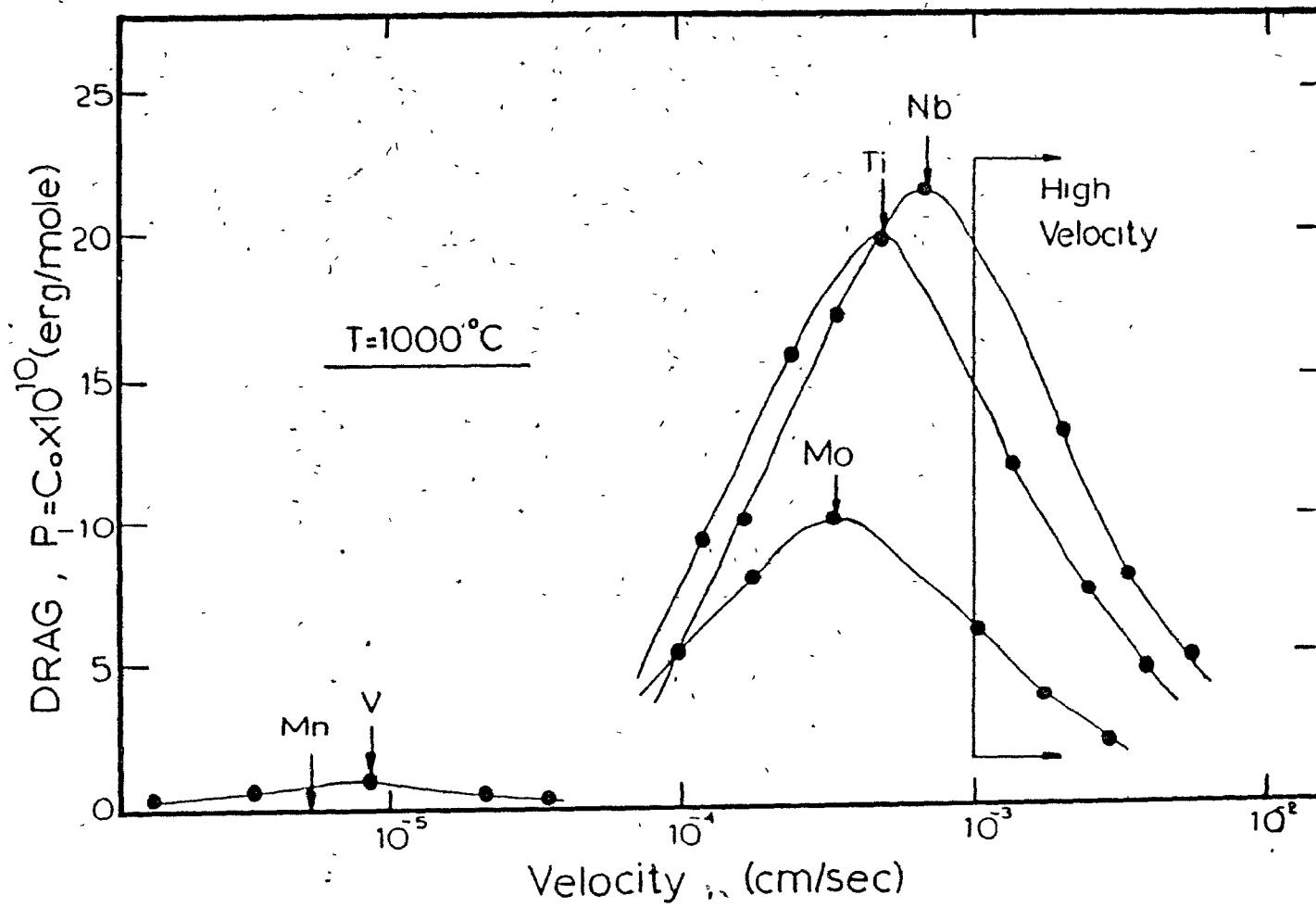


Figure 5.19(b) Impurity drag vs. velocity profiles for various elements in γ -iron.

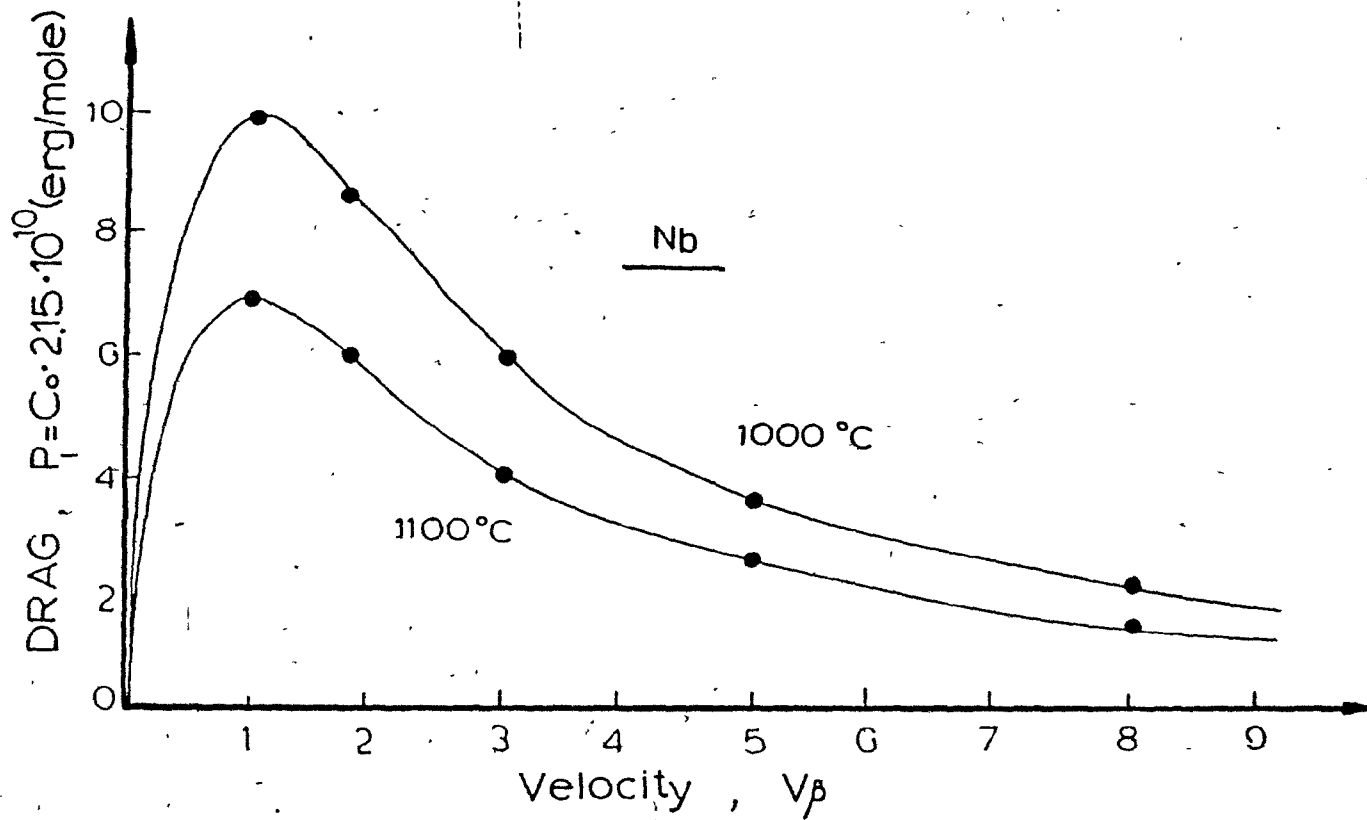


Figure 5.20 Impurity drag vs. normalized velocity profiles for Nb at 1000 and 1100°C.

5.1.6.2.2 The Effect of the Type of $E(x)$ and $D(x)$ Profiles on the Magnitude of Solute Drag

At this point of the discussion, two important remarks concerning the interaction energy E_0 and the diffusivity D must be emphasized. First, the calculation of the interaction energy is based solely on the difference in atomic radius and the possible influence of differences in valence (i.e. of electronic structure) is completely ignored, as is the effect of differences in elastic modulus. Indeed, it has been suggested in the literature (79, 80) that these other properties may also contribute to the different influences of the various impurities on the increase in the recrystallization temperature that they cause. Second, so far in the present analysis, matrix impurity diffusion (DM) was considered as the dominant transport mechanism, mainly because the foreign atoms remain behind the boundary and move in the matrix towards the boundary. However, it is now known that grain boundary diffusion (DGB) becomes an important transport mechanism for stationary grain boundaries when $DGB/DM > \text{grain diameter/grain boundary width}$ (122). Also it has been shown by Hoffman and Turnbull (123) that the two contributions to the total diffusion flux are equal when the grain sizes and ratios of DGB to DM have the values shown in Table 5.8.

TABLE 5.8 - Relationship Between Ratio of Matrix DM and Boundary DGB Diffusion Coefficients and Grain Size at Which Equal Amounts of Diffusion Take Place by the Two Processes (123)

DGB/DM	Grain Size (μm)
10^6	2×10^3
10^5	1.4×10
10^4	2.1×10^{-1}
10^3	$< 10^{-2}$

From the diffusivity data in references (19, 105), the ratio D_{GB}/D_M for Fe at 1000°C was found to be approximately equal to 6×10^5 : ($D_{GB}/D_M \approx 6 \times 10^5$). It is also suggested in reference (122) that the activation energy for diffusion along the grain boundaries is approximately one half that through the matrix; thus by using the diffusion data for Nb given in Table 5.4, it can be shown that $D_{GB}/D_M \approx 7.4 \times 10^5$.

Because these two estimated ratios were independently derived and have similar values, it seems reasonable to consider that the ratio D_{GB}/D_M is approximately equal to 6×10^5 . Now the metallographically determined grain size for this temperature is about $40 \mu\text{m}$. Consequently, from the values presented in Table 5.8, grain boundary diffusion can be calculated to be important with regard to stationary grain boundaries and therefore also important for the case of moving grain boundaries (122). As a result, we conclude that the grain boundary diffusivities must be taken into consideration for the calculation of the drag force vs. velocity profiles. This was done in the present investigation for the assumed profiles shown in Figure 5.21 (124) (case I has already been considered). These profiles are only defined for positive x , but it should be born in mind that they are symmetric about the grain boundary center. The interaction potentials were arbitrarily chosen as negative, indicating the adsorption of impurity atoms at the boundaries. The equations for calculating α and α/β^2 are given for each case in Table 5.9 and the values for α , β and $P_{i \max}$ estimated in this way by the present author for Nb and Mo at 1000°C are shown in Tables 5.10 and 5.11.

It is evident from these results that the calculated drag depends very much on the type of energy $E(x)$ and diffusivity $D(x)$ profile used. The interesting point arising from the comparison of the $P_{i \max}$ values in Tables 5.10 and 5.11 is that the Nb drag forces are always higher than the corresponding values for Mo showing once again that Nb is expected to be more effective in retarding recrystallization than Mo.

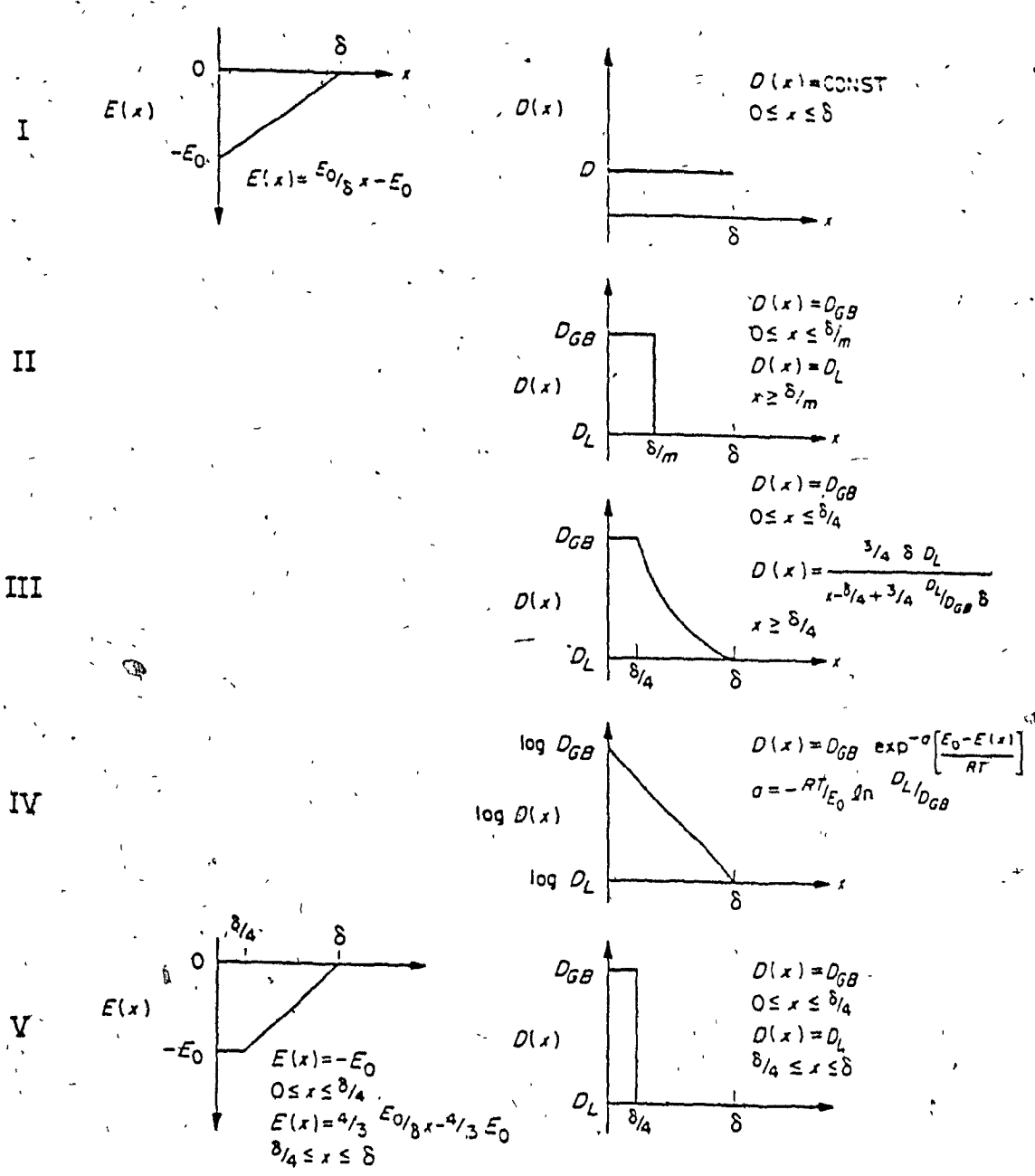


Figure 5.21 The interaction energy profiles $E(x)$ and diffusivity profiles $D(x)$ used in calculating the impurity drag parameters α and α/β^2 in Table 5.9.

TABLE 5.9 - Theoretical Equations for α and α/β^2

Profile Combination I	
$\alpha = \frac{4RT}{V_m} \frac{\delta}{D} \frac{RT}{E_0} \left[\sinh \frac{E_0}{RT} - \frac{E_0}{RT} \right]$	(A1)
$\frac{\alpha}{\beta^2} = 2 \frac{RT}{V_m} \frac{D}{\delta} \left(\frac{E_0}{RT} \right)^2$	(A2)
Profile Combination II	
$\alpha = \frac{4RT}{V_m} \frac{\delta}{D_L} \frac{RT}{E_0} \left[\sinh \frac{E_0}{RT} \left(1 - \frac{1}{m} \right) - \frac{E_0}{RT} \left(1 - \frac{1}{m} \right) + \frac{D_L}{D_{GB}} \left(\sinh \frac{E_0}{RT} - \frac{E_0}{RT} \right) \right]$	(A3)
$\frac{\alpha}{\beta^2} = \frac{2RT}{V_m} \left(\frac{E_0}{RT} \right)^2 \frac{1}{\delta} \left(\frac{D_{GB}}{m} + \frac{D_L}{m-1} \right)$	(A4)
Profile Combination III	
$\alpha = \frac{2RT}{V_m} \left\{ \frac{\delta}{4D_{GB}} \frac{RT}{E_0} \left(\sinh \frac{E_0}{RT} - \sinh \frac{3}{4} \frac{E_0}{RT} - \frac{E_0}{4RT} \right) + \frac{2}{3} \frac{\delta}{D_L} \left(\frac{RT}{E_0} \right)^2 \left[\cosh \frac{3}{4} \frac{E_0}{RT} - 1 - \frac{9}{32} \left(\frac{E_0}{RT} \right)^2 \right] \right\}$	(A5)
$\frac{\alpha}{\beta^2} = \frac{1}{2} \frac{RT}{V_m} \left(\frac{E_0}{RT} \right)^2 \frac{D_{GB} + 3D_L \log D_{GB}/D_L}{\delta}$	(A6)
Profile Combination IV	
$\alpha = \frac{4RT}{V_m} \frac{RT}{E_0} \frac{\delta}{D_L} \frac{1}{a^2 - a}$	(A7)
where $a = -(RT/E_0) \ln(D_L/D_{GB})$.	
$\frac{\alpha}{\beta^2} = \frac{2RT}{V_m} \frac{E_0}{RT} \frac{D_{GB}}{\delta} \frac{1}{a} \left(1 - \frac{D_L}{D_{GB}} \right)$	(A8)
Profile Combination V	
$\alpha = \frac{2RT}{V_m} \left\{ \frac{\delta}{D_{GB}} \sinh^2 \frac{E_0}{2RT} + \frac{3}{2} \frac{RT}{E_0} \frac{\delta}{D_L} \left(\sinh \frac{E_0}{RT} - \frac{E_0}{RT} \right) \right\}$	(A9)
$\frac{\alpha}{\beta^2} = \frac{3}{2} \frac{RT}{V_m} \left(\frac{E_0}{RT} \right)^2 \frac{D_L}{\delta}$	(A10)

TABLE 5.10 - Calculated Values of α , β and $P_{i \max}$ for Nb at 1000°C

Profile Combination	α (erg sec/mole cm)	β (sec/cm)	$P_{i \max}$ (erg/mole)
I	6.43×10^{14}	1.50×10^3	$C_0 \cdot 2.14 \times 10^{11}$
III	6.15×10^{13}	1.21×10^0	$C_0 \cdot 2.53 \times 10^{13}$
IV	4.28×10^{12}	0.56×10^0	$C_0 \cdot 3.8 \times 10^{12}$
V	1.92×10^{15}	3.25×10^3	$C_0 \cdot 2.95 \times 10^{11}$

TABLE 5.11 - Calculated Values of α , β and $P_{i \max}$ for Mo at 1000°C

Profile Combination	α (erg sec/mole cm)	β (sec/cm)	$P_{i \max}$ (erg/mole)
I	5.83×10^{14}	2.9×10^3	$C_0 \cdot 1.00 \times 10^{11}$
III	6.03×10^{13}	6.92×10^0	$C_0 \cdot 4.35 \times 10^{12}$
IV	7.9×10^{12}	4.22×10^0	$C_0 \cdot 9.36 \times 10^{11}$
V	1.52×10^{15}	5.8×10^3	$C_0 \cdot 1.31 \times 10^{11}$

5.1.6.2.3 The Hillert and Sundman Model of Solute Drag

In more recent years, Hillert and Sundman (125) have developed a still more detailed approach to the solute drag force in which the integral dissipation of free energy due to solute diffusion within the moving boundary is equated to the drag. In doing so, they derived the drag force as a function of velocity V as:

$$P_t = -\frac{1}{V} \int_{-\infty}^{\infty} J_B \frac{d(G_B - G_A)}{dy} dy \quad (5.24)$$

where $d(G_B - G_A)/dy$ is the driving force for interdiffusion when a solute B diffuses in a solvent A, G_A and G_B are the chemical potentials of solvent and solute, respectively, and $J_B = -J_A$ are the fluxes. Furthermore, they developed the following two approximate equations for the low and high velocities:

$$P_t = \frac{RTV}{V_m} x_A^0 x_B^0 \int_{-\infty}^{\infty} \frac{1}{D} \left[\exp \Delta^0 G / 2RT - \exp -\frac{\Delta^0 G}{2RT} \right]^2 dy \quad (5.25)$$

and

$$P_t = \frac{x_A^0 x_B^0}{VRTV_m} \int_{-\infty}^{\infty} D \left[d \frac{\Delta^0 G}{dy} \right]^2 dy \quad (5.26)$$

where x_A^0 , x_B^0 can be identified as the matrix and alloy compositions far from the boundary, V_m is the unit volume element and $d\Delta^0 G/dy = d(G_B - G_A)/dy - RT/x_A x_B \cdot dx_B/dy$.

Equations 5.25 and 5.26 are similar to the equations proposed by Cahn (Eqs. 5.19 and 5.20), but they have the following advantages: (a) they can easily

be applied to the whole range of compositions in a binary system; (b) they can be applied to phase transformations as well as to the migration of grain boundaries in a single phase material; (c) they lead to numerical estimations of the magnitude of the solute drag because the integrand is everywhere positive; and (d) the analysis provides information on where the free energy is dissipated in the boundary. For their treatment of grain boundary drag, Hillert and Sundman chose the solute-boundary interaction potential profiles shown in Fig. 5.22. Their calculations were carried out with various values for the diffusivity in the central region of the grain boundary relative to the bulk diffusivity. The logarithm of the ratio of diffusivities was varied linearly through the two side regions (Zones 1 and 3) of the boundary, where the energy was also assumed to vary linearly. Figure 5.23 shows the solute drag as a function of migration rate for variable diffusivity and Figure 5.24 the drag vs. migration rate for two different ratios together with the drag contributions from different zones of the grain boundary.

In Figure 5.24, the predictions obtained from the approximate equations presented by Chan (broken lines) can be seen. It is evident that this particular model of the boundary leads to a large deviation from the approximate relation on the low velocity side if the grain boundary diffusivity is much larger than the bulk diffusivity. Since the approximate equations are probably accurate for low velocities, the results indicate that there is a deviation from the proportionality between drag and velocity even at low velocities, i.e., even at low values of the drag. Furthermore, they also indicate that the maximum value of the drag may be much smaller than that obtained from the approximate relations. This may seriously affect the conditions for the spontaneous transition from the low velocity to the high velocity regime (125). The above observations indicate that, in order to make quantitative predictions regarding solute drag, it is necessary to know the properties of the boundary in great detail, a type of understanding which is incomplete at the present time.

The above analyses have dealt with the effects of *substitutional* solutes on grain boundary drag. By contrast, we are interested here in the influence of boron, a largely *interstitial* solute in iron. The development of a solute drag model applicable to interstitial elements (e.g. C, N, H, B, etc.) is well beyond the scope of the present investigation, which was essentially experimental in nature. It may also not be of primary interest in that it is not the effect of boron

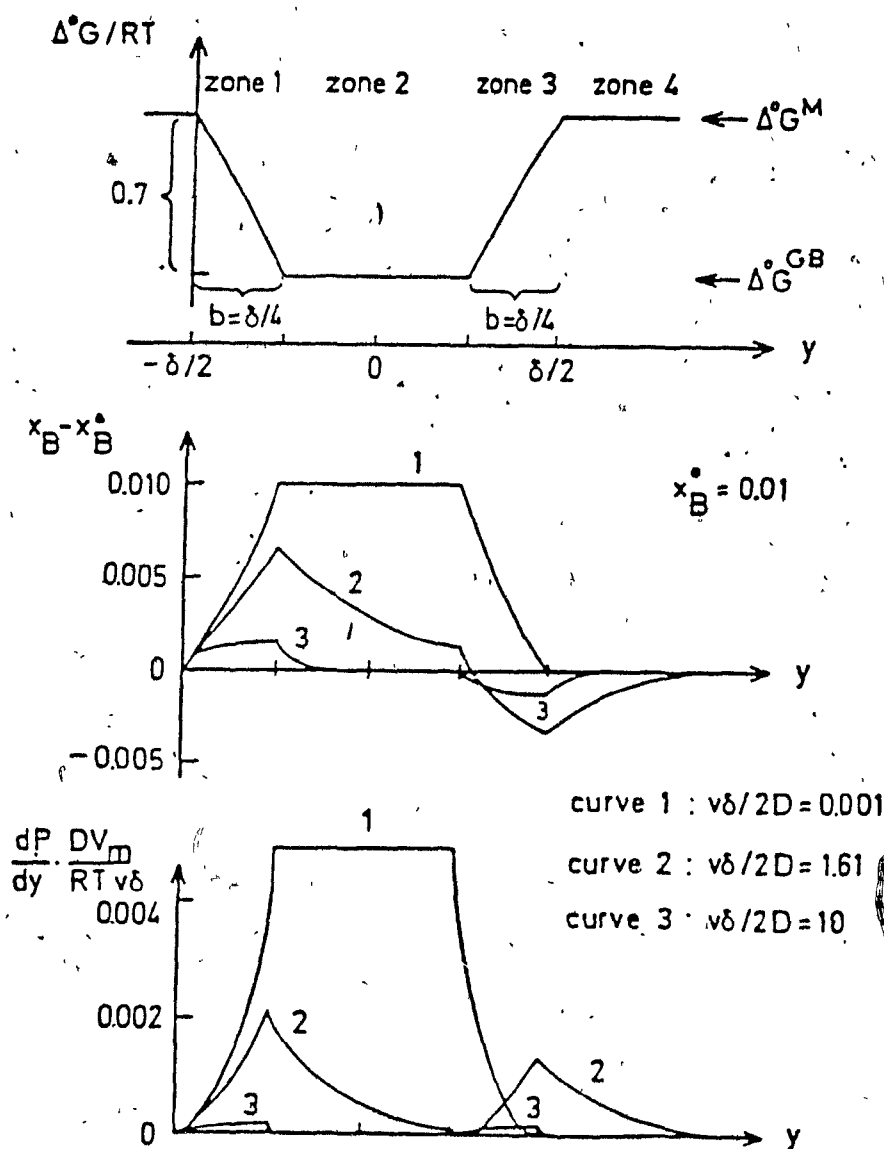


Figure 5.22 Top diagram: A grain boundary model with four different zones. Middle diagram: Concentration profiles calculated for three migration rates. Bottom diagram: The integrand in the calculation of solute drag from the concentration profiles (125).

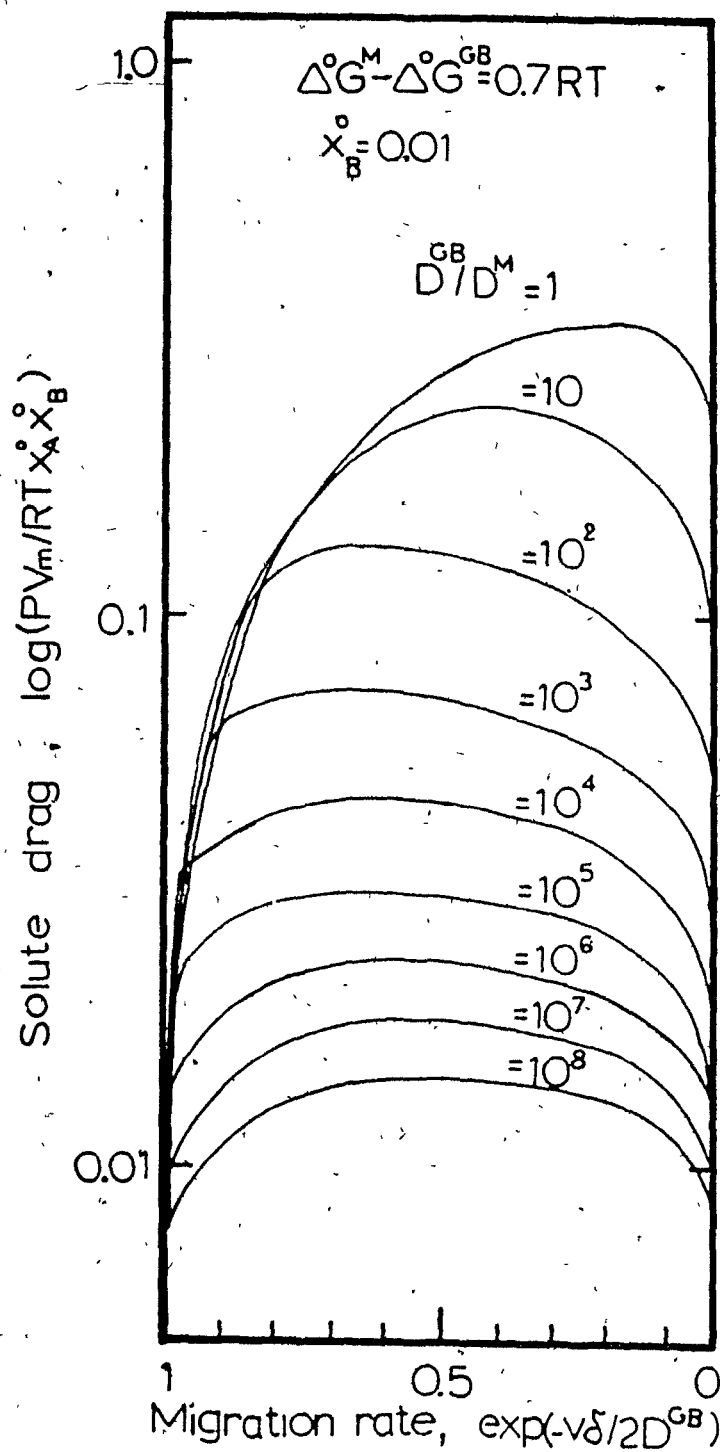


Figure 5.23 The solute drag as a function of the migration rate, calculated for a variable diffusivity. D^{GB} holds in the center of the boundary and D^M holds in the undisturbed crystals.

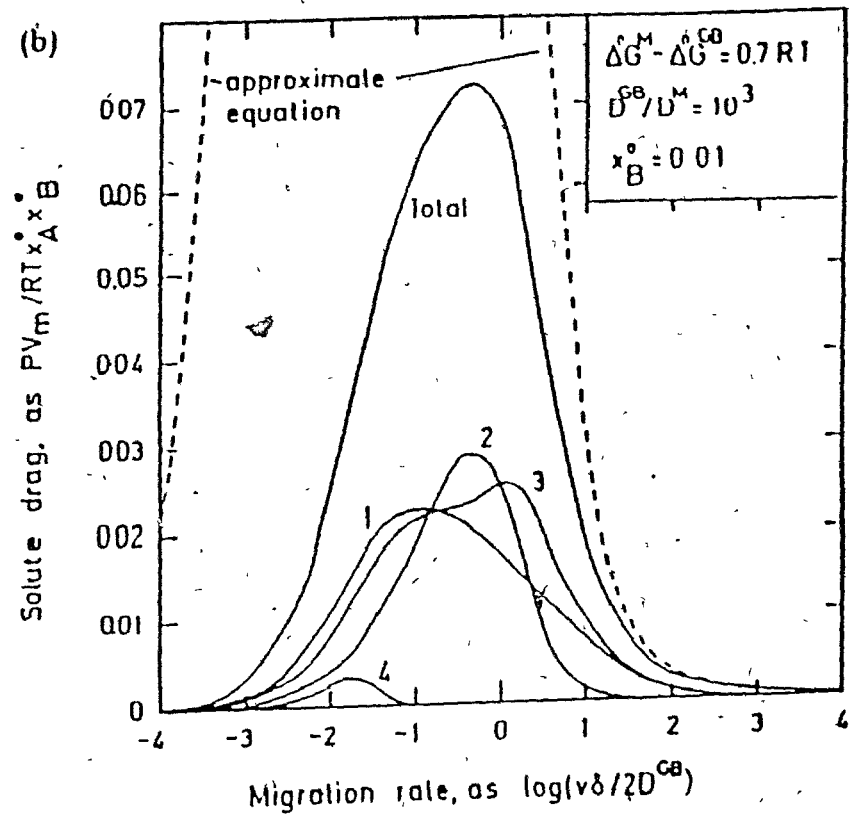
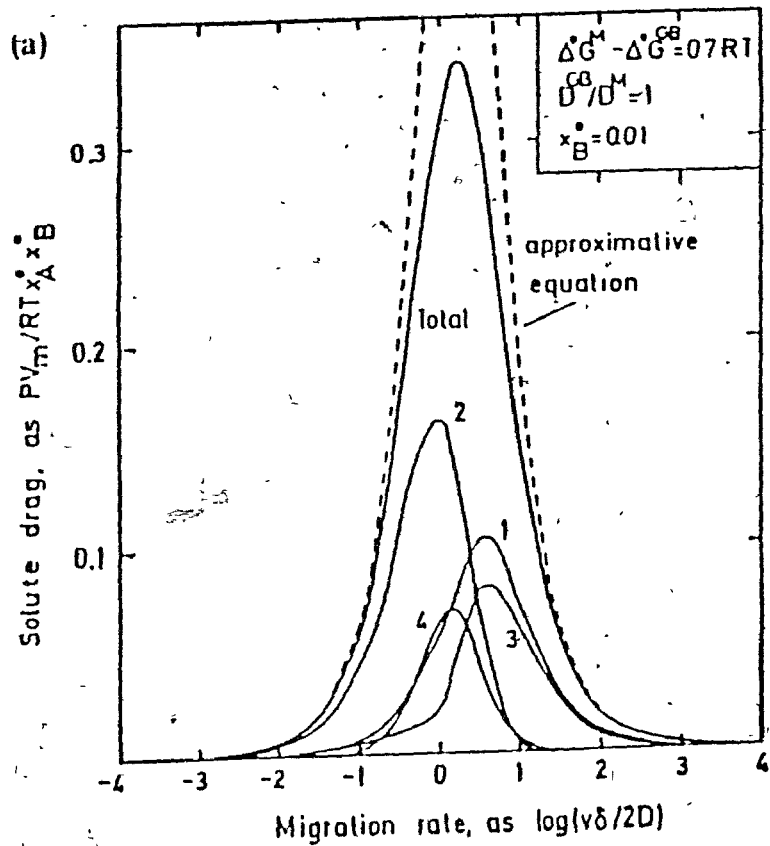


Figure 5.24 The solute drag contributions from different zones in the grain boundary, evaluated for two different ratios of D^{CB}/D^M (125).

addition as such that is at issue, but rather the effect of the *joint* addition of Nb + B. Accordingly, the synergistic effect can be analyzed instead in terms of how B addition *modifies* the solute drag produced by Nb when both are present in combination. If the improved analysis of solute drag proposed by Hillert and Sundman is correct, as well as their representation of the grain boundary regions (Fig. 5.22), the addition of boron to steel can increase the drag in three different ways. 1) By increasing the matrix diffusivity of Nb, which results in smaller values of the ratio D_{GB}/D_M . 2) By decreasing the grain boundary diffusivity of Nb, which again results in smaller values of D_{GB}/D_M . 3) By simultaneously decreasing the grain boundary and increasing the matrix diffusivities of Nb.

Clearly, the solute drag theory presented here can provide a useful and physically reasonable explanation of how and why alloying elements retard recrystallization, and why some elements are more effective than others. As explained above, it can even throw light on how boron addition is able to influence the retarding ability of Nb. However, it does not explain why the relative difference in kinetics between the Nb and Nb + B steels depends on the deformation conditions; something which is taken up in the section that follows.

5.1.6.3 Dynamic or Strain Induced Segregation of Boron

From the experimentally determined softening curves (Figures 4.5(a), 4.7(a) and 4.8), it is evident that the relative difference between the softening curves for the Nb and Nb + B steels changes with temperature. A good reference unit for the comparison of these differences is the time for 50% recrystallization ($t_{0.5}$) for each steel. The relative difference in the kinetics of the Nb and Nb + B steels (after a constant predeformation) can be expressed as the ratio of these times (i.e. $t_{0.5}(\text{Nb} + \text{B})/t_{0.5}(\text{Nb})$). These ratios are illustrated in Figure 5.25 as a function of temperature for the three predeformations employed (i.e. $\epsilon = 0.12, 0.25, 0.5$). It is evident that the points for each predeformation follow a bell shaped curve. The amplitudes of these curves change with predeformation and the largest corresponds to a predeformation of 50%. It is also apparent that, as the temperature is reduced, the synergistic

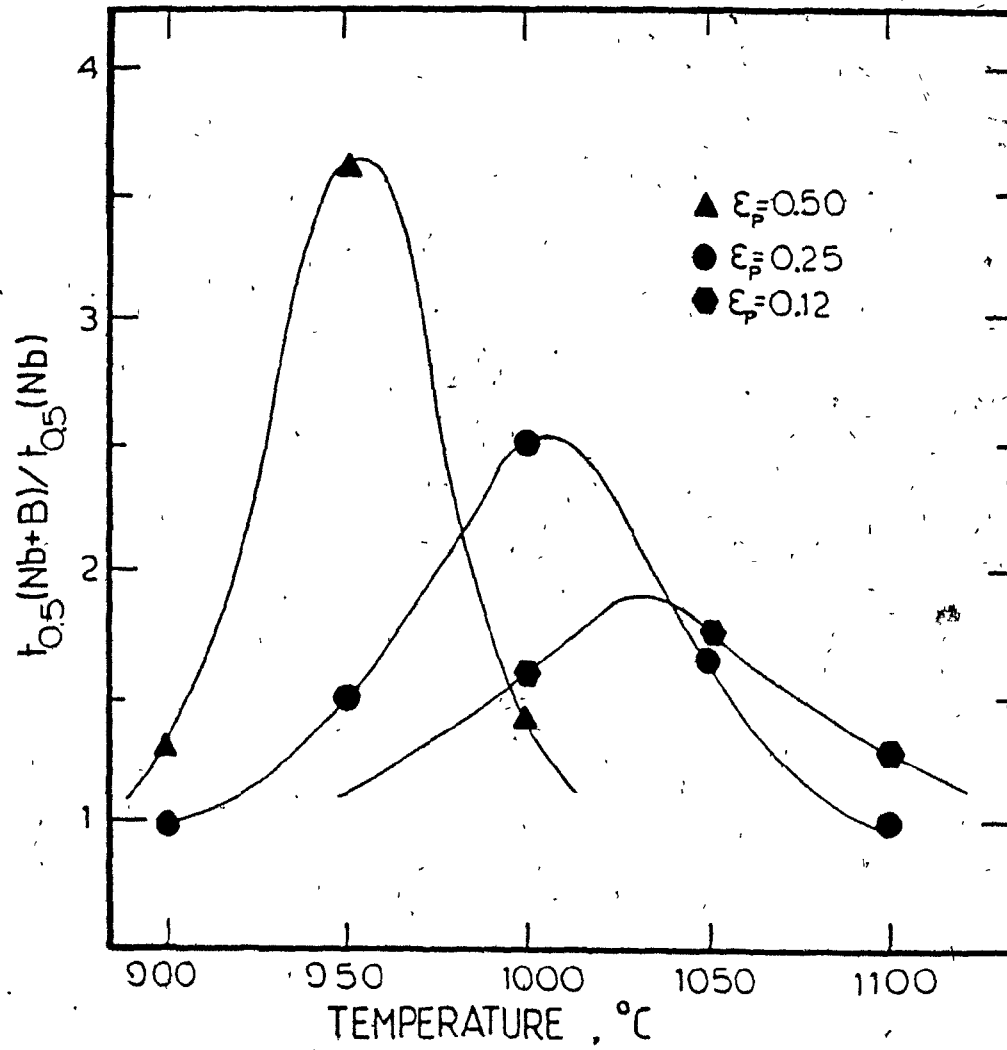


Figure 5.25 Ratio of times for 50% recrystallization of the Nb + B and Nb steels vs. temperature.

effect peaks at higher and higher prestrains (i.e. driving forces for recrystallization).

The softening curves for the same test temperature (1000°C) but for different amounts of prestrain were presented in Figure 5.14. Again the difference in softening rate between the Nb and Nb + B steels changes with prestrain. Because the prestrain determines the driving force for recrystallization, this set of experimental results suggests that there may be a correlation between the velocity of the recrystallizing boundaries and the relative difference in kinetics described above. The relative difference in the kinetics of the Nb and Nb + B steels, expressed as the ratio of the half recrystallization times, was therefore plotted versus the log of the velocity of the moving boundaries, as illustrated in Fig. 5.26.

Here, the estimate of the velocity is always based on the corresponding softening curve for the Nb steel. Interestingly enough, the three bell shaped curves have their peaks at approximately the same velocity. Such an optimum velocity implies that the synergistic effect is difficult to observe if the time (of recrystallization) is either too short or too long.

The above observations, coupled with the autoradiographic results showing boron segregation at the recrystallizing grain boundaries (Figures 4.25 and 4.26), raise the possibility that the *dynamic or strain induced* segregation of boron is taking place. Such an interpretation has already been employed by Watanabe et al. (42), who observed that boron segregates at moving austenite grain boundaries, in a manner similar to that determined in the present investigation. In their case, the sweeping action of the boundaries collected the boron atoms to lead to a geometry consistent with the solute drag theory. Furthermore, they suggested that the degree of segregation of the boron atoms during hot rolling is controlled by relations between 1) the matrix diffusivity of the boron atoms, 2) the grain boundary diffusivity of these atoms, and 3) the sweep velocity of the recrystallizing grain boundaries. Before continuing further, it will therefore be useful to review some of the experimental evidence concerning boron segregation which has been published in recent years.

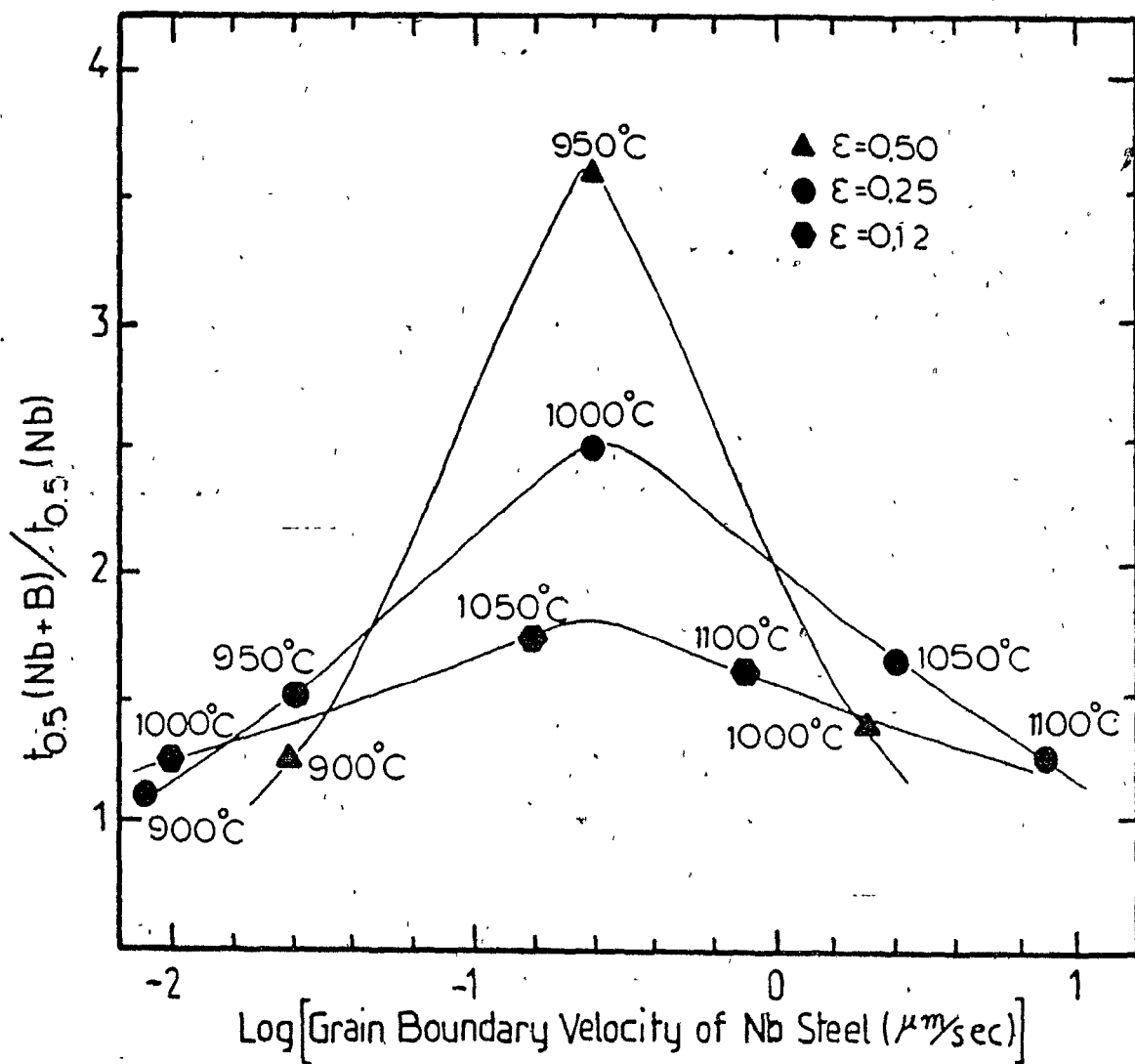


Figure 5.26 Ratio of times for 50% recrystallization of the Nb + B and Nb steels vs. grain boundary velocity of the Nb steel.

5.1.6.3.1 The Mechanism of Boron Segregation

It has been reported in the literature (45, 46, 127, 128) that boron forms monovacancy complexes (at temperatures below 1000°C) or divacancy complexes (at temperatures above 1000°C) and that both species are present in the intermediate temperature region. These complexes diffuse faster than single vacancies and are actually responsible for the non-equilibrium segregation of boron at stationary austenite grain boundaries. This is produced by a high temperature anneal, followed by isothermal holding at a lower temperature, see Figure 5.27. As the temperature of a sample is decreased from the austenitizing temperature, a number of excess vacancies is produced (this increases exponentially with the amount of cooling); the availability of the vacancies leads to the formation of a number of complexes (Table 5.12), as has already been discussed in paragraph 2.1.4. The complexes carry the boron to the grain boundaries, which act as vacancy sinks, releasing the boron. Furthermore, measurements of the width of the boron depleted zones from autoradiographic plates (128) as a function of quenching temperature and cooling rate have provided values for the diffusion parameters of these complexes: $D_0 = 2.54 \times 10^{-4} \text{ cm}^2/\text{sec}$, $Q = 21,000 \text{ cal/mole}$ for the monovacancy boron complexes and $D_0 = 0.78 \times 10^{-2} \text{ cm}^2/\text{sec}$ and $Q = 27,600 \text{ cal/mole}$ for the divacancy-boron complexes.

In the case of the present experiments, prior to the application of deformation, there is no boron segregated at the stationary grain boundaries (Figure 4.23). This is because of the relatively slow cooling rates (2 to 3°C/sec) together with the fairly long times needed for the stabilization of test temperature (2 to 3 minutes). However, the introduction of deformation creates a large number of vacancies ($\rho_v \approx 10^{-4} \cdot \epsilon$, where ρ_v is the vacancy concentration and ϵ the deformation) in a manner similar to the effect of undercooling; it also provides the driving force for the migration of the recrystallizing grain boundaries. It can be seen from the above that the strain induced segregation of boron can be expected to depend, not only on the matrix and grain boundary diffusivities of the boron, but on the matrix diffusivities of the boron-complexes as well. Moreover, the degree of the segregation should be influenced, not only by the velocity of the moving boundary, but also by the number of the boron complexes (i.e. the strain).

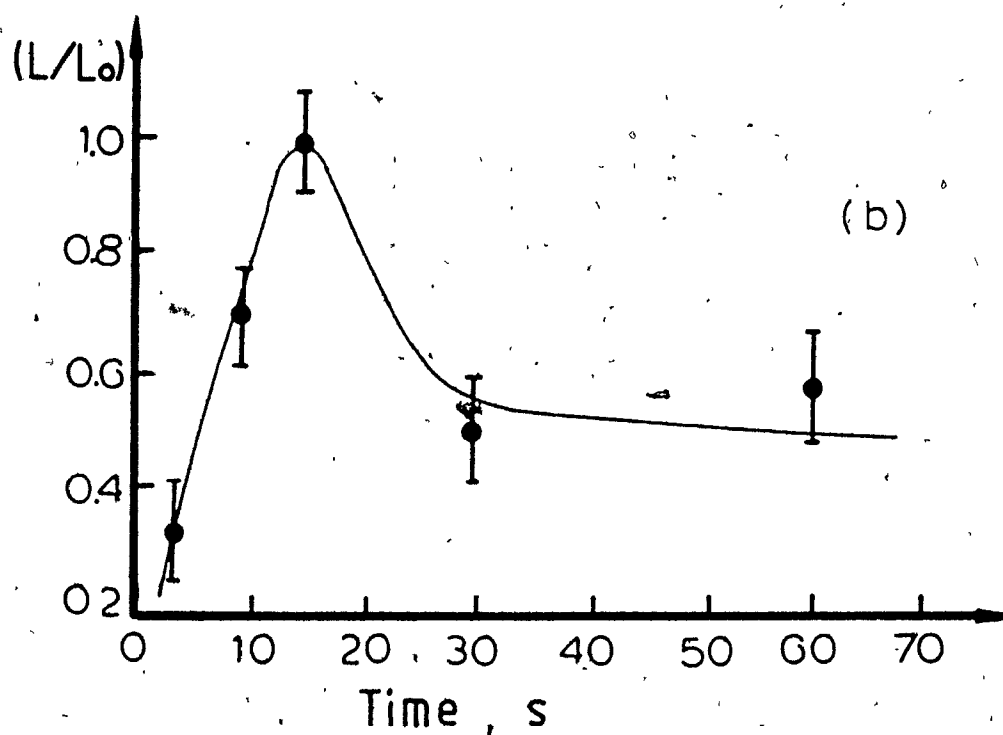
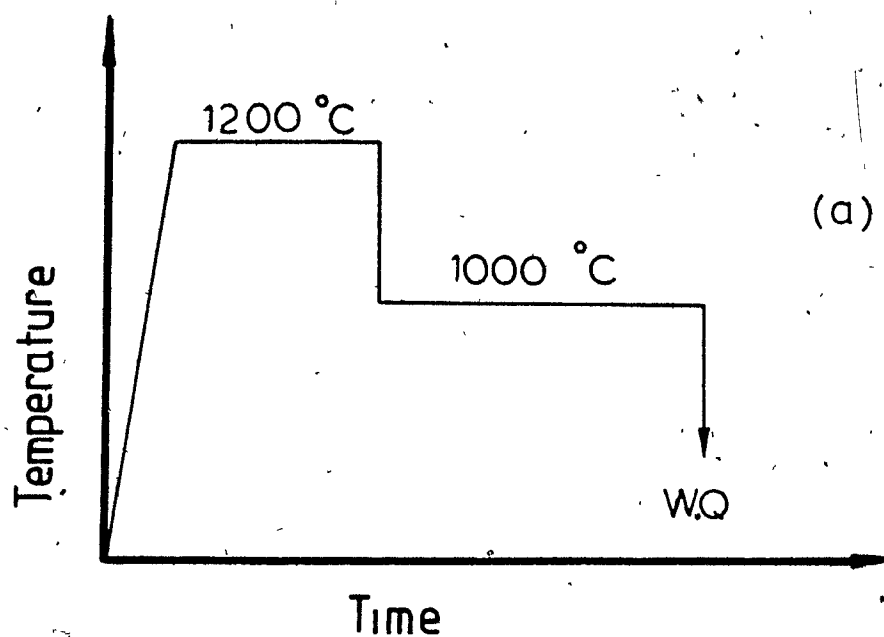


Figure 5.27(a) Schematic time/temperature diagram for isothermal heat treatment. (b) The ratio (L/L_0) as a function of isothermal holding time at 1000°C . L : the total length of grain boundary with boron segregation revealed by PTA on unit area. L_0 : the total length of austenite grain boundary per corresponding unit area (127).

TABLE 5.12 - Vacancy [V], Complex [C] and Boron [I] Concentrations as a Function of Solution Treatment Temperature

Temperature		[V] x 10 ⁶	[C] x 10 ⁶	[I] x 10 ⁶
°C	K			
900	1173	3.9	0.6	89.4
1000	1273	11.4	1.2	88.8
1100	1373	29.0	2.1	87.9
1200	1473	64.7	3.5	86.5
1300	1573	130.6	5.3	84.7
1350	1623	180.0	6.4	83.6

It was noted above that the grain boundary velocity (i.e. the recrystallization time) of the Nb steel under the condition of maximum relative difference between the Nb and Nb + B steels remained relatively fixed at the different experimental temperatures. The times for 80% softening (i.e. recrystallization about 3/4ths complete) were approximately 65 seconds in all the cases. The values of the diffusivity and diffusion distance were therefore estimated for 65 seconds and the appropriate temperature; these are presented in Table 5.13. The calculations show that there is little difference in the diffusion distance over the temperature range 950 to 1050°C. The average recrystallized austenite grain sizes under conditions of maximum difference between the Nb and Nb + B steels ($\epsilon = 0.25$, $\dot{\epsilon} = 2 \text{ s}^{-1}$, test temperature 1000°C, holding time 100 seconds) were measured to be approximately 20 μm ; the initial grain size in these materials was approximately 40 μm . The diffusion distances, as well as the distances travelled by the recrystallizing boundaries are therefore very similar, so that the proposal that the non-equilibrium segregation of boron is responsible for the synergistic effect seems to be both physically reasonable and quantitatively acceptable.

5.1.6.3.2 Implications of the Proposed Strain Induced Segregation Model

The above model of strain induced segregation has the potential for providing reasonable explanations for several important questions arising from the present investigation. First of all, the synergistic action of boron and Nb in reducing the recrystallization rate of hot worked austenite can be interpreted, as indicated above, as resulting from the influence of the segregating boron on the matrix and grain boundary diffusivities of the Nb. According to this picture, the boron segregates as a boron-monovacancy complex, which travels faster than a single vacancy. Thus, during the process of recrystallization, more vacancies will be available for the matrix diffusion of Nb atoms in the regions close to the grain boundaries in the Nb + B steel than in the Nb steel. This is expected to result in an apparent increase in the matrix diffusivity of the Nb atoms in the former material. Furthermore, as suggested by Herzig and Geise (126), the presence of even small amounts of interstitials at the grain boundaries (e.g. 20 to 40 wt. ppm) can seriously reduce the grain boundary diffusivity of the substitutional solutes which are present there. Consequently,

TABLE 5.13 - Boron Monovacancy Complex Diffusivities and Diffusion Distances for 65 Seconds at 950, 1000 and 1050°C

Test Temperature (°C)	Diffusivity of Boron Monovacancy Complexes ($\mu\text{m}^2/\text{sec}$)	Diffusion Distance $x(\mu\text{m})$ for $t = 65$ sec $x \sim \sqrt{Dt}$
950	4.5	17.1
1000	6.4	20.3
1050	8.7	23.8

the presence of boron at the grain boundaries can reduce the grain boundary diffusivity of Nb. The above change can reduce the ratio $D_{GB_{Nb}}/D_{M_{Nb}}$, which is expected in turn to produce larger drag forces when B is present.

If this is the case, similar synergistic effects should occur when boron is added in the presence of other "influential" substitutional elements such as Ti or Mo. Indeed, in a recent investigation (129) of HSLA steels, it has been found that the combined addition of boron and Nb or boron and Ti raises the recrystallization stop temperature of γ by more than the addition of any single alloying element. Moreover, as illustrated in Figure 5.28, Nb + B raises the recrystallization stop temperature more than Ti + B. By contrast, the amount of solute retardation due to the addition of B in the absence of Nb (Figure 4.6), or in the presence of Nb, but when the grain boundary velocity differs considerably from the critical one (Figures 4.7(a) and 4.8), can be readily estimated. In terms of the solute retardation parameter (SRP) given by

$$SRP(\%) = \log(t_x/t_{ref}) (0.1/at.\% B) \times 100 \quad (130)$$

this works out to be 50%.

Here t_x and t_{ref} are the times for 50% recrystallization (for example) in the B and reference steels, respectively, and the form of the expression is selected so that the addition levels are normalized to 0.1 atomic percent. This degree of retardation is similar to that exerted by additions of Ti and Mo (normalized to 0.1 at.%), but is less than that attributable to Nb addition (130). The combined addition of B and V therefore can only lead to a small synergistic effect.

Two of the remaining questions raised by this investigation will now be considered: (i) why are there optimum conditions associated with maximum retardation? and (ii) why is the relative difference under optimum conditions larger when the deformation is larger? For a given grain boundary velocity, which is a function of the temperature and pre-strain, the number of boron atoms collected is a function of the diffusion parameters associated with the various species of boron. When the distance swept by a moving grain boundary at a specific time matches the diffusion distance travelled by one of the diffusing species (e.g. the boron monovacancy complex), the number of

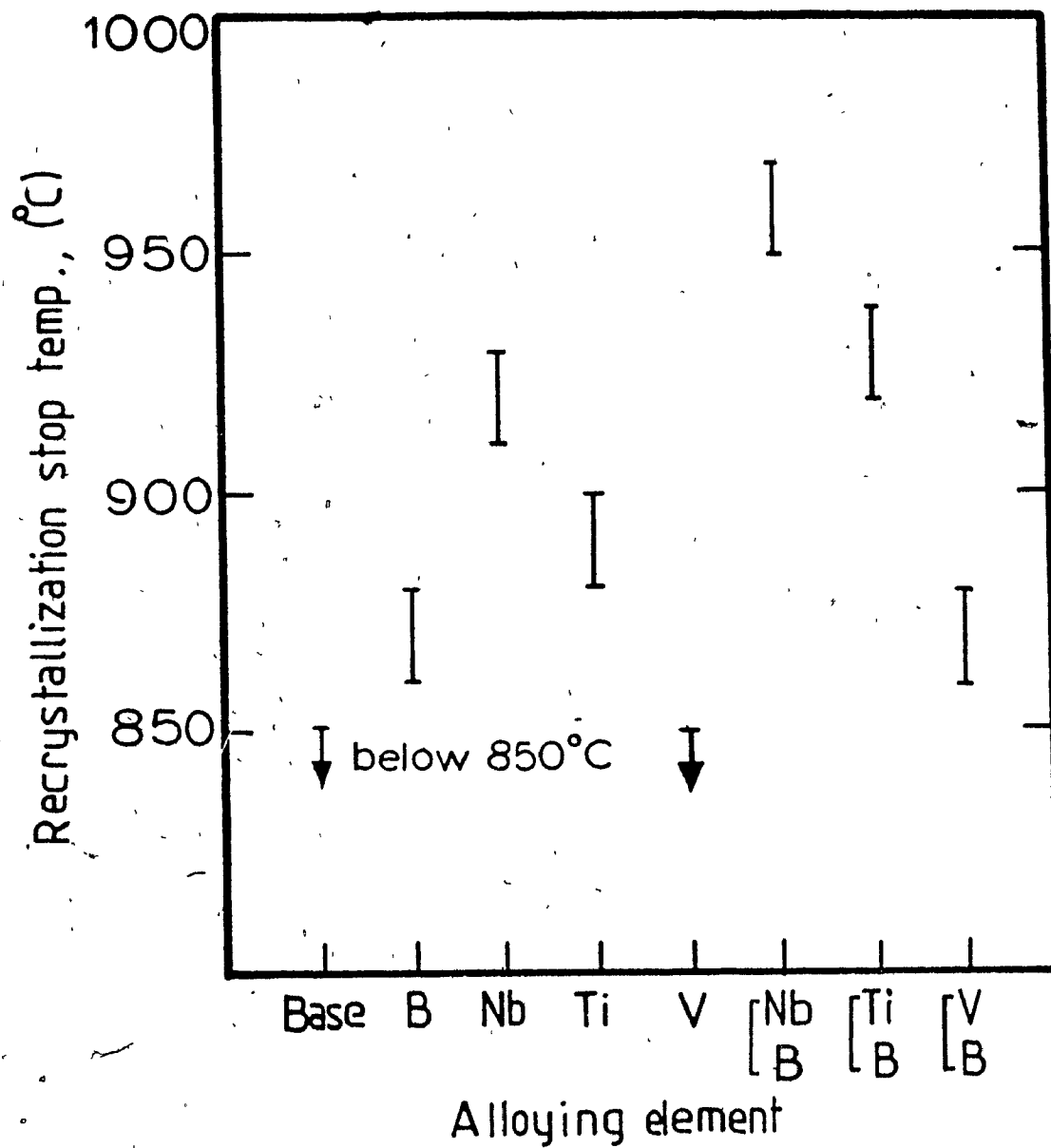


Figure 5.28 Effect of selected alloying elements on recrystallization stop temperature of austenite (129).

segregated boron atoms will be at a maximum, as will the number of vacancies liberated in the grain boundary region. Consequently the retardation of recrystallization can be expected to be at a maximum. According to the model, the reason why the relative difference in recrystallization rate between the Nb and Nb + B steel increases with deformation (Figure 5.27) is that, at a given temperature, the vacancy concentration increases with the amount of the deformation ($\rho_v \approx 10^{-4} \epsilon$). Larger vacancy concentrations produce larger complex concentrations, which in turn increase both the boron and vacancy concentrations at the grain boundary.

In the above model, boron makes its presence felt by modifying the diffusivity of the Nb atoms, whether at grain boundaries or in the matrix. However, it remains possible that there are chemical or thermodynamic interactions between boron and the other elements. These could also provide the basis for a model that explains the experimental results of the present investigation. Due to the scarcity of both theoretical analyses as well as appropriate experimental results, the above possibilities were not explored in any detail in this study.

5.1.6.4 Boron in Solid Solution: Interstitial or Substitutional?

An important question related to the present work is the following: what makes boron so special? After all, carbon has a similar diffusivity and also forms complexes and segregates to grain boundaries. Despite these similarities, boron and carbon are different in size ($d_B = 1.96 \text{ \AA}$, $d_C = 1.83 \text{ \AA}$) and electronic structure (B: $1S^2 2S^2 2P^1$, C: $1S^2 2S^2 2P^2$). Although carbon is clearly an interstitial element in iron, there is some diversity of opinion as to whether boron forms an interstitial or a substitutional solid solution with iron and indeed its atomic size is borderline for both modes of solution. X-ray measurements of the lattice parameter of α iron indicate substitutional solid solution (131, 132). On the other hand, internal friction investigations indicate an interstitial solid solution in α iron (133, 134), although the latter conclusion is refuted by other work (135). Some researchers (136, 137) have suggested that boron can occupy both interstitial and substitutional sites in α iron, and that substitutional boron atoms may interact with and be stabilized by other

interstitial atoms such as carbon. Diffusion investigations indicate that the activation energy for boron diffusion in α iron is of the order expected from substitutional solid solution (138). Identification of the sites for boron solution in α iron is even less positive (135), but diffusion data do indicate an activation energy appropriate for interstitial migration (139). The situation can become still more confusing at grain boundaries which are the sites of interest for us. However, due to the size difference between the carbon and boron atoms, it appears possible that the carbon and boron atoms may occupy *different* lattice sites. If carbon occupies the interstitial sites and boron the substitutional ones, then the boron atoms can be expected to be more effective in retarding the recrystallization process. The above proposal does not have any supporting evidence at this point and must be regarded as just an educated guess. Furthermore, because the experimental temperatures of this investigation are fairly high, the differences in electronic structures between carbon and boron may play a reduced role.

5.2 THE EFFECT OF BORON ON DYNAMIC STRUCTURAL CHANGE

The metallographic examination of rapidly quenched samples after hot deformation has provided indisputable evidence for the occurrence of dynamic recrystallization (68) in metals which recover rather slowly during deformation (e.g. austenitic steels and Cu). Even though the dynamically recrystallized grains are very fine (due to the high driving force and small critical nucleus size (140)), the process has only limited commercial interest, except for those working operations in which the unit strain is sufficiently large (e.g. extrusion and planetary hot rolling). Unfortunately, the fine microstructure coarsens appreciably unless the temperature of the material is rapidly reduced after hot working. Nevertheless, dynamic and static recrystallization are very similar processes and dynamic tests can provide qualitative data regarding the influence of microalloying elements on static recrystallization. This is of particular interest with respect to the recrystallization occurring between passes in plate or hot strip mills.

In the present investigation, dynamic tests were conducted for the sake of verification and to complete the results obtained under static conditions.

Furthermore, due to the rapidity of the experimental method, many fewer tests were required to establish patterns. In this series of tests, two important deformation parameters not treated in the static tests, the austenitization temperature and strain rate, were examined.

5.2.1 EFFECT OF TEST TEMPERATURE ON ϵ_p AND ϵ_x

The effect of test temperature on the onset (ϵ_p) and duration of recrystallization (ϵ_x) can be seen in Figures 4.12(a) and 4.12(b), respectively, for the four steels tested. Recrystallization starts and finishes earlier as the temperature is increased. This is because both the nucleation and growth of new grains are thermally activated processes (68). As the temperature is decreased, higher dislocation densities are needed to initiate recrystallization, so that greater amounts of strain are required to attain the peak stress (ϵ_p). The lower temperature also increases ϵ_x because of the sluggishness of the process. However, of greater importance in these figures is the way in which B, Nb and Nb + B additions influence the values of ϵ_p and ϵ_x . Evidently, single additions of boron have a very small retarding influence, while the combined addition of Nb + B causes appreciable retardations, the amount of which depends on the test temperature.

From the above set of experiments, dynamic RTT (DRTT) diagrams can be readily constructed because the onset time for recrystallization (R_s) can be defined as

$$R_s = \epsilon_p / \dot{\epsilon} \quad (5.27)$$

and the finishing time for recrystallization (R_f) as

$$R_f = (\epsilon_p + \epsilon_x) / \dot{\epsilon} \quad (5.28)$$

A comparison between DRTT (Figs. 5.29 and 5.30) and RTT (Figs. 5.18 and 5.19) diagrams can now be made, which reveals considerable similarity in the general recrystallization behaviour of the four steels tested. This is in spite of the fact that the recrystallization start and finish times under dynamic and

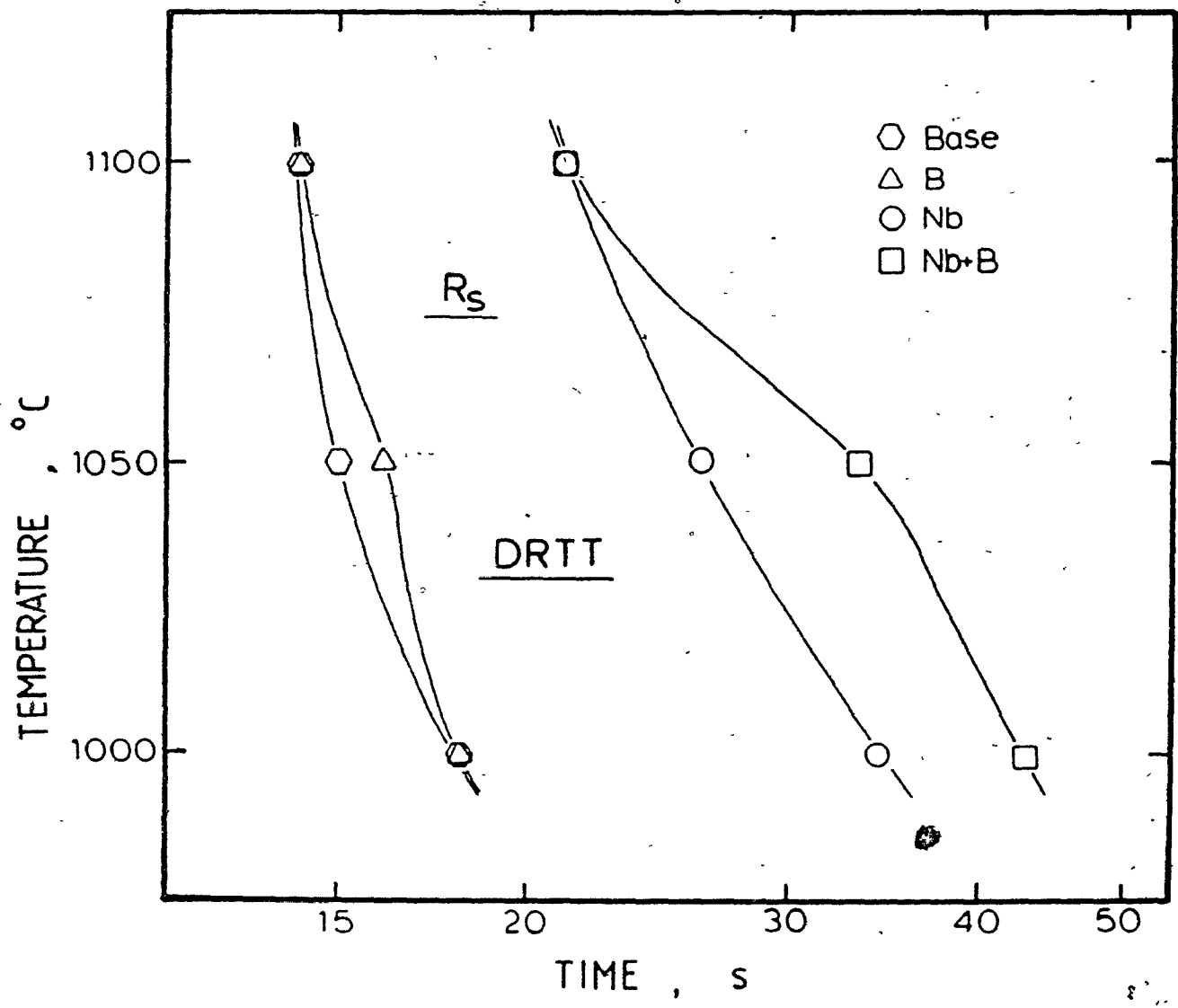


Figure 5.29 Dynamic recrystallization start times (R_s) as a function of temperature for the four steels investigated.

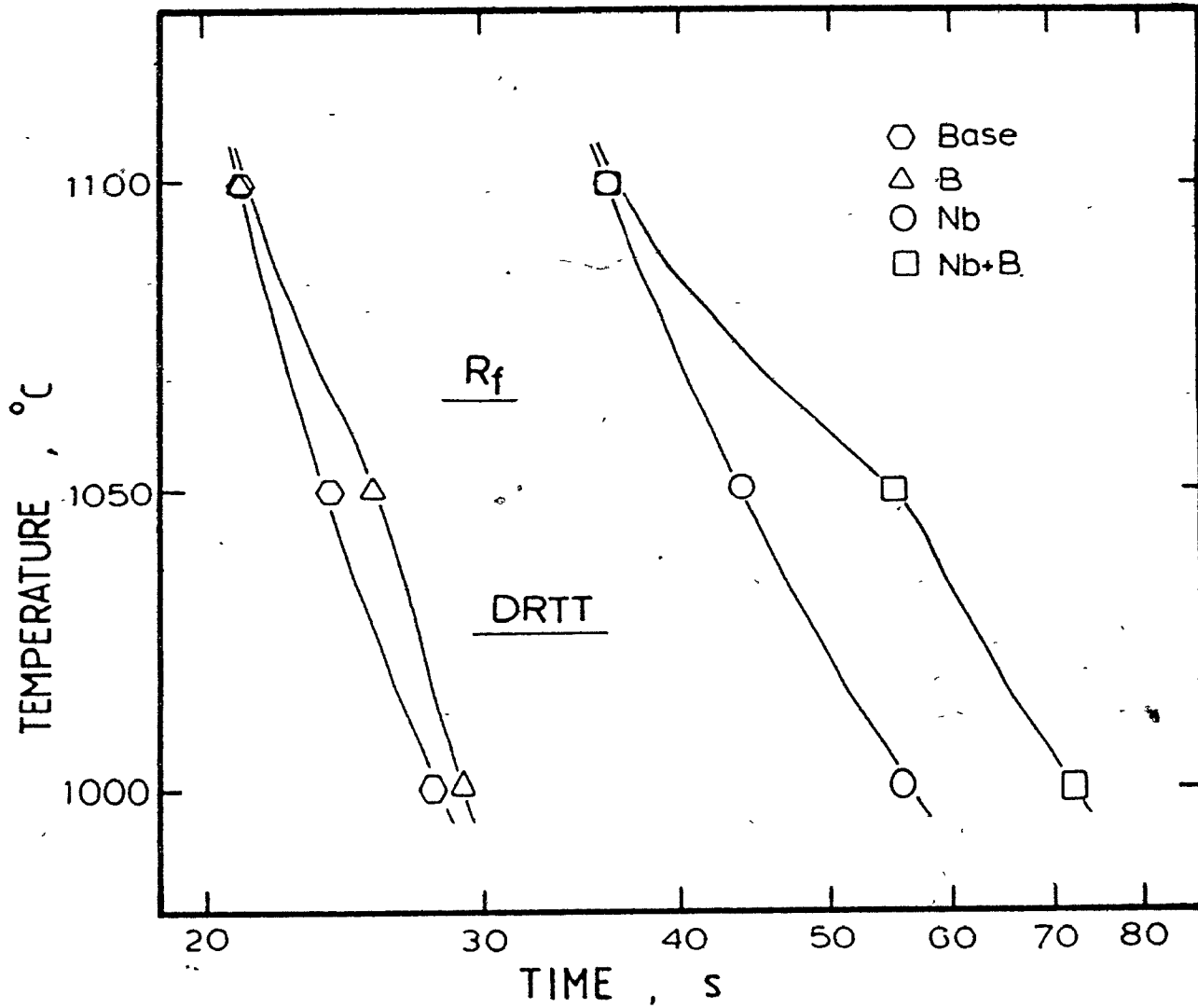


Figure 5.30 Dynamic recrystallization finish times (R_f) as a function of temperature for the four steels investigated.

static conditions are numerically different. Although ϵ_p and ϵ_x could not readily be determined by compression testing at 950 and 900°C, and the temperature condition associated with maximum retardation could not be established for the Nb and Nb + B steels, the relative difference in recrystallization rate between the two steels of interest depends, as in the static case, on the velocity of the recrystallizing grain boundaries.

5.2.2 EFFECT OF AUSTENITIZATION TEMPERATURE ON ϵ_p AND ϵ_x

The austenitization temperature is an important parameter in the hot rolling of steels for two main reasons: first, it determines the initial grain size of the material; second, if it is above the solution temperature of the precipitates present, it can ensure that they are dissolved.

The influence of austenitization temperature on the onset strain for dynamic recrystallization as well as on the recrystallization strain was presented in Figures 4.13(a) and 4.13(b), respectively. It is evident from these results that the critical strain increases with austenitization temperature. This is a well known phenomenon (141-143) and is related to the larger initial grain sizes produced at the higher austenitization temperatures (Fig. 4.27). If it is accepted that dynamic recrystallization is initiated at the austenite grain boundaries (141), then it is apparent that larger initial grain sizes make it more difficult to acquire a high density of nuclei, resulting in a larger strain being required to attain the peak flow stress.

Furthermore, larger grains not only start to recrystallize later, but the duration of recrystallization is also longer due to the larger number of 'necklace strands' or 'cascades' of recrystallization which must be generated for the recrystallization front to attain the grain interior (145).

The addition of boron to the Nb steel leads to extra retardation of the onset and progress of recrystallization, especially at the lower temperatures. These observations, coupled with the facts presented above, again indicate that the effectiveness of boron in retarding grain boundary motion is rate dependent.

5.2.3 EFFECT OF STRAIN RATE ON ϵ_p AND ϵ_x

The dependence of ϵ_p and ϵ_x on testing strain rate was illustrated in Figures 4.14(a) and 4.14(b), respectively. Here, as the strain rate is increased, ϵ_p and ϵ_x are observed to increase as well. This is due to the fact that, at constant temperature, there is a decrease in the time required for recrystallization to begin. As this decrease is insufficient to offset the increase in strain rate, there is an increase in the critical strain (144). Furthermore, the recrystallization strain also increases with strain rate for reasons similar to those described above for ϵ_p . The comparison of ϵ_p and ϵ_x for the Nb and Nb + B steels demonstrates that the retardation is maximum at a strain rate of 0.1 s^{-1} . This again indicates that the retarding effect of boron involves a critical time, which cannot be very short or very long.

All the observations extracted from the dynamically tested samples show good agreement with the results of the static tests. They also support the validity of the strain induced boron segregation model proposed and described in detail in section 5.1.6.3.

CHAPTER 6

CONCLUSIONS

The present investigation involved the effect of small amounts of boron (30 ppm) on the recrystallization behaviour of hot worked austenite in a plain C and a Nb steel. These tests were conducted isothermally under both interrupted and continuous loading conditions. Prior to testing, for the interrupted experiments, the samples were austenitized at 1100°C for 15 minutes, after which they were prestrained to equivalent strains of 0.12, 0.25 and 0.5, unloaded for increasing times, and then reloaded for a further deformation of 0.25. The loading strain rate was held constant at 2 s⁻¹ and test temperatures of 900, 950, 1000, 1050 and 1100°C were employed. The progress of recrystallization was studied from the amounts of softening taking place during the unloading and isothermal holding intervals.

For the continuous loading tests, the peak ϵ_p and recrystallization ϵ_v strains were taken as measures of the onset and progress of recrystallization. Austenitization and test temperatures in the range 1050 to 1250°C and 1000 to 1100°C, respectively, were employed and the strain rates used were in the range 10⁻³ to 0.5 s⁻¹. As a result of this study, and with the aid of data obtained from the literature, the following general conclusions were drawn:

1. The retardation of recrystallization produced by B addition when added alone is equivalent to a solute retardation parameter (SRP) of about 50% (normalized to 0.1 at.% B). This is comparable to that produced by an equal atom fraction of Mo.
2. The simultaneous presence of Nb and B leads to the greater retardation of recrystallization than the simple sum of the retardations produced by each solute alone. Furthermore, the magnitude of this synergistic effect changes with the deformation conditions. It is a maximum at 1050, 1000 and 950°C for prestrains of 0.12, 0.25 and 0.5, respectively.

Under these three sets of conditions, the velocities of the grain boundaries during recrystallization in the Nb steel are approximately equal.

3. The increased retarding ability of B when added in the presence of Nb is due to the strain induced segregation of boron. This non-equilibrium effect results in the formation of a temporary solute atmosphere in the vicinity of the moving grain boundaries. This mode of segregation is affected by:
 - i) the matrix diffusivity of the boron atoms;
 - ii) the grain boundary diffusivity of the boron atoms;
 - iii) the boron-monovacancy complex diffusivity; and
 - iv) the sweep velocity of the moving grain boundaries.
4. From measurements on quenched samples under conditions of maximum relative difference between the Nb and Nb + B steels, the mean distance travelled by the grain boundaries during recrystallization was determined to be approximately 20 μm . This distance is comparable to the mean distance ($x = \sqrt{Dt}$) travelled by the boron-monovacancy complexes during the same time interval. This suggests that boron transport via these complexes produces the segregation responsible for maximum retardation.
5. Other interstitial elements (C: $r = 0.91 \text{ \AA}$, N: $r = 0.92 \text{ \AA}$) could display segregating abilities similar to that of boron (B: $r = 0.98 \text{ \AA}$). However, due to its size, boron is at the dividing line between acting as a substitutional and as an interstitial solute. It may, therefore, play a role in part as a

substitutional, permitting it to have a larger effect on grain boundaries than C in this way.

6. The synergistic interaction between Nb and B can be rationalized in terms of the influence of boron grain boundary atmospheres on the grain boundary diffusivity of Nb ($D_{GB_{Nb}}$) and consequently on the ratio of the grain boundary to matrix diffusivities of Nb ($D_{GB_{Nb}}/D_{M_{Nb}}$). As suggested in the literature, even small amounts of interstitial impurities (20 to 40 ppm in the bulk) can reduce the grain boundary diffusivity of substitutional elements e.g. Nb, when the former are segregated at the boundaries. According to the solute drag model of Hillert and Sundman, the reduction in the ratio $D_{GB_{Nb}}/D_{M_{Nb}}$ produced in this way increases the drag forces exerted by the Nb on the moving boundaries.
7. Comparison of the relative differences in recrystallization rate under optimum segregation conditions clearly shows that the greatest difference corresponds to the greatest (50%) deformation. According to the present model, this is due to the effect of deformation on the number of boron atoms transported to the boundary. Increasing the deformation increases the vacancy concentration ($\rho_v = 10^{-4} \cdot \epsilon$) which increases in turn the concentration of the boron-monovacancy complexes responsible for the transfer of boron to the boundaries.
8. By assuming that the effect of doping the base steel with Nb resembles that of doping pure iron with Nb, and as long as no precipitation is taking place, the solute drag model proposed by Cahn can be applied to the present experimental conditions. According to this model, at high grain boundary velocities, the element with the highest grain boundary interaction energy exerts the largest drag. Experimental evidence obtained on HSLA steels has

shown that the retarding ability of the microalloying elements increases in the following ascending order: $Ni < Cr < Mn < V < Mo < Ti < Nb$. Furthermore, comparison of the diffusivities of the above substitutional elements in γ -iron indicates that the strongest retarding species (Nb) is also the fastest one, followed by Ti, Mo, V, Mn, Cr, and Ni. These observations are consistent with the solute drag theory because the fastest diffusing elements are also those displaying the highest grain boundary interaction energies. Although seemingly contradictory, this is because both the interaction energy and the diffusivity increase with the extent of distortion caused by introducing a particular alloying element into a metal matrix.

9. Based on the present model for the synergistic interaction between Nb and B, boron can be predicted to display a synergism when accompanied by other alloying elements such as Ti and Mo. However, the combined effects of Ti + B or of Mo + B are expected to be less than that of Nb + B because of the weaker grain boundary interaction energies displayed by these elements.
10. The present model does not exclude the possibility that chemical and thermodynamic interactions between Nb and B also play a role in the synergism when both of these elements are present at an austenite grain boundary.
11. Finally, the presence of boron seems to accelerate the precipitation kinetics of NbC.

STATEMENT OF ORIGINALITY AND CONTRIBUTION TO KNOWLEDGE

The present investigation produced the following original contributions:

1. It was shown that the single addition of boron to a base steel results in a measurable retardation of recrystallization. The amount of this retardation is comparable to that produced by an equal atom fraction of Mo.
2. The presence of both Nb and B was shown to result in retardations which are larger than the sum of the effects produced by the elements added separately. The amount of the synergism was demonstrated to vary with the deformation conditions. The maximum retardations were observed at 1050, 1000 and 950°C when the prestrains were 0.12, 0.25 and 0.5, respectively. The present analysis indicates that the above sets of deformation conditions impose approximately equal velocities on the recrystallizing grain boundaries in the Nb steel.
3. The rates of recovery and recrystallization under static holding conditions were described in terms of the Avrami equation. Separate values of the rate parameter k and n were derived for the individual contributions of recovery and recrystallization. The amount of softening preceding recrystallization has been shown to be about 25 percent. Values of the time exponent n^r for recovery of 0.46, 0.61 and 0.77 for predeformations of 0.12, 0.25 and 0.5, respectively, were shown to apply to the Nb-containing materials. The rate constant k^r was demonstrated to depend on temperature, deformation and alloy composition. The time exponent for recrystallization n^R has been found to be independent of temperature and deformation with an average value of approximately 0.9. These parameters are

of considerable use in the computer modelling of steel rolling; some of them are presented here for the first time for such microalloyed steels.

4. The strain induced segregation of boron (a non-equilibrium phenomenon) was concluded to be responsible for the increased retarding ability of boron in the presence of Nb. The concentration of the segregated atoms, which form an atmosphere around the moving grain boundaries, has been suggested to depend on the following:

- i) the matrix diffusivity of the boron atoms;
- ii) the grain boundary diffusivity of the boron atoms;
- iii) the boron-monovacancy complex diffusivity; and
- iv) the sweep velocity of the moving grain boundaries.

From measurements on quenched samples under conditions of maximum relative difference between the rates of recrystallization in the Nb and Nb + B steels, the mean distance traversed by the grain boundaries during recrystallization was determined to be approximately 20 μm . This distance is comparable to the mean distance ($x = \sqrt{Dt}$) travelled by the boron-monovacancy complexes during the same time interval. From the above observations, a case was made that boron transport via these complexes leads to the segregation responsible for maximum retardation.

5. The observation that the relative difference in recrystallization rate between the Nb and Nb + B steels increases with deformation has been attributed here to the effect of deformation on the number of vacancies produced ($\rho_v = 10^{-4} \cdot \epsilon$). According to the present model, more

deformation leads to higher vacancy concentration; the vacancies combine with boron atoms to form complexes in greater concentration, which ultimately leads to more boron transport to the moving boundaries.

6. It has been suggested in the literature that small amounts of interstitial impurities (e.g. 20 to 40 ppm in the bulk) can reduce the grain boundary diffusivity of substitutional elements such as Nb when the former are present at grain boundaries. In the present investigation, the synergistic interaction between Nb and B has been rationalized in terms of the influence of boron grain boundary atmospheres on the grain boundary diffusivity of Nb ($D_{GB,Nb}^{B}$) and consequently on the ratio of the grain boundary to matrix diffusivity of Nb. According to the solute drag model of Hillert and Sundman, a decrease in the $D_{GB,Nb}^{B}/D_{Nb}^M$ ratio should result in larger drag forces being exerted by Nb on the recrystallizing grain boundaries.
7. The solute drag model proposed by Cahn has been applied here under the assumption that the effect of doping the base steel with Nb resembles that of doping pure iron with Nb. The predictions of this model have been shown to be consistent with the recrystallization behaviour of the microalloyed steels studied in this investigation. In particular, the experimentally determined order of effectiveness of the various microalloyed elements has been shown to be in very good agreement with the calculated magnitudes of the interaction energies E_0 and the observed diffusivities of the above elements. Furthermore, the order of retarding ability for seven different alloying elements has been demonstrated to correlate very well with the order of their diffusivities, with the fastest one having the greatest interaction energy and therefore being the most effective (Nb > Ti > Mo > V > Mn > Cr > Ni).

REFERENCES

- 1) P.D. Deeley and K.J.A. Kundig, "Review of Metallurgical Applications of Boron Steels", Shieldalloy Corporation, Newfield, New Jersey.
- 2) T.W. Lippert, "Boron", The Iron Age, Nov. 19, (1942).
- 3) R. Walter, British Patent 160, 792, 1921; U.S. Patent 1, 519, 388, Aug. 13, 1921.
- 4) G.F. Comstock, "Effects of Eight Complex Deoxidizers on Some 0.4 Carbon Forging Steels", Trans. AIME, 150 (1942), p. 408.
- 5) M.A. Grossman, "Hardenability Calculated from Chemical Composition", Trans. AIME, 150 (1942), p. 227.
- 6) W. Crafts and J.L. Lamont, "Effect of Some Elements on Hardenability", Trans. AIME 158 (1944), p. 157.
- 7) R.A. Grange, "Boron in Iron and Steel", Boron, Calcium, Columbium and Zirconium in Iron and Steel Alloys of Iron, Research Monograph Series, John Wiley and Sons, Inc., N.Y., N.Y., (1957), p. 3-57.
- 8) W.E. Jominy and A.L. Boegehold, "A Hardenability Test for Carburizing Steel", Trans. AIME, 26 (1938), p. 574.
- 9) G.F. Melloy, P.R. Slemmon and P.P. Podgursky, Met. Trans. 4 (1973), p. 2279.
- 10) Ph. Maitrepierre, D. Thivellier, J. Rofes-Vernis, D. Rousseau and R. Tricot, "Hardenability Concepts with Applications to Steel", D. Doane and J.S. Kirkaldy, ed., AIME (1978), p. 421.
- 11) B.M. Kapadia, Ibid., p. 448.

- 12) B.M. Kapadia, R.M. Brown and W.J. Murphy, Trans. AIME, 242 (1968), p. 1689.
- 13) C.R. Simcoe, A.R. Elsea and G.K. Manning, Trans., AIME, 203 (1955), p. 193.
- 14) C.R. Simcoe, A.R. Elsea and G.K. Manning, Ibid, 206 (1956), p. 984.
- 15) D.T. Llewellyn and W.T. Cook, Met. Tech., 1 (1974), p. 517.
- 16) J.C. Fisher, Trans. AIME, 200 (1954), p. 1146.
- 17) Ph. Maitrepierre, D. Thivellier and R. Tricot, Trans. ASM, 6A (1975), p. 287.
- 18) J.E. Morral and T.B. Cameron, "Boron Hardenability Mechanisms", Boron in Steel, S.K. Banerji and J.E. Morral, eds., TMS/AIME, (1980), p. 19.
- 19) V.T. Borisov, V.M. Golikov and G.V. Scherbedkinskiy, Phys. Metals and Metallography, 17 (1960), p. 80.
- 20) R.C. Sharma and G.R. Purdy, Metall. Trans., 4 (1973), p. 2303.
- 21) J.E. Morral and T.B. Cameron, Metall. Trans., 8A (1977), p. 1817.
- 22) V.V. Levitin, Phys. Metals and Metallography, 10 (1960), p. 130.
- 23) R.W. Balluffi, "Interfacial Segregation", W.C. Johnson and J.M. Blakely, eds., ASM, (1979), p. 193.
- 24) C. Zener, Trans. AIME, 167 (1946), p. 550.
- 25) H.I. Aaronson, "Decomposition of Austenite by Diffusional Processes", Interscience Publishers New York, (1962), p. 387.

- 26) Y. Ohmori and K. Yamanaka, Boron in Steel, S.K. Banerji and J.E. Morral, eds., TSM/AIME, (1980), p. 44.
- 27) K. Yamanaka and Y. Ohmori, 'Effect of Boron on Transformation of Low-Carbon Low-Alloy Steels', Trans. ISIJ, 17 (1977), p. 92.
- 28) F.B. Pickering, "Microalloying 75", Union Carbide Corporation, New York, (1977), p. 9.
- 29) G.D. Rather and C.D. Armstrong, Trans. ASM, 40 (1948), p. 1099.
- 30) D.J. Hayes, Proc. 14th Mechanical Working and Steel Processing Conference, Chicago, (1972).
- 31) Ph. Maitrepierre, J. Rofes-Vernis and D. Thivellier, "Boron in Steels", S.K. Banerji and J.E. Morral, eds., AIME, (1980), p. 1.
- 32) G.J. Sojka, M.R. Krishnadev and S.K. Banerji, Ibid., p. 165.
- 33) R.A. Grange and J.B. Mitchell, "On the Hardenability Effect of Boron in Steel", Trans. ASM, 53 (1961), p. 157.
- 34) K.J. Irvine, F.B. Pickering, W.C. Haselwood and M. Atkins, "The Physical Metallurgy of Low-Carbon, Low-Alloy Steels Containing Boron", Jour. Iron Steel Inst., May (1957), p. 54.
- 35) M. Ueno and T. Inoue, "Distribution of Boron at Austenite Grain Boundaries and Bainitic Transformation in Low Carbon Steels, Trans. ISIJ, 13 (1973), p. 210.
- 36) W.F. Jandeska, Jr. and J.E. Morral, "Distribution of Boron in Austenite", Metal. Trans., 3 (1972), 2933.
- 37) S.R. Keown and F.B. Pickering, "Some Aspects of the Occurrence of Boron in Alloy Steels", Met. Science, July (1977), p. 225.

- 38) H.J. Goldschmidt, *J. Iron Steel Inst.*, 209 (1971), p. 900.
- 39) T.M. Williams and K. Gott, *J. Nuclear Materials*, 95 (1980), p. 265.
- 40) A.F. Padilha and G. Schanz, *Ibid.*, p. 229.
- 41) A. Habu, M. Miyata, S. Sekino and S. Goda, *Trans. ISIJ*, 18 (1978), p. 492.
- 42) S. Watanabe, H. Ohtani and T. Kunitake, *Ibid.*, 23 (1983), p. 31.
- 43) S. Watanabe and H. Ohtani, *Ibid.*, p. 38.
- 44) Mitsuru Tanino, *Nippon Steel Technical Report*, No. 21, June (1983).
- 45) T.M. Williams, A.M. Stoneham and D.R. Harries, *Metal Sci.*, 10 (1976), p. 14.
- 46) Chu Youyi and He Xin Lai, *Proc. High Strength Low Alloy Steels*, D.P. Dunne and T. Chandra, eds., Wollongong, N.S.W., Australia, (1984), p. 327.
- 47) K.T. Aust, J.S. Armijo, E.F. Coch and J.H. Westbrook, *Trans. Amer. Soc. Met.* 60 (1967), p. 360.
- 48) K.T. Aust, R.E. Hanneman, P. Niessen and J.H. Westbrook, *Acta Met.*, 16 (1968), p. 291.
- 49) T.R. Anthony, *Ibid.*, 17 (1969), p. 603.
- 50) D.R. Harries and A.D. Marwick, *Phil. Trans. Roy. Soc.*, A295 (1980), p. 197.
- 51) G.S. Hauser, "Cold Forming Techniques - And How Applications Could be Expanded by More Suitable Steels", *J. Metals*, Sept. (1965), p. 969.

- 52) Ya. E. Gol'dshtein and A.L. Sarikova, *Metal Science and Heat Treatment*, Nos. 5-6, May-June, (1963), p. 250.
- 53) J. Field, "Effect of Boron on the Overheating Temperatures of Steel", *Metal Progress*, (1953) Reprint.
- 54) S.F. Urban and G.F. Comstock, U.S. Patent No. 2,602,028 (1952).
- 55) B.J. Thomas and G. Henry, *Boron in Steels*, S.K. Banerji and J.E. Morral, eds., TMS/AIME, Warrendale, PA, (1980), p. 80.
- 56) R. Viswanathan, *Met. Eng. Quart.*, 15-16 (1975), p. 50.
- 57) N. Takahashi, T. Fujita and T. Yamanaka, *Trans. ISIJ*, 15 (No. 8) (1975), p. 438.
- 58) I. Kozasu, C. Ouchi, T. Sampei and T. Okita, "Microalloying 75", Union Carbide Corporation, New York (1977), p. 120.
- 59) M. Cohen and W.S. Owen, *Ibid*, p. 2.
- 60) L.J. Cuddy, *Metall. Trans.*, 12A (1981), p. 1313.
- 61) M. Fukuda, T. Hashimoto and K. Kunishige, "Microalloying 75", Union Carbide Corporation, New York (1977), p. 136.
- 62) T. Tanaka, T. Enami, M. Kimura, Y. Saito and T. Hatomura, "Thermomechanical Processing of Microalloyed Austenite", eds., A.J. DeArdo, G.A. Ratz and P.J. Wray, AIME, Warrendale, Pa., USA (1982), p. 195.
- 63) J.P. Sah, G.J. Richardson and C.M. Sellars, *Met. Sci.*, 8 (1974), p. 325.
- 64) M. Katsumata; M. Machida and H. Kaji, "Thermomechanical Processing of Microalloyed Austenite", eds., A.J. DeArdo, G.A. Ratz and P.J. Wray, AIME, Warrendale, Pa., USA (1982), p. 101.

- 65) T. Hashimoto, H. Ohtani, T. Kobayashi, N. Hatano and S. Suzuki, *Ibid.*, p. 501.
- 66) S. Gohda, K. Watanabe, Y. Hashimoto, H. Hirayama and S. Kijima, *Trans. ISIJ*, 21 (1981), p. 360.
- 67) T. Tanaka, T. Funakoshi, M. Ueda, J. Tsuboi, T. Yasuda and ~~U~~Utahashi, "Microalloying 75", Union Carbide Corporation, New York (1977), p. 399.
- 68) H.J. McQueen and J.J. Jonas, "Treatise on Material Science and Technology", R.J. Arsenault ed., Academic Press, New York, N.Y. 6 (1975), p. 393.
- 69) "Introduction to Dislocations" 2nd Edition, D. Hull, International Series on Materials Science and Technology, Vol. 16, p. 19.
- 70) P.G. Shewmon, "Transformations in Metals", Met. Science and Eng. Series, McGraw-Hill, Toronto (1969).
- 71) "Recrystallization of Metallic Materials", F. Haessner, ed., Dr. Rieder-Verlag GMBH, Stuttgart (1978).
- 72) I. Weiss and J.J. Jonas, *Metall. Trans.*, 10A (1979), p. 831.
- 73) A. Le Bon, J. Rofes-Vernis and C. Rossard, *Met. Sci.*, 9 (1975), p. 36.
- 74) R.A. Petkovic, M.J. Luton and J.J. Jonas, *Ibid.*, p. 68.
- 75) R. Coladas, J. Masounave and J.P. Bailon, "The Hot Deformation of Austenite", J.B. Ballance ed., AIME, N. Y. (1977), p. 341.
- 76) J.J. Jonas and I. Weiss, *Met. Sci.*, 13 (1979), p. 238.
- 77) T. Gladman and F.B. Pickering, *J. Iron Steel Inst.*, 205 (1967), p. 653.

- 78) M.J. Luton, R. Dorvel and R.A. Petkovic, *Metal. Trans.*, 11A (1980), p. 411.
- 79) K. Lucke, G. Masing and P. Nölting, *Z. Metallk.* 76 (1956), p. 64.
- 80) K. Lucke and K. Detert, *Acta Met.* 5 (1957), p. 628.
- 81) A.H. Cottrell, *Dislocations and Plastic Flow in Crystals*, Oxford 1953, p. 57.
- 82) J.W. Rutter and K.T. Aust, *Trans. Met. Soc., AIME*, 218 (1960), p. 68.
- 83) J.W. Cahn, *Acta Met.*, 10 (1962), p. 789.
- 84) M.G. Akben, Ph.D. Thesis, McGill University, Montreal (1980).
- 85) B. Bacroix, M.Eng. Thesis, McGill University, Montreal (1982).
- 86) M.J. Luton, Ph.D. Thesis, McGill University, Montreal (1971).
- 87) R.A. Petkovic, Ph.D. Thesis, McGill University, Montreal (1975), p. 22.
- 88) J.N. Cordea, *Symposium on Low Alloy High Strength Steels, Nurnberg, BRD* (1970), *Metallurg. Companies*, p. 61.
- 89) J.D. Garnish and J.D.H. Hughes, *J. Matl. Sci.*, 7 (1972), p. 7.
- 90) X.L. He and Y.Y. Chu, "The Application of $^{10}\text{B}(n, \alpha)^7\text{Li}$ Fission Reaction to Study Boron Behaviour in Materials", *J. Phys. D; Appl. Phys.*, 16 (1983), p. 1145.
- 91) L.C. Berthiaume and Q.A. Walker, "Newtron Radiography at Chalk River", June (1971), CRNL - 628.

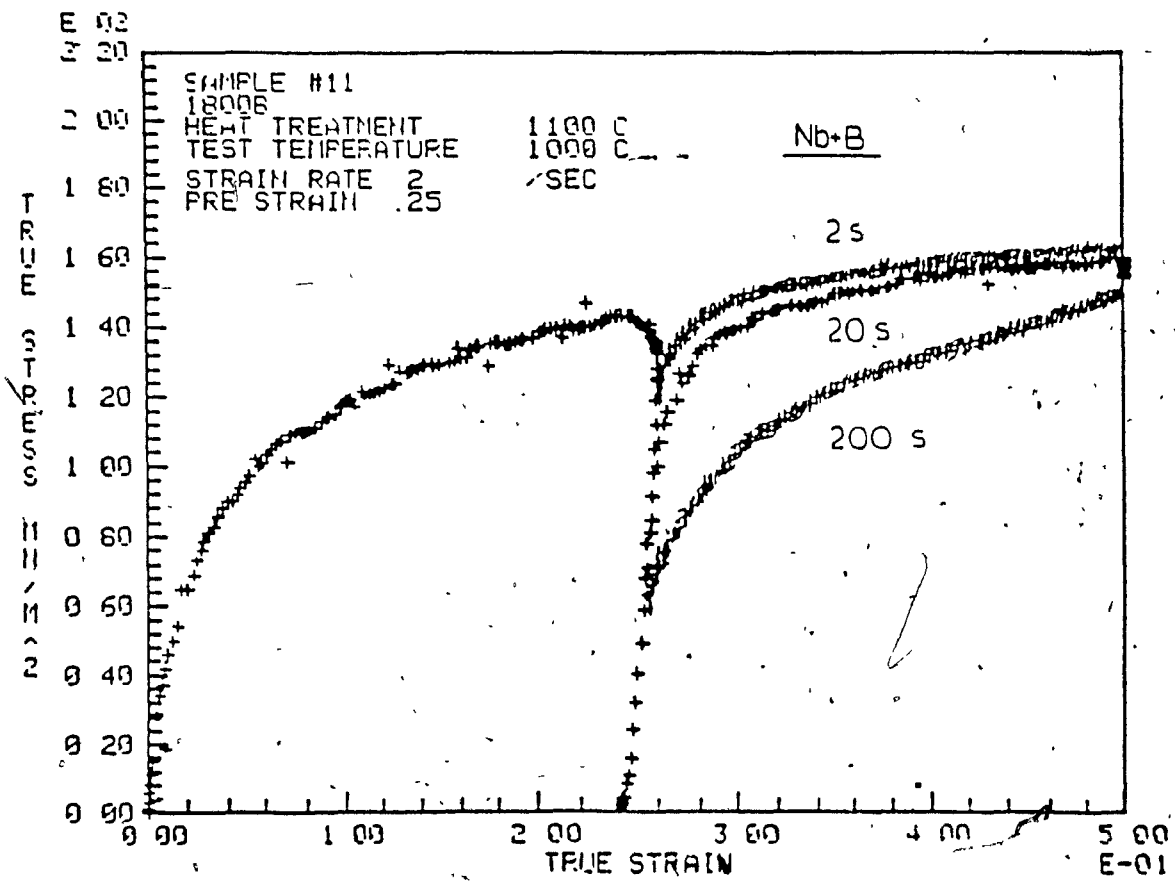
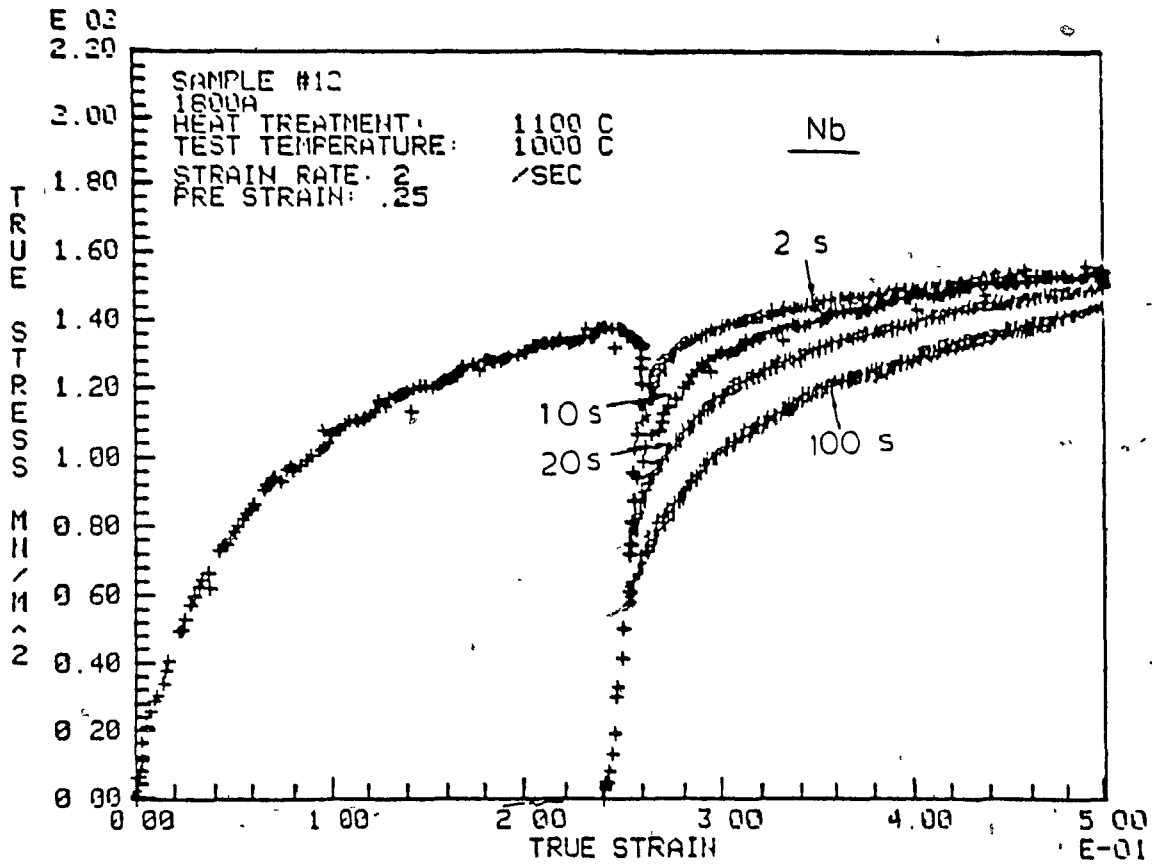
- 92) T. Sakai, M.G. Akben and J.J. Jonas, "Thermomechanical Processing of Microalloyed Austenite", Eds. A.J. DeArdo, G.A. Ratz and P.J. Wray, AIME, Warrendale, Pa., USA (1982), p. 237.
- 93) M. Avrami, J. Chem. Phys., 7 (1939), p. 1103.
- 94) M. Avrami, J. Chem. Phys., 8 (1940), p. 212; (1941), p. 177.
- 95) M.J. Luton, R.A. Petkovic and J.J. Jonas, Acta Met., 28 (1979), p. 729.
- 96) D.R. Barraclough and C.M. Sellars, Metal Sci., 13 (1979), p. 257.
- 97) W.B. Morrison, J. Iron Steel Inst., 210 (1972), p. 618.
- 98) R.A.P. Djaic and J.J. Jonas, Metall. Trans., 4 (1973), p. 621.
- 99) C.M. Sellars, "Hot Working and Forming Processes", C.M. Sellars and G.J. Davies, eds., The Metals Society, London (1980), p. 3.
- 100) C.K. Bullough, J.K. Jenkins and C.A. English, "A Study of Precipitation and Boron Distribution in 20 Cr 25 Ni Base Stainless Steels", AERE Harwell, Oxfordshire, March (1984), AERE-M 3353.
- 101) J. Davidson, P. Balladou, Y. Honnorat and X. Waché, Mém. Scient. Rev. Mét., 70 (1973), p. 543.
- 102) W.C. Leslie, "The Physical Metallurgy of Steels", 1st ed., McGraw-Hill Book Co., New York, N.Y. (1981), p. 136.
- 103) J.J. Jonas and M.G. Akben, Metals Forum, 4 (Nos. 1 and 2) (1981), p. 92.
- 104) S. Yamamoto, C. Ouchi and T. Osaka, "Thermomechanical Processing of Austenite", eds. A.J. DeArdo, G.A. Ratz and P.J. Wray, AIME, Warrendale, Pa., USA (1982), p. 613.

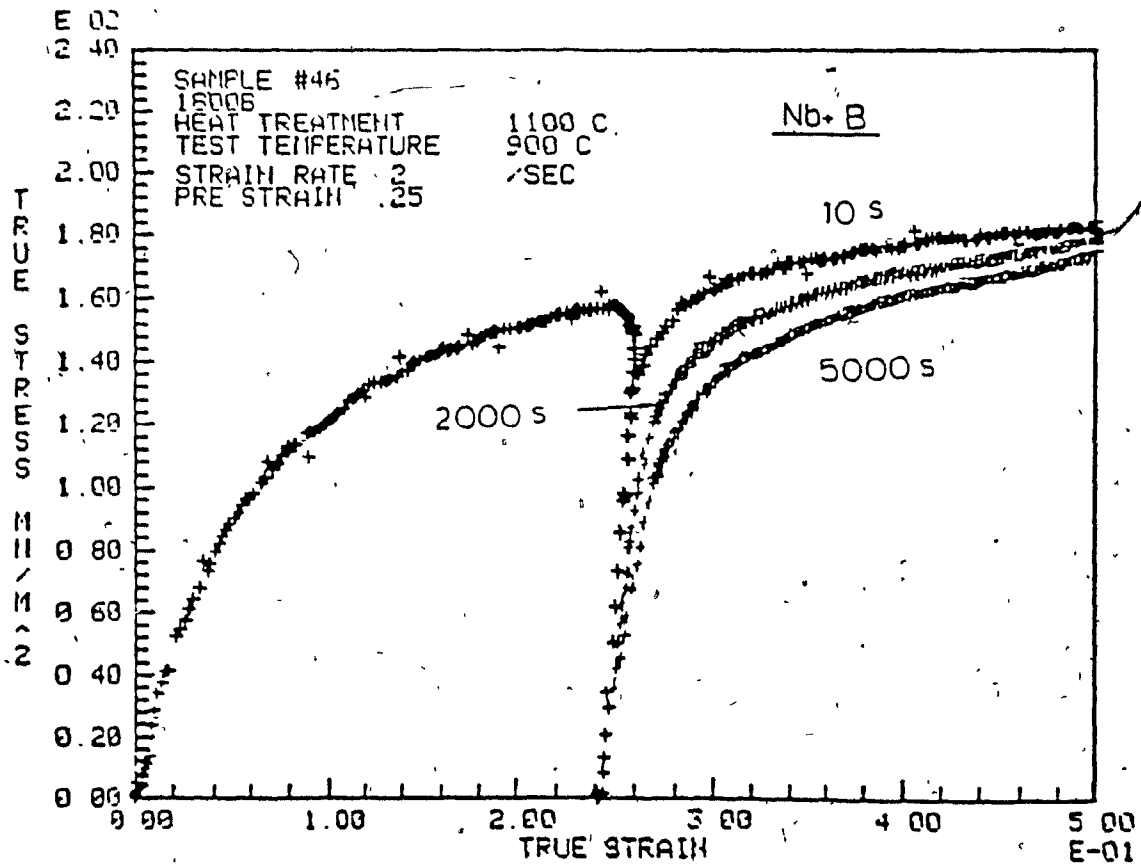
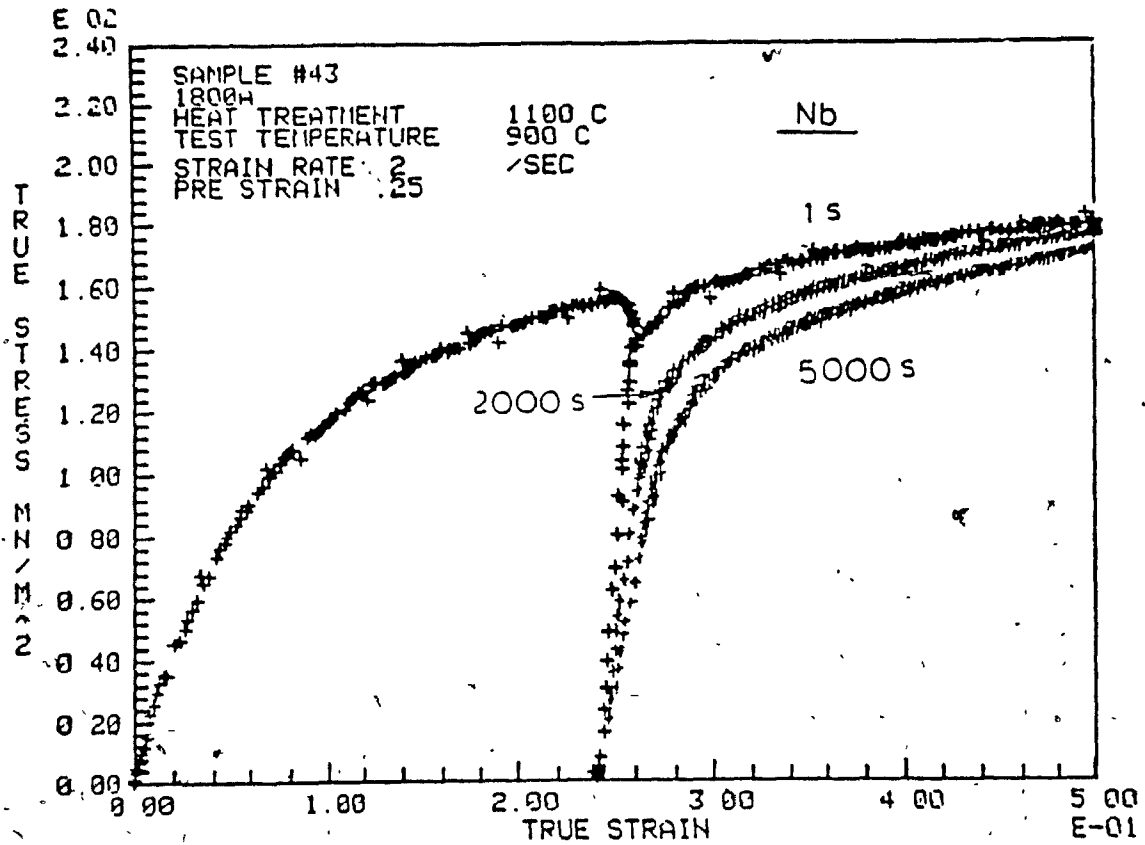
- 105) H. Oikawa, "Lattice Self-Diffusion in Solid Iron: A Critical Review", Tech. Rep. Tohoku Univ., 46 (1982), p. 67.
- 106) T. Ustad and H. Sørum, Phys. Stat. Sol., 20 (1973), p. 285.
- 107) J.R. MacEwan, J.U. MacEwan and L. Yaffe, Canad. J. Chem., 37 (1959), p. 1626.
- 108) J.I. Goldstein, R.A. Hanneman and R.E. Ogilvie, Trans. Metall. Soc. AIME, 233 (1965), p. 812.
- 109) G. Henry and G. Cizeron, Ann. Chim. (Paris), 3 (1978), p. 167.
- 110) A.M. Huntz, P. Guiraldenq, M. Aucouturier and P. Lacombe, Mém. Sci. Rev. Metall., 66 (1969), p. 85.
- 111) P.J. Alberry and C.W. Haworth, Met. Sci., 8 (1974), p. 407.
- 112) K. Nohara and K. Hirano, "Proc. Intern. Conf. on Sci. and Tech. of Iron and Steels", Suppl. to Trans. Iron Steel Inst. Jpn. (1971), p. 1267-73.
- 113) S. Tsuji and H. Yamanaka, J. Jpn. Inst. Metals, 34 (1970), p. 486.
- 114) A.W. Bowen and G.M. Leak, Metall. Trans., 1 (1970), p. 1695.
- 115) M.A. Krishtali A.P. Mokrov, Zaved. Lab., 33 (1967), p. 827.
- 116) J.L. Ham, Trans. Am. Soc. Met., 35 (1945), p. 331.
- 117) S. Tsuji, J. Jpn. Inst. Metals, 40 (1976), p. 844.
- 118) B. Sparke, D.W. James and G.M. Leak, J. Iron Steel Inst., 203 (1965), p. 152.
- 119) Jürgen Geise and Christian Herzig, Z. Metallkunde., 76 (1985), p. 622.

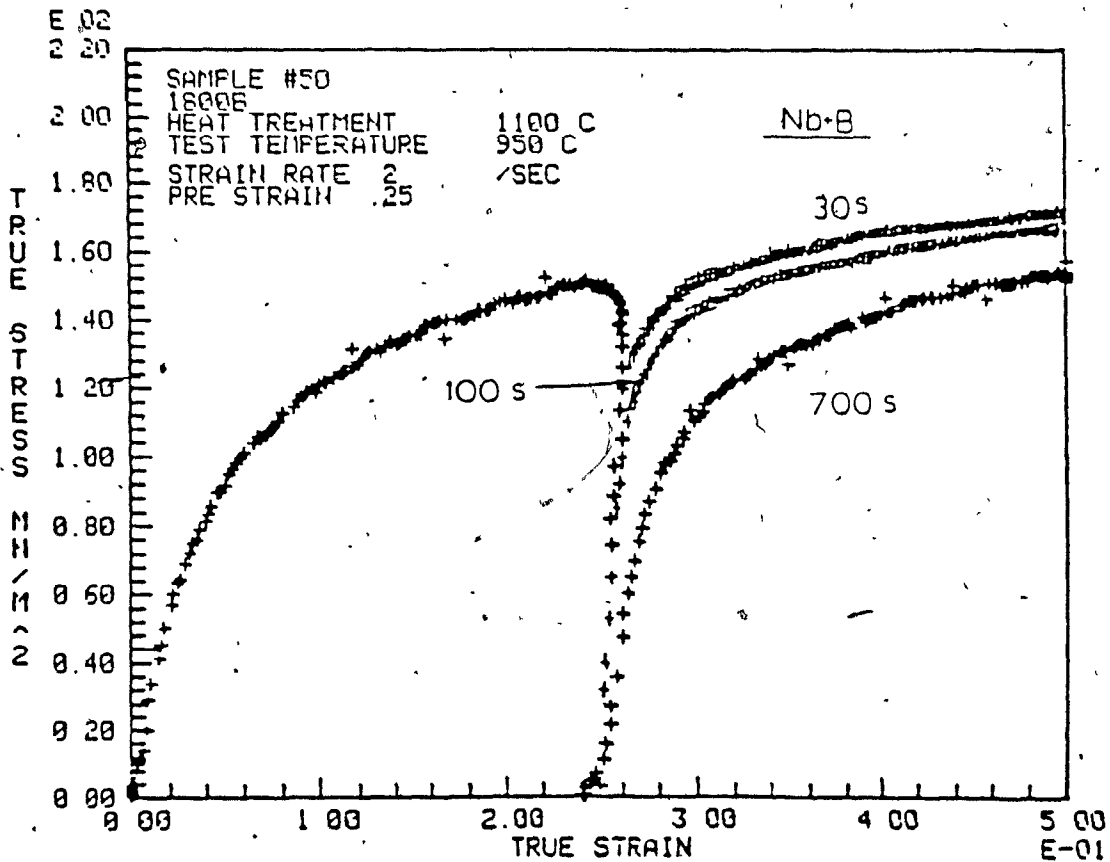
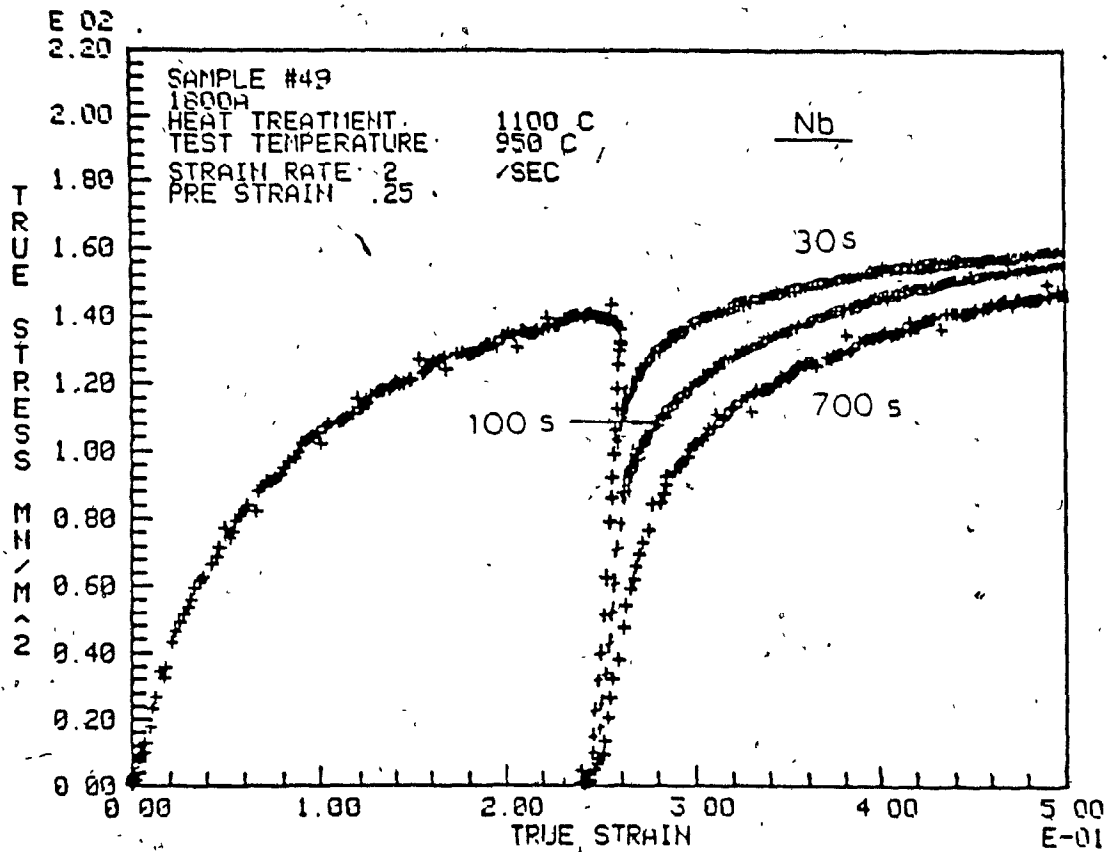
- 120) Deformation - Mechanism Maps The Plasticity and Creep of Metals and Ceramics, eds. Harold J. Frost and Michael F. Ashby, Pergamon Press, (1982).
- 121) W.B. Pearson, The Crystal Chemistry and Physics of Metals and Alloys, Wiley, New York (1972).
- 122) Grain Boundaries in Metals, D. McLean, Oxford (1957), p. 225.
- 123) R.E. Hoffman and D. Turnbull, J. Appl. Phys., 22 (1951), p. 634.
- 124) P. Gordon and R.A. Vandermeer, "Recrystallization, Grain Growth and Textures", Metals Park, Ohio (ASM), 1966, p. 205.
- 125) M. Hillert and B. Sundman, Acta Metall., 24 (1976), p. 731.
- 126) Chr. Herzig, P. Neuhaus and J. Geise, Solute-Defect Interaction Theory and Experiment, S. Saimoto, G. Purdy and G. Kidson, eds., Pergamon Press, Kingston, Canada, (1935), p. 271.
- 127) He Xinlai, Chu Youyi, Tang Li, Zhou Zhenxin and T. Ko, "The Process of Nonequilibrium Segregation of Boron to Austenite Grain Boundaries", Symposium of Grain Boundary Structure and Related Phenomena, Minakami Spa Japan, 25-29th Nov. (1985).
- 128) He Xinlai, Chu Youyi and Ke Jun, The China-USA Bilateral Metallurgical Conference, Beijing, Nov. 15-18, (1981), p. 532.
- 129) Hiroshi Tamehiro, M. Murata and R. Habu, "Effect of Combined Addition of Niobium and Boron on Thermomechanically Processed Steel", Conf. Proc., 4-8 November (1985), Beijing, China.
- 130) M.G. Akben, T. Chandra, P. Plassiard and J.J. Jonas, Acta Metall., 32 (1984), p. 591.
- 131) M.E. Nicholson, Trans. AIME, 200 (1954), p. 185.

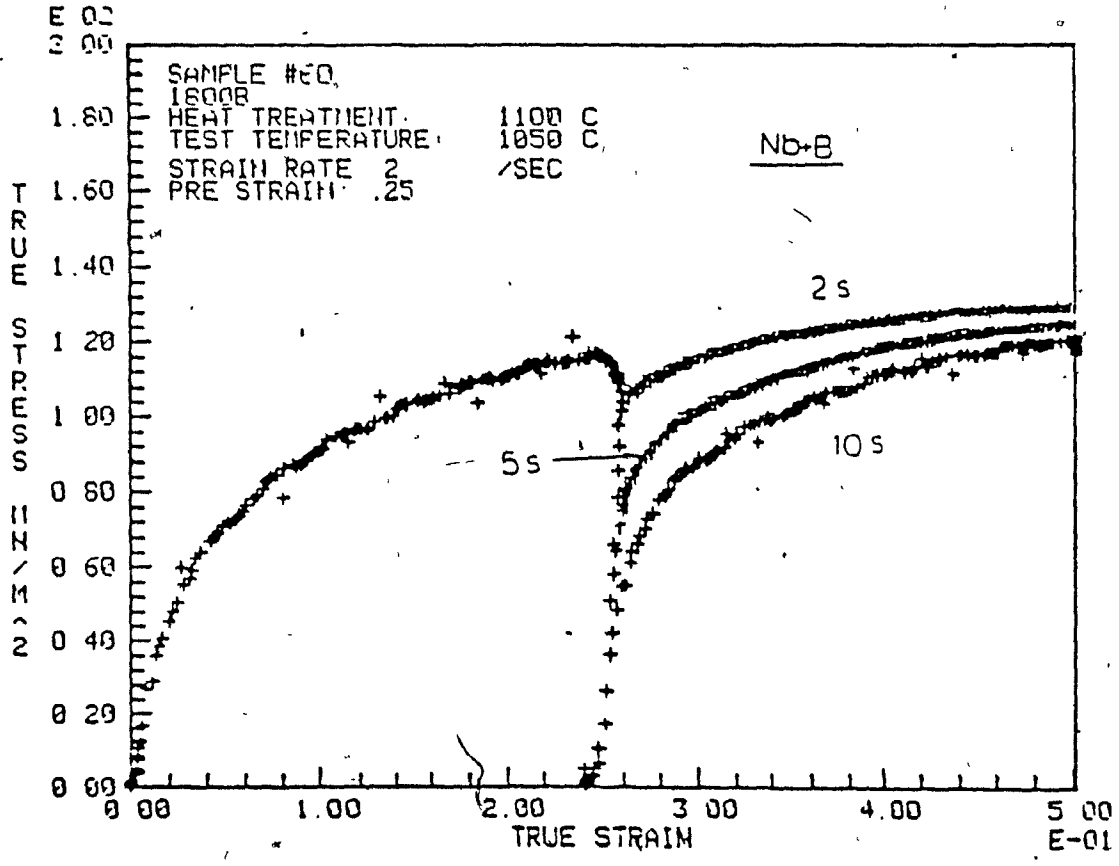
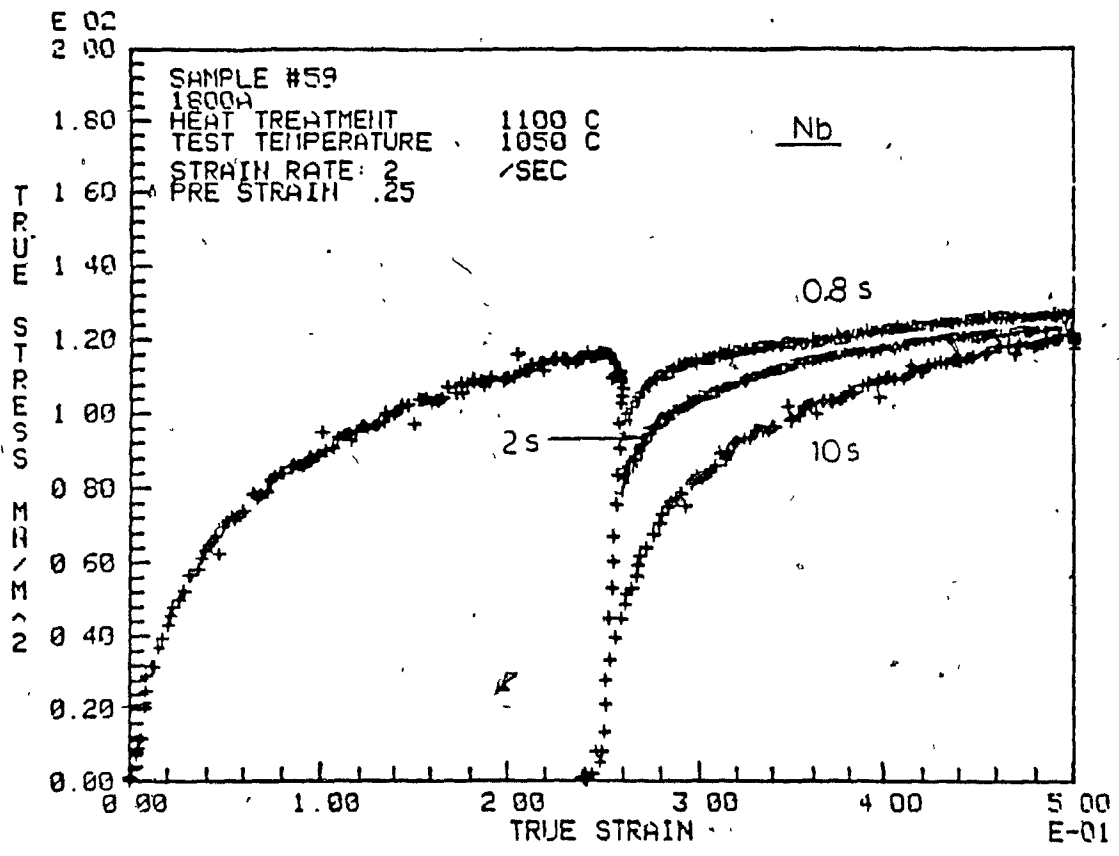
- 132) R.M. Goldhoff and J.W. Spretnak, *Ibid.*, 209 (1957), p. 1278.
- 133) W.R. Thomas and G.M. Leak, *Nature*, 176 (1955), p. 29.
- 134) G.M. Leak, *Metal Treatment*, 21 (1956), p. 45.
- 135) A. Brown, J.D. Garnish and R.W.K. Honeycombe, *Metal Sci. J.*, 8 (1974), p. 317.
- 136) A. Lucci, G. Della Gatta and G. Venturello, *Ibid.*, 3 (1969), p. 14.
- 137) H. Hayashi and T. Sugeno, *Acta Met.*, 18 (1970), p. 693.
- 138) P.E. Busby and C. Wells, *Trans. AIME*, 200 (1954), p. 972.
- 139) P.E. Busby, M. Warga and C. Wells, *Ibid.*, 197 (1953), p. 1463.
- 140) W. Roberts and B. Ahlblom, *Acta Metall.*, 26 (1978), p. 801.
- 141) W. Roberts, H. Bodén and B. Ahlblom, *Metal Sci.*, 13 (1979), p. 195.
- 142) L. Blaz, T. Sakai and J.J. Jonas, *Ibid.*, 17 (1983), p. 609.
- 143) P.J. Wray, *Metal. Trans.*, 15A (1984), p. 2009.
- 144) J.P. Sah, G.J. Richardson and C.M. Sellars, *J. Aust. Inst. Metals*, 15 (1969), p. 292.
- 145) J.J. Jonas and T. Sakai, *24ème Colloque de Métallurgie de Saclay*, 16, 17 et 18 juin 1981, p. 35.

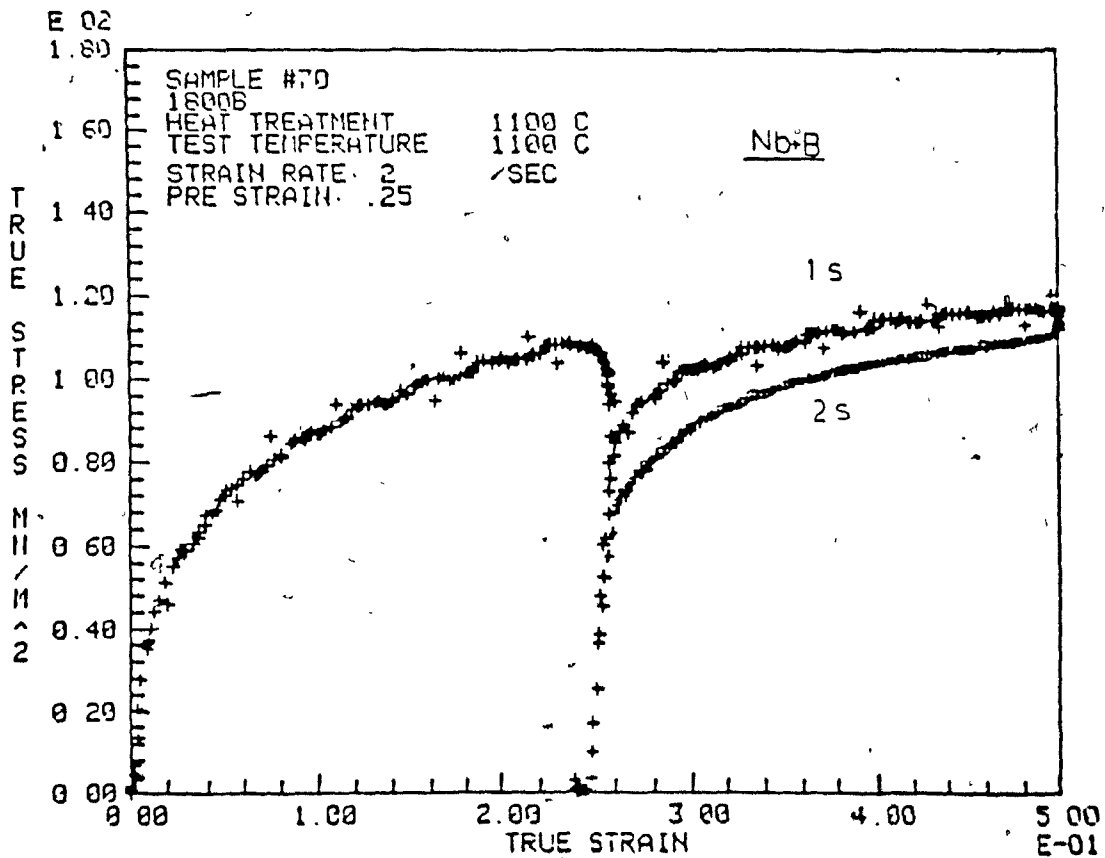
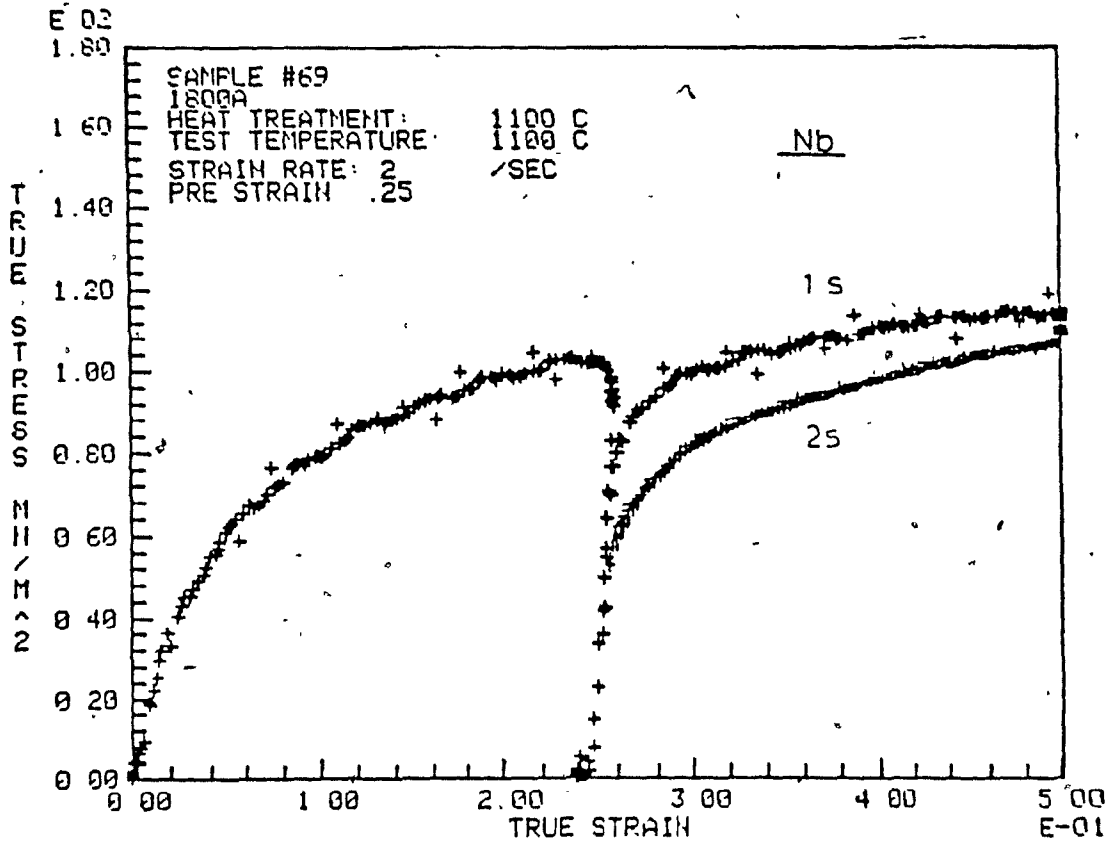
APPENDIX I
INTERRUPTED COMPRESSION TEST FLOW CURVES

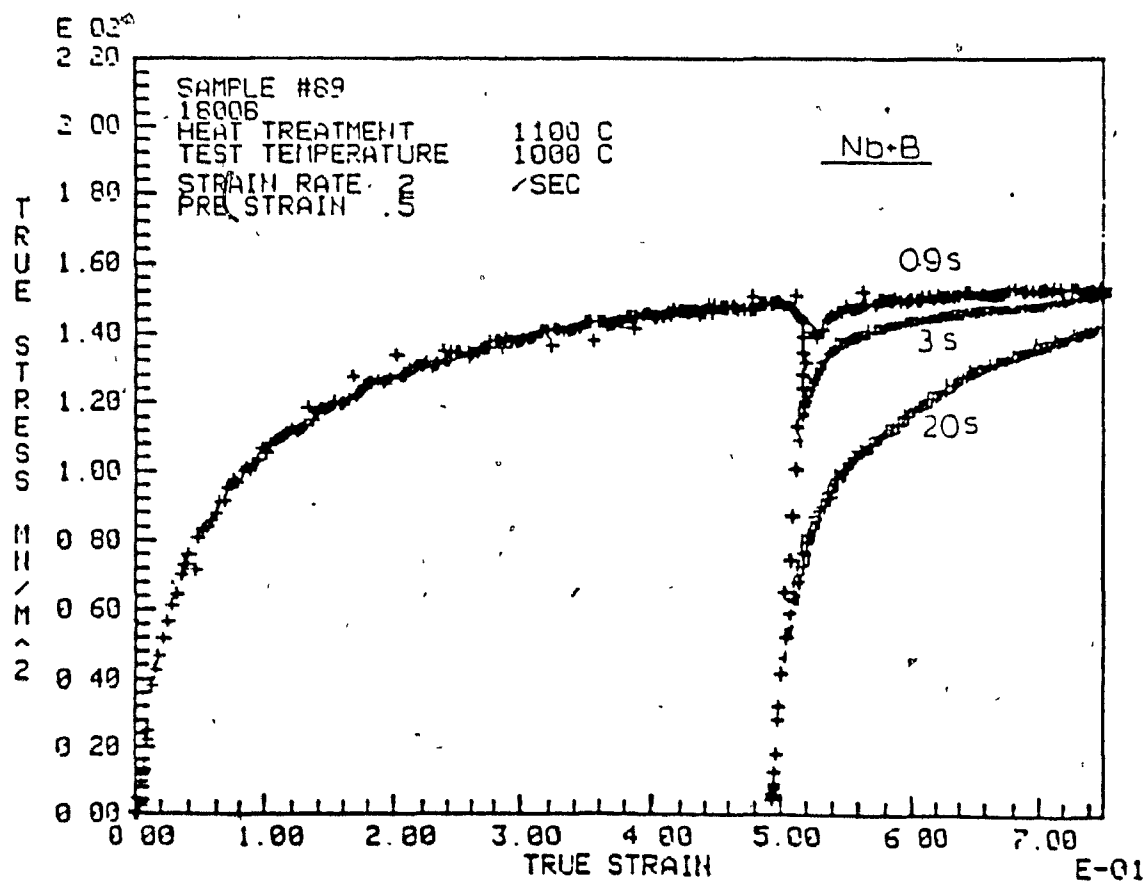
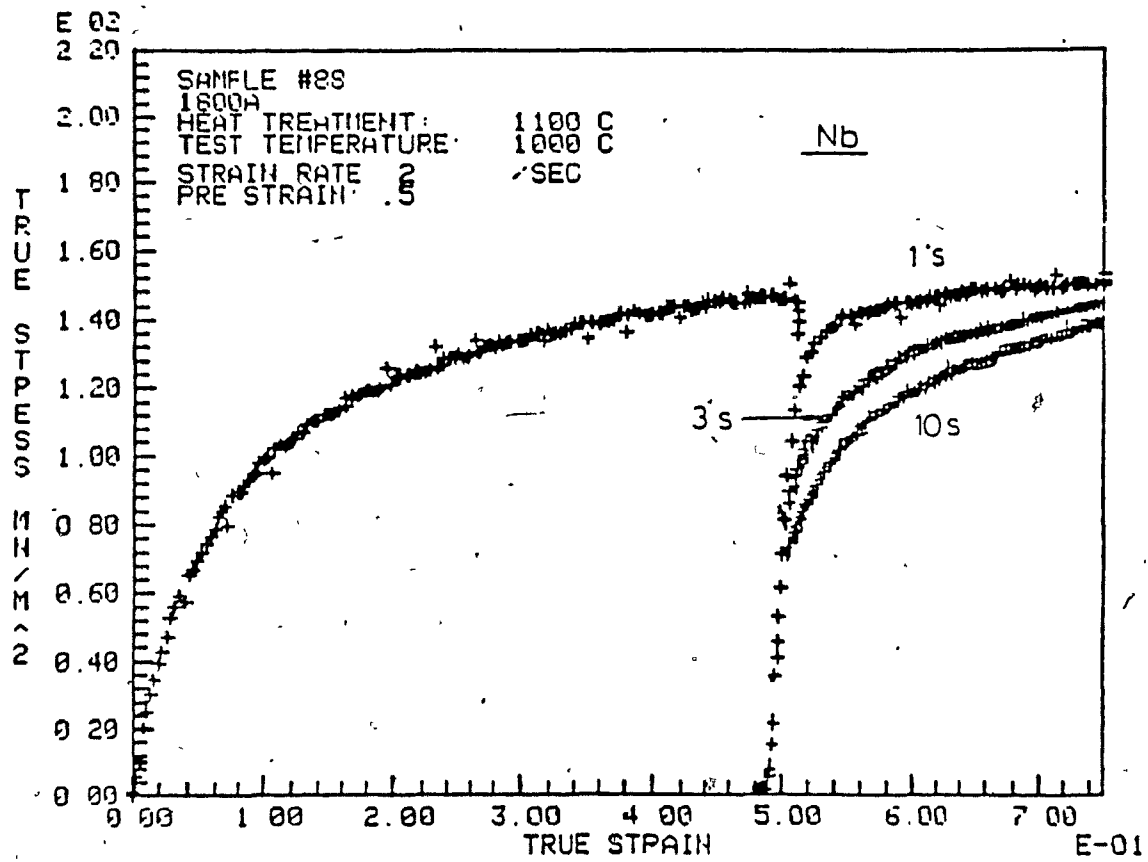


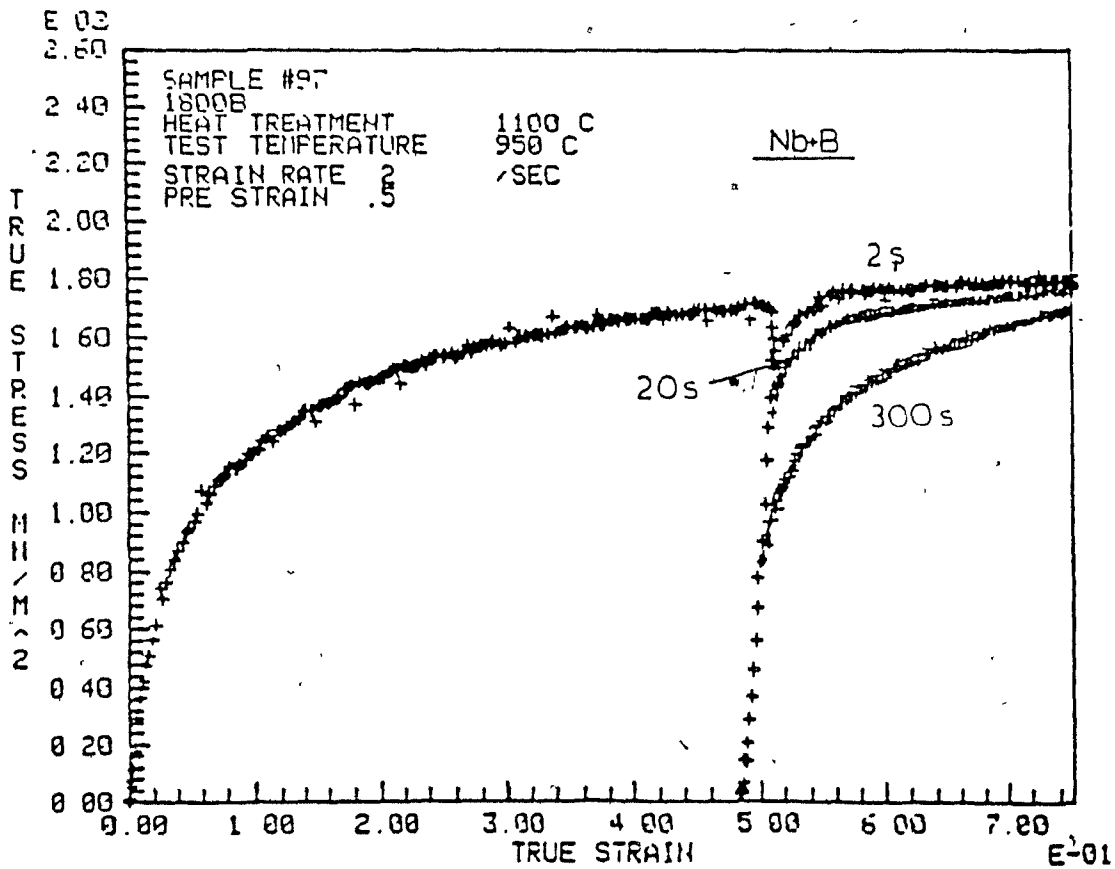
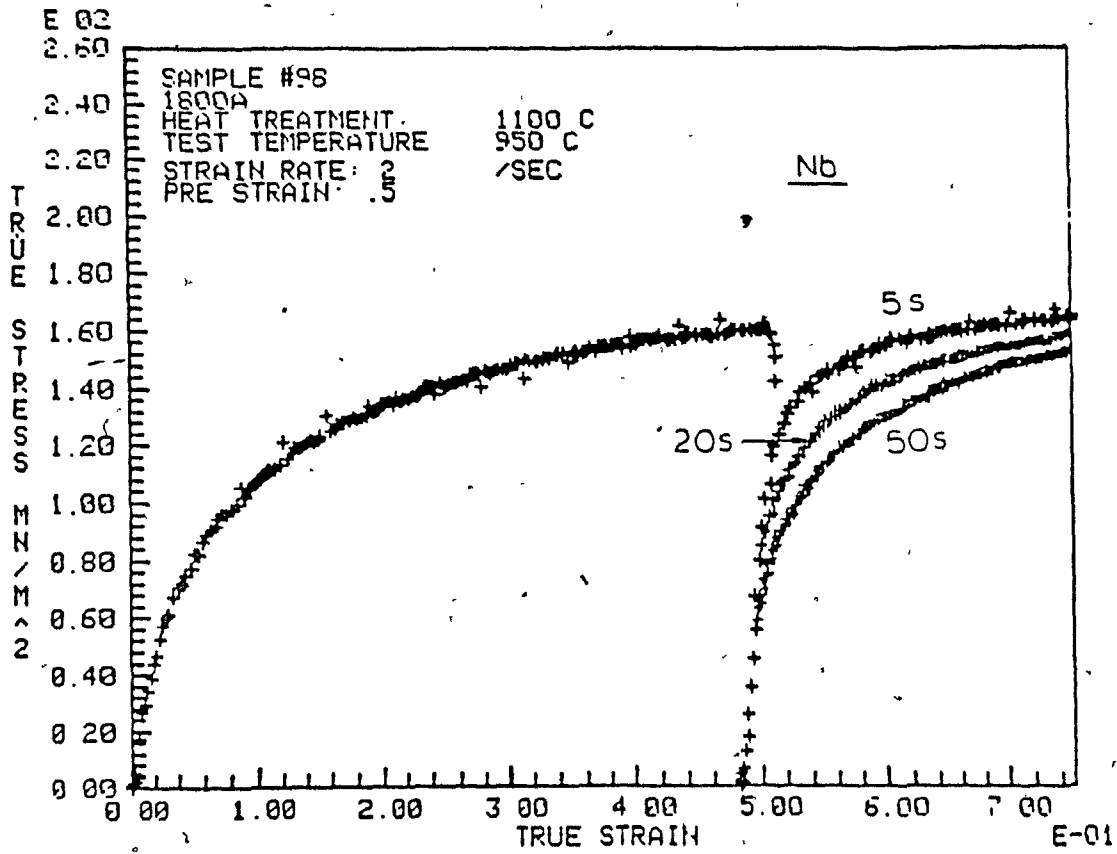


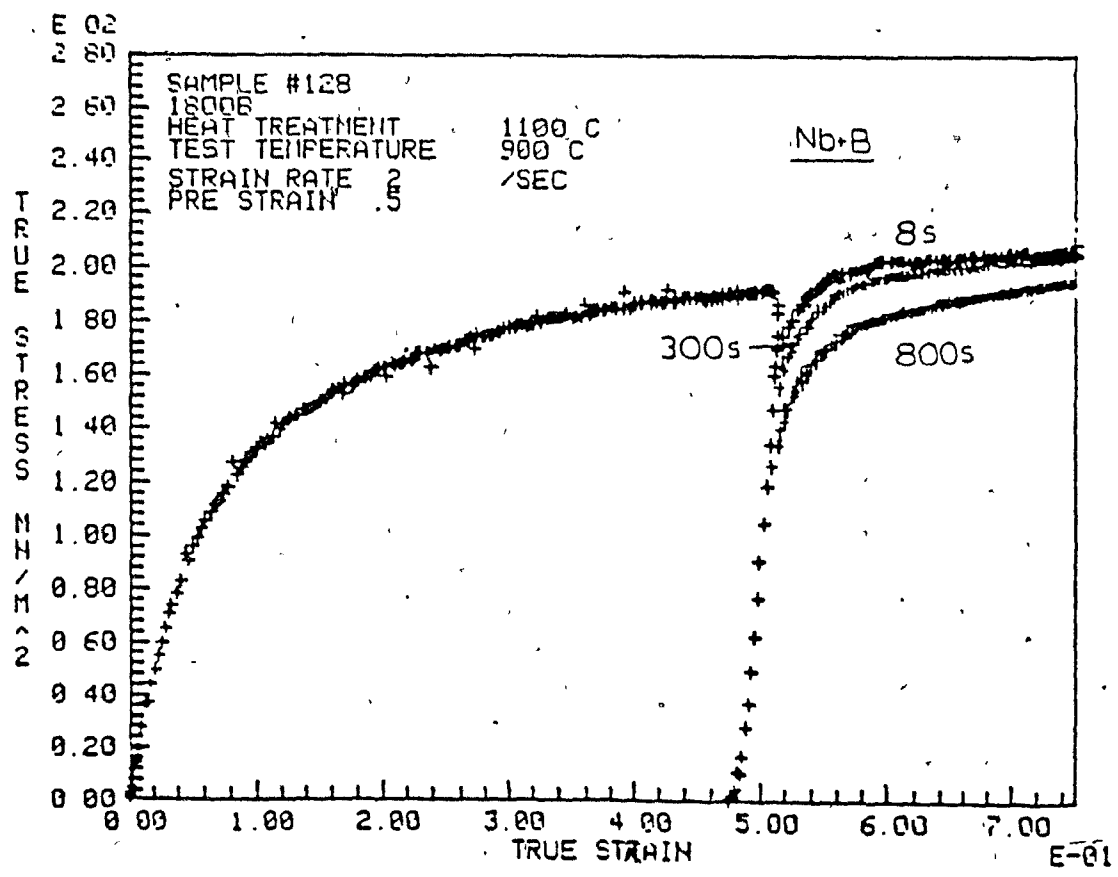
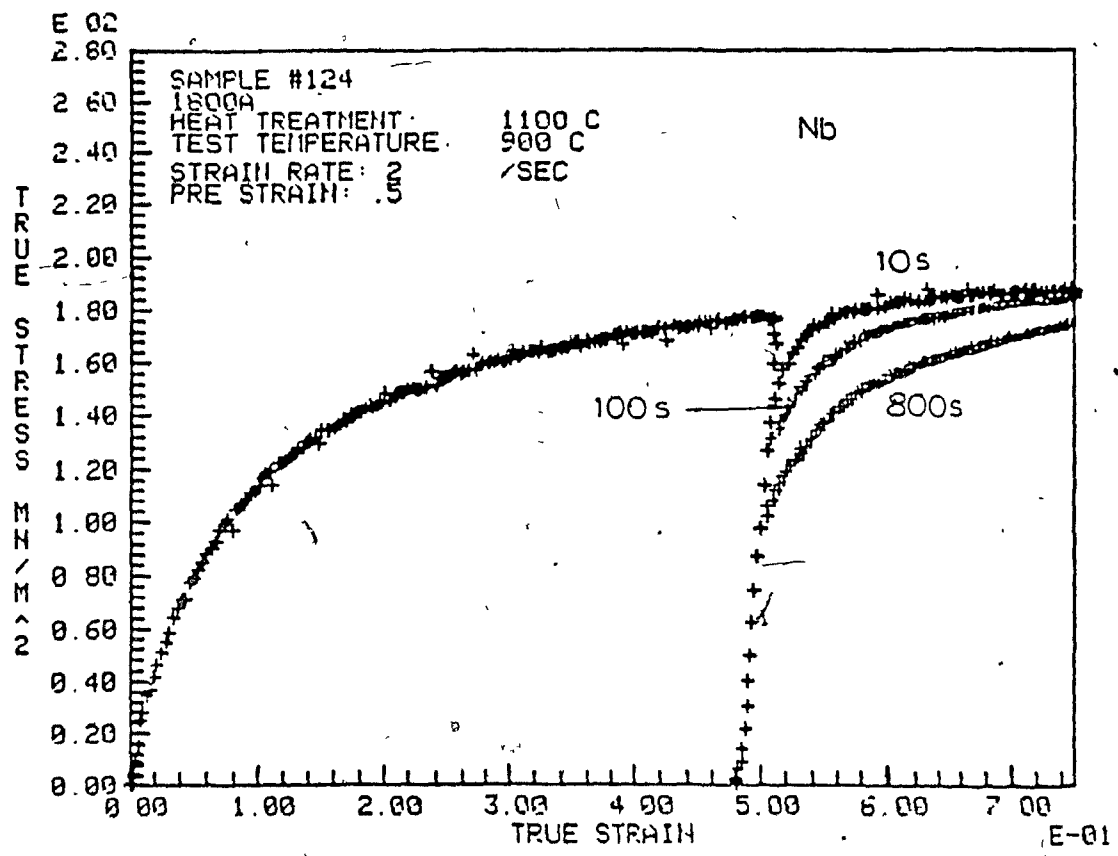


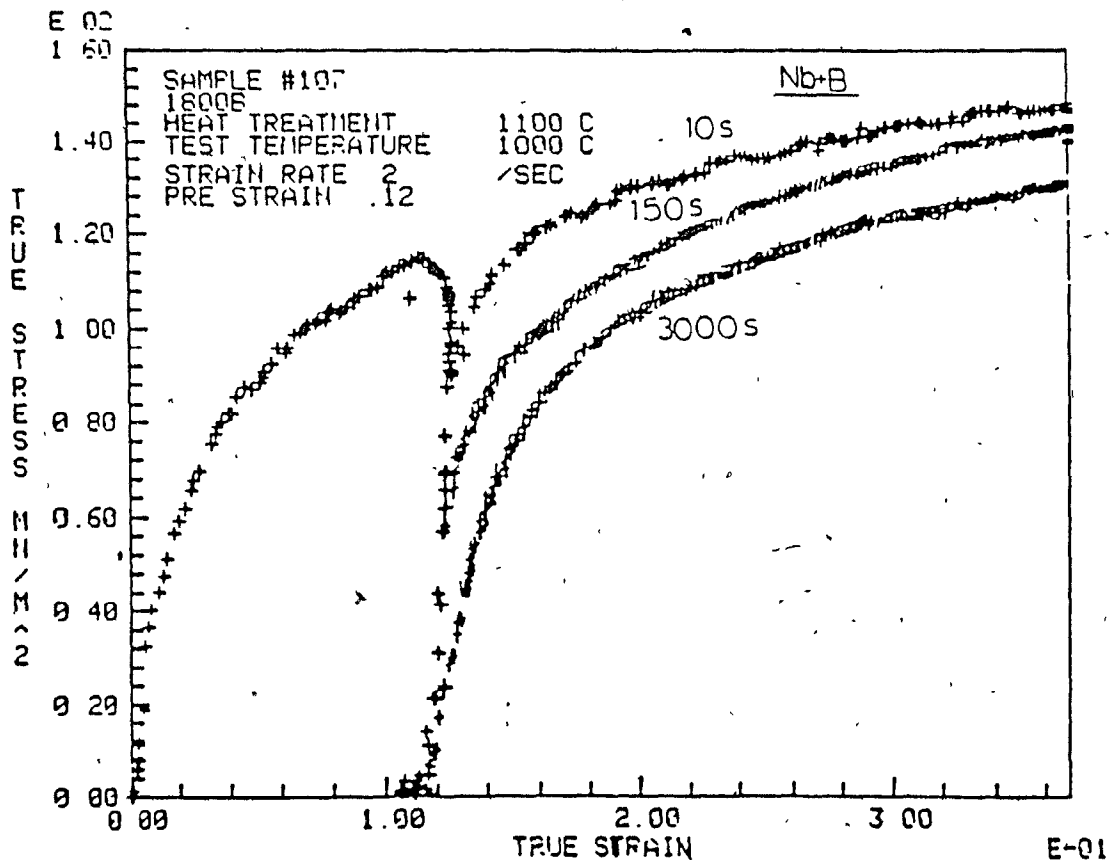
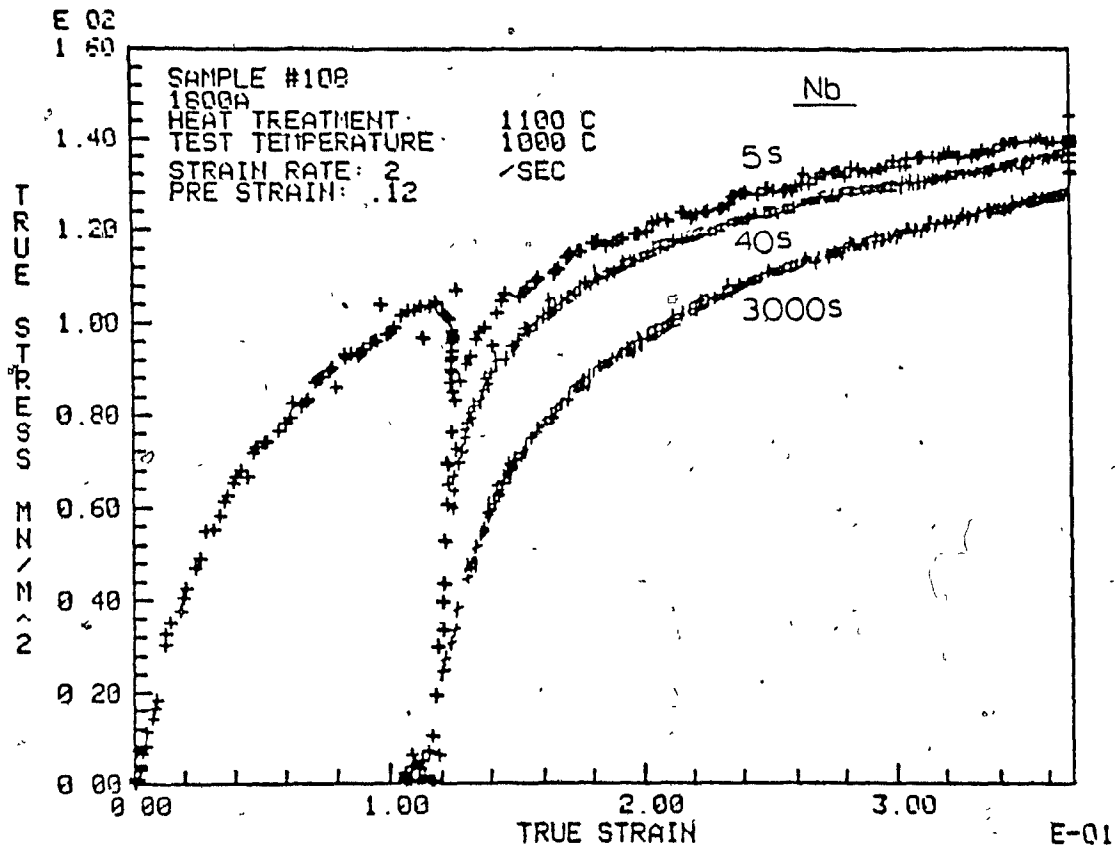


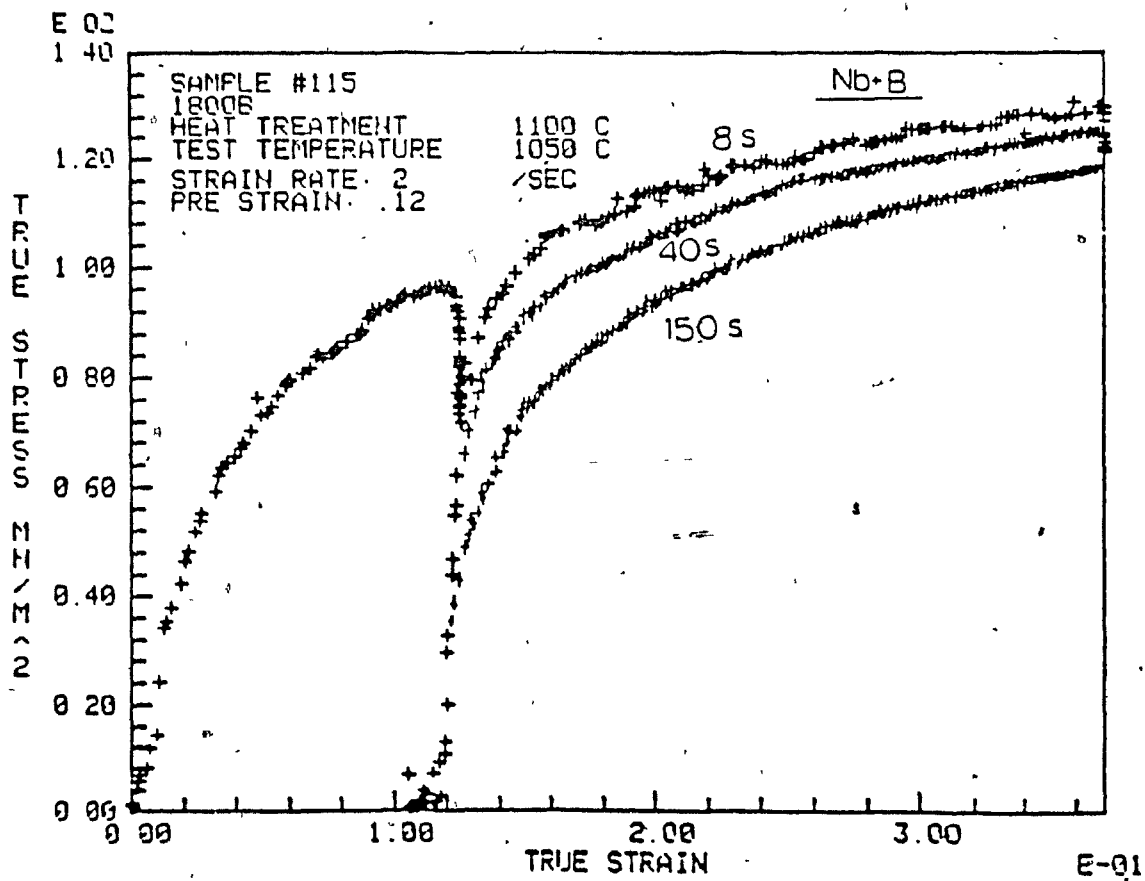
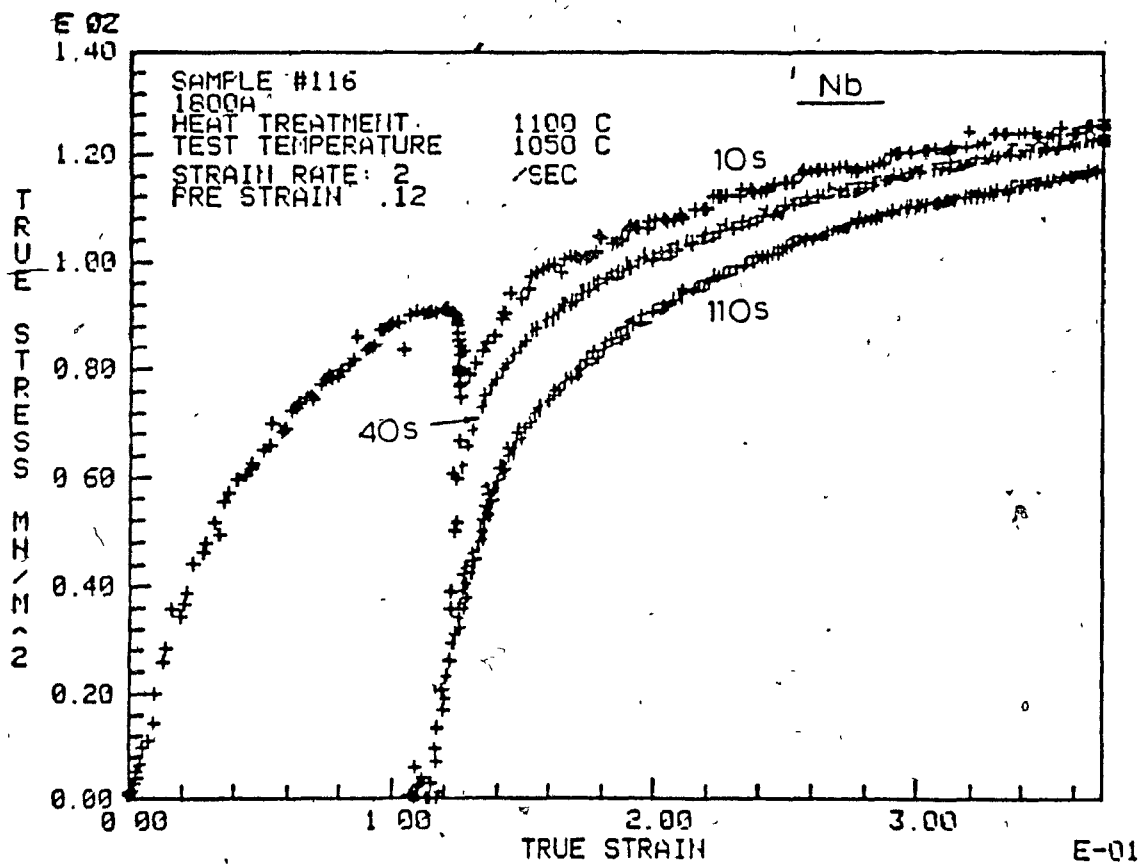


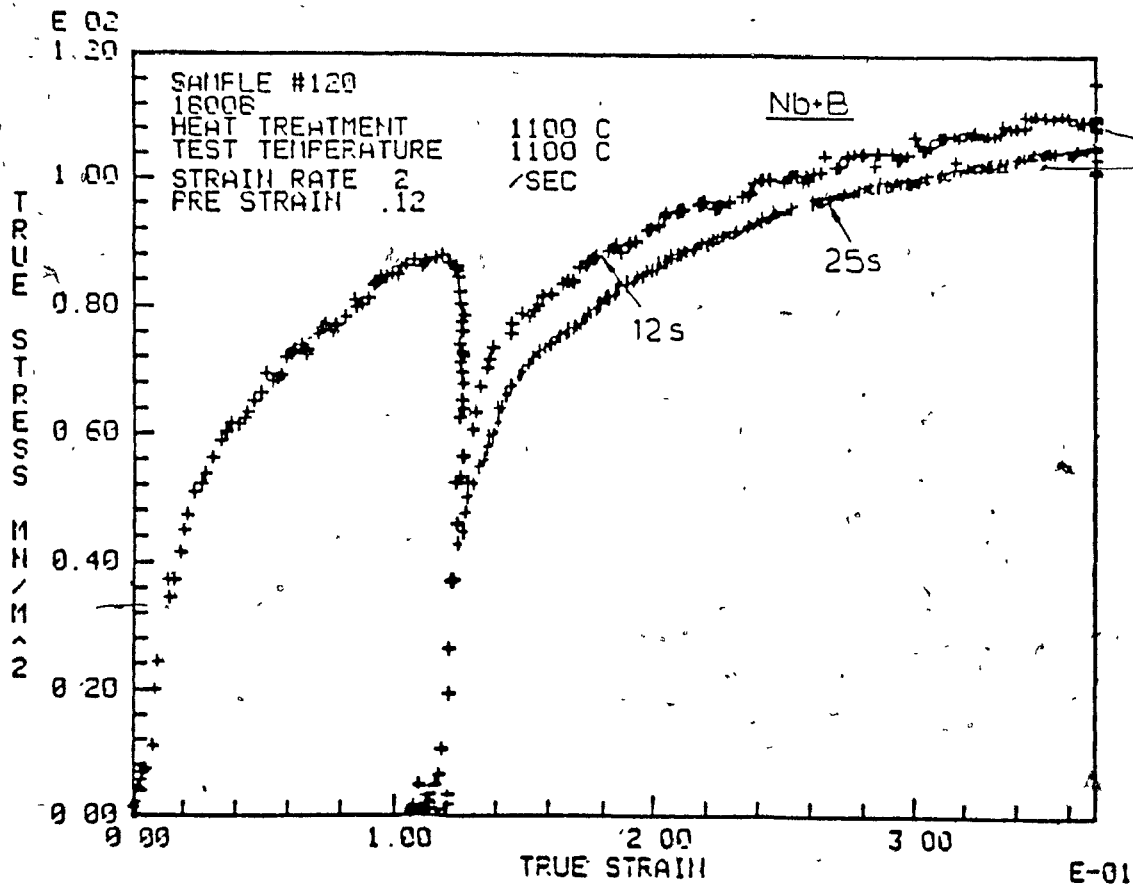
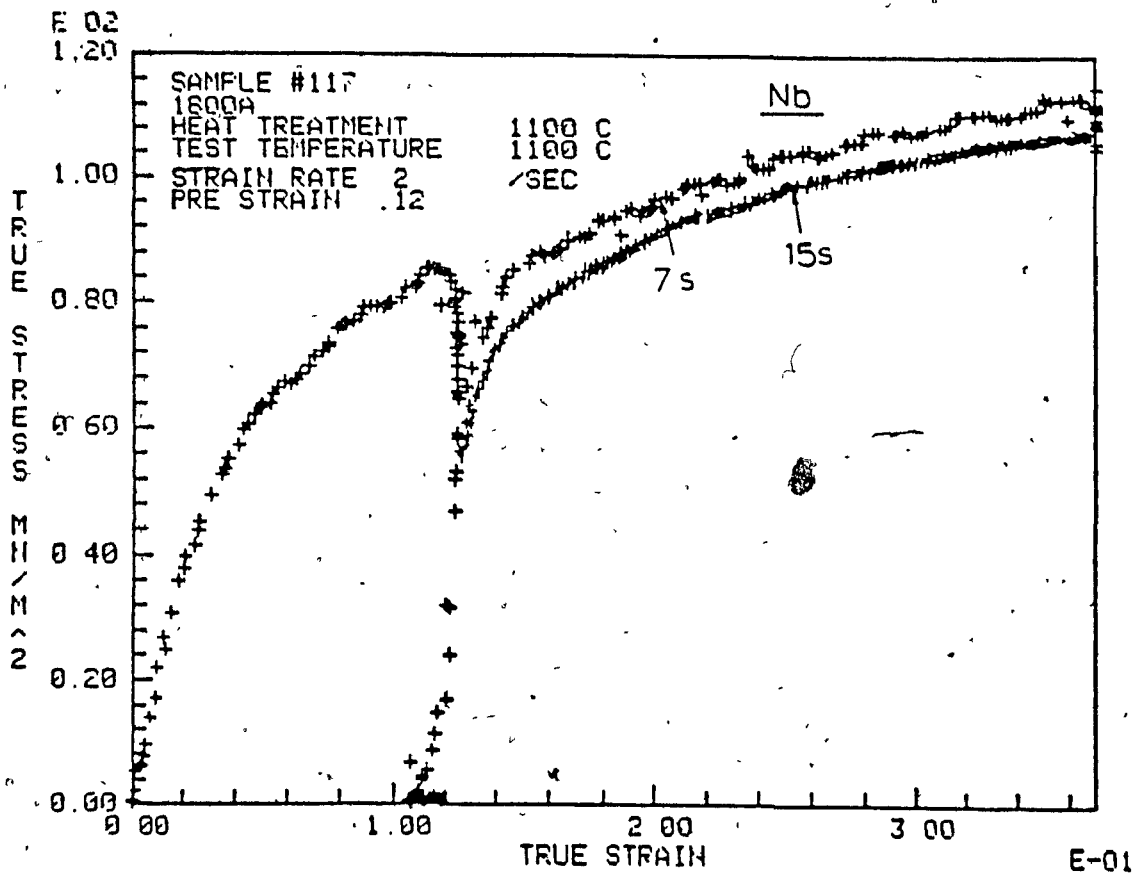


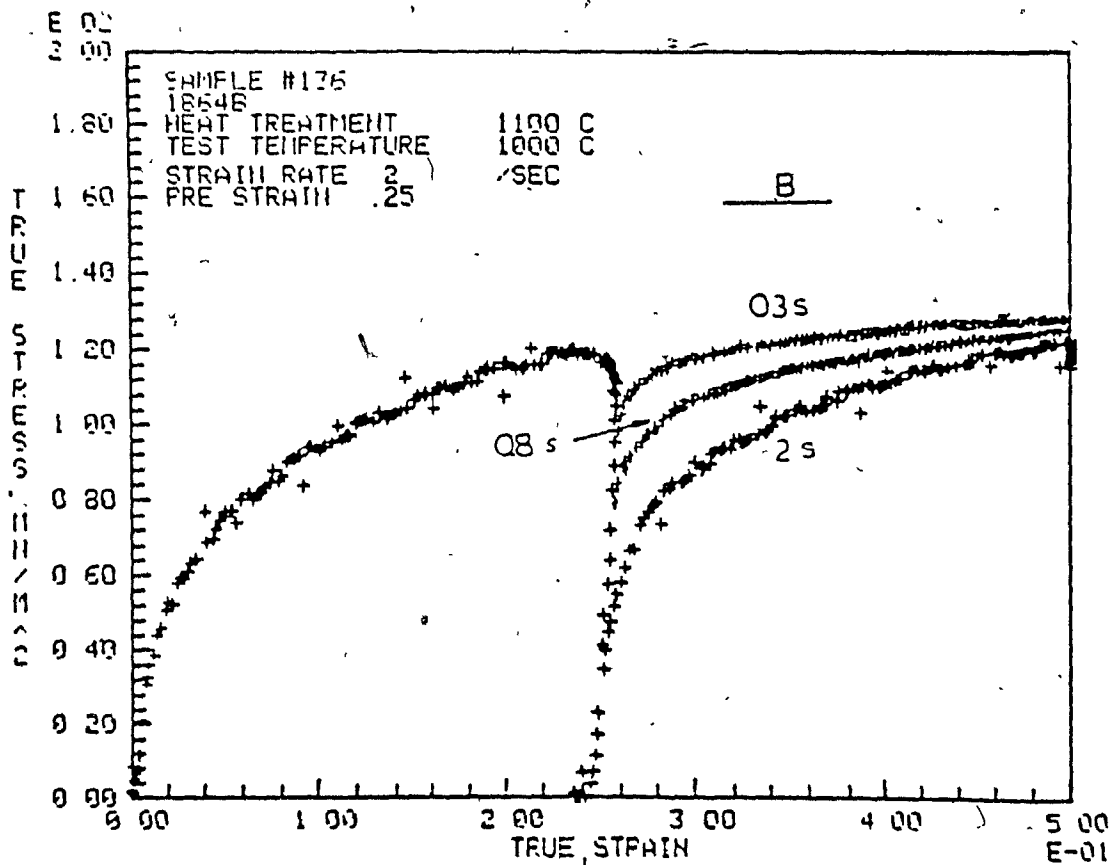
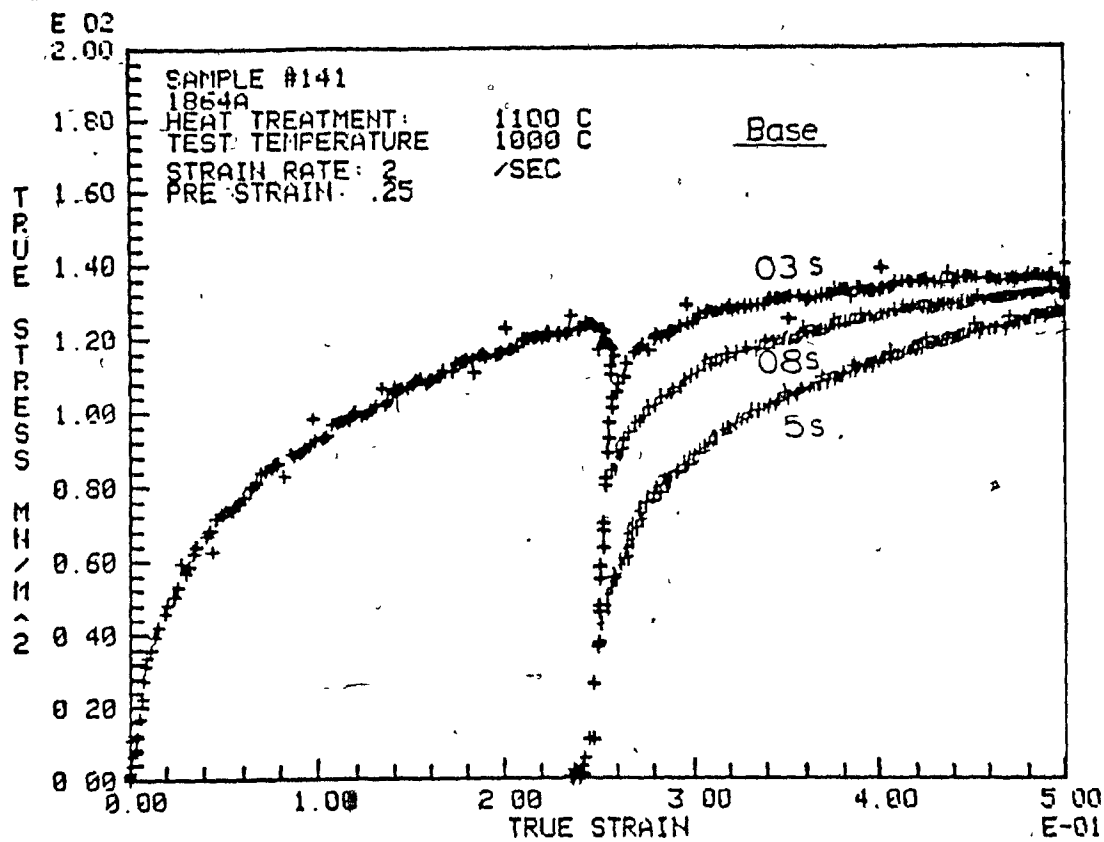


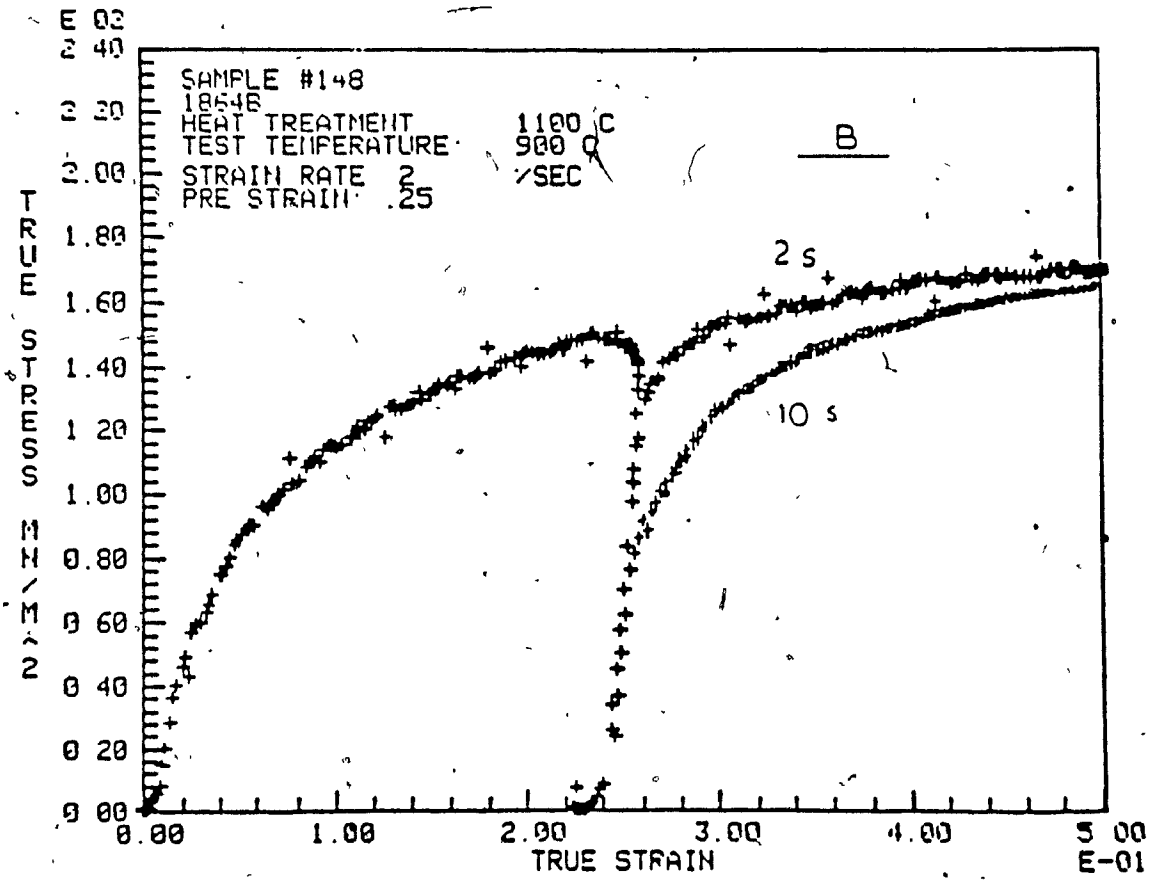
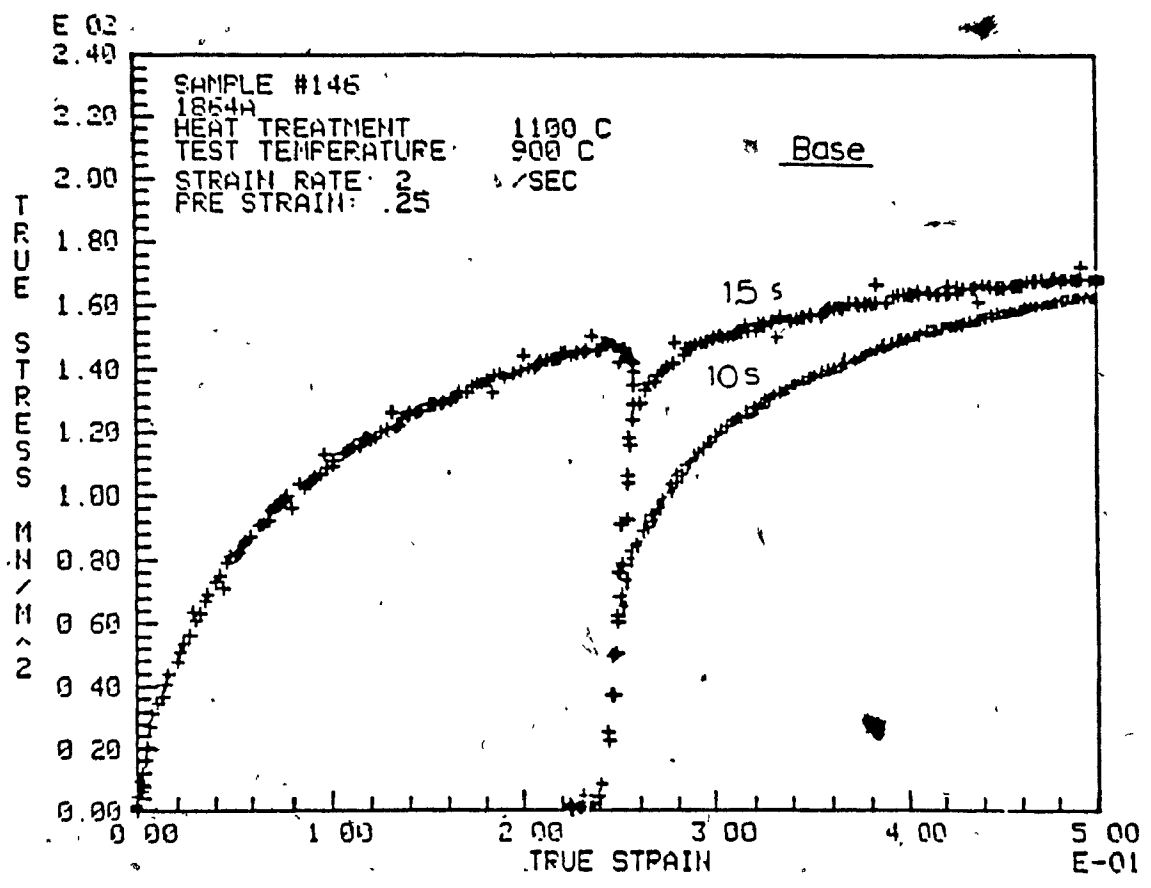






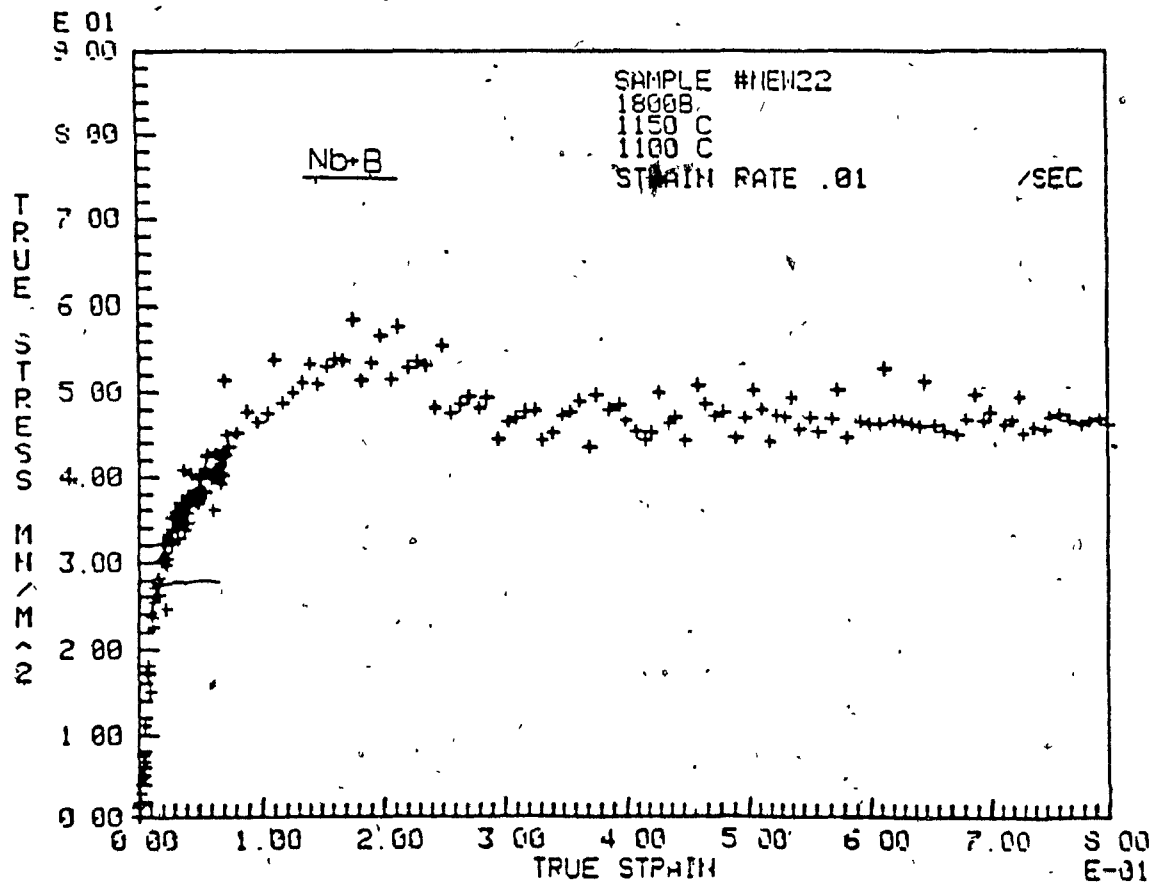
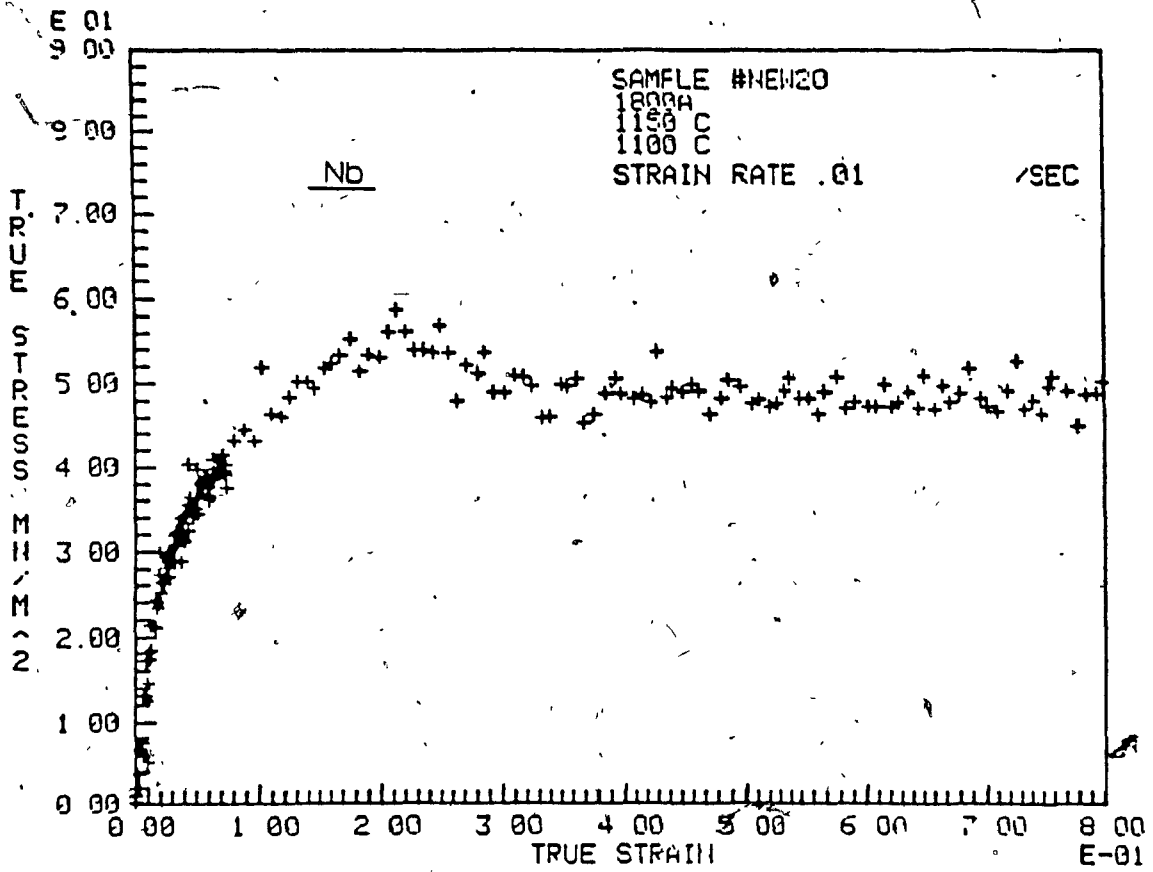


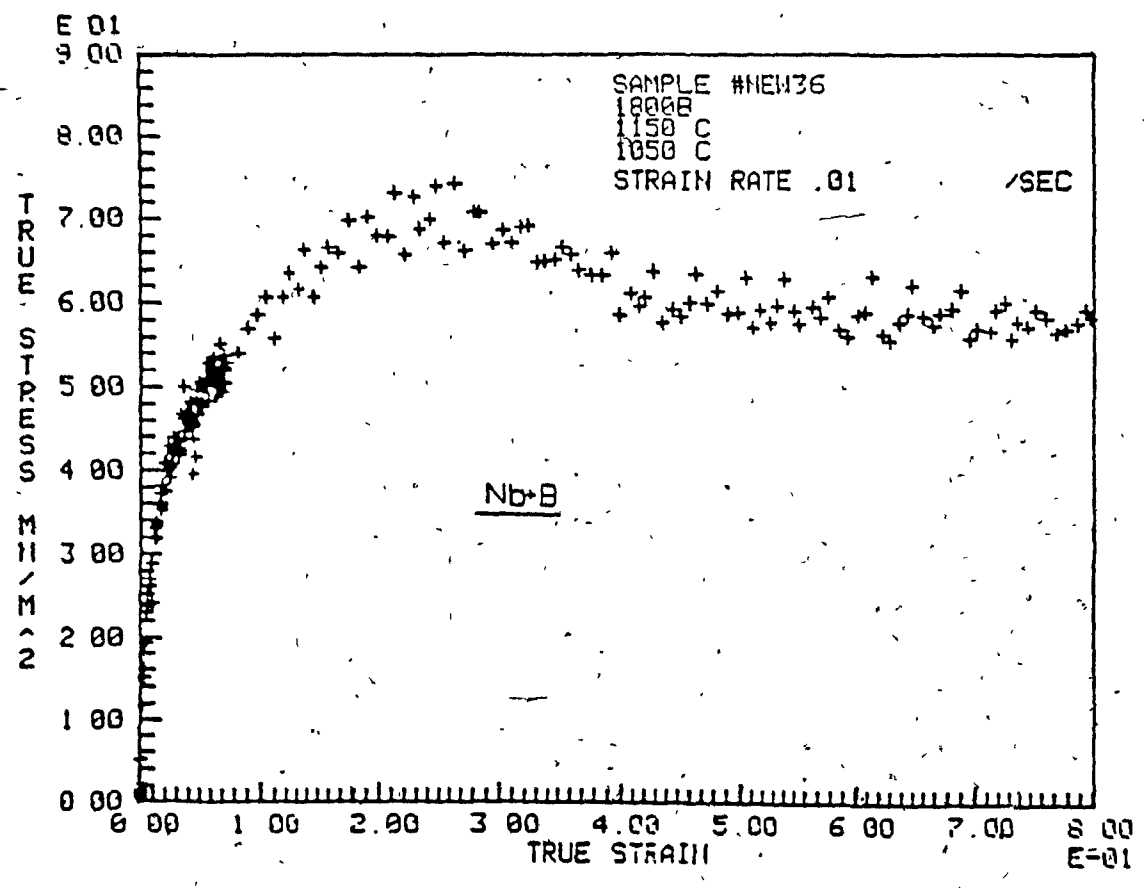
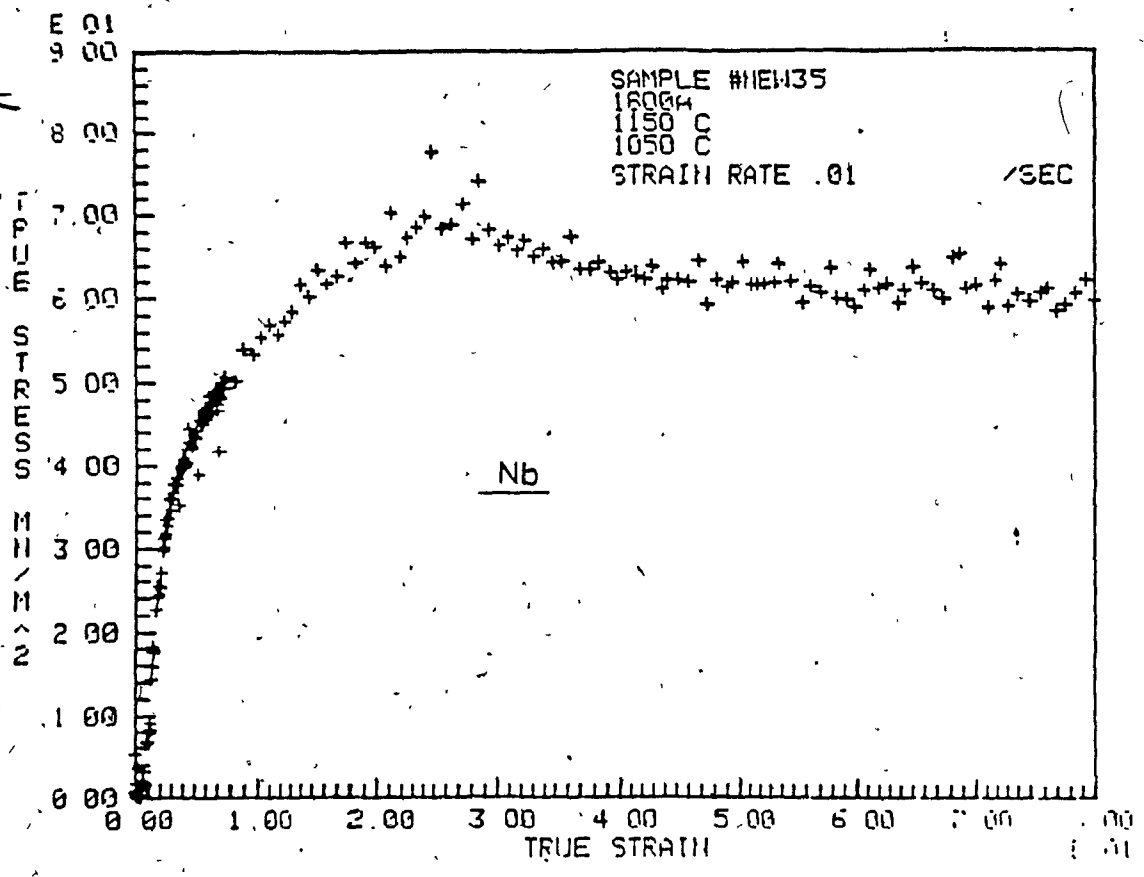


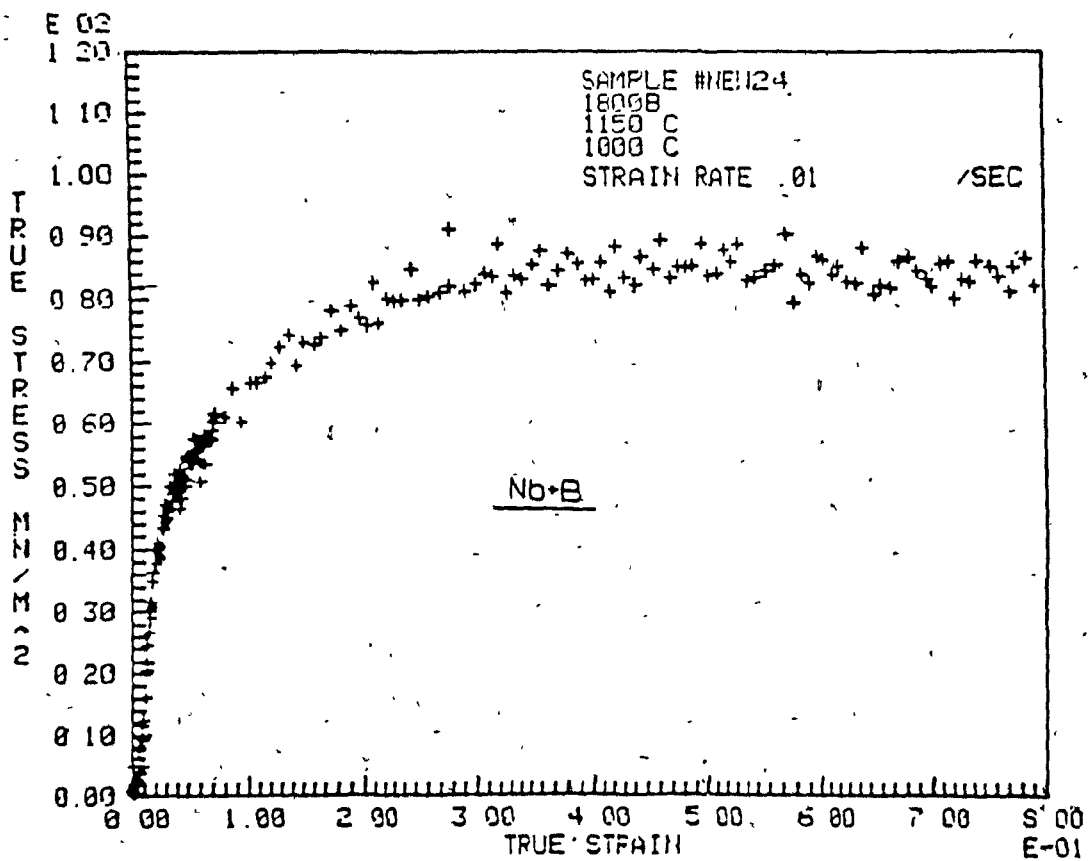
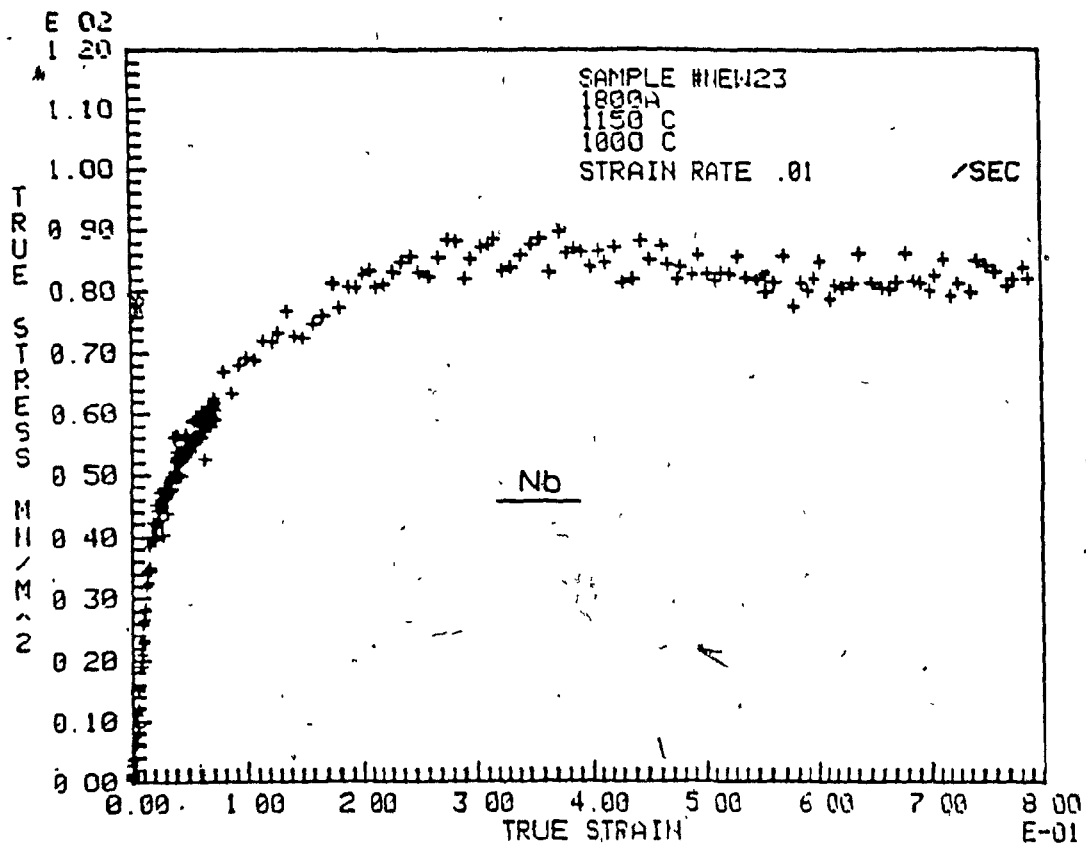


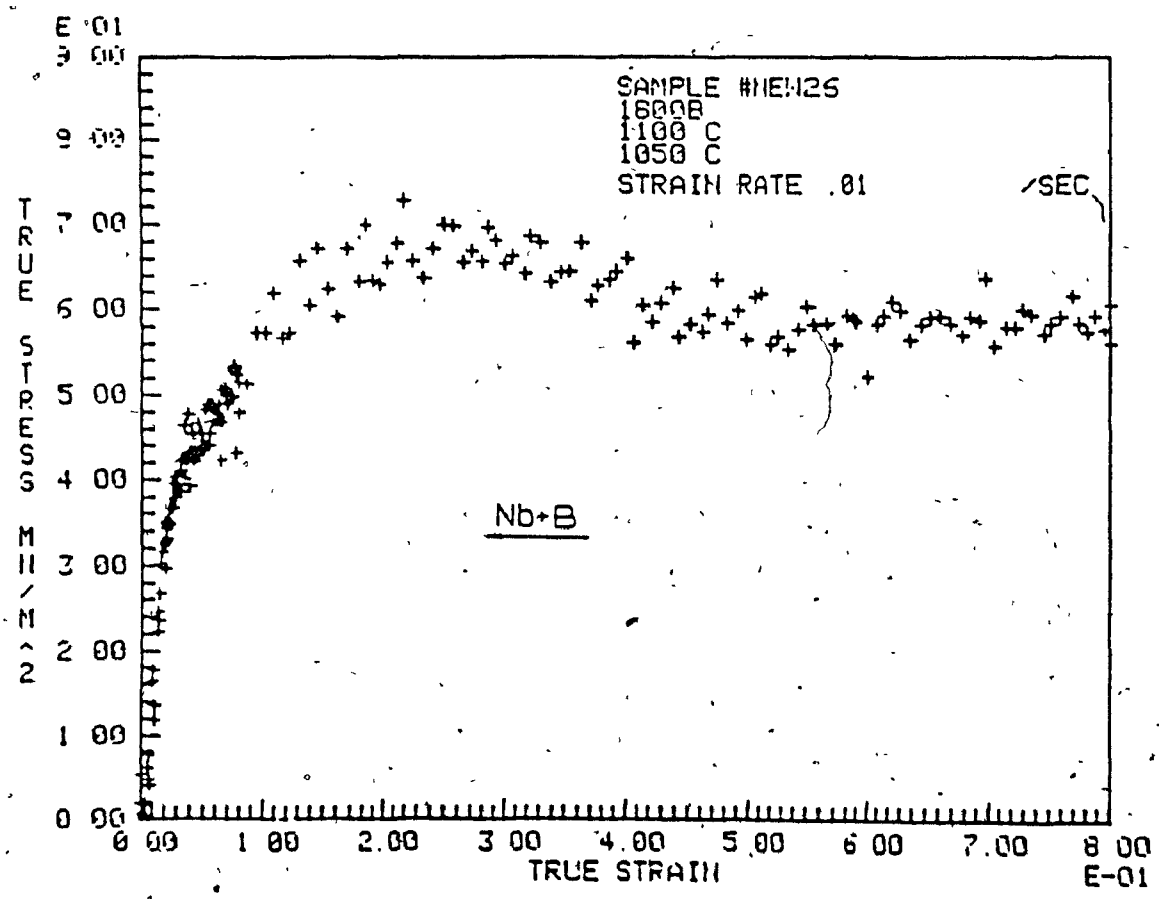
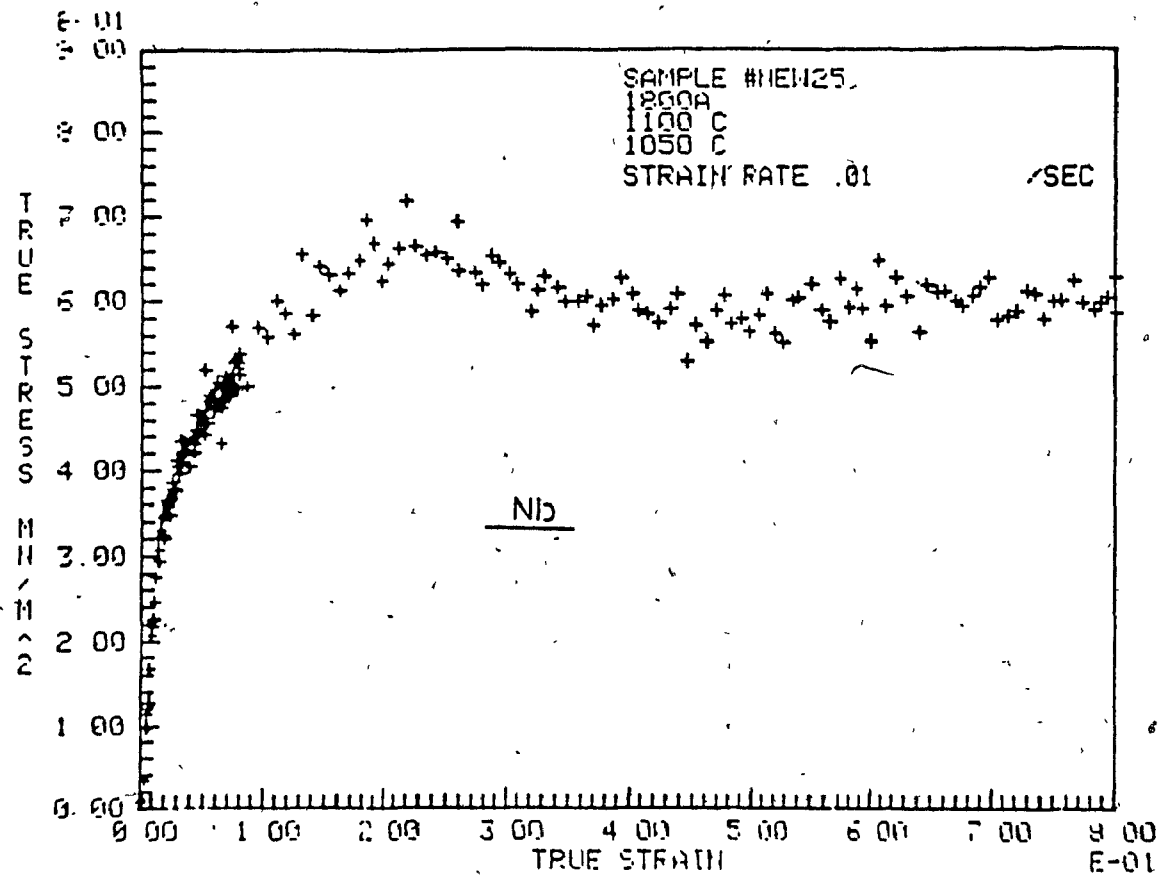
APPENDIX II

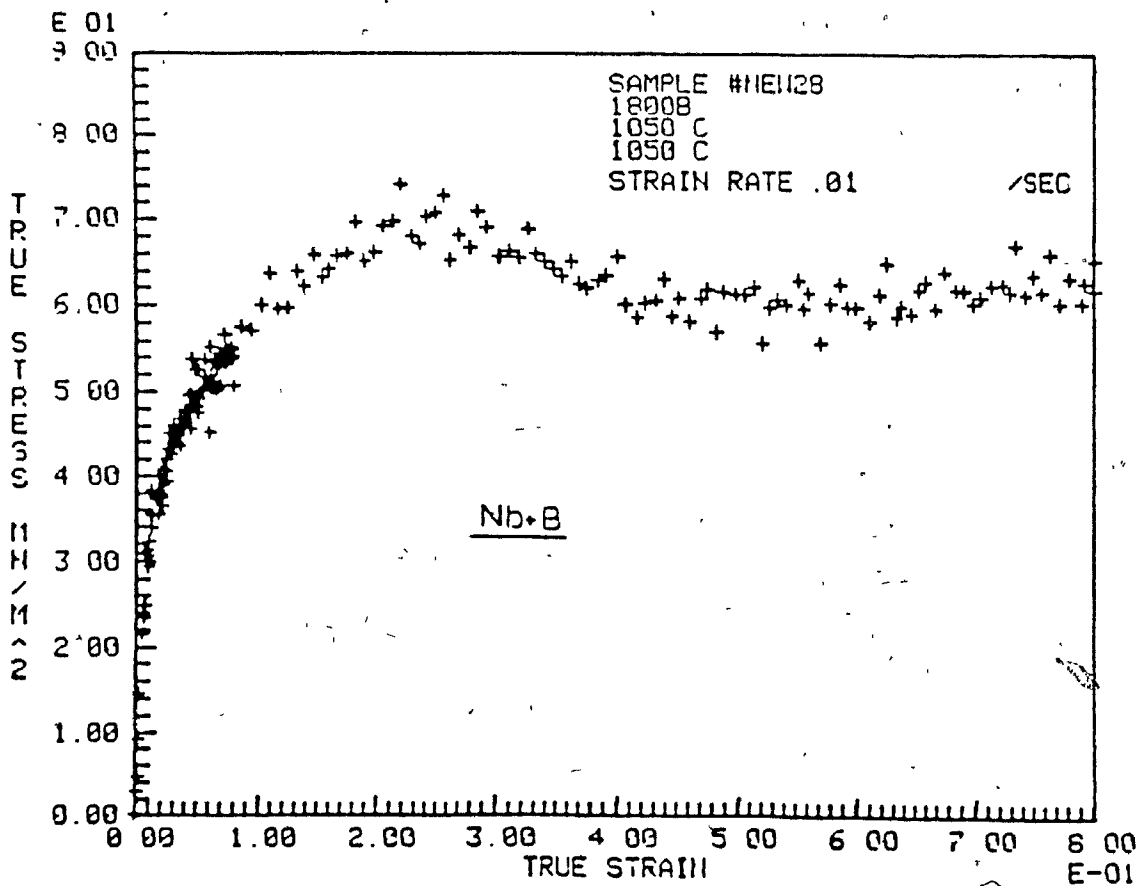
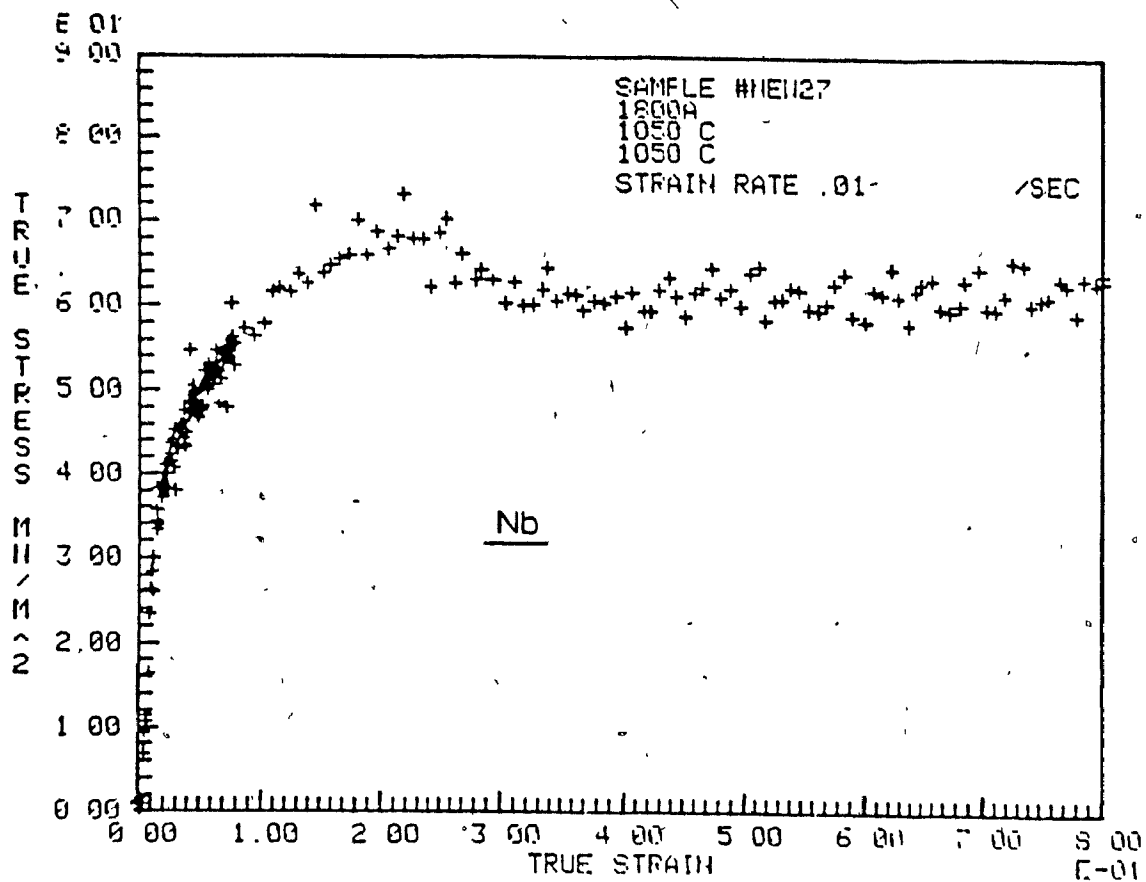
CONTINUOUSLY COMPRESSED TEST FLOW CURVES

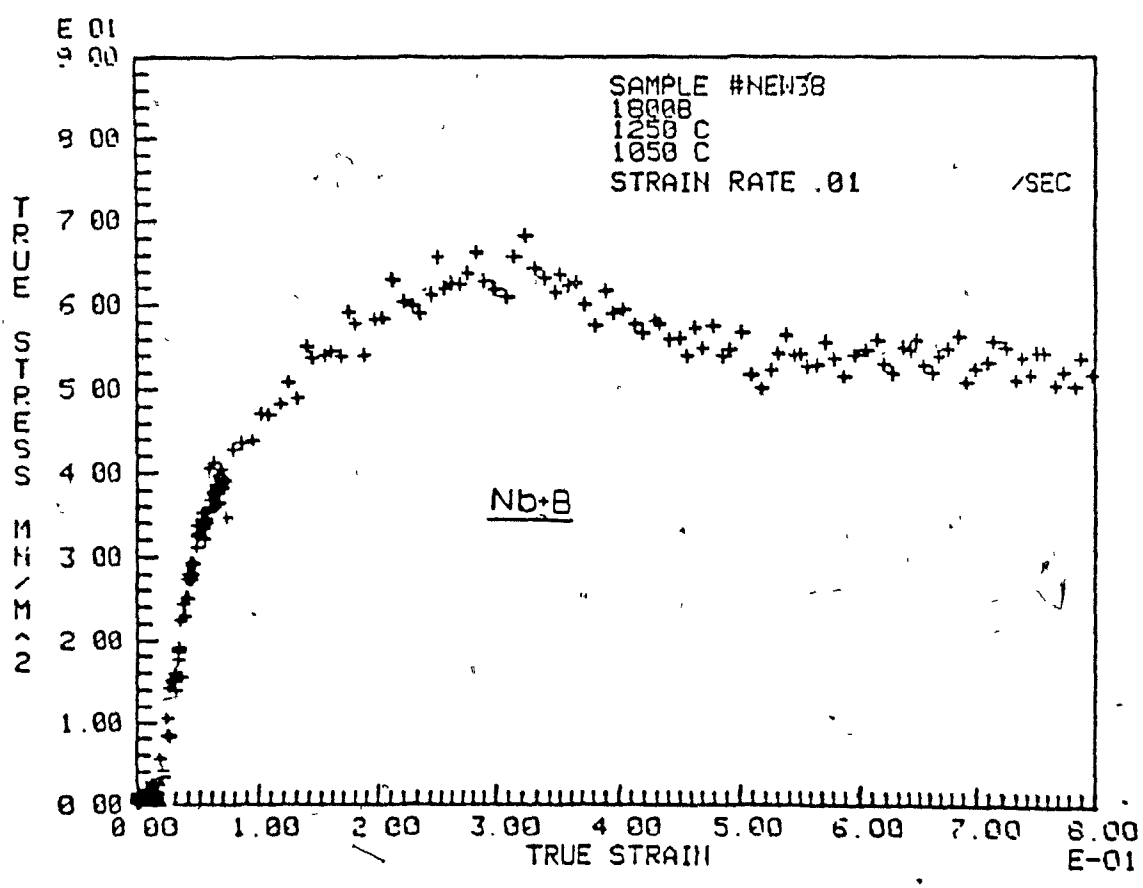
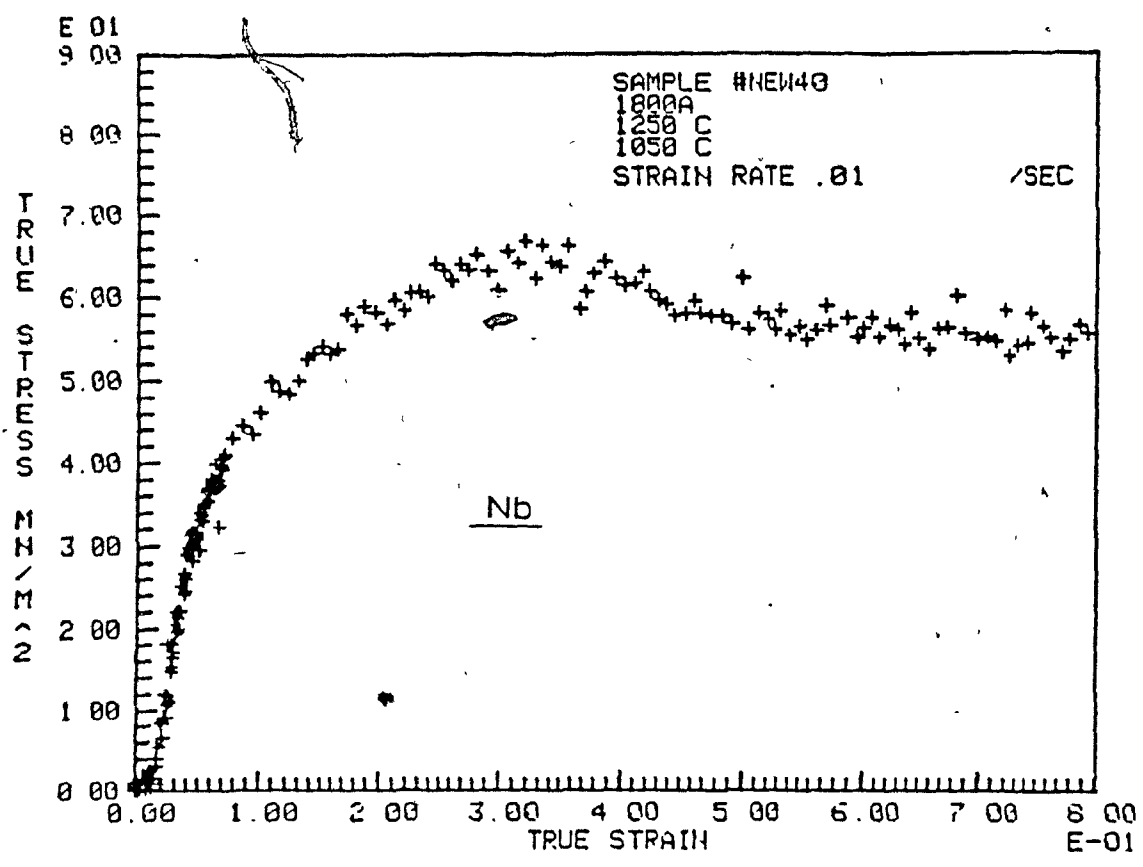


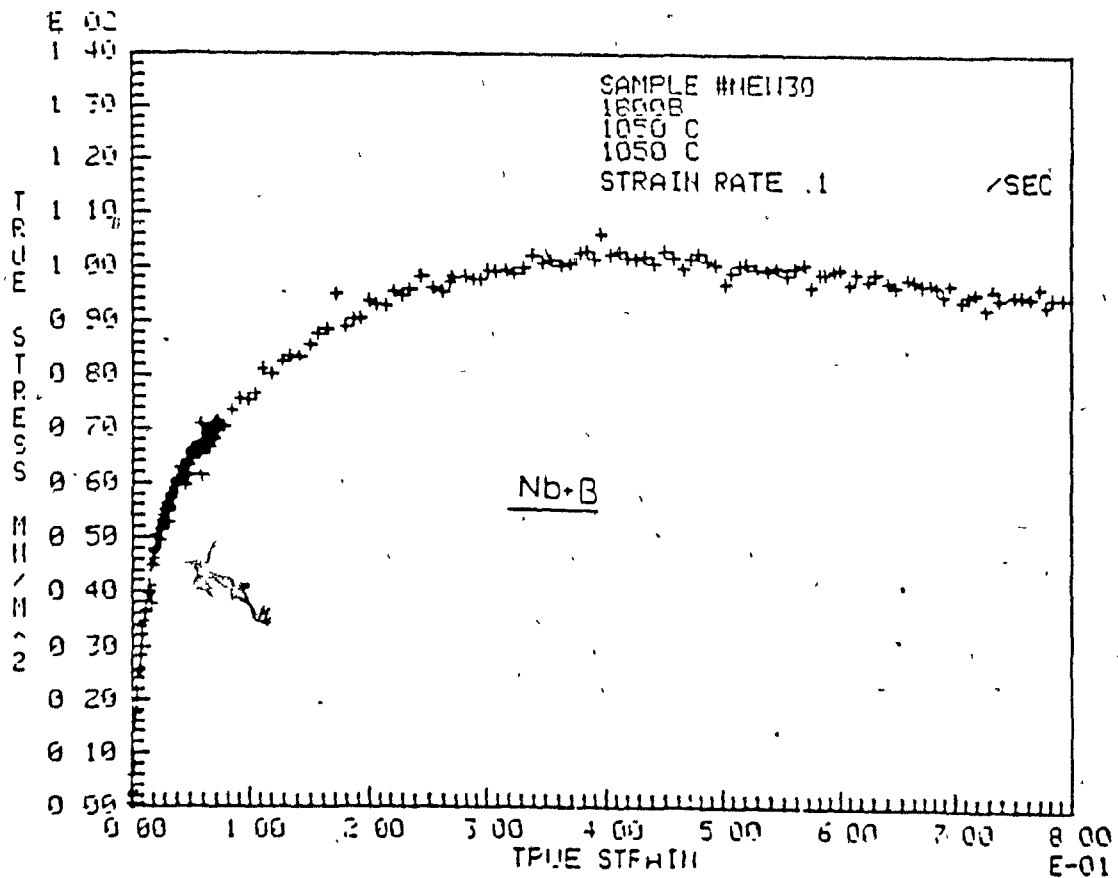
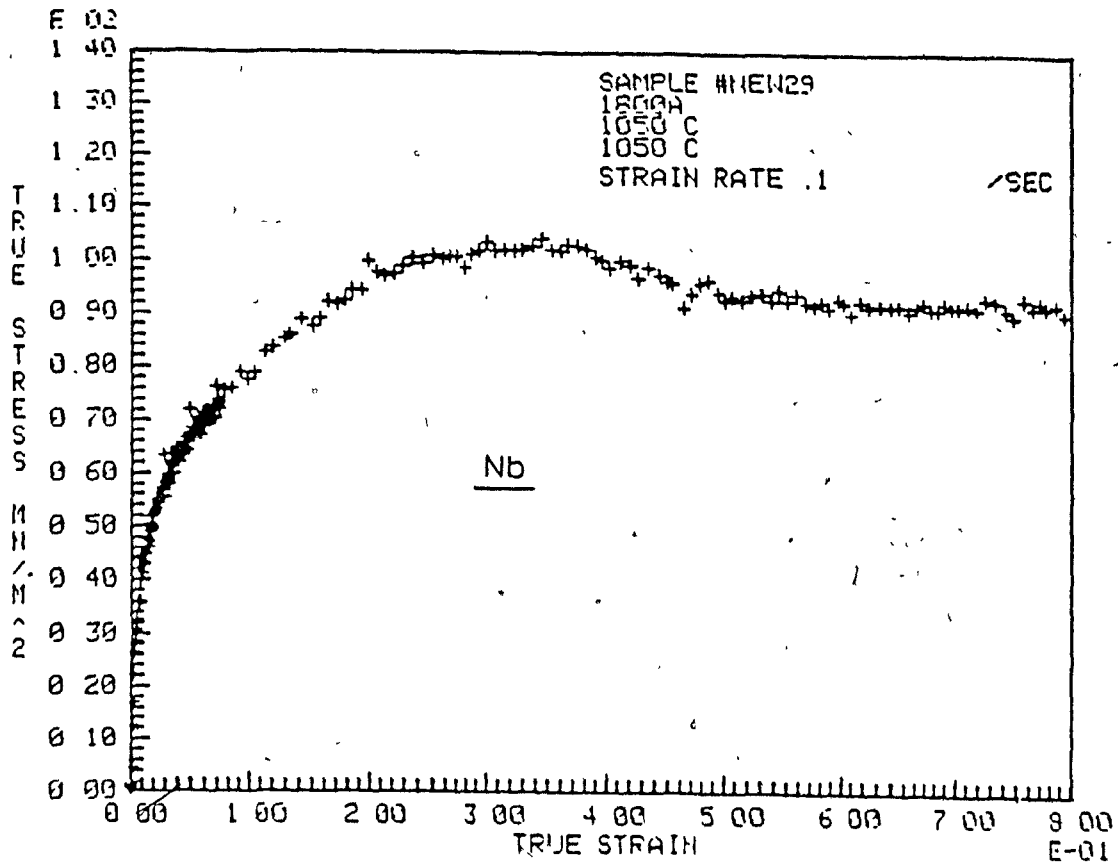


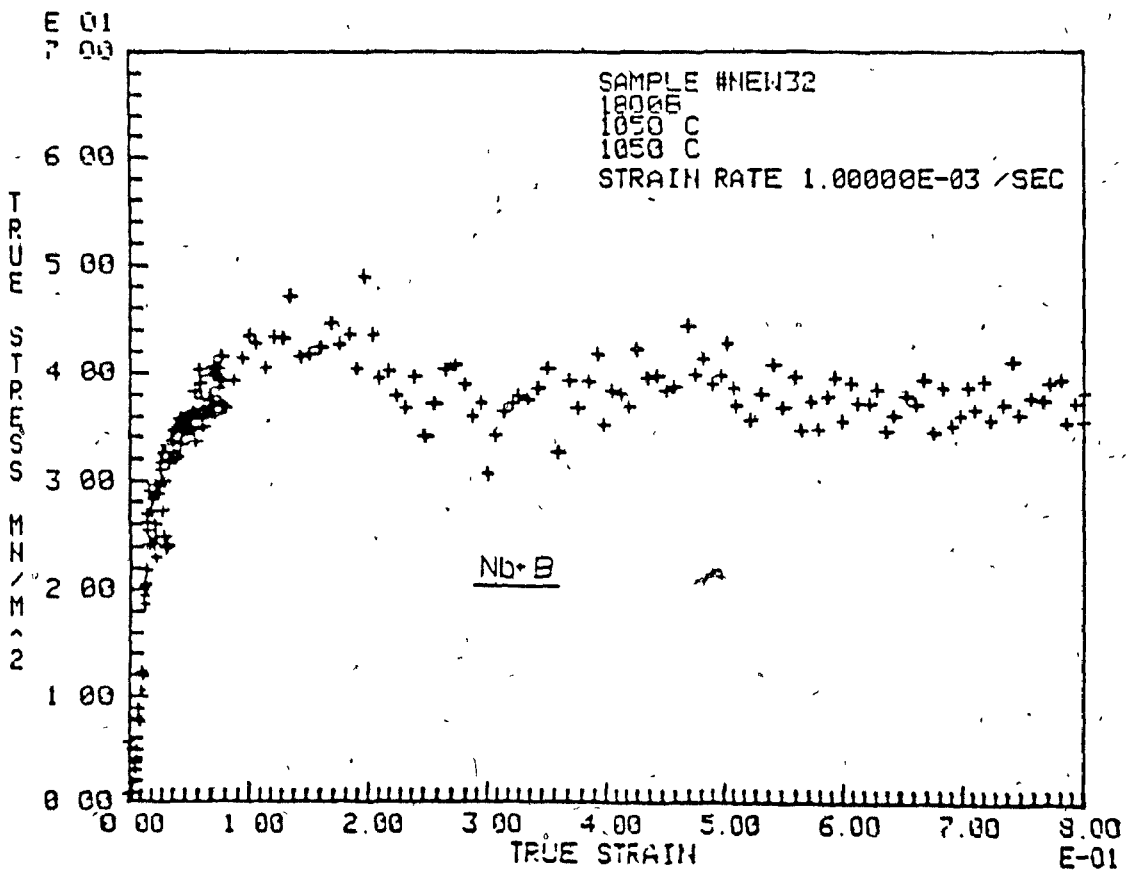
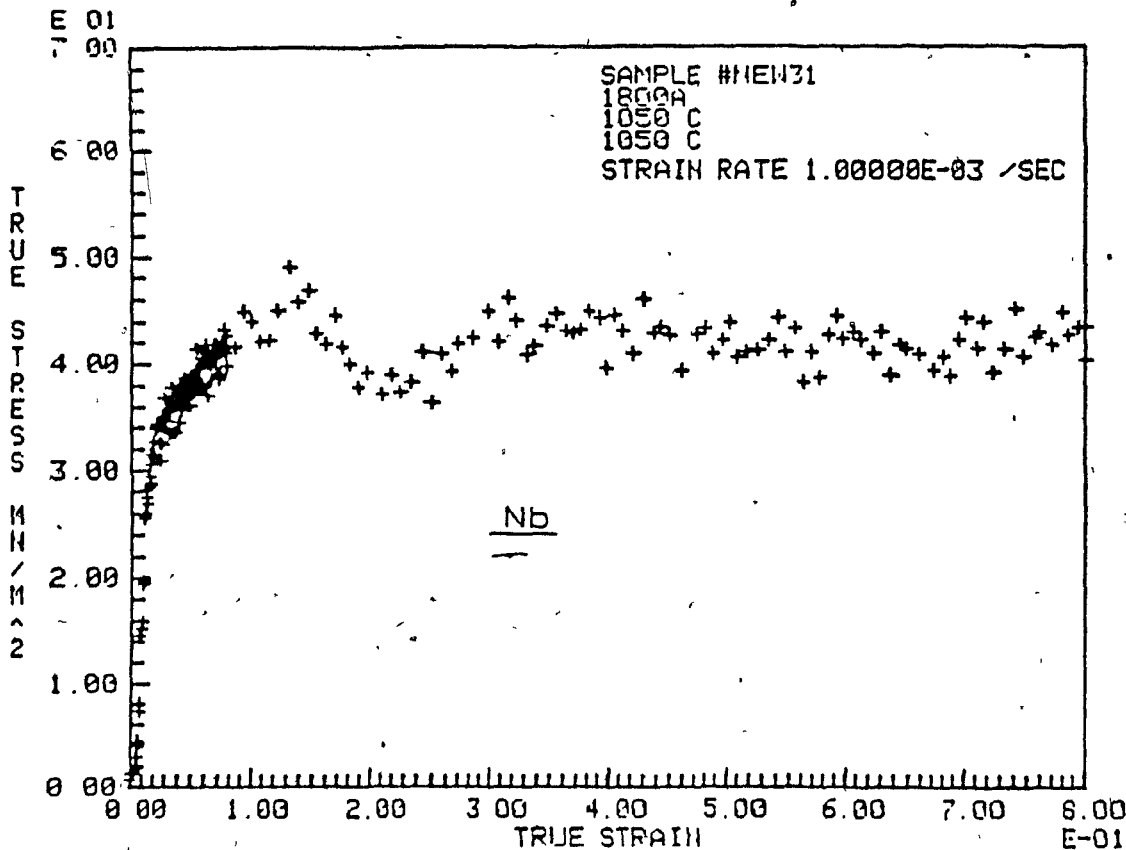


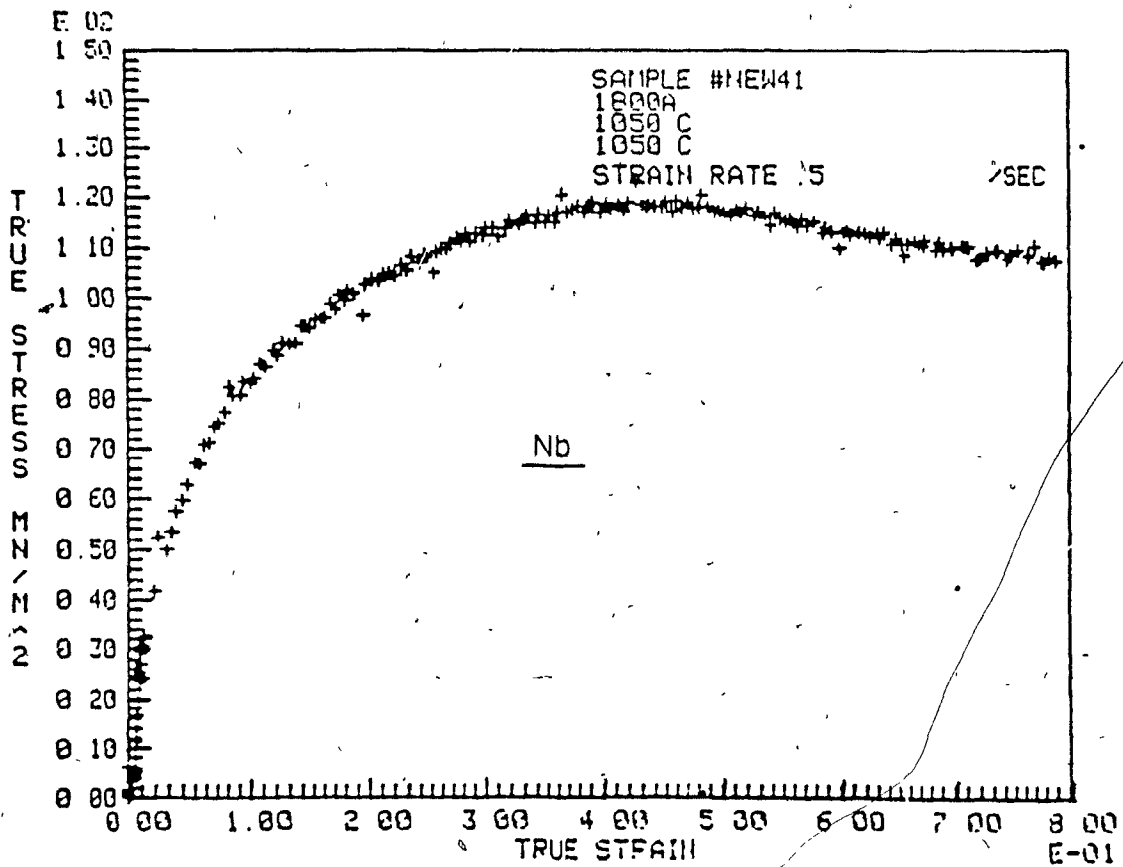
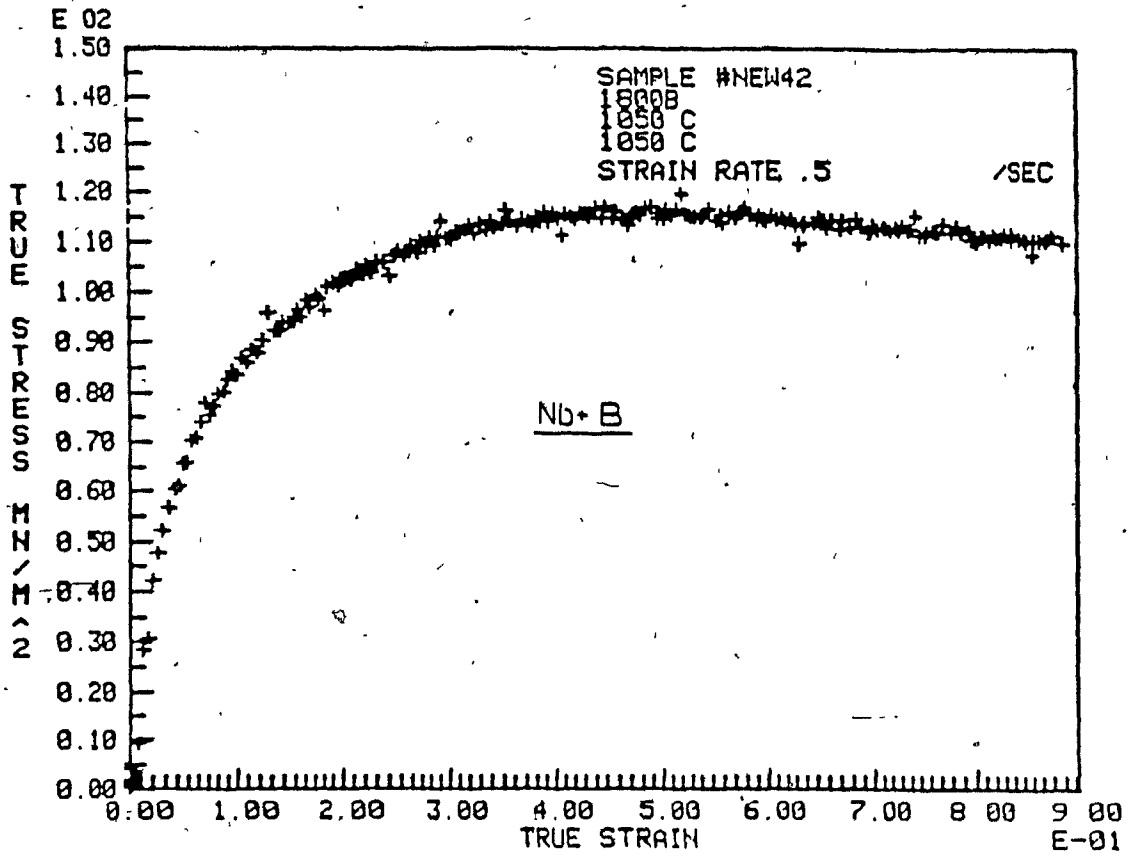












APPENDIX III**COMPUTER PROGRAMS FOR CONTINUOUS AND
INTERRUPTED COMPRESSION TESTS.**

CMPRES MTS BASIC V01B-020

20 REM
40 REM
60 REM
80 REM

A P P E N D I X II

100 REM
120 REM
140 REM
160 REM
180 REM
200 REM
220 REM
240 REM
260 REM

CONSTANT TRUE STRAIN RATE COMPRESSION TEST

PROGRAMMED BY ARMANDO SALINAS RODRIGUEZ

REVISED WITH THE ASSISTANCE OF RICHARD BERGLY OF MTS

280 DIM P(300), S(300), X(405), S3(300), E2(300), P3(300)

300 QUIT

320 FG1(0)

340 MSW1(2)

360 PRINT "WOULD YOU LIKE TO RECALL DATA FOR PLOTTING ? (Y OR 'CR')";

380 INPUT I1\$

400 REM

420 REM

EXPERIMENTAL CONDITIONS

440 REM

460 PRINT "TEST I.D."; \INPUT N\$

480 PRINT "MATERIAL "; \INPUT M\$

500 PRINT "HEAT TREATMENT "; \INPUT H\$

520 PRINT "TEST TEMPERATURE "; \INPUT T\$

540 PRINT "TOTAL STRAIN "; \INPUT E

560 PRINT "TRUE STRAIN RATE (1/SEC) "; \INPUT E1

580 PRINT "STROKE RANGE (MM)"; \INPUT R1

600 PRINT "LOAD RANGE (LBS) "; \INPUT R2

620 PRINT "SPECIMEN HEIGHT (MM)"; \INPUT L0

```

640 PRINT "SPECIMEN DIAMETER (MM)" \INPUT D0
660 AO=PI*D0^2/4
680 T=E/EI\K=2047/R1\K1=2047/R2
700 IF I1$<"Y" THEN 820
720 GOSUB 4340
740 GO TO 2380
760 REM -----
780 REM          CALCULATE FUNCTION GENERATOR PARAMETERS
800 REM -----
820 IF T>200 THEN 980
840 H=200
860 IF T>=100 THEN 1000
880 IF T>=50 THEN 1020
900 IF T>=10 THEN 1040
920 IF T>=5 THEN 960
930 IF T>=1 THEN 940
940 R=100\A4=0\H=100\GO TO 1060
960 R=50\A4=1\GO TO 1060
980 H=400\R=1\A4=7\GO TO 1060
1000 R=5\A4=5\GO TO 1060
1020 R=10\A4=4\GO TO 1060
1040 R=20\A4=2
1060 X(1)=4095*H/T/R/2
1080 U=T
1100 Y=10
1120 Y2=INT(9*Y+.5)
1140 REM -----
1160 REM          SET UP THE SYSTEM
1180 REM -----
1200 CNTR(3)\MSW1(2)\FG1(0)
1220 PRINT "CHECK THE FOLLOWING:" \PRINT
1240 PRINT "DC ERROR IS 0" ,
1260 PRINT "REMOTE/LOCAL SWITCH TO REMOTE"
1280 PRINT "SPAN 1 IS AT ZERO"
1300 PRINT "STROKE CONTROL" \PRINT

```

```

1320 PRINT "PRESS RETURN TO CONTINUE";\INPUT F$\PRINT
1340 PRINT "TURN ON THE HYDRAULICS";\PRINT
1360 PRINT "SET 'SPAN 1' TO 10"
1380 PRINT \PRINT "PRESS RETURN TO CONTINUE";\INPUT F$\PRINT
1400 REM-----
1420 REM          DUMP CHECK
1440 REM-----
1460 EDMP
1480 SOMPC(1,A)\IF A=0 THEN 1620
1500 PRINT "DUMP CARD PROBLEM. UNABLE TO FINISH TEST."
1520 PRINT \PRINT "TURN OFF THE HYDRAULICS."
1540 STOP
1560 REM-----
1580 REM          EXPERIMENT STARTS
1600 REM-----
1620 PRINT "IS THE PISTON IN THE RIGHT POSITION ?";\INPUT A2$
1640 IF A2$<"Y" THEN 1620
1660 DACQ(0,S1,2,0)
1680 FOR I=2 TO N+2
1700 X(I)=K*L0*(EXP(-E*(I-2)/N)-1)+S1+.5\NEXT I
1720 X=N+2
1740 TIME(Y,E9)\DACQ(3,P,0,U)\DACQ(6,S,2,2)
1760 FG1(X,1,7,A4)\STAR
1780 IF P<=60 THEN 1780
1800 QUIT(1)\P=61\S=P
1820 TIME(Y2,E8)\STAR
1840 BUF1(Z)\IF Z>-1 THEN 1840
1860 QUIT
1880 REM----- EXPERIMENT IS FINISHED -----
1900 DACQ(0,S4,2,0)
1920 REM----- RETURN PISTON TO INITIAL POSITION -----
1940 FOR I=S4 TO 0
1960 FG1(I)
1980 NEXT I
2000 PRINT "YOU CAN TURN OFF THE HYDRAULICS NOW"

```

```

2020 PRINT "HIT A 'CR' WHEN READY";\INPUT C$
2040 PRINT "WOULD YOU LIKE TO STORE THE DATA ?";\INPUT C$
2060 IF C$<"Y" THEN GO TO 2320
2080 REM -----
2100 REM          STORING EXPERIMENTAL DATA ON A FLOPPY DISK
2120 REM -----
2140 FOR I=P+2 TO 3 STEP -1\P(I)=P(I-2)\NEXT I
2160 P(1)=P\P(2)=S1\P=P+2
2180 OPEN "DX1:"&N$ FOR OUTPUT AS FILE #1
2200 AOUT(P,1,0,E4)
2220 AOUT(S,1,1,E5)
2240 CLOSE #1
2260 REM -----
2280 REM          CALCULATE TRUE STRESS & TRUE STRAIN
2300 REM -----
2320 PRINT "DO YOU WANT TO MAKE A CORRECTION FOR MACHINE COMPLIANCE ?"
2340 INPUT G$
2360 IF G$="NO" THEN 2700
2380 U=0
2400 FOR I=1 TO P
2420 L=ABS(P(I))*9.81/K1/1000/2.2046
2440 L1=6.58960E-05*L^2-.0164243*L
2460 L2=(S(I)-S1)/K
2480 L3=L0+L2-L1
2500 E2(I)=-LOG(L3/L0)
2520 S3(I)=1000*L*L3/A0/L0
2540 PRINT I,S3(I),E2(I)
2560 IF U<S3(I) THEN U=S3(I)
2580 NEXT I
2600 PRINT "MAX. STRESS : "U
2620 PRINT "ENTER MAX. STRESS LEVEL FOR SCAL";\INPUT U
2640 PRINT "ENTER STRESS AND STRAIN INCREMENTS";\INPUT Z1,Z2
2660 PRINT "ENTER 2D STRESS INCREMENT";\INPUT Z3
2680 GO TO 2780
2700 GOSUB 4540

```

```

2710 GO TO 2640
2720 REM -----
2740 REM          PLOT TRUE STRESS VS. TRUE STRAIN
2760 REM -----
2780 CNTR(3)\CNTR(0)\PHYL(100,900,80,700)
2800 SCAL(0,0,E,0,U)\CNTR(2)\PLOT(0,0)
2820 LABL("TRUE STRAIN","TRUE STRESS MN/M^2",22,21,1)
2840 LABL(" "," ",.01,23,3)\CNTR(0)\PLOT(0,0)
2860 PLOT(E,0)\PLOT(E,U)\PLOT(0,U)\PLOT(0,0)\CNTR(1)
2880 COMM("SAMPLE #",.5*E,.96*U)\PRINT N$
2900 COMM(M$,.5*E,.93*U)\COMM(H$,.5*E,.9*U)
2920 COMM(T$,.5*E,.87*U)\COMM("STRAIN RATE",.5*E,.83*U)
2940 PRINT E1\COMM(" /SEC",.9*E,.83*U)\CNTR(2)
2960 PLOT(0,0)\CNTR(0)
2980 FOR I=1 TO P\MARK("+",E2(I),S3(I))\NEXT I
3000 CNTR(2)\INPUT F$\CNTR(3)
3020 PRINT "WAS THE STRESS LEVEL OK. ? ";\INPUT J$
3040 IF J$<"Y" THEN 2620
3060 CNTR(3)
3080 REM -----
3100 REM          PLOT INITIAL YIELD REGION
3120 REM -----
3140 PRINT "INITIAL YIELD REGION"
3160 PRINT
3180 PRINT "ENTER MAX. STRESS LEVEL FOR SCAL";\INPUT U
3200 PRINT "ENTER MAX. STRAIN FOR SCAL";\INPUT E5
3220 PRINT "ENTER STRAIN INCREMENT";\INPUT Z4
3240 PRINT "ENTER 2D STRAIN INCREMENT";\INPUT Z5
3260 CNTR(3)
3280 CNTR(0)\PHYL(100,900,80,700)
3300 SCAL(0,0,E5,0,U)\CNTR(2)\PLOT(0,0)
3320 LABL("TRUE STRAIN","TRUE STRESS MN/M^2",24,21,1)
3340 LABL(" "," ",25,23,3)\CNTR(0)\PLOT(0,0)\PLOT(0,U)
3360 PLOT(E,U)\PLOT(E,0)\PLOT(0,0)\CNTR(1)
3380 COMM("INITIAL YIELD REGION",E5/2,.96*U)

```

```

3400 COMM("SAMPLE #",E5/2,.92*U)\PRINT N$\CNTR(2)
3420 PLOT(0,0)\CNTR(0)
3440 FOR I=1 TO P\MARK("+",E2(I),S3(I))\NEXT I
3460 CNTR(2)\INPUT F$\CNTR(3)\CNTR(1)
3480 PRINT "WAS THE PLOT OK. ?",\INPUT H$
3500 IF H$<"Y" THEN 3180
3520 REM -----
3540 REM          PLOT TRUE STRAIN VS. TIME
3560 REM -----
3580 U=T
3600 CNTR(3)\CNTR(0)\PHYL(100,900,80,700)
3620 SCAL(0,0,T,0,E)\CNTR(2)\PLOT(0,0)
3640 LABL("TIME","TRUE STRAIN",T/10,.1,1)
3660 CNTR(0)\PLOT(0,0)\PLOT(T,0)\PLOT(T,E)\PLOT(0,E)
3680 PLOT(0,0)\CNTR(0)\A8=0
3700 FOR I=1 TO 60
3720 A8=A8+U/1000\MARK(" ",A8,E2(I))\NEXT I
3740 FOR I=61 TO P\A8=A8+9*U/1000
3760 MARK(" ",A8,E2(I))\NEXT I
3780 CNTR(1)\COMM("STRAIN-TIME",.6*T,.96*E)
3800 COMM("SAMPLE # ",.6*T,.92*E)\PRINT N$
3820 REM -----
3840 REM          PLOT LOAD VS. TIME
3860 REM -----
3880 CNTR(2)\INPUT F$\CNTR(3)\CNTR(1)
3900 PRINT "ENTER ESTIMATED LOAD LEVEL IN LB FOR SCAL",\INPUT F
3920 CNTR(3)\CNTR(0)\PHYL(100,900,80,700)
3940 SCAL(0,0,T,0,F)\CNTR(2)\PLOT(0,0)
3960 LABL("TIME","LOAD",T/10,F/20,1)
3980 CNTR(0)\PLOT(0,0)\PLOT(T,0)\PLOT(0,0)
4000 PLOT(0,F)\PLOT(0,0)
4020 CNTR(0)\A8=0
4040 FOR I=1 TO 60
4060 A8=A8+U/1000\P3(I)=ABS(P(I))\K1
4080 MARK(" ",A8,P3(I))\NEXT I

```

```

4100 FOR I=61 TO P:A6=A6+9*U/1000
4120 P3(I)=ABS(P(I))*K1\MARK(" ",A6,P3(I))\NEXT I
4140 CNTR(1)\COMM("LOAD-TIME",.7*T,.96*F)
4160 COMM("SAMPLE # ",.7*T,.92*F)\PRINT N#
4180 CNTR(2)\INPUT F#\CNTR(3)\CNTR(1)
4200 PRINT "WAS THE LOAD LEVEL RIGHT ?";\INPUT W#
4220 IF W#<"Y" THEN GO TO 3900
4240 CNTR(3)
4260 STOP
4280 REM -----
4300 REM          RECALL PREVIOUS TEST DATA FOR PLOTTING
4320 REM -----
4340 OPEN "DX1."&N# FOR INPUT AS FILE #1
4360 AINP(P,1,0.E6)
4380 P=P(1)\S1=P(2)\P=P-2
4400 FOR I=1 TO P\P(I)=P(I+2)\NEXT I
4420 AINP(S,1,1.E7)
4440 CLOSE #1
4460 RETURN
4480 REM -----
4500 REM -----
4520 REM -----
4540 U=0
4560 FOR I=1 TO P
4580 L1=L0+(S(I)-S1)/K
4600 S3(I)=9.81*ABS(P(I))*L1/2.2046/A0/K1/L0
4620 E2(I)=-LOG(L1/L0)
4640 IF U<S3(I) THEN U=S3(I)
4660 NEXT I
4680 FOR I=1 TO P
4700 PRINT I,S3(I),E2(I)
4720 NEXT I
4740 PRINT "MAX. STRESS ",U
4760 PRINT "ENTER STRESS LEVEL FOR SCAL"\INPUT U
4780 RETURN

```

STATC MTS BASIC U01B-02D

```
10 REM-----
20 REM                I N T E R
30 REM
40 REM                THIS PROGRAM PROVIDES REAL TIME CONTROL AND DATA
50 REM                ACQUISITION, VIA AN MTS 433 HARDWARE INTERFACE UNIT,
60 REM                FOR CONSTANT TRUE STRAIN RATE INTERRUPTED COMPRESSION TESTING
70 REM                ON AN MTS CLOSED-LOOP ELECTROHYDRAULIC MATERIAL TESTING SYSTEM.
80 REM
85 REM                PROGRAMMED BY ALFRED A. MACCHIONE.
90 REM                REVISED WITH THE ASSISTANCE OF RICHARD BERGLY OF MTS.
95 REM-----
120 COMMON N$,M$,H$,T$,P,E,E1,R1,R2,R3,L0,D0,A0,T1,T2,T3,T
130 COMMON P1,P2,P3,P6,S1,S7,Y1,Y2,U2,B(610),C(610)
150 DIM X(610),Y(610),Z(610)
160 DIM B1(200),B2(210),B3(150),C1(200),C2(210),C3(150)
180 REM-----
190 REM                INPUT TEST CONDITIONS
200 REM-----
210 CNTR(3)\PRINT "SAMPLE NUMBER "\INPUT N$
220 PRINT "MATERIAL "\INPUT M$
230 PRINT "HEAT TREATMENT "\INPUT H$
240 PRINT "TEST TEMPERATURE "\INPUT T$
250 PRINT "PRE-STRAIN "\INPUT P
260 PRINT "TOTAL STRAIN "\INPUT E
270 PRINT "TRUE STRAIN RATE (1/SEC) "\INPUT E1
280 PRINT "STROKE RANGE (MM) "\INPUT R1
290 PRINT "LOAD RANGE (KN) "\INPUT R3\R2=R3/4.4482*1000
300 PRINT "SPECIMEN HEIGHT (MM) "\INPUT L0
310 PRINT "SPECIMEN DIAMETER (MM) "\INPUT D0
320 PRINT "HOLDING TIME DURING INTERRUPTION (SEC) "\INPUT T2
330 PRINT "STROKE OFFSET DURING INTERRUPTION (MACHINE UNITS) "\INPUT S7
```

```

340 CNTR(3)\MSW1(2)\FG1(0)
350 PRINT "CHECK THE FOLLOWING:"\PRINT
360 PRINT "DC ERROR IS 0"
370 PRINT "REMOTE/LOCAL SWITCH TO REMOTE"
380 PRINT "SPAN 1 IS AT ZERO"
390 PRINT "STROKE CONTROL"\PRINT
400 PRINT "PRESS RETURN TO CONTINUE";\INPUT F$\PRINT
410 PRINT "TURN ON THE HYDRAULICS"\PRINT
420 PRINT "SET 'SPAN 1' TO 10"
430 PRINT \PRINT "PRESS RETURN TO CONTINUE";\INPUT F$\PRINT
440 REM-----
450 REM          DUMP CHECK
460 REM-----
470 EOMP\SDMP(1,A)\IF A=0 THEN 530
480 PRINT "DUMP CARD PROBLEM. UNABLE TO FINISH TEST."
490 PRINT \PRINT "TURN OFF THE HYDRAULICS." \STOP
500 REM-----
510 REM          AUTOMATIC POSITIONING OF PISTON
520 REM-----
530 QUIT\B=0\C=0\B1=0\B2=0\B3=0\C1=0\C2=0\C3=0\CNTR(3)
540 DACQ(0,Q1,0,0)\DACQ(0,S1,2,0)
550 PRINT "THE PISTON IS AT "S1" MACHINE UNITS"
560 PRINT "THE LOAD ON THE SAMPLE IS "Q1" MACHINE UNITS"
570 PRINT "DO YOU WISH TO POSITION THE PISTON AUTOMATICALLY "
580 INPUT F$\IF F$="YES" THEN 610
590 PRINT "PRESS RETURN WHEN PISTON IS IN THE PROPER POSITION"
600 INPUT F$\GO TO 660
610 FOR I=1 TO 2047
620 IF I>1500 THEN STOP
630 I2=S1-I\EG1(I2)\DACQ(0,Q1,0,0)
640 IF Q1<=-4 THEN 660
650 NEXT I
660 DACQ(0,Q1,0,0)\DACQ(0,S1,2,0)
670 PRINT "THE PISTON IS AT "S1" MACHINE UNITS"
680 PRINT "THE LOAD ON THE SAMPLE IS "Q1" MACHINE UNITS"\PRINT

```

```

690 REM-----
700 REM          COMPUTE TEST PARAMETERS
710 REM-----
720 T1=P/E1\REM-CALCULATE DURATION OF PRE-STRAIN AND RESUMED TEST
730 T3=LOG(EXP(E-P)+S7*R1/2047*EXP(E)/L0)/E1\T=T1+T3
740 A0=PI*(D0/2)^2\N=INT(T*100)\R=100\A4=0
750 N1=INT(P/(E1*T)*N)\N3=N-N1
760 IF T2<10000 THEN 780
770 N2=600\R5=1\A3=7
780 IF T2<1000 THEN 800
790 N2=400\R5=1\A3=7\GO TO 890
800 IF T2<100 THEN 820
810 N2=90\R5=1\A3=7\GO TO 890
820 IF T2<10 THEN 840
830 N2=5\R5=1\A3=7\GO TO 890
840 IF T2<1 THEN 860
850 N2=2\R5=20\A3=2\GO TO 890
860 IF T2<.1 THEN 880
870 N2=2\R5=50\A3=1\GO TO 890
880 N2=1\R5=100\A3=0
890 X(1)=INT(2047*N1/(T1*R)+.5)\X=N1+1
900 Y(1)=INT(2047*N2/(T2*R5)+.5)\Y=N2+1
910 Z(1)=INT(2047*N3/(T3*R)+.5)\Z=N3+1
920 FOR I=2 TO N1+1
930 X(I)=2047/R1*L0*(EXP(-P*(I-1)/N1)-1)+S1\NEXT I
940 I2=X(N1+1)+S7
950 FOR I=2 TO N2+1
960 Y(I)=X(N1+1)+S7\NEXT I
970 M1=2047/R1*L0*(EXP(-P)-1)+S7
980 FOR I=2 TO N3+1
990 Z(I)=(2047/R1*L0*EXP(-P)+S7)*(EXP((-E1*T+P)*(I-1)/N3)-1)+S1+M1
1000 NEXT I
1010 Y1=INT(E/E1*40+.5)
1020 IF T2>.2 THEN GO TO 1040
1030 Y2=10\U2=1\GO TO 1310

```

```
1040 IF T2>.5 THEN GO TO 1060
1050 Y2=25\U2=1\GO TO 1310
1060 IF T2>1 THEN GO TO 1080
1070 Y2=50\U2=1\GO TO 1310
1080 IF T2>2 THEN GO TO 1100
1090 Y2=100\U2=1\GO TO 1310
1100 IF T2>4 THEN GO TO 1120
1110 Y2=200\U2=1\GO TO 1310
1120 IF T2>8 THEN GO TO 1140
1130 Y2=400\U2=1\GO TO 1310
1140 IF T2>16 THEN GO TO 1160
1150 Y2=800\U2=1\GO TO 1310
1160 IF T2>32 GO TO 1180
1170 Y2=1600\U2=1\GO TO 1310
1180 IF T2>64 GO TO 1200
1190 Y2=1600\U2=2\GO TO 1310
1200 IF T2>128 THEN GO TO 1220
1210 Y2=1600\U2=4\GO TO 1310
1220 IF T2>256 GO TO 1240
1230 Y2=1600\U2=8\GO TO 1310
1240 IF T2>512 GO TO 1260
1250 Y2=1600\U2=16\GO TO 1310
1260 IF T2>1024 THEN GO TO 1280
1270 Y2=1600\U2=32\GO TO 1310
1280 IF T2>10000 THEN GO TO 1300
1290 Y2=1600\U2=300\GO TO 1310
1300 Y2=1600\U2=3200
1310 REM-----
1320 REM COMPRESSION TEST
1330 REM-----
1340 PRINT "PRESS RETURN TO BEGIN COMPRESSION TEST"\INPUT F$
1350 TIME(Y1,E9)\DACQ(3,B1,0,1)\DACQ(6,C1,2,2)
1360 FG1(X,1,7,A4)\STAR
1370 BUF1(Z4)\IF Z4>-1 GO TO 1370
1380 FG1(I2)
```

```

1385 BUF1(Z7)\IF Z7>-1 GO TO 1385
1390 QUIT\P1=B1
1400 TIME(Y2,E8)\DACQ(3,B2,0,U2)\DACQ(6,C2,2,2)
1410 FG1(Y,1,7,A3)\STAR
1420 BUF1(Z5)\IF Z5>-1 GO TO 1420
1430 QUIT\P2=B2
1440 TIME(Y1,E7)\DACQ(3,B3,0,1)\DACQ(6,C3,2,2)
1450 FG1(Z,1,7,A4)\STAR
1460 BUF1(Z6)\IF Z6>-1 GO TO 1460
1470 QUIT\P3=B3
1480 FOR I=S4 TO 0\FG1(I)\NEXT I
1490 P6=P1+P2+P3\CNTR(3)
1500 PRINT "TEST TERMINATED"\PRINT
1510 PRINT "TURN OFF THE HYDRAULICS"
1520 REM-----
1530 REM          OUTPUT EXPERIMENTAL CONDITIONS
1540 REM-----
1550 PRINT "PRESS RETURN FOR OUTPUT"\INPUT F$\CNTR(3)
1560 PRINT "          INTERRUPTED COMPRESSION TESTING"\PRINT
1570 PRINT "SAMPLE NUMBER: "N$""
1580 PRINT "MATERIAL:      "M$""
1590 PRINT "HEAT TREATMENT:    "H$""
1600 PRINT "TEST TEMPERATURE:  "T$""\PRINT
1610 PRINT "TRUE STRAIN RATE: "E1" 1/SEC"
1620 PRINT "PRE-STRAIN: "P""
1630 PRINT "TOTAL STRAIN: "E""
1640 PRINT "TOTAL DEFORMATION TIME: "T" SECOND(S)"
1650 PRINT "INTERRUPTION TIME: "T2" SECOND(S)"\PRINT
1660 PRINT "STROKE OFFSET DURING INTERRUPTION: "S?" MACHINE UNIT(S)"
1670 PRINT "RATE OF DATA ACQUISITION"
1680 PRINT "   DURING LOADING:  "Y1" TENTHS MSEC"
1690 PRINT "   DURING INTERRUPT: "Y2" TENTHS MSEC"
1700 PRINT "   MULTIPLES OF "U2" "
1710 PRINT "STROKE RANGE: "R1" MM"
1720 PRINT "LOAD RANGE: "R3" KN"\PRINT

```

```

1730 PRINT "SPECIMEN HEIGHT: "L0" MM"
1740 PRINT "SPECIMEN DIAMETER: "D0" MM"
1750 PRINT "SPECIMEN CROSS-SECTIONAL AREA: "A0" SQUARE MM"\PRINT
1760 PRINT ""H1" LEVELS FOR FUNCTION GENERATION DURING PRE-STRAIN"
1770 PRINT ""H3" LEVELS FOR FUNCTION GENERATION DURING RESUMPTION"
1780 PRINT ""H2" LEVEL(S) FOR FUNCTION GENERATION DURING INTERRUPTION"
1790 PRINT "FREQUENCY RANGE DURING INTERRUPTION: "R5" HZ"\PRINT
1800 PRINT "DATA POINTS DURING PRE-STRAIN AND UNLOADING: "P1" "
1810 PRINT "DATA POINTS DURING INTERRUPTION: "P2" "
1820 PRINT "DATA POINTS DURING RESUMPTION: "P3" "\CNTR(4)\CNTR(3)
1830 FOR I=1 TO P1\B(I)=B1(I)\C(I)=C1(I)\NEXT I
1840 FOR I=1 TO P2\B(I+P1)=B2(I)\C(I+P1)=C2(I)\NEXT I
1850 FOR I=1 TO P3\B(I+P1+P2)=B3(I)\C(I+P1+P2)=C3(I)\NEXT I
1860 PRINT "DO YOU WANT TO SEE A PLOT OF THE EXPERIMENT "\INPUT D$
1870 IF D$="YES" THEN 1900
1880 IF D$="NO" THEN 1910
1890 GO TO 1870
1900 CHAIN "DX:PLOT.BAS" LINE 670
1910 PRINT "DO YOU WANT TO SAVE THE DATA "\INPUT F$
1920 IF F$="YES" THEN 1960
1930 IF F$="NO" THEN 1950
1940 GO TO 1910
1950 DUMP\MSW1(2)\STOP
1960 FOR I=P6+2 TO 3 STEP -1\C(I)=C(I-2)\NEXT I
1970 C(1)=P6\C(2)=S1
1980 OPEN "DX1:TEST"&N$ FOR OUTPUT AS FILE #1
1990 AOUT(C,1,0,E4)
2010 AOUT(B,1,2,E5)
2020 CLOSE #1\GO TO 1950
2030 END

```

READY

PLOT

NTS BASIC V01B-02D

```
100 REM-----
110 REM          P L O T
120 REM
130 REM          THIS PROGRAM PRODUCES GRAPHICAL OUTPUT OF EXPERIMENTAL
140 REM          DATA OBTAINED DURING INTERRUPTED COMPRESSION TESTING AND
150 REM          STORES DATA FOR FUTURE USE.  THE PROGRAM MAY ALSO BE USED
160 REM          TO RECALL OLD DATA FOR PLOTTING.
170 REM
180 REM          PROGRAMMED BY ALFRED A. MACCHIONE.
190 REM          REVISED WITH THE ASSISTANCE OF RICHARD BERGLY OF MTS.
200 REM-----
210 CNTR(3)
220 COMMON N$,M$,H$,T$,P,E,E1,R1,R2,R3,L0,D0,A0,T1,T2,T3,T
230 COMMON P1,P2,P3,P6,S1,S7,Y1,Y2,U2,B(610),C(610)
240 DIM S3(610),E2(610)
250 REM-----
260 REM          INPUT TEST PARAMETERS
270 REM-----
280 PRINT "SAMPLE #"\INPUT N$
290 PRINT "MATERIAL "\INPUT M$
300 PRINT "HEAT TREATMENT "\INPUT H$
310 PRINT "TEST TEMPERATURE "\INPUT T$
320 PRINT "PRE-STRAIN"\INPUT P
330 PRINT "TOTAL STRAIN"\INPUT E
340 PRINT "TRUE STRAIN RATE(1/SEC) "\INPUT E1
350 PRINT "STROKE RANGE (MM) "\INPUT R1
360 PRINT "LOAD RANGE (KN) "\INPUT R3\R2=R3/4.4482*1000
370 PRINT "SPECIMEN HEIGHT (MM) "\INPUT L0
380 PRINT "SPECIMEN DIAMETER (MM) "\INPUT D0
390 PRINT "HOLDING TIME DURING INTERRUPTION (SEC) "\INPUT T2
400 PRINT "STROKE OFFSET DURING INTERRUPTION (MACHINE UNITS) "\INPUT S7
```

405 CNTR(3)

```
410 PRINT "TIME INTERVAL FOR DATA ACQUISITION (TENTHS MSEC)"
420 PRINT "DURING LOADING, UNLOADING, RELOADING"\INPUT Y1
430 PRINT "DURING INTERRUPTION"\INPUT Y2
440 PRINT "DATA ACQUISITION MULTIPLIER DURING INTERRUPTION"\INPUT U2
450 PRINT "ENTER NUMBER OF DATA POINTS"
460 PRINT "DURING PRE-STRAIN AND UNLOADING"\INPUT P1
470 PRINT "DURING INTERRUPTION"\INPUT P2
480 PRINT "DURING RESUMPTION"\INPUT P3\ P6=P1+P2+P3
490 A0=PI*DB^2/4
500 T1=P/E1
510 T3=LOG(EXP(E-P)+S7*R1/2047*EXP(E)/L0)/E1
520 T=T1+T3
530 REM-----
540 REM DATA RECALL
550 REM-----
560 OPEN "DX1:TEST"&N$ FOR INPUT AS FILE #1
570 AINP(C,1,0,E6)
580 P6=C(1)\S1=C(2)
590 FOR I=3 TO P6\AINP(C,1,0,E6)\NEXT I
610 AINP(B,1,2,E7)
620 FOR I=1 TO P6\C(I)=C(I+2)\NEXT I
630 CLOSE #1
640 REM-----
650 REM TRUE STRESS TRUE STRAIN PLOT
660 REM-----
670 U=0
680 FOR I=1 TO P6\L1=L0+(C(I)-S1)/2047*R1
690 S3(I)=9.81*ABS(B(I))*L1/2.2046/A0/2047*R2/L0\E2(I)=-LOG(L1/L0)
700 IF U<S3(I) THEN U=S3(I)
710 NEXT I
720 U=4*U/3\PRINT "MAXIMUM STRESS",U," MPA"
730 PRINT "ENTER STRESS LIMIT (MPA)"\INPUT U
740 PRINT "ENTER STRESS INTERVAL (MPA)"\INPUT U1
750 PRINT "PRESS RETURN TO CONTINUE"
```

```

760 INPUT K$
770 CNTR(3)\CNTR(0)\PHYL(100,900,80,700)
780 SCAL(0,0.E,0.U)\CNTR(2)\PLOT(0,0)
790 LABL("TRUE STRAIN","TRUE STRESS MN/M^2",.1,U1,1)
800 LABL(" "," ",.02,U1/5,3)\CNTR(0)\PLOT(0,0)\PLOT(0,U)
810 PLOT(E,U)\PLOT(E,0)\PLOT(0,0)\CNTR(1)
820 COMM("SAMPLE #",.05*E,.96*U)\PRINT H$
830 COMM(M$,.05*E,.93*U)
840 COMM("HEAT TREATMENT:",.05*E,.9*U)\COMM(H$,.4*E,.9*U)
850 COMM("TEST TEMPERATURE:",.05*E,.87*U)
860 COMM(T$,.4*E,.87*U)\COMM("STRAIN RATE:",.05*E,.83*U)
870 PRINT E1\COMM("/SEC",.4*E,.83*U)
880 COMM("PRE STRAIN:",.05*E,.8*U)\PRINT P
890 COMM("HOLDING TIME:",.05*E,.77*U)\PRINT T2
900 COMM("SEC.",.4*E,.77*U)\CNTR(2)
910 PLOT(0,0)\CNTR(0)
920 FOR I=1 TO P1\MARK("+",E2(I),S3(I))\NEXT I
930 FOR I=P1+P2+1 TO P6\MARK("+",E2(I),S3(I))\NEXT I
940 INPUT F$\CNTR(3)
950 PRINT "ENTER STRESS LIMIT (MPA)"\INPUT U
960 PRINT "ENTER STRESS INTERVAL (MPA)"\INPUT U1
970 PRINT "PRESS RETURN TO CONTINUE"\INPUT F$
980 CNTR(3)\CNTR(0)
990 PHYL(100,900,80,700)\SCAL(0,.75*P,1.1*P,.5*U,U)
1000 CNTR(2)\PLOT(.75*P,.5*U)
1010 LABL("TRUE STRAIN","TRUE STRESS MN/M^2",.02,U1/5,1)
1020 LABL(" "," ",4.00000E-03,U1/20,3)\CNTR(0)\PLOT(.75*P,.5*U)
1030 PLOT(.75*P,U)
1040 PLOT(1.1*P,U)\PLOT(1.1*P,.5*U)\PLOT(.75*P,.5*U)
1050 CNTR(1)\COMM("SAMPLE #",.77*P,.95*U)
1060 PRINT H$\COMM("MAXIMUM FLOW STRESS DETERMINATION",.77*P,.92*U)
1070 CNTR(2)\PLOT(.75*P,.5*U3)\CNTR(0)
1080 FOR I=1 TO P1
1090 IF S3(I)<.5*U THEN GO TO 1110
1100 IF E2(I)>.75*P THEN MARK("+",E2(I),S3(I))

```

```

1110 NEXT I
1120 CNTR(2)\INPUT F$\CNTR(3)
1130 REM-----
1140 REM          INITIAL YIELD REGION - PRESTRAIN
1150 REM-----
1150 U=0
1170 FOR I=1 TO P1
1180 IF E2(I)>.075 THEN 1200
1190 IF U<S3(I) THEN U=S3(I)
1200 NEXT I
1210 U=4*U/3\PRINT "MAXIMUM STRESS",U
1220 PRINT "ENTER STRESS LIMIT (MPA)"\INPUT U
1230 PRINT "ENTER STRESS INTERVAL (MPA)"\INPUT U1
1240 CNTR(3)\CNTR(0)\PHYL(100,900,80,700)
1250 SCAL(0,0, .075,0,U)\CNTR(2)\PLOT(0,0)
1260 LABL("TRUE STRAIN","TRUE STRESS MN/M^2",.01,U1,1)
1270 LABL(" "," ",2.00000E-03,U1/5,3)\CNTR(0)\PLOT(0,0)
1280 PLOT(0,U)\PLOT(.075,U)\PLOT(.075,0)\PLOT(0,0)\CNTR(1)
1290 COMM("INITIAL YIELD REGION",4.00000E-03,.96*U)
1300 COMM("PRE-STRAIN",4.00000E-03,.92*U)
1310 COMM("SAMPLE #",4.00000E-03,.88*U)\PRINT N$
1320 CNTR(2)\PLOT(0,0)\CNTR(0)
1330 FOR I=1 TO P1\IF E2(I)<=.075 THEN MARK("+",E2(I),S3(I))\NEXT I
1340 CNTR(2)\INPUT F$
1350 CNTR(3)
1360 REM-----
1370 REM          INITIAL YIELD REGION - RESUMPTION
1380 REM-----
1390 U=0
1400 FOR I=P1+P2+1 TO P6
1410 IF U<S3(I) THEN U=S3(I)
1420 NEXT I
1430 U=4*U/3
1440 PRINT "MAXIMUM STRESS",U," MPA"
1450 PRINT "ENTER STRESS LIMIT (MPA)"\INPUT U

```

```

1460 PRINT "ENTER STRESS INTERVAL (MPA)"\INPUT U1
1470 CNTR(3)\CNTR(0)\PHYL(100,900,80,700)
1480 SCAL(0,P-.02,P+.055,0,U)\CNTR(2)\PLOT(P-.02,0)
1490 LABL("TRUE STRAIN","TRUE STRESS MN/M^2",.01,U1,1)
1500 LABL(" " " ",2.00000E-03,U1/5,3)\CNTR(0)\PLOT(P-.02,0)
1510 PLOT(P-.02,U)\PLOT(P+.055,U)\PLOT(P+.055,0)
1515 PLOT(P-.02,0)
1520 CNTR(1)\COMM("INITIAL YIELD REGION",P+4.00000E-03,.96*U)
1530 COMM("RESUMPTION",P+4.00000E-03,.92*U)
1540 COMM("SAMPLE #",P+4.00000E-03,.88*U)\PRINT N$
1550 CNTR(2)\PLOT(0,0)\CNTR(0)
1560 FOR I=P1+P2+1 TO P6\IF E2(I)<=P+.075 THEN MARK("+",E2(I),S3(I))
1570 NEXT I
1580 REM-----
1590 REM          LOAD-TIME AND STRAIN-TIME PLOT
1600 REM-----
1610 CNTR(2)\INPUT F$\CNTR(3)
1620 T5=(P1+P3)*Y1/10000
1630 PRINT "TEST TIME: "T5" SEC"
1640 PRINT "ENTER TIME SCALE (SEC)"\INPUT T4
1650 PRINT "ENTER TIME INTERVAL (SEC)"\INPUT T6
1660 CNTR(3)\CNTR(0)\PHYL(100,900,80,700)
1670 SCAL(0,0,T4,0,E)\CNTR(2)\PLOT(0,0)
1680 CNTR(0)\PLOT(0,0)\PLOT(0,E)\PLOT(T4,E)\PLOT(T4,0)
1690 PLOT(0,0)\LABL("TIME","TRUE STRAIN",T6,.1,1)
1700 LABL(" " " ",T6/10,.05,3)
1710 COMM("SAMPLE #",.1*T4,.9*E)\PRINT N$
1720 CNTR(0)\A8=0
1730 FOR I=1 TO P1
1740 MARK(" ",A8,E2(I))
1750 A8=A8+Y1/10000
1760 NEXT I
1770 FOR I=P1+P2+1 TO P6
1780 MARK(" ",A8,E2(I))
1790 A8=A8+Y1/10000

```

```

1800 NEXT I
1810 CNTR(2)\INPUT F$\CNTR(3)
1820 U=0
1830 FOR I=1 TO P6
1840 U2=ABS(B(I))/2047*R3
1850 IF U<U2 THEN U=U2
1860 NEXT I
1870 T5=((P1+P3)*Y1+P2*Y2*U2)/10000
1880 PRINT "TOTAL TIME:"T5" SEC."
1890 PRINT "ENTER TIME SCALE (SEC.)"\INPUT T4
1900 PRINT "ENTER TIME INTERVAL (SEC.)"\INPUT T6
1910 PRINT "MAXIMUM LOAD",U," KN"
1920 PRINT "ENTER MAXIMUM LOAD LEVEL (KN)"\INPUT U
1930 PRINT "ENTER LOAD INTERVAL (KN)"\INPUT U1
1940 CNTR(3)\CNTR(0)\PHYL(100,900,80,700)
1950 SCAL(0,0,T4,0,U)\CNTR(2)\PLOT(0,0)
1960 LABL("TIME","LOAD KN",T6,U1,1)
1970 LABL(" "," ",T6/10,U1/5,3)
1980 CNTR(0)\PLOT(0,0)\PLOT(0,U)\PLOT(T4,U)\PLOT(T4,0)
1990 PLOT(0,0)\CNTR(1)\COMM("SAMPLE #",.1*T4,.9*U)\PRINT N$\AB=0
2000 FOR I=1 TO P1\P5=ABS(B(I))/2047*R3
2010 MARK(" ",AB,P5)\AB=AB+Y1/10000\nEXT I
2020 FOR I=P1+1 TO P2
2030 P5=ABS(B(I))/2047*R3
2040 MARK(" ",AB,P5)\AB=AB+Y2*U2/10000
2050 NEXT I
2060 FOR I=P1+P2+1 TO P6
2070 P5=ABS(B(I))/2047*R3
2080 MARK(" ",AB,P5)\AB=AB+Y1/10000
2090 NEXT I
2100 CNTR(2)\INPUT F$\CNTR(3)
2110 REM-----
2120 REM DATA STORAGE
2130 REM-----
2140 PRINT "DO YOU WANT TO SAVE THE DATA?"\INPUT F$

```

```
2150 IF F$="YES" THEN 2190
2160 IF F$="NO" THEN 2180
2170 GO TO 2140
2180 DUMP\MSN1(2)\STOP
2190 FOR I=P6+2 TO 3 STEP -1\C(I)=C(I-2)\NEXT I
2200 C(1)=P6\C(2)=S1
2210 OPEN "DX1:TST"&N$ FOR OUTPUT AS FILE #1
2220 AOUT(C,1,0,E4)
2240 AOUT(B,1,2,E5)
2250 CLOSE #1
2260 GO TO 2180
2270 END
```

READY